

Sensing Voltage Dynamics with Differential Intensity Surface Plasmon Resonance System

by Sidahmed Abayzeed, MSc

Thesis submitted to the University of Nottingham
for the degree of Doctor of Philosophy

December 2015

Abstract

The voltage sensitivity of surface plasmon resonance is investigated as a potential method for label-free detection of the dynamics of the transmembrane potential of excitable cells. Development of such a method for reliable detection of these signals is one of the modern challenges in biomedical research. Since they are key physiological signals that control a number of vital functions, they report the system's behaviour in health and disease. Labelling methods are currently used to detect these signals, often with subcellular resolution, but fluorescent labels (i) have a short lifetime, which limits the timescale of the experiments and (ii) they can be toxic to cells.

Surface plasmon resonance (SPR) is sensitive to perturbation of the potential at the metal-electrolyte interface. This perturbation alters the charge density of the interface, which is characterised by the well-known theory of the double-layer capacitance. Charge density on the electrolyte side is mirrored by an excess or deficiency of electrons at the metal surface. The latter shifts the resonance conditions of surface plasmons. To assess SPR capacity in the detection of the electrical signals from excitable cells, the limit of voltage detection of the SPR has to be well-characterised.

First, theoretical approaches were used to estimate the voltage detection limit of surface plasmon resonance. Since different SPR systems are characterised by their refractive index sensitivity, voltage sensitivity was estimated relative to the equivalent refractive index change. This approach enables the generalisation of the outputs of this research regardless of the SPR system. A one-dimensional multilayer model was used combining the electrical properties of the metal-electrolyte interface to the optical properties of the layers. The model was used to calculate the voltage-induced changes to the optical properties of the metal surface. Then, light reflectivity from the model structure was calculated using the transfer matrix of the structure and Fresnel equations to produce SPR curves (reflectance versus angle of incidence) for

a series of voltages in the double-layer charging range (±200mV).

Second, to test the theoretical estimates of the voltage sensitivity of surface plasmon resonance, a differential-intensity surface plasmon resonance (DI-SPR) system was constructed and combined with an electrochemical system to control the potential at the metal-electrolyte interface. The detection limit of the system is in the range of 3×10^{-7} - 5×10^{-7} refractive index units (RIUs) at 1 kHz bandwidth, without averaging.

Third, the SPR response to changes in the interfacial voltage was evaluated experimentally. A non-linear relation between the obtained SPR response (i.e. resonance position shift) and the applied voltage is observed; this nonlinearity is attributed to the nonlinear behaviour of the interfacial capacitance as confirmed by comparison with theoretical analysis. Experimental voltage sensitivity of SPR systems is 1mV that maps to 0.4 μRIUs. This figure is close to the expected theoretical estimate: 0.5 μRIUs for 1 mV. These figures were calculated 9 seconds after applying a direct voltage. However, voltage sensitivity is reduced by an order of magnitude when a pulse of duration of 5ms is applied. This drop is attributed to the extended response time of the sensor. This effect shifts the detection limits of the system to 10 mV for the case of these signals.

The coupling efficiency of the energy transfer between the capacitance of the cell membrane and the double-layer capacitance is estimated to be 2%; therefore, a 100 mV change in the transmembrane potential is reduced to 2mV at the electrode-electrolyte interface. Real-time detection of the electrical signals requires at least 4 $\times 10^{-8}$ RIUs, per the region of interest. In conclusion, with the current detection limit of 10 mV per 5 ms, real-time detection of the electrical potential of cardiac cells is still possible since their action potential extends for 200ms. Moreover, the signal-to-noise ratio can be improved by averaging over 100 samples of the signal for 10 times sensitivity enhancement.

Acknowledgements

First of all, I would like to express my sincere appreciation and thanks to Dr Chung See, Dr Richard Smith and Dr Kevin Webb for their supervision, guidance and encouragement throughout my PhD study. I would like to express my deep gratitude to Prof Michael Somekh for supervision, advice and guidance during my first year of the research and for his continuous support, discussions and enthusiasm. I was privileged to be mentored and directed by such a helpful and supportive multidisciplinary team of supervisors.

I would also like to acknowledge the members of IBOIS for their help and assistance, many thanks to Dr Roger Light, Dr Joana Richens, Prof Melissa Mather, Dr Jing Zhang, Dr Darren Albutt and Mr David Jung. I would like to thank Prof Matt Clark for providing the access to facilities of SIOS (sputtering, 3D printing). My gratitude to the members of SIOS for their kind support and help; thanks to Dr Rikesh Patel, Dr Theodosia Stratoudaki and Mr Fernando Perez.

I would like to thank the Faculty of Engineering, the University of Nottingham, Engineering and Physical Sciences Research Council (EPSRC) and Gordon Memorial College Trust (GMCTF) for funding my PhD. I would like also to thank the Graduate School and the Advanced Optics Group for giving me the opportunity to attend conferences.

Many thanks to all my friends; you really made life and work easier for me. Tremendous thanks to my father, mother and siblings for their patience, continuous support, help and prayers. Thanks to my beloved family for their tremendous support; special thanks to my wife for her continuous encouragement and invaluable support through all the ups and downs of this work especially during the writing-up time.

Publications and Conference Presentations

Sidahmed Abayzeed, Richard J Smith, Kevin F Webb, Michael G Somekh, Chung See,
Responsivity of the Differential-intensity Surface Plasmon Resonance Instrument, *sensors and acuators B: chemical* (under review).

Sidahmed Abayzeed, Richard Smith, Kevin Webb, Michael Somekh and Chung See
Voltage Sensitivity of Surface Plasmon Resonance for Biological Applications
Abstract published at 3rd IEEE Biophotonics Conference, Florence, Italy, May 2015

Grants

EPSRC/Nottingham Doctoral Prize fellowship (2016 -2018), total award of 56,827K *titled* Plasmonic-based Electrochemical Impedance Micro-Spectroscopy of Living Cells

List of Abbreviations, Symbols and Definitions

SPs	Surface plasmons
SPR	Surface plasmon resonance
RIUs	Refractive index units
ITO	Indium-tin-oxide
TF	Thomas-Fermi length
DI-SPR	Differential-intensity SPR
FWHM	Full width at half maximum
WE	Working electrode
RE	Reference electrode
CE	Counter electrode
$\theta(deg)$	Angle of incidence
$\theta_0\ (deg)$	SPR angle
$\Delta\theta_0\ (deg)$	Shift/change in the SPR angle
A and B	Signals of the units the bi-cell detector.
$\Delta\frac{A-B}{A+B}$	DI-SPR output signal
$\eta\ (deg^{-1})$	Responsivity defined as DI-SPR signal units per one degree of resonance shift.
Angular width (θ_w)	The half of the convergence angle of the excitation beam.
Double-layer capacitor	A nano-scale capacitor that is formed at the metal-electrolyte interface.
Stern-Gouy-Chapman models	Electrochemistry models that characterise the behaviour of double-layer capacitors.
Transmembrane potential	A term defines the "voltage" across the cell membrane.
Excitable cells	Cells that can be stimulated to be electrically active by reversing the polarity of their cell membranes.

Contents

Abstract i

Acknowledgements iii

1 Introduction 1

1.1 Motivation 1

1.1.1 The electrical activity of excitable cells 2

1.1.2 Measurement of the electrical activity of excitable cells 6

1.2 Objectives and experimental strategy 9

1.2.1 Objectives 9

1.2.2 Theoretical and experimental strategy 9

1.3 Thesis layout 11

2 Background and Literature Review 13

2.1 Surface plasmon resonance 13

2.1.1 Basic principles and optical configurations 13

2.1.2 Detection approaches 19

2.1.3 Factors that influence the sensitivity of surface plasmon resonance 27

2.1.4 Factors that influence the spatial resolution of surface plasmon resonance 29

2.1.5 Applications of surface plasmon resonance 30

2.2 Plasmonic detection of bioelectrical activity 33

2.2.1 Experimental attempts 33
2.2.2 Theoretical work 38
2.3 A Review of plasmonic voltage sensing 41
2.3.1 History of voltage measurement using the optical properties of metals 41
2.3.2 Modelling the interfacial double-layer capacitance 44
2.3.3 Plasmonic systems for voltage sensing 52

3 Theoretical Analysis of Voltage Sensitivity of Surface Plasmon Resonance 56
3.1 Introduction 56
3.2 Modelling of voltage sensitivity of SPR 59
3.2.1 Reflection of light from the mulitlayer sensing structure 61
3.2.2 The bulk layer of the gold thin film 64
3.2.3 Thomas-Fermi screening layer 64
3.2.4 The Debye layer 65
3.2.5 The bulk electrolyte 66
3.3 Modelling procedure and outputs 67
3.3.1 Charge density at the electrode-electrolyte interface 69
3.3.2 Properties of free electrons in the metal surface 70
3.3.3 Optical properties of the metal surface 71
3.4 Voltage-modified surface plasmon resonance curve 74
3.5 Effects of electrolyte concentration on voltage sensitivity 82
3.6 Effect of temperature on voltage sensing 85
3.7 Conclusions 90

4 Design and Testing of Voltage-sensitive Surface Plasmon Resonance System 92
4.1 Introduction 92
4.2 System Design 93

4.2.1 Optical system design 93
4.2.2 Processing of the bi-cell photodiode outputs 97
4.2.3 Electrochemical system 105
4.3 Sample preparation and testing 108
4.4 Testing of the voltage sensing system 110
4.5 Conclusions 113

5 Sensitivity of Differential-intensity Surface Plasmon Resonance Applied to Voltage Sensing 114
5.1 Introduction 114
5.2 Theoretical and experimental evaluation of the DI-SPR's responsivity 115
5.2.1 Theoretical analysis of the responsivity 115
5.2.2 Experimental evaluation of the responsivity 119
5.2.3 A comparison between the theoretical and the experimental responsivity 120
5.2.4 The effect of the sensing structure on the responsivity 122
5.3 Noise performance of the DI-SPR system 126
5.3.1 Theoretical Analysis of DI-SPR noise 126
5.3.2 Experimental validation of the analytical expressions of the DI-SPR noise 128
5.3.3 Evaluation of the noise of the DI-SPR using bi-cell detector . 135
5.4 Sensitivity 146
5.5 The effect of the balance of the bi-cell detector on the sensitivity of the DI-SPR 149
5.5.1 Refractive index stepping 149
5.5.2 DI-SPR signal and noise when the detector is unbalanced . . . 150
5.5.3 Responsivity and the dynamic range 155
5.6 Conclusions 158

6 Experimental Voltage Sensitivity of Surface Plasmon Resonance

Systems **160**

6.1 Introduction 160

6.2 Materials and Methods 161

6.3 Results and Discussions 163

6.3.1 Voltage-dependant voltage responsivity 163

6.3.2 Voltage-equivalent refractive index units 166

6.3.3 Response time of the gold-electrolyte interface to applied voltage 170

6.3.4 Charge mass at the interface 175

6.3.5 SPR Sensitivity to fast voltage signals 178

6.3.6 Imaging locally-applied voltage 182

7 Conclusions and Future Work **186**

7.1 Conclusions 186

7.2 Future Work 191

A Derivation of the second-order expression for the DI-SPR responsivity **197**

Bibliography **197**

Chapter 1

Introduction

1.1 Motivation

Electrical signals play a critical role in coordinating the function of many physiological systems. For instance, they control the mechanical work produced by the heart receiving and pumping blood from/to the lungs and the rest of the body [1]. Another important example is their central role in the function of the nervous system. They are the core signals in the communication of sensory information to the central nervous system, the processing of this information and the actuation of various systems to perform specific motor functions [1]. At the cell level, electrical signals are generated by excitable cells: a class of cells whose transmembrane polarity is reversed in response to chemical [2] or electrical excitation [3]. Neurons, cardiac cells and skeletal muscle cells are examples of excitable cells. The excitation of these cells generates the action potential which is characterised by depolarisation of the cell membrane (i.e. transmembrane potential is changed from ∼-60mV to ∼+40mV) for a duration in the range of 5 - 200 ms depending on the type of cell.

As discussed in more detail in Sec. 1.1.2, reliable measurements of the action potential at cellular levels will pave the way towards understanding the behaviour of a

number of physiological systems in health and disease [4]. This project is directed at the development of a new method for measuring these signals. Before highlighting the advantages and the potential of the proposed technique, an introduction to the nature of these signals is presented.

1.1.1 The electrical activity of excitable cells

Electrical signals in biological systems, in contrast to electronic systems, are mediated by ions rather than free electrons. In these systems, there are mainly three charge carriers: sodium, potassium and calcium ions. The generation of these electrical signals originates from the nature of the structure of the cell membrane. Cell membrane is a dielectric that separates the conducting intracellular medium from the conducting extracellular environment. This membrane contains many specialised pores, channels, constructed from specialised proteins. Some of these channels are ion-specific and they can be activated (to open or close) by mechanical, electrical or chemical stimuli [5]. This sophisticated channel structure and charge carriers represent the fundamentals of the bioelectrical signals as will be described for the two cases below.

The state of an excitable cell in terms of electrical activity is a key contribution to the integral message or the output of the physiological system (information in the case of neurons or contraction-relaxation in the case of cardiac myocytes) [6, 7]. In the following paragraph, we will briefly describe the electrical activity of two main cells; neurons and cardiac myocytes.

Neurons are excitable cells, which are the main specialized cells in the nervous system. The active ion pumps, an energy-driven ion channels in the cell membrane, maintain the concentration gradient of sodium and potassium ions across the cell membrane as shown in Fig. 1.1. This concentration gradient leads to a resting membrane potential of $\sim$ -60 mV. As shown in Fig. 1.1, the sodium concentration

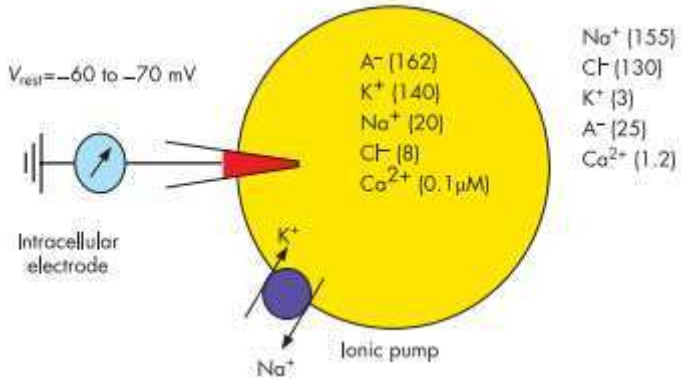


Figure 1.1: A cartoon for a neuron that illustrates the extracellular and intracellular concentration of the different current carriers. All concentrations are in mM unless they are otherwise specified. Diagram taken from [8]

is higher outside the cell than inside while the potassium concentration is higher inside the cell than outside. Each of these two ions has a voltage-activated channel that is specifically permeable to it. As illustrated in Fig. 1.2, sodium channels are activated at a specific threshold potential, passing an inward sodium current; this current reverses the polarity of the cell membrane to +40 mV. At this potential, sodium channels are inactivated while potassium channels are activated [8]. The latter pass an outward potassium current and return the cell to its resting state. The late deactivation of the channels leads to hyperpolarization of the cell membrane [6]. These two currents construct an impulse-like signal "spike", which is called the action potential. This spike lasts only for ∼2-5 ms. Resting membrane potential is then maintained by active ion pumps which moves sodium and potassium ions against their concentration gradient [9].

Cardiac myocytes, another example of excitable cells, are the individual cells of the heart muscle. They are also characterized by a resting membrane potential of around -60 mV and an action potential of +40 mV when they are stimulated. As illustrated in Fig. 1.3, cardiac action potential has five phases. Phase 0 is the depolarization of the cell membrane, resulting from the influx of sodium ions into the cell. Phase

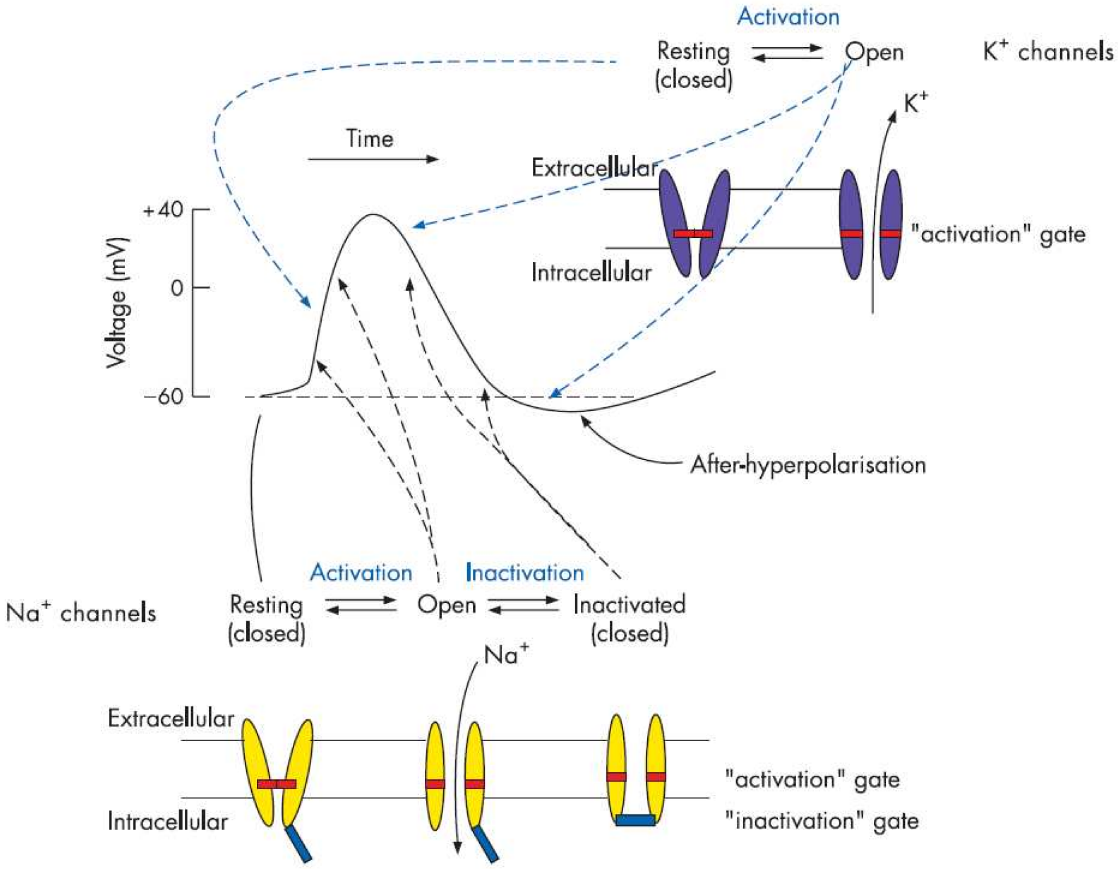


Figure 1.2: A diagram describing the mechanism of the generation of the action potential in neurons and the role of sodium (yellow colored) and potassium channels (violet-colored). Diagram taken from [8]

1 is the rapid repolarization resulting from potassium efflux, which is neutralized by calcium inward current and produces phase 2 (the plateau). When calcium permeability decreases, potassium current dominates and thus results in phase 3 (repolarization). In phase 4, the cell is at the resting state and there is no activation of ion channels. Cardiac action potential is different from the neuronal one because it is derived by calcium currents in addition to sodium and potassium currents. Therefore, this additional ion (i.e. calcium), which plays a mechanistic role in muscle contraction, produces the characteristic cardiac action potential (Fig. 1.3). Calcium inward current and its flux into the cytoplasm from the endoplasmic reticulum delays the rapid repolarization (i.e. the return to the resting membrane potential) by the outward potassium current [7]. This effect is seen as a plateau in the signal that lasts for approximately 0.2s, as shown in Fig. 1.3.

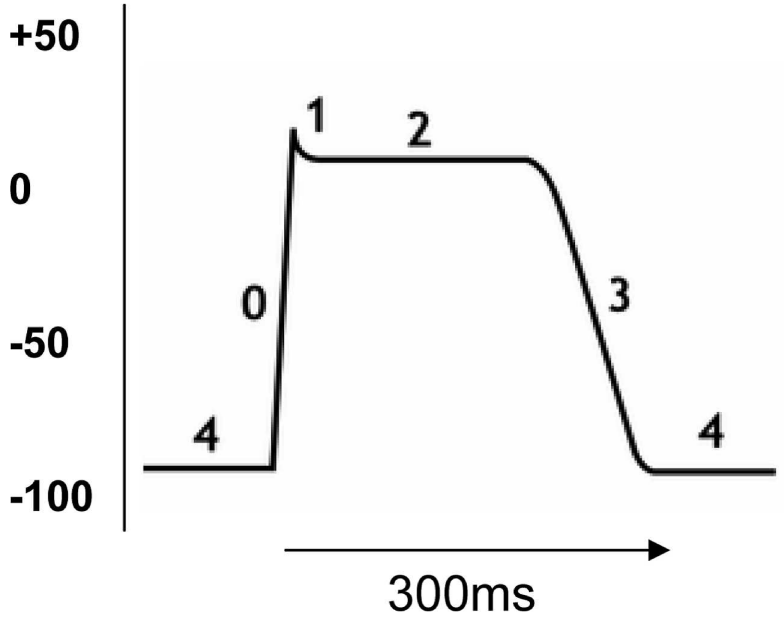


Figure 1.3: The diagram shows the cardiac action potential which has five phases. Phase 0 describes the depolarisation while phase 1 marks the rapid repolarisation. Phase 2 indicates the effect of calcium currents while 3 and 4 describe the repolarisation and the resting membrane potential respectively. Diagram taken from Pinnell et al [10].

1.1.2 Measurement of the electrical activity of excitable cells

Measurements of these signals at different levels (in vitro or in vivo) are essential for demanding biomedical research with applications in neuroscience [11], cardiology [12], drug screening [13], tissue engineering and future therapeutics [14]. For example assessment of the electrical activity is one of the core methods for characterization of therapeutic cardiac myocytes that are produced from differentiated stem cells [14].

The state-of-the-art methods for measuring electrical signals are classified into electrical and optical. In the first category, ionic signals are transduced to electronic signals using electrodes while in the second case custom-designed stains are used, whose fluorescence is responsive to the state of the electrical energy in their vicinity. These two categories are described in more detail in the following paragraph.

Electrical techniques

Electrical measurements are performed either intracellularly or extracellularly [15]. In the intracellular recordings, two electrodes are used. One is a reference electrode that is placed in the extracellular solution (also called bath electrode) while the other is placed inside a micropipette filled with physiological saline. This saline has the same ions and concentrations as the intracellular solution. This setup is used to perform different kinds of procedures, which can be found in Ogden et al [16]. In one of these procedures, a micropipette-electrode setup is kept in continuous contact with the intracellular solution, as illustrated in Fig. 1.4. Although, this setup enables an accurate recording of the voltage across the the cell membrane, it has two fundamental limitations. First, its spatial resolution is limited to the single cell or single point on the cell surface in addition to being a low throughput. Second, the procedure is highly invasive and experimentally demanding.

The other approach uses substrate-integrated micro-electrode arrays [17]. Cells are

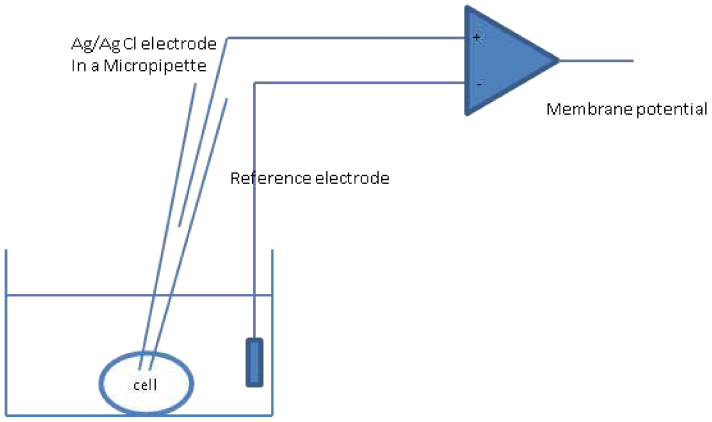


Figure 1.4: A typical setup for the intracellular recording of the electrical activity

cultured on these substrates and the extracellular currents are detected by the nearby electrode whose electrical potential is changed compared with a reference electrode. Because these electrodes have dimensions similar to the cell, they suffer poor localization of the electrical signals. Signals recorded by these electrodes are attenuated because there is a poor seal between the electrode and the cell. Some efforts to improve these limitations by using ultra-small and high-density electrode arrays are reviewed by Spira et al [18].

Optical methods

Voltage-sensitive dyes are designed to overcome the limitations of the electrical methods. These are characterized by membrane-located molecules whose fluorescence intensity is altered by changes in the membrane potential. The principles of operation of these dyes are reviewed by Chemla et al [19, 20]. An example of these mechanisms is 90° re-orientation of the membrane-bound molecule upon change in membrane potential that induces changes in fluorescence.

Although these dyes are successful in reporting localized and sub-cellular signals, they suffer photo-bleaching that limits their lifetime. This disadvantage reduces the experiment time to minutes due to the limited total number of emitted photons.

For instance, long term monitoring of electrical signals is critical to studying the function of neuronal networks of which behaviour develops over extended periods of time [4]. Moreover, this process can produce toxins that affect the function of stained cells or lead to structural changes in the cell membrane [21]. Therefore, label-free methods are candidates with the ability to overcome the limitations of the voltage-sensitive dyes.

Surface plasmon resonance is a candidate for a label-free measurement of the electrical activity. Surface plasmons are light-excitable collective oscillations of free electrons at the metal-dielectric interface. As they are sensitive to local dielectric properties of the medium and the metal, they are used to probe processes at the cell membrane [22] or interactions of surface-bound biomolecules. In this research, they are being investigated as transducers with the ability to probe perturbations of the electrical potential at the metal-electrolyte interface. As will be explained later in chapter 3 on page 56, this sensing principle will be investigated with respect to the detection of changes in membrane potential during the electrical activity of excitable cells. The sensing mechanism is based on the effect of the intracellular and the extracellular ionic currents, which underlie the action potential, on the charge density at electrode-electrolyte interface. This investigation is based on two well-known principles: (i) changes in the electric potential at the interface alter the free electron density of the metal surface [23] and (ii) the conditions of the excitation of surface plasmons are highly dependent on the concentration of the free electrons [24]. The efforts of this thesis are directed at investigating their sensitivity in regard to the detection of the electrical signals from the excitable cells.

1.2 Objectives and experimental strategy

1.2.1 Objectives

This project aims to achieve the following objectives:

(a) Provide an estimate for the voltage detection limits of surface plasmon resonance using theoretical approaches from electrochemistry and optics.

(b) Design a high-sensitivity surface plasmon resonance sensing system and provide an in-depth understanding of factors that affect its sensitivity, using both theoretical and experimental approaches.

(c) Experimentally validate the voltage sensitivity using electrochemical methods combined with the surface plasmon resonance sensing system.

1.2.2 Theoretical and experimental strategy

Sensitivity of surface plasmon resonance will be investigated theoretically and experimentally using the methods described below.

(a) **Theoretical voltage sensitivity of surface plasmon resonance**

Electrode-electrolyte interface is modelled with a one-dimensional multilayer structure. This structure will be used to quantify voltage sensitivity of surface plasmon resonance (SPR) using models from both electrochemistry and optics. As the externally applied energy at the gold-electrolyte interface is coupled to the surface through the capacitive route, plasmonic voltage sensing is modelled by considering the capacitive properties of the interface. This statement is valid only for small voltages, ± 200 mV, which characterize the interfacial capacitor charging-discharging window [25]. At higher potential electrochemical reactions occur that are characterized by a different mechanism.

The accumulation of charges on the plasmonic sensor, due to the applied voltage, will be calculated using Gouy-Chapman-Stern theory of the interfacial capacitance. The translation of this effect to the optical constant of the metal will be found from the McIntyre and the Drude models. Finally, the Fresnel model will be used to calculate the reflection coefficients and construct SPR curves for a set of voltages.

(b) **SPR system**

There is a vital need for a highly sensitive SPR system for quantifying voltage sensitivity. A simple, sensitive and mechanically-stable system based on differential detection using bi-cell photodetector is reported [26]. It provides the advantage of cancelling the common mode noise and instability while producing a response to refractive index change that is higher than the competing systems. Due to its high sensitivity ($\approx 1\times10^{-8}$ refractive index units (RIUs)), it has been used in a number of chemical and biological applications. Moreover, this system has a fast response time (1 μs)[26]. Therefore, it will be constructed and combined with electrochemical methods to investigate voltage sensitivity experimentally.

(c) **Experimental voltage sensitivity using electrochemical methods**

Electrochemical methods have been used to study the effect of the voltage on the surface plasmon sensors. Three-electrode systems [27] have been used as well as two-electrode systems [28]. In this project, a three-electrode system has been used, in which the voltage of the SPR thin-film is adjusted against a reference electrode that is placed near the thin film. This is performed by driving a current between thin film and a third electrode (called counter electrode). In this method, the potential of the working electrode (i.e., the gold thin film) is perturbed more accurately since it is measured against a reference electrode with a constant potential.

These methods will be used to manipulate the potential of the electrode-electrolyte interface while monitoring the response of the SPR system. For this purpose, an electrochemical system will be integrated with the SPR optical system configuration.

1.3 Thesis layout

This thesis starts with highlighting the theoretical basis of this project in Chapter 2. In this chapter, the theory of surface plasmon resonance is presented before describing how it can be voltage-sensitive. This chapter also presents a critical review of the recent attempts to use SPR for measuring the electrical activity.

Among the methods that we will use in this project is modelling the SPR response to the interfacial potential and other interface-related parameters. Chapter 3 presents the design of an integrated theoretical model that will be used to predict the voltage detection limits of SPR by calculating the voltage-equivalent RIUs. This will be used to validate and explain experimental results in Chapter 4, 5 and 6.

Chapter 4 presents the design of a voltage-sensitive SPR system, which combines the optical system with the electrochemical system. The integrated system has been tested by applying voltage while monitoring the output of the electrochemical system and the optical system, simultaneously. The obtained results are compared with the predicted values presented in Chapter 3.

Although the applied voltage signal is considered an equivalent to dynamic refractive index change, it is still affected by the static point of the system or the background refractive index (i.e. the DC offset) of the system. Therefore, Chapter 5 presents work on the optimization of the differential-SPR system for accurate and sensitive detection of the interfacial potential considering different factors that may affect the response of the system. This work investigated how to optimize this reference point

for improving sensitivity.

Chapter 6 presents the investigation of the minimal detectable voltage and the role of voltage-related and interface-related factors. This chapter also presents experimental results that confirm the theoretical values of the voltage-equivalent RIUs.

Finally, chapter 7 summarizes the work that has been done in the different stages of the project. It provides a detailed discussion of the findings in the context of the research question.

Chapter 2

Background and Literature Review

In this chapter, the theoretical background of surface plasmon resonance is presented followed by a review of the development of the plasmonic-based voltage sensing techniques. Then, it also presents a critical review of attempts to use surface plasmon resonance for the detection of the electrical activity of the excitable cells and tissues. Finally, it is concluded by stating the hypothesis of presenting SPR-based voltage sensing as a promising technique to tackle this problem.

2.1 Surface plasmon resonance

2.1.1 Basic principles and optical configurations

What are surface plasmons?

Surface plasmons (SPs) are collective oscillations of free electrons at the metal-dielectric interface. These light-excitable waves propagate along the interface of the

metal (with $\epsilon_r < 0$ and $|\epsilon_r| > \epsilon_i$) with electromagnetic field perpendicular to the metal surface that decays exponentially on both sides of the metal. Starting from the wave equation, their dispersion relation

$$k_x = \frac{\omega}{c}\sqrt{\frac{\epsilon_s \epsilon_m}{\epsilon_s + \epsilon_m}} \tag{2.1}$$

is derived in Raether [24] where k_x is the SPs' wavevector , ϵ_s is the permittivity of the sample and ϵ_m is the complex permittivity of the of the metal ($\epsilon_m = \epsilon_r + i\epsilon_i$). As ϵ_m is complex, $k_x = k_x^r + ik_x^i$.

Their sensitivity to the properties of the interface and their confinement to it in addition to their light excitability provide an intriguing opportunity for sensing applications.

Surface plasmon resonance (SPR)

As explained in Fig. 2.1-(line a), surface plasmons oscillate with a spatial frequency greater than that of light in air. So, they cannot be excited directly with light. In order to overcome this, the spatial frequency of light is increased by one of three techniques: (i) prism-coupling in a Kretchman-Raether configuration - Fig. 2.2-(a), (ii) diffraction grating - Fig. 2.2-(b) and (iii) optical wave-guiding - Fig. 2.2-(c). In the case of the prism and the waveguide, the spatial frequency of the light is enhanced by passing through the prism or the waveguide and it is tuned by the angle of incidence to match the spatial frequency of SP waves. In case of diffraction gratings, spatial frequency is increased by the diffraction and the resonance occurs at a specific diffraction order.

To illustrate SPR phenomena, the widely-used Kretchmann-Raether configuration [31] is refered to as in Fig. 2.1-(inset). This configuration consists of multi-layer of: glass prism (1), metal thin film (m) and sample (3). The incident beam passing

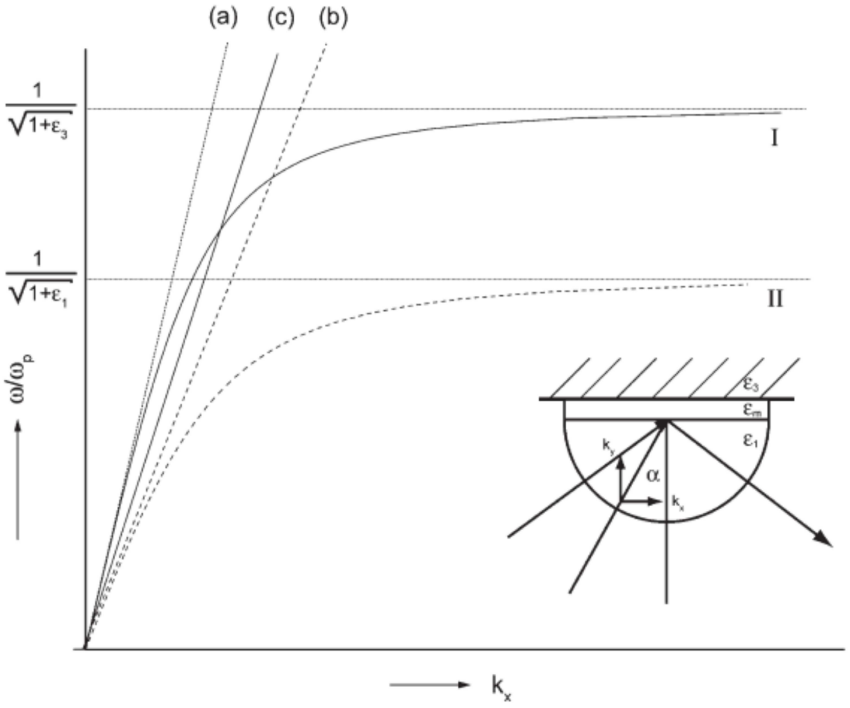


Figure 2.1: Surface plasmons propagate with a spatial frequency that is greater than the k-vector of light in air (line (a)). Momentum enhancement methods, such as the prism presented in the inset, are used to translate this to line b and c. Diagram taken from Schasfoort et al[29]

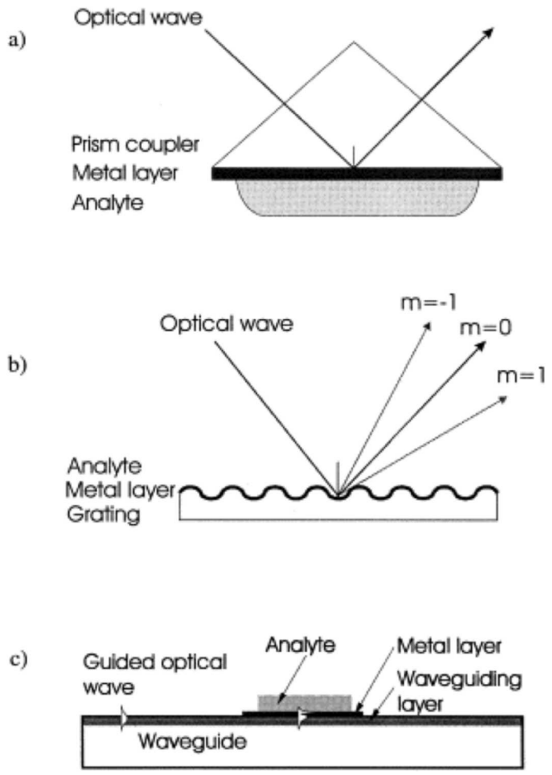


Figure 2.2: Common configurations for the excitation of surface plasmons (SPs): a) Prism coupling b) diffraction -grating coupling and c) waveguide coupling. Diagrams taken from Homola et al [30]

.

through the glass is reflected at the glass-metal interface, but an exponentially-decaying wave is transmitted through the metal thin film. This wave excites surface plasmons at the metal-sample interface and light is re-radiated to the metal and the prism. The total internal reflection (r_{01m}), from the metal surface, is obtained by the sum of the multiple reflections from the interfaces (i.e. glass-metal, metal-sample) Eq. 2.2. The interference between these multiple reflections marks the resonance by a drop in the intensity of the reflected light [24] in addition to a sharp change in its the phase as in Fig. 2.3.

$$r_{01m} = \frac{r_{1m} + r_{m3}e^{2j\beta}}{1 + r_{1m}r_{m3}e^{2j\beta}} \tag{2.2}$$

where r: reflection coefficient, 1m: glass metal interface, m3: metal sample interface and $e^{2j\beta}$ accounts for the phase change due to the metal thickness.

In order to produce an analytical expression for the reflectivity in the Kretchmann-Raether configuration, Eq. 2.3 is derived in Raether [24] starting from Eq. 2.2. The presence of a metal film with a finite thickness sandwiched between two dielectric media adds another component Δk_x to the propagation constant of SP waves (k_x) (as in Eq. 2.1). The correction factor Δk_x is also a complex term with its real part displaces the resonance position while its imaginary parts adds a radiation damping ζ_{rad} to the internal damping of the metal ζ_i. The resulted reflectivity expression accounts for the drop in the reflectivity at the resonance position (when $kx_{ph} = k_x + \Delta k_x$) and includes the effect of the metal thickness on the depth of the dip (optimal at $\zeta_{rad} = \zeta_i$).

$$R = 1 - \frac{4\zeta_i\zeta_{rad}}{kx_{ph}^2 - (k_x + \Delta k_x)^2 + (\zeta_i + \zeta_{rad})^2} \tag{2.3}$$

where kx_{ph} is the wavevector of the incident light.

Propagation length

Since metal has a complex refractive index (permittivity as in Eq. 2.1), the wavevector of the SP is also complex. Its imaginary part is related to the absorption properties of the metal and this parameter determines the decay length of the propagation of the surface wave as in Eq. 2.4. This explains why silver is more sensitive than gold since it has a smaller imaginary part and therefore longer propagation length (L_x)[29]. The propagation length of SPs plays a critical role in the sensitivity and the resolution of SPR systems as will be discussed later in this chapter.

$$L_x = \frac{1}{2Kx_i} \tag{2.4}$$

where K_x^i is the imaginary part of the plasmon wavevector and L_x is the propagation (coherence) length of the SPs.

Penetration depth

When total internal reflection occurs at a sensing structure as shown in the inset of Fig. 2.1, a standing wave (evanescent wave) is generated at the interface between the metal and the dielectric interface. This wave has a penetration depth, the depth at which the field drops to 1/e of its maximum, of the order of quarter of the wavelength [24, 29]. It is noted that this depth is independent of the noble metal thickness as described by the formula

$$d_p = \frac{\lambda}{2\pi\sqrt{n_1^2 \sin^2\theta_i - n_3^2}} \tag{2.5}$$

where θ_i is the angle of incidence, n_1 is the refractive index of the glass and the n_3 is the refractive index of the sample. For instance, the penetration depth d_p is $\sim$ 180 nm for a wavelength of 633nm, angle of incidence of 72°, BK7 glass ($n_1 = 1.515$

at 633nm) and sample of refractive index $n_3 = 1.3333$. Penetration depth is an important concept for designing sensors to detect interfacial processes (within 100 nm from the surface).

2.1.2 Detection approaches

The different detection approaches that are used to probe the properties of surface plasmons are presented here for Kretcmann-Raether configurations. Performing measurements with varying the k-vector of the reflected light (i.e. either the incident angle or the wavelength), there is a sharp drop in the phase associated with a minimum in the intensity at the resonance spatial frequency (wavelength or angle of incidence)- see Fig. 2.3 (a) and (b) respectively. These two curves are the characteristic resonance curves, which are used to detect the interfacial processes due to their effect on the resonance position. As illustrated in Fig. 2.3, a change in the refractive index of the sample results in a shift in the resonance position. For a specific angle of incidence, the change in the phase or the intensity due to this shift is amplified by the gradient of the curve as in Fig. 2.3-(c) and(d). There are mainly three methods that are used to reveal information about the change in the refractive index of the sample from the characteristics of the resonance curve. These methods are (i) resonance position tracking systems, (ii) amplitude systems and (iii) phase systems.

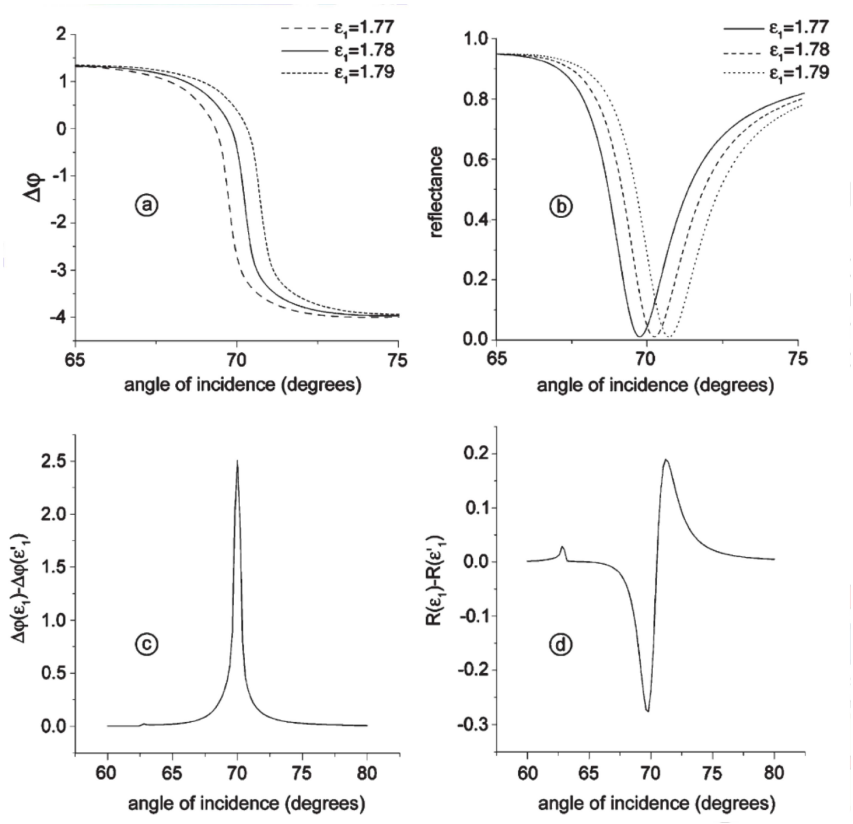


Figure 2.3: (a, b) Phase and amplitude SPR curves with the effect of the change in the refractive index of the sample on the resonance position. (c, d) The factor of the angle of incidence in the change of the phase or the amplitude of the reflected light with amplification occurs at the highest gradient. Figures taken from Schasfoort et al [29]

Tracking the resonance position

This method is commonly used in commercial systems. Prior to tracking the position of the resonance angle, SPR curve is obtained using a pixelated camera. In order to produce the experimental SPR cuve, the dark current of the camera is subtracted and the result is normalised by the background total internal reflection when SPs are not excited. The minimum of the curve is found using a number of algorithms [32], but the common ones are fitting the curve to a polynomial and finding the minimum or finding the zero-crossing point of the first derivative of the curve.

Amplitude systems

There are two categories of the systems that use the amplitude of the reflected light; The first category is the single angle method [33] and the second is the differential intensity method [26].

(a) **Single angle method**: In this approach, SPs are excited with a light beam at specific angle of incidence and the light is reflected internally at the same angle. This excitation angle is selected to match the highest gradient of the SPR curve (Fig. 2.3 (d) - 20). This selection guarantees the maximum change in the intensity due to the resonance shift. When the SPR curve shifts, the intensity of the reflected light changes depending on the direction of the shift. The change in the refractive index of the sample (Δn) can be found from

$$\Delta n = \Delta R\Big(\frac{dR}{dn}\Big)^{-1} = \Delta R\Big(\frac{dR}{d\theta}\frac{d\theta}{dn}\Big)^{-1} \tag{2.6}$$

where (ΔR) is the measured change in the reflectivity, θ is the angle of incidence and (n) is the refractive index of the sample. Eq. 2.6 is used with the prior knowledge (dR/dn) which can be found from simulations or analytical expressions such as in Eq. 2.3 [33]. Similarly, it can be found from the gra-

dient of the SPR curve ($dR/d\theta$) and the change in the resonance angle upon refractive index change ($d\theta/dn$). This approach suffers of the influence of the fluctuations of the intensity of the input power on the sensitivity.

(b) **Differential intensity method**: This method has been introduced by the Tao group [26], in which SPs are excited by focusing a beam on the gold surface (Fig. 2.4). The excitation beam is centred at the resonance angle and thus the profile of the reflected light features a window of the resonance curve with the resonance position in its centre. This profile is balanced on a bi-cell photodiode. The outputs of the bi-cell (A and B) are used to calculate $(A-B)/(A+B)$. This signal is mapped to the equivalent shift in the resonance angle ($\Delta\theta_0$) by

$$\frac{A-B}{A+B} = \frac{3\Delta\theta_0}{\theta_w} \tag{2.7}$$

where θ_w is the angular width of the excitation beam in Fig. 2.4. This approach provides great advantages for the amplitude systems; the system response is higher than fixed angle approach [26] and the resonance angle tracking [34]. Moreover, noise is reduced by the differential signal $(A-B)/(A+B)$ processing. All of these improvements result in a significant increase in the sensitivity of the amplitude systems by two orders of magnitudes [26, 35]; Tao et al [26] reported a sensitivity of $10^{-8} RIUs$. This method is described later in more details in Chapter 4 and 5 on pages 93 and 115 respectively.

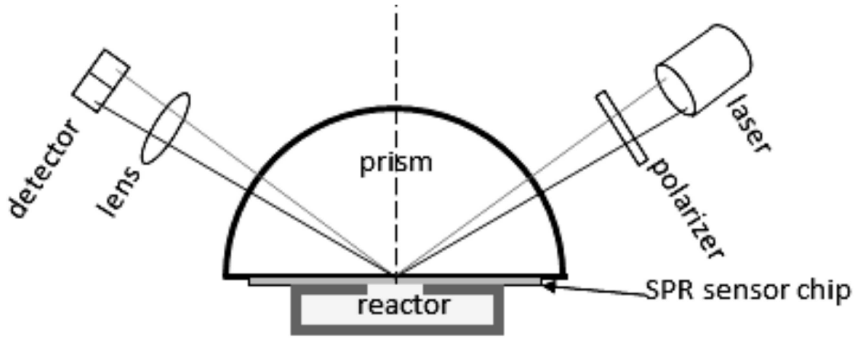


Figure 2.4: Bicell surface plasmon resonance system. Diagram taken from Mao et al [36]

Phase systems

Surface plasmons' excitation features a sharp transition in the phase of the reflected p-polarized light (2π radians [37]). Similar to the fixed angle approach in the intensity based measurement, there is change in the phase of the reflected light as the resonance position shifts. In contrast to the case of amplitude, measurement of this phase is not straightforward since there are no detectors fast enough to capture this high frequency signals (on the order of 10^{14} Hz) - [38]. Therefore, different approaches have been used to convert this phase shift to a signal compatible with optical detectors. These approaches include heterodyne interferometry, polarimetry and homodyne interferometry [38]. In the first method, two low frequency signals with a specific beat frequency are constructed by mixing two high frequency signals. One is used as reference arm while the other is used for exciting SPs. The phase shift is then retrieved by comparing the difference in the beat frequency between the reference and the measurement signals [38].

In the second method, interference between a reference signal that does not undergo a phase change and a measurement signal is used to reveal the change in the phase of p-polarized due to the excitation of the SPs. This has been used for the first time by Kabashin et al [39, 40], in which a classical interferometer, as described in Fig. 2.5 is designed using a beam splitter to form the required sensing and reference arm. After passing the sensing beam through the sample at the resonance angle,

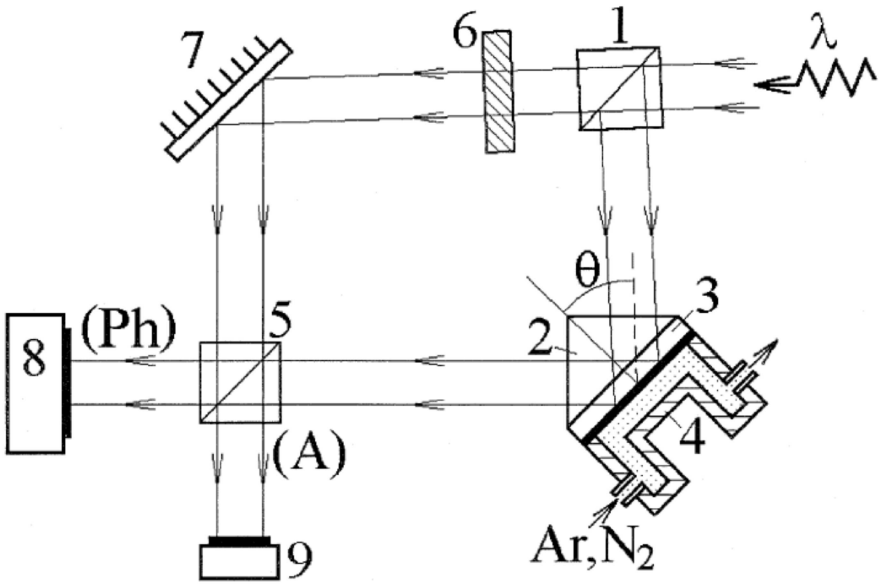


Figure 2.5: Phase SPR system using Mach-Zehnder interferometer . Diagram taken from Kabashin et al [39]

the two beams were combined using another beam splitter before passing to the detector (see Fig. 2.5). The resulting interference fringes and their spatial shift are used to calculate the phase change. The distribution of the phase over the sample has been exploited later to design micro-array sensors [41]. A sensitivity of 4×10^{-8} RIUs has been achieved using silver-based sensor structure.

To improve the sensitivity of interferometry-based systems, a differential interferometer has been designed to suppress the common-path noise - see Fig. 2.6 [42]. Both s and p polarized light are used to form two interference signals. The signal from the sensing and the reference of the p-polarized carries the phase change due the change in refractive index of the sample in addition to common-path noise while the s-polarised signal carries no phase change but noise and instability. A Wollaston prism has been used to split the signal into s and p at the detector. The difference in the phase of p and s polarized light reveals the phase change due to the change in refractive index of the sample while cancelling the noise. Similar sensitivity levels have been achieved using gold which normally results in less sensitivity compared

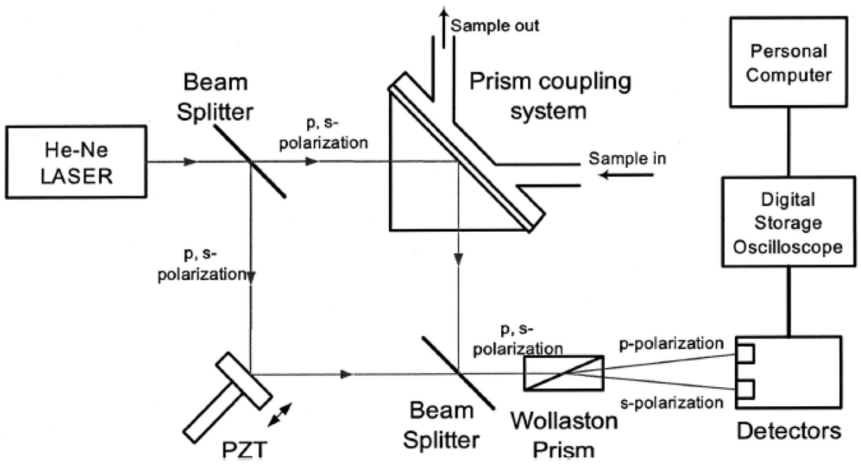


Figure 2.6: Differential interferometer SPR system. Diagram taken from Wu et al [42].

to silver [41].

Phase-based SPR systems have been developed at Nottingham using objective lens to excite surface plamons adopting V(z) theory that is used in acoustic microscopy [43]. Considering the optical system in Fig. 2.7 [44], the interference signal is constructed by using the normal incidence beam as a reference and the plasmon excitation beam as a signal beam. As there is a phase difference between the two beams, the magnitude of interference signal will oscillate. This interference signal is generated for different defocus levels while the change in intensity is detected with confocal setup. The resulting V(z) curve reflects the properties of the sample and the change in its periodicity is used for imaging and sensing applications.

The effect of the phase change, due to the excitation of the SPs, on the ellipse of the polarized light has been also exploited as a technique to retrieve this phase information. This technique has been developed by Ho et al [45] and our group. A polarimetry configuration has been used to measure the phase information due to SP excitation, adding a phase contrast by retarding the reference beam [45]. This approach provided the advantage of multipoint measurements with higher sensitivity (10^{-7} RIUs). Phase modulation, using photoelastic modulators along with phase

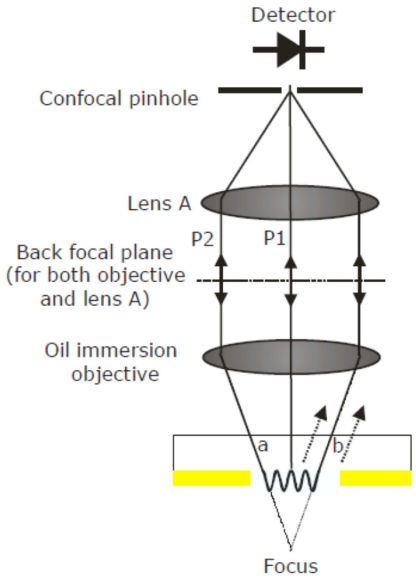


Figure 2.7: Objective-based confocal SPR system. Diagram taken from Zhang et al [44]

sensitive detection has been achieved [45]. In our group, polarization modulation using electro-optic modulator has been used with a custom designed modulated camera [46] - see Fig. 2.8. The modulation depth or index of the signal is related to the change in refractive index of the sample .This provided an elegant flexibility to trade between the sensitivity and the dynamic range by adjusting the analyser and the polarizer angle.

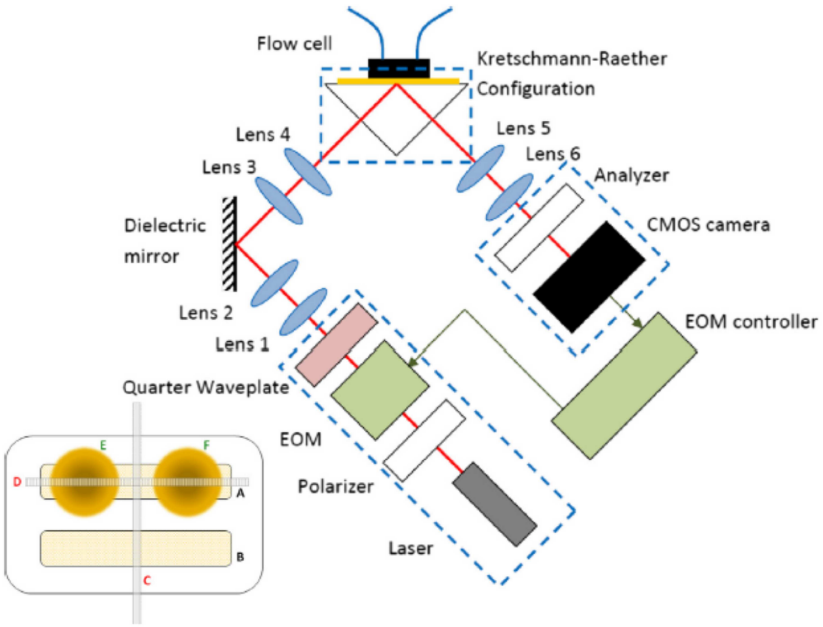


Figure 2.8: Polarization-modulation SPR system with custom phase modulation camera. Diagram taken from Wang et al [46].

2.1.3 Factors that influence the sensitivity of surface plasmon resonance

Sensitivity (also named as resolution in some texts [30, 47]) of surface plasmon resonance systems is analysed in the light of two variables: the responsivity of the system (η_t) to the changes in refractive index (in the units of the detected signal per RIU) and the noise in the system (σ) [46] and [47]). It is generally expressed in the terms of the minimal detectable refractive index in refractive index units (RIUs) and is found using

$$s = \frac{\sigma}{\eta_t} \tag{2.8}$$

where (s) refers to the sensitivity or the minimum detectable change in refractive index. Factors that affect the responsivity of the system are mainly: (i) the properties of the sensing device (e.g use of gold vs. silver as plasmon supporting material),

(ii) optical system configuration and (iii) the detection method. The contribution of these factors to responsivity could be analysed by splitting the overall responsivity (η_t) into two multiplicands: the angular responsivity η_θ (deg/RIUs) and the detection responsivity η_d (signal units/deg) given by

$$\eta_t = \eta_\theta \eta_d \tag{2.9}$$

In the case of single angle SPR systems, the angular responsivity and the detection responsivity are $d\theta/dn$ and $dR/d\theta$ respectively as shown in Eq. 2.6.

Angular responsivity: This responsivity is determined by the optical system configuration (prism, or waveguide as in Sec. 2.1.1)which is measured in terms of the produced resonance shift (in deg) per refractive index unit [30]. For instance, SPR systems based on prism configurations yield greater angular responsivity (deg/RIUs) compared to diffraction grating based systems [30, 48] whose sensitivity is therefore reduced by an order of magnitude compared to the prism systems.

Detection responsivity: This responsivity is controlled mainly by the detection method in addition to the effect of the sensing device.

(a) The detection methods provide a way for maximizing information retrieval from the resonance curve which is reflected in the signal units normalised by the shift in the resonance position. For instance, the use of the phase jump at the resonance angle (see Fig. 2.3) has resulted in a high phase shift per a degree of resonance position shift and therefore led to the development of very sensitive SPR systems compared to amplitude systems boosting the sensitivity by an order of magnitude [38].

(b) The sensing device controls the quality of the resonance curve (minimum reflectivity and FWHM). For instance, silver demonstrates better SPR quality in comparison to gold. In other words, it has smaller imaginary part of the permittivity as well as higher real part part of permittivity. Therefore, it

produces better resonance quality in terms of FWHM and the minimum reflectivity. The thickness of this material is also an important factor [24] with the optimized response at $50nm$. The addition of metallic adhesion layer between the gold and glass also affects the quality of the resonance curve; increasing the FWHM and the minimum reflectivity of the curve [49].

To sum up, phase-based SPR systems demonstrate a higher sensitivity (10^{-8} refractive Index Units -RIUs), but usually require complex optical system design and do not usually offer a wide dynamic range [46]. On the other hand, amplitude-based detection systems are relatively simple, but their typical sensitivity is 10^{-5} to 10^{-6} RIUs [30]. However, the use of differential intensity has resulted in improvement of the sensitivity of amplitude systems to levels comparable with phase systems while featuring simple optical system design [26]. Therefore, this system is adopted for sensitive detection of the interfacial potential perturbations.

2.1.4 Factors that influence the spatial resolution of surface plasmon resonance

Resolution of SPR microscopes depend on the optical configuration and is also anisotropic; the lateral resolution in the direction of SP propagation (x) is different from the direction perpendicular to it (y) [50, 51]. Pechprasarn et al [50] has presented a framework for analysing the resolution of the SPR microscope. In that analysis, two contrast mechanisms have been presented: (a) a point scatterer and (b) a uniform dielectric layer disrupting the gold surface.

The first mechanism attenuates the energy of the plasmon (because of the scattering) and this could be seen in the far field resulting in diffraction limited resolution, depending on the optics. The other mechanism is direction dependent:

(a) In the direction parallel to the propagation of the SP wave, it is limited by the

propagation length of SPs ($3\mu m$ in water for 633nm) [51, 30](see Sec. 2.1.1) even if a high NA objective is used unless some exceptional arrangement are made [50, 51]. For example, V(z) approach (Sec. 2.1.2) is introduced as a way to increase the resolution since it is limited by the defocus; a controlled propagation length [50].

(b) In the direction perpendicular to the propagation of the SP, it is limited by the optical system design and thus is ideally diffraction limited when high-NA objectives are used.

2.1.5 Applications of surface plasmon resonance

Using the concept of surface plasmon resonance, sensing and imaging systems have been designed and widely used in scientific and biomedical applications. In this section, some of these systems are described.

Sensing systems

The sensitivity of the surface plasmons to the properties of the interface has been utilised to detect biomolecules binding to the specific functional groups on the surface [52]. Main challenges in this context are:

(a) The effect of the signal arising from the non-specific binding of unwanted molecules in the sample. The dilemma has been investigated by Lane et al [53] designing buffers to block the non-specific interaction added to the existed efforts of using reference channels to cancel this background signal [54].

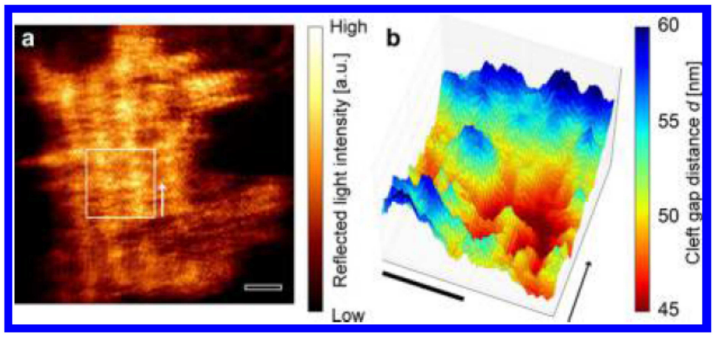
(b) Enhancing the sensitivity of the sensors to detect small molecules [55] such as enzymes and also DNA with no need for amplification [56]. Some of research efforts in this track used plasmonic nanoparticles [56] and graphene-based surface plasmon resonance sensors [57] to enhance the sensitivity.

In addition, to the refractive index sensitivity of surface plasmons, it is also sensitive to voltage change at the sensor's interface which behaves like an electrode, with optical readout. Charge carries (electrons) could be added to this electrode (i.e. reduction) or subtracted from it (i.e. oxidation). This characteristic has been exploited to design all-optical electrochemical sensors [58]. The theory of these sensors has been described intensively in ref [59] and they have been widely applied to detect interfacial electrochemical reactions.

A typical sensing SPR system, as in Fig. 2.8, is designed using a number of modules: the optical system, a flow cell that is normally mounted on the surface of the prism and a fluid handling system to deliver different samples to the sensing area. In addition to that, the flow cell is modified to hold electrodes in the case of the electrochemical systems and a potentiostat is used to control the potential at the metal-electrolyte interface [26].

Imaging systems

Surface plasmons have been suggested to achieve a surface imaging technique as early as 1980s [60] resolving scatterers or dielectric coatings when they perturb the propagating waves. These findings, in addition to providing high contrast images, opened a new horizon for a sensitive quantitative method to map inhomogeneity in the interfacial refractive index being applied to image cell surface. For instance, it has been used to map the cleft gap between the cell and the sensor at a subcellular resolution employing a statistical data analysis [61] and such analysis allowed testing different surface functional molecules (Fig. 2.9). Also, molecular interaction on the cell membrane has also been studied revealing a spatio-temporal interactions between the ligands and different membrane's molecules in vitro [22]. The close contact between the biological samples and the sensor has been attempted to detect the changes in the transmembrane potential, as will be discussed in detail in Sec. 2.2. Imaging systems based on the intensity or phase detection have been designed using



gap.png

Figure 2.9: SPR mapping of the cleft gap between a single cell and an electrode with sub-cellular resolution. Diagram taken from Toma et al [61].

either a prism [62] or high NA objective lens [51]. Fig. 2.10 shows an example of intensity surface plasmon resonance system using a high NA objective lens with high refractive index glass ($n = 1.78$).

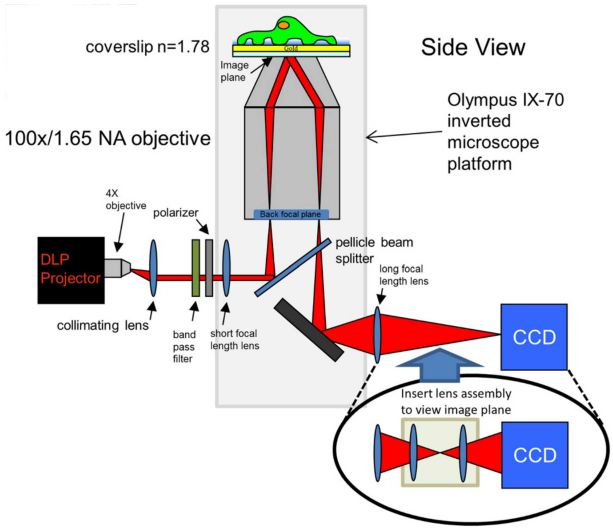


Figure 2.10: An example of High NA objective based SPR imaging system. Diagram taken from Toma et al [61].

2.2 Plasmonic detection of bioelectrical activity

2.2.1 Experimental attempts

As stated previously, there is a necessity for the development of a reliable optical label-free recording of the electrical activity of excitable cells. Towards resolving this problem, surface plasmon resonance has been recently used to detect the electrical activity of (i) a rat's sciatic nerve [63], (ii) rat's cerebral cortex in vivo [64], and (iii) neurons in a cultured neuronal network [65]. These attempts envision plasmonic methods as promising tools for solving the problem of label-free recording of the bio-electrical signals.

The first experimental observation of the use of surface plasmon resonance in the detection of neural activity has been reported by Kim et al [63]. Changes in refractive index resulted from the structural changes in rat sciatic nerve, which was reported by Cohen et al [66], has been exploited to measure the electrical signal. Fig. 2.11 demonstrates a successful correlation between the optically-recorded elec-

trical activity and the reference electrical recording. For further validation, control experiments have been provided using nerve blocker (lidocaine) to verify the recorded signal.

In the second experiment, the electrical activity of a rat cerebral cortex has been detected in vivo using a tailored optical fibre-based surface plasmon sensing system [64] Fig. 2.12. In this experiment, low frequency local field potentials, which results from integration of activity of many neurons, have been detected. Voltage gated channel blocker has been applied as a negative control to validate that recorded signal was electrical activity rather than other kind of artefact. The drawback of this study is presenting a single point measurement which makes the voltage sensitive dyes, which map multi-cellular activity, superior since they offer better spatial resolution.

An interesting observation is that the signal contains artefacts from electrical stimulation (marked by the up arrow) unlike the previous nerve recording Fig. 2.11-(b). The study presented a refractive index based explanation for the experiment in general. However, the refractive index theory does not provide a reliable explanation for the effect of electrical stimulation observed in the signal - see Fig. 2.12-(b) which is absent in the case of the nerve in Fig. 2.11. There is a fundamental difference between the two studies. The nerve is electrically insulated in contrast to the cortex where the optical fibre has been inserted to the access neural tissue. Therefore, it is more plausible to discuss these findings in terms of the electrical field effect on the surface plasmon in addition to the refractive index effect.

Generally, surface plasmon is used as a refractive index sensor but it could also be used as a voltage sensor (or electrical field sensor), as will be described later in Sec. 2.3.1. Changes in electrical field (or potential) resulted from the activity of the neural tissue might be used to explain the findings of this study and the artefacts associated with electrical stimulation in particular.

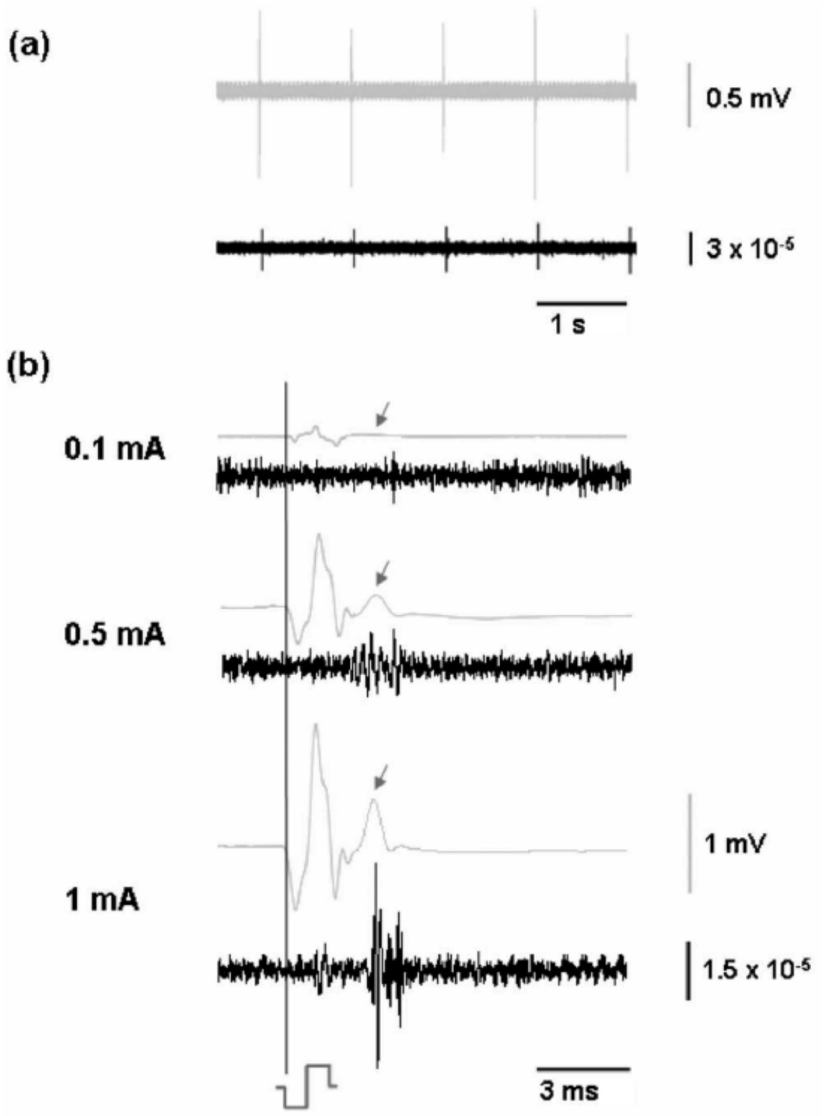


Figure 2.11: Plasmonic response to electrical activity from rats sciatic nerve. a) a magnified scale presents the correlation between the optical recording and the reference electrical recording. b) magnified version of the artefact-like plasmon response. Figures taken from [63].

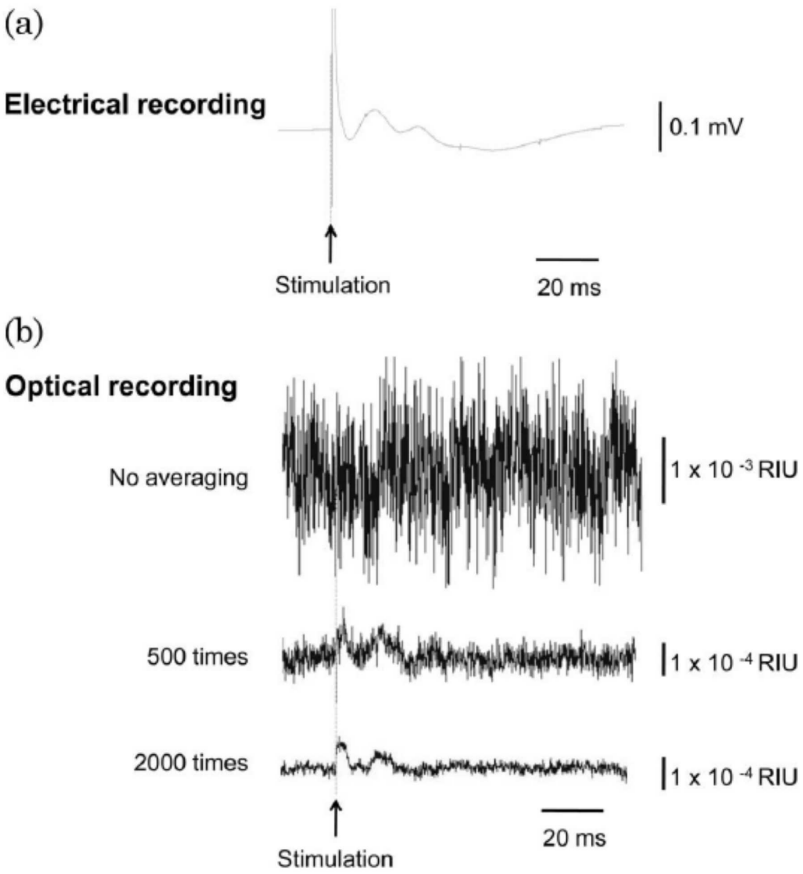


Figure 2.12: Surface plasmon measurement of local field potential from rats somatosensory cortex. a) electrical recording b) simultaneous plasmon resonance measurement. Figures taken from Kim et al [64].

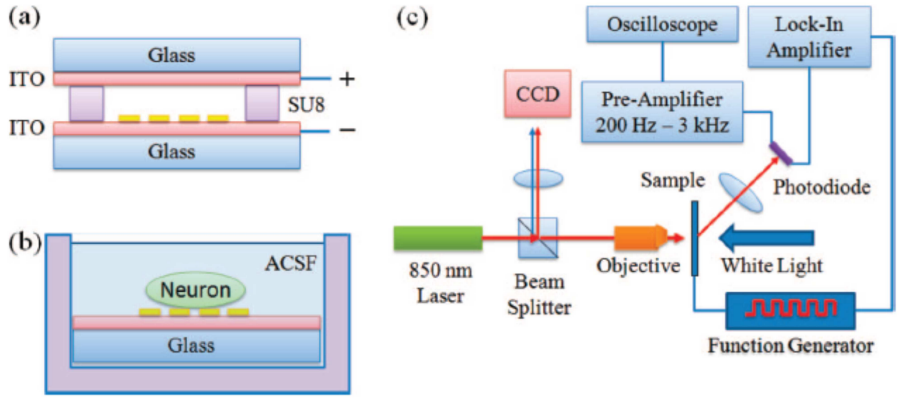


Figure 2.13: Plasmonic nanoparticles' imaging system presented by Zhang et al [65]

In the third experiment, plasmonic sensing of electric fields has been exploited by Zhang et al [65] to measure the electrical activity of cultured hippocampal neurons. Using gold nanoparticles immobilized on Indium-Tin-Oxide (ITO) coated glass slides (see Fig. 2.13), the study reported a linear relationship between the voltage and scattered light in addition to an agreement between modelling and experimental observations. However, this model suffers two drawbacks.

(a) Voltage has been tested using an air-gold interface which does not represent the extracellular characteristics. Moreover, the applied voltage was in the range between 0 and 10 V with a step of 1V. Both the range and the resolution are a lot higher than the values of the interest (i.e. mV).

(b) Although, Zhang et al [65] claimed a detection of the electrical activity but no strong validation of the acquired signal was provided, given the vulnerability of these sensitive measurements to artefacts. The absence of a control experiment, for example blocking the electrical activity, or a simultaneous recording with the gold standard methods questions the reliability of the obtained results presented in Fig. 2.14.

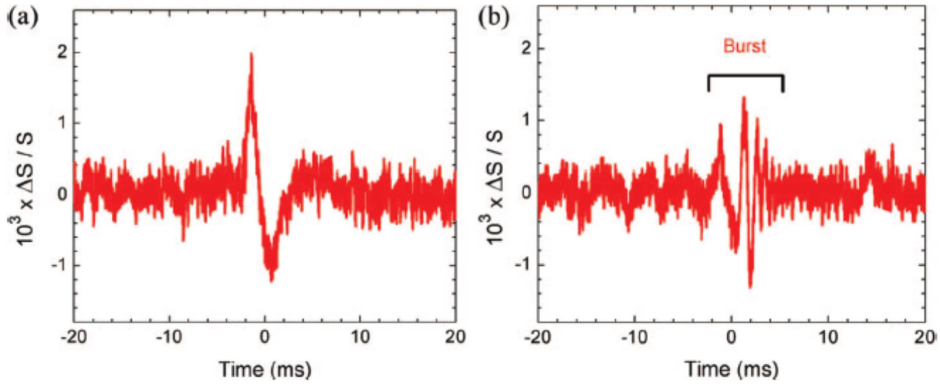


Figure 2.14: Zhang et al [65] claimed plasmonic recording of (a) single action potential and (b) repeated action potentials or bursting. Signals, presented here, are light scattering from nanoparticles in fractional change in intensity. Figures taken from Zhang et al [65].

2.2.2 Theoretical work

Choi el al [67] claimed that the plasmonic response to the nerve excitation features a bipolar signal which does not contain artefacts from electrical stimulation. Starting from this observation, they carried out further theoretical investigations to explain the characteristics of this signal [67]. They argued that this signal is a resultant of sequential mechanical and electrostatic forces resulted from the collision of outward potassium ions (chapter 1) on the gold atoms, as shown in Fig. 2.15. So, this mechanical force and the electrostatic force is suggested to change electron density in the metal and thus changes the dielectric constant of the gold as calculated from a modified Drude-Lorenntz model. From this effect, the response of the plasmonic system is simulated using the multilayer structure in Fig. 2.15-(b). However, this model is hard to be adapted to explain this response for two reasons.

(a) It is well established that gold-electrolyte interface is characterized by a double-layer of ions that results from electrostatic interactions between the metal and the electrolyte as will be explained in details in Sec. 2.3.2. These ions screens the gold atoms from the direct collision of the potassium ions, which is argued

in ref [67]. Moreover, this hypothesis ignored the electrostatic interactions of the potassium ions with the charge carriers in both gold and electrolyte.

(b) The model overlooked the anatomical structure of the nerve that represents the source of the potassium current. Nerve fibres are surrounded by a dense connective tissue which acts as a diffusion barrier.

As there is no direct electrical contact between the nerve and the gold thin film, no ionic current will pass from the nerve to the gold atoms. This also supported by Kim et al [63] experimental observation that SPR response doesn't contain artefacts from electrical stimulation.

To sum up, Kim et al [64], in comparison to other two studies, shows a potential of using SPR for direct detection of the voltage signal rather than exploiting the associated physical and physiological signals. Kim el al's signals [64] demonstrated that SPR picked up electrical stimulation signal before membrane depolarization supports the hypothesis of direct voltage sensing. Therefore, it is necessary to provide a solid understanding of the fundamentals of plasmonic voltage sensing as will be presented in the next section.

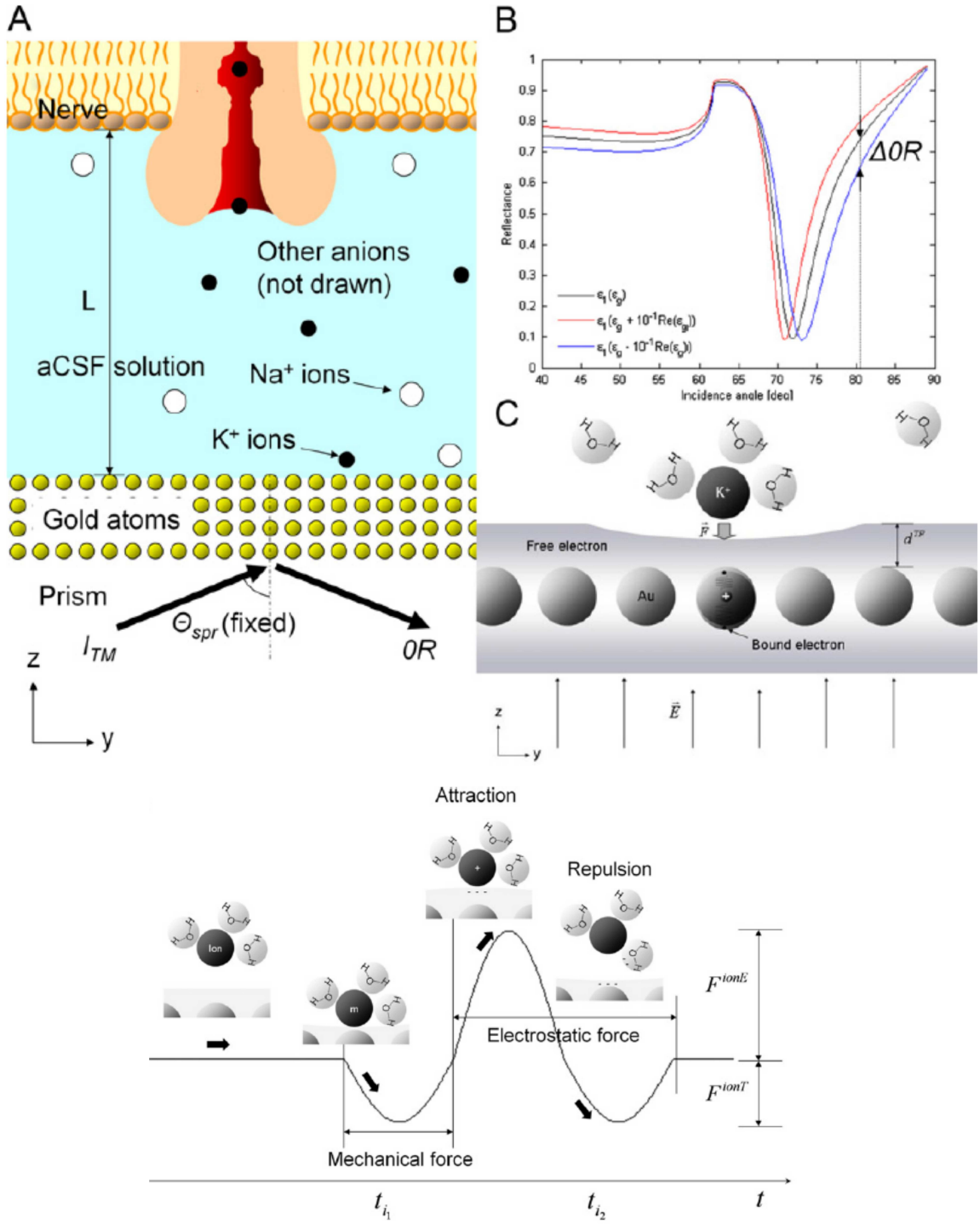


Figure 2.15: Modelling of surface plasmon response to electrical activity. (A) the constructed signal (B) the multilayer model for the nerve-surface interface. Diagrams and figures are taken from Choi et al [67]

2.3 A Review of plasmonic voltage sensing

2.3.1 History of voltage measurement using the optical properties of metals

The early work on the electroreflectance phenomena represents the theoretical basis of plasmonic response to interfacial electric potential. Given a metal-electrolyte interface, electroreflectance is defined as changes in light's reflectance from the metal surface as a result of altering its potential versus a reference point in the electrolyte. This spectroelectrochemical phenomena has been observed by Feinleib [68] during experiments using KCl electrolyte in contact with a thin film of gold. A typical electroreflectance system is presented in Fig. 2.16. In this experiment, a wideband light source has been used to study the spectrum of the electroreflectance. The results show a change in the reflectivity of the metal following the applied potential. In addition, the spectrum of the change in reflectivity featured some peaks at specific photon energies or wavelengths [68]. It was claimed that these observed peaks are due to change in the band structure of gold. This statement does not agree with the established theory regarding the screening of the low-frequency electric field by free electrons within a penetration depth of few Angstroms [69]. Furthermore, it was not supported with further theoretical or experimental validation. These peaks are observed also by Hansen [69] and Kolb [70] - see Fig. 2.17. The sharper one is located at the energy of the volume plasma [70]. Thus, it might be due the shift in the plasma frequency induced by the applied potential. Therefore, it is rather derived by the high gradient in the reflectance spectrum at the plasma frequency. Later, Hansen [69] suggested that the applied potential modifies the density of free electrons of the metal which accounts for the electroreflectance.

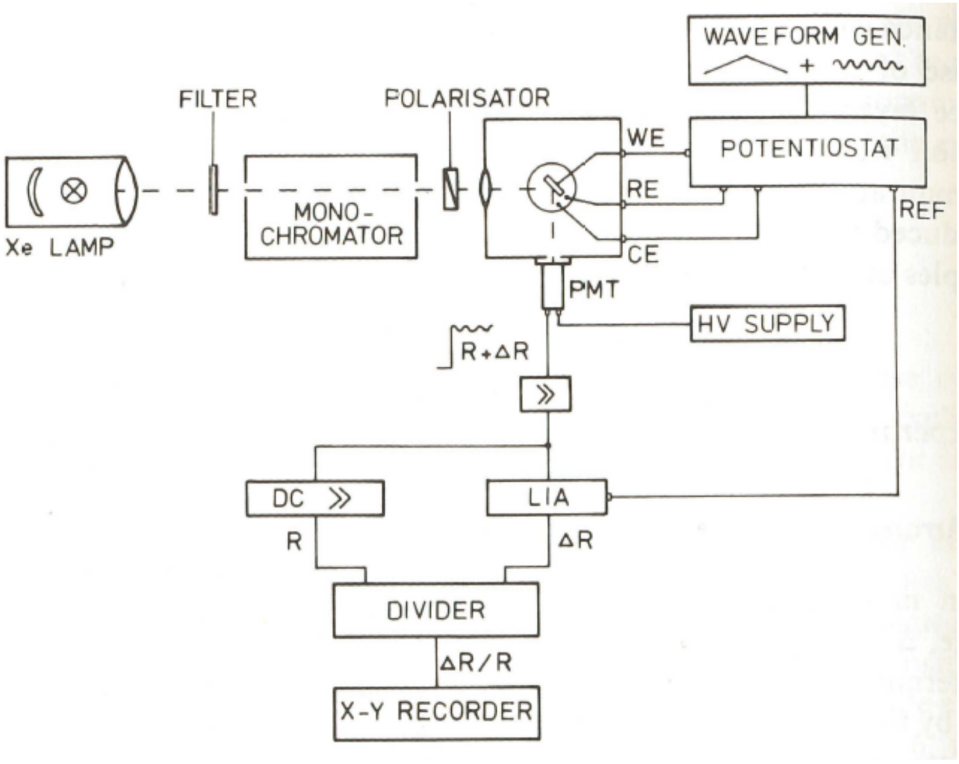


Figure 2.16: An example of the experimental setups that were used in the electroreflectance experiments. Diagram taken from [71]

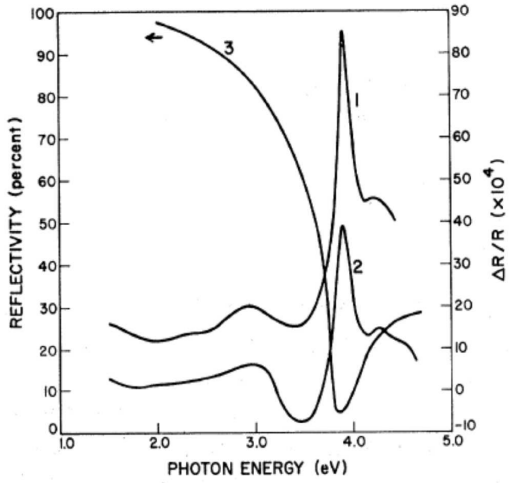


Figure 2.17: Electro-reflectance (expressed as relative change in reflectivity) of silver for two samples 1) high purity sample, 2) commercial samples and 3) reflectance spectrum of silver. Figure taken from [71]

McIntyre Procedure

The change in the free electrons density, due to the external voltage, shifts the plasma frequency of the metal and its optical constant. The changes in the optical constant of the gold as a result of change of free electron density has been estimated by McIntyre [23]. According to this procedure, voltage is sensed via double-layer capacitive coupling, which was used to explain this phenomena (Eq. 2.10). Charge carriers in the electrolyte are are balanced by the change in electron density in the metal side (i.e. Gaussian box at the interface). The resultant charge accumulation is confined within the Thomas-Fermi screening length (d_{TF}) - see Eq. 2.11. This is because the low-frequency electric field is screened by the free electrons in the metal surface and does not penetrate into the bulk of the metal. The change of free electron density leads to changes in the plasma frequency of the metal (Eq. 2.12), modification to its optical constant (ϵ) as a result and shift in the resonance position of surface plasmon resonance. The associated change in electron density is used to calculate the optical constant of the gold using the Drude model, Eq. 2.13.

$$Q = CV \tag{2.10}$$

$$\Delta N = \frac{Q}{-ed_{TF}} \tag{2.11}$$

$$\omega_p = \sqrt{\frac{(N + \Delta N)e^2}{m\epsilon}} \tag{2.12}$$

$$\epsilon = 1 - \frac{\omega_p^2}{\omega^2 - i\tau\omega} \tag{2.13}$$

where ω is angular frequency of the light and τ is the damping constant of the metal.

Understanding the electroreflectance has been extended to explore the electric field effects on surface plasmon excitation. Kolb [70] investigated the influence of the electric field on SPs of silver employing McIntyre's theory. The change in the resonance position, due to the modification of the optical properties of the metal, opens the opportunity of using surface plasmon resonance for electrochemical [72, 73] and voltage sensing [28] applications.

2.3.2 Modelling the interfacial double-layer capacitance

The voltage applied to the electrode-electrolyte interface is optically detected due to a sequence of processes associated with charging the interfacial capacitance [23]. So, it is important to review the different models that explain these capacitive properties. There are three major investigations in this track: Helmholtz model, Gouy-Chapman and Stern modifications see Fig. 2.18. This first principles approach is adopted since it provides more accurate estimate of the capacitance compared to generalizing the experimental capacitance, which was used by Foley et al [73]. This inaccuracy is attributed to the change in the capacitance when the experimental conditions are different (i.e. the effect of the type and the concentration of the electrolyte) as will be investigated in Sec. 2.3.2.

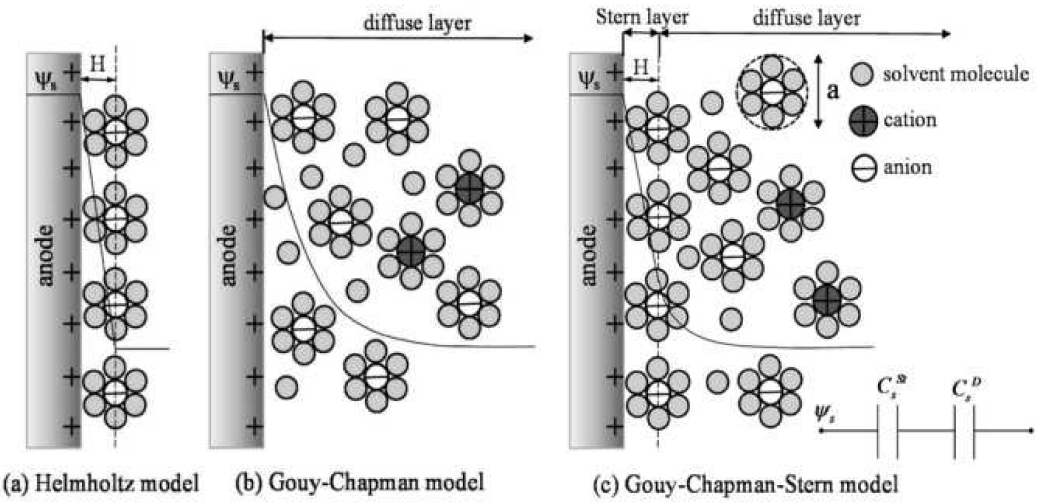


Figure 2.18: The three major models for the electrical double layer capacitance at the metal electrolyte interface. a)Helmholz model b)Gouy-Chapman model and c) Stern Model. Diagrams are taken from [74]

Helmholtz model

According to Helmholtz model, the interface is modelled as a parallel plate capacitor. One plate is in the solution side and the other in the metal side in addition to a separating dielectric medium (ϵ) that is characterized by the properties of the solvent (e.g. water molecule as a result of the hydration shell of the ion). Therefore, the distance between the two plates (d) is in the order of water molecule and it is modelled with the dielectric constant of the water. (see Eq. 2.14 that shows the charge density σ in this layer) [75].

$$\sigma = \frac{\epsilon\epsilon_0}{d}V \tag{2.14}$$

Gouy-Chapman model

Helmholtz model does not include an interpretation of the dependence of this capacitance on the electric field across the interface and the concentration of the electrolyte.

These parameters have been investigated by Gouy and Chapman independently [75]. This theory suggests a spatially-variable electric field for the interface. According to this, the interface could be envisioned as a set of laminae with different energy levels. The occupation of these energy levels by ions is driven by competitive effect of the electrostatic energy (i.e. the effect of the applied potential and or the concentration of the electrolyte) and the thermal fluctuations that gives the diffuse property to the interface. The diffuse layer capacitance that arises from this charge distribution is found by the following analysis.

The total charge per unit volume in each lamina (x) is given by $\rho(x) = \Sigma_i(n_i z_i e)$, where n_i is the density of the ion (i) in the bulk electrolyte, z_i is valence of the ion (i) and e is elementary charge. The distribution of charges from all ion species in the diffuse layer can be described with Boltzmann equation [76]:

$$\rho(x) = \Sigma_i n_i z_i e \exp\left(\frac{z_i\, e\, \psi(x)}{kT}\right) \tag{2.15}$$

where $\rho(x)$ is the charge density at each lamina denoted by x, $\psi(x)$ is the potential at x and kT is the thermal energy in joules. All potentials are measured with respect to the bulk electrolyte.

Charge density in each lamina is also related to the local potential by Poisson equation:

$$\rho(x) = -\epsilon_0 \epsilon \frac{d^2\psi(x)}{dx^2} \tag{2.16}$$

where ϵ is the permittivity of the solvent. Poisson-Boltzman equation is formed by combining Eq. 2.15 and Eq. 2.16:

$$\frac{d^2\psi(x)}{dx^2} = \frac{-e}{\epsilon_0 \epsilon} \Sigma_i n_i z_i e \exp\left(\frac{z_i\, e\, \psi(x)}{kT}\right) \tag{2.17}$$

Eq. 2.17 is solved for the conditions: (i) at $x = \infty$ (i.e. far from the electrode surface), ψ=0 and hence $d\psi/dx$=0 and (ii) a symmetrical electrolyte (e.g. NaCl) is used. The Potential gradient in the diffuse layer can then be found by

$$\frac{d\psi(x)}{dx} = -\sqrt{\frac{8\,k\,T\,n_0}{\epsilon\epsilon_0}}\sinh\left(\frac{ze\psi(x)}{2kT}\right) \tag{2.18}$$

Eq. 2.18 describes the local potential gradient at the electrode-electrolyte interface. From this equation, the electric field can be found at each point (x) in the direction perpendicular to the electrode surface. The potential profile can be found by solving Eq. 2.18 under the condition $\psi = \psi_0$ at $x = 0$ and that $Ze\psi/4kT < 0.5$. The potential profile can be calculated from

$$\psi = \psi_0 \exp(-\lambda x) \tag{2.19}$$

where

$$\lambda = \sqrt{\frac{2n_0 z^2 e^2}{\epsilon\epsilon_0 kT}} \tag{2.20}$$

The charge density can then be found by employing Gauss law [75]. If a Gaussian box of a surface area A and a height (x) is attached perpendicular to the electrode surface. As indicted by Eq. 2.19, the potential decays exponentially as distance from the surface of the electrode increases. Therefore, electric field will be zero on all the surfaces of the Gaussian box except at the metal surface. From Gauss law, charge enclosed by the box is

$$q = \epsilon_0 \epsilon A\left(\frac{d\psi}{dx}\right)_{x=0} \tag{2.21}$$

Combining Eq. 2.21 and Eq. 2.18 under the condition $\psi = \psi_0$ at $x = 0$, one can find the charge density in the diffuse layer (σ):

$$\sigma = -\sqrt{8\,k\,T\,n_0\epsilon\epsilon_0}\sinh\left(\frac{ze\psi_0}{2kT}\right) \tag{2.22}$$

Gouy Chapman (GC) capacitance is then be found by taking the first derivative of Eq. 2.22 with respect to potential:

$$C_d = \frac{d\sigma}{d\psi} = \sqrt{\frac{2\,\epsilon_0\,\epsilon\,n_0\,z^2\,e^2}{kT}}\cosh\left(\frac{ze\psi_0}{2kT}\right) \tag{2.23}$$

As indicated by Eq. 2.23, GC capacitance is dependent on the concentration of electrolyte, the applied potential and temperature [75].

Stern contribution

Although, Gouy-Chapman (GC) model was successful in the explanation of the effect of the applied potential and the concentration of the electrolyte, it is based on the assumption that ions are point charges and therefore ignores the distance between the ion and the surface (and consequently Helmholtz layer). Therefore, Stern [75] has combined the two models (i.e. Helmholtz and Gouy-Chapman) so that the interface is made up of two layers, the compact region and the diffuse one. This could be better understood by looking into the potential profile in Fig. 2.19, in which three regions are identified:

(a) **Stern layer**: This layer (or Helmholtz layer) is characterized by a constant electric field (Fig. 2.20-(b)) and its thickness is equivalent to the dimensions of the solvent molecule (x_s). The potential profile in this layer ($0 \leq x \leq x_s$) is given by Eq. 2.24.

$$\psi(x) = \psi_0 - x\sqrt{\frac{8\,k\,T\,n}{\epsilon\epsilon_0}}\sinh\left(\frac{ze\psi_s}{2kT}\right) \tag{2.24}$$

(b) **Diffuse layer**: This layer is described with a variable electric field (Fig. 2.20-(b)) and the potential profile from the end of Stern layer ($x \geq x_s$) follows Eq. 2.25 and its approximation Eq. 2.26 under the condition that $Ze\psi/4kT < 0.5$

$$\tanh\left(\frac{ze\psi}{4kT}\right) = \tanh\left(\frac{ze\psi_s}{4kT}\right)\exp(-\lambda x) \tag{2.25}$$

$$\psi = \psi_s \exp(-\lambda x) \tag{2.26}$$

where λ is given by Eq. 2.20 and ψ_s is potential at $x = x_s$.

(c) **Debye layer**: This is rather a conceptual region, which is defined as the distance from the surface where the potential (ψ) drops to $1/e$ from its initial value (ψ_0). So it can be obtained from Eq. 2.27 and Eq. 2.20. It is observed that Debye layer is inversely related to the square root of the bulk ion density. Therefore, shorter interaction distance (i.e. Debye layer) is obtained by increasing the concentration of electrolyte leading to a rapid potential decay [75].

$$l_d = \frac{1}{\lambda} \tag{2.27}$$

Beyond the diffuse layer, the potential gradient is zero (i.e. zero electric field - Fig. 2.20-(b)) which indicates a neutral bulk electrolyte [75]. The equivalent circuit for the Gouy-Chapman-Stern model is series of compact layer capacitance and diffuse layer capacitance (i.e. the differential capacitance). The value of the total double layer capacitance (see Eq. 2.28) is limited by the diffuse capacitance and therefore, it is limited by the concentration of the electrolyte and the applied potential [75].

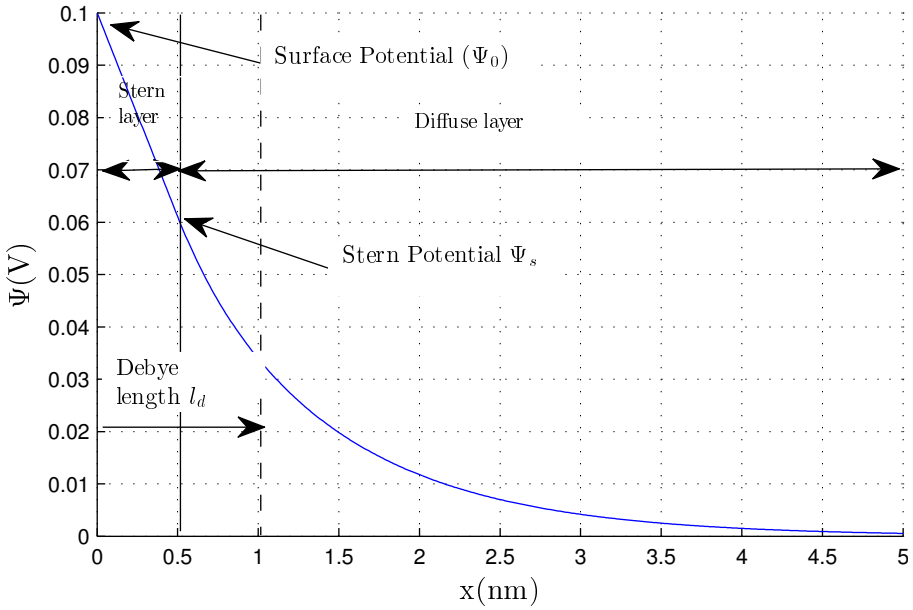


Figure 2.19: A sketch shows the key regions near the metal-electrolyte interface with respect to the potential profile at the electrode-electrolyte interface.

$$\frac{1}{C_T} = \frac{x_s}{\epsilon_0 \epsilon} + \frac{1}{\sqrt{\frac{2\,\epsilon_0\,\epsilon\,n_0\,z^2\,e^2}{kT}}\cosh\left(\frac{ze\psi_s}{2kT}\right)} \tag{2.28}$$

The potential, electric field and charge profiles at the metal electrolyte interface are sketched in Fig. 2.20. For a positive potential at the metal surface, negative charges in the electrolyte are attracted to the metal surface. As shown in Fig. 2.20, the charge on the electrolyte side is neutralised by the opposite charge on the metal side ($x < 0$) and similarly electric field changes it sign in the metal side. The potential in the metal side has the same sign as the charge on the metal. The electric field, charge and potential decays rapidly in the metal with a decay length of 0.5 A° equivalent to Thomas-Fermi screening length [77].

After presenting the history and the physical principles of the plasmonic voltage sensing, a review of the recent studies, systems and models that have been used in voltage sensing for different scientific and biomedical applications will be presented in the next section.

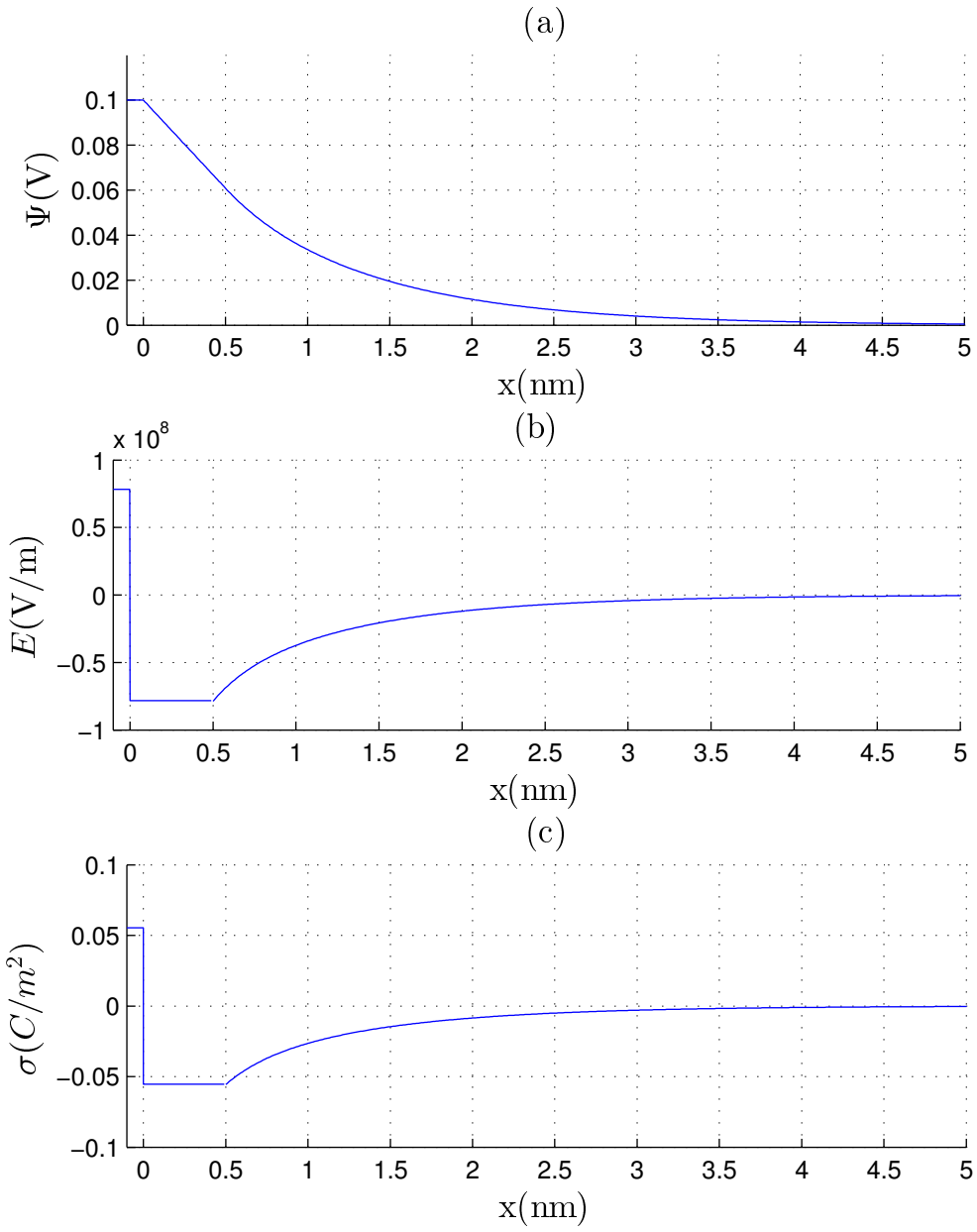


Figure 2.20: A sketch illustrating the profiles and the signs of the potential, charge and electric field at the metal-electrolyte interface. The signs of these quantities are shown over a small scale on the metal side ($x < 0$ and $|x| << d_{TH}$) where d_{TH} is Thomas Fermi length.

2.3.3 Plasmonic systems for voltage sensing

Plasmonic nanoparticles voltage sensing systems

In principle, all plasmonic structures are voltage-sensitive. Therefore, plasmonic nano-particles immobilized on conductive substrates (such as Indium Tin-oxide) have been used for voltage sensing [78, 25, 79]. For instance, Huang et al [78] have investigated the effect of the shape and morphology on the voltage sensitivity of plasmonic nanoparticles exploiting the shift in resonance peak of the absorption spectrum. These investigations revealed that a gold ultra-thin film, which is made of connected islands, is more sensitive compared to nanospheres or nanorods due its high aspect ratio. Therefore, a single wavelength at the highest gradient of the absorption spectrum has been used to investigate its time-dependent response. The study reported a feasibility of detecting signals of 10 kHz bandwidth when phase sensitive detection is used. To do these experiments, a dark-field imaging system was designed and combined with a three-electrode electrochemical system - see Fig. 2.21. In this system, nanoparticles on Indium Tin-oxide (ITO) served as a working electrode of which potential is controlled against the Ag/AgCl reference electrode. Phase-sensitive detection has been designed to only acquire signals at the voltage modulation frequency.

The effect of the voltage on the response of the plasmonic nano-particles has been applied to the detection of the change in the refractive index of the sample, which shift the absorption spectrum of the plasmonic structure. This shift is normally detected by using a broadband light source with a spectrometer. At fixed wavelength, the voltage scan is used to constructed the first order derivative of the spectrum [80] providing a simple and fast way to construct the absorption spectrum and calculate the shift in the resonance peak.

Although the voltage sensitivity of plasmonic nanoparticles has been characterized, propagating surface plasmon supported by the metal thin film has more advantages

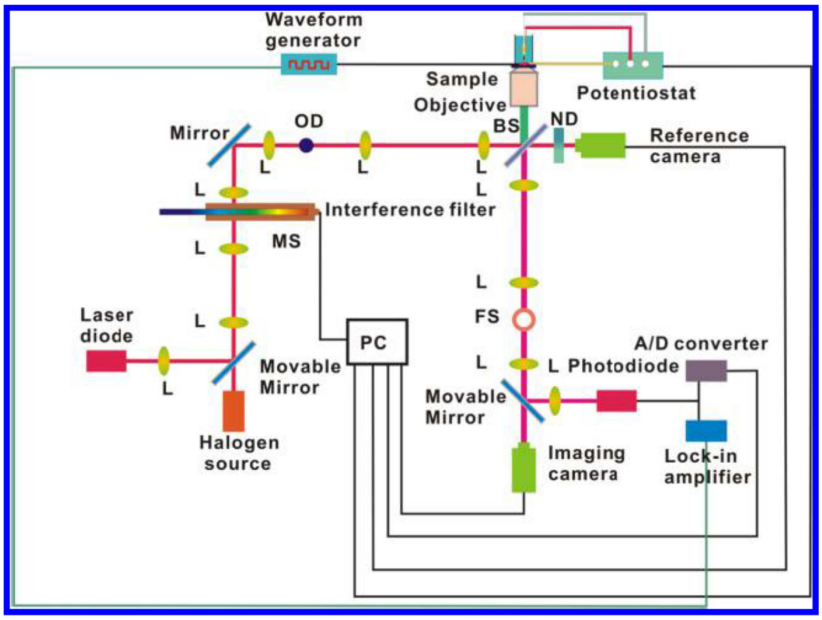


Figure 2.21: A micro-spectroscopy system to detect the voltage-modulated scattering from plasmonic nanoparticles. Diagram taken from Huang et al [25]

compared to the nanoparticles arrays. It offers a higher imaging resolution and is generally more sensitive compared to the nanoparticles [81]. These advantages motivate us to explore voltage sensitivity of surface plasmon resonance. Some of the recent studies in this field are discussed here.

Thin film voltage sensing systems

The use of propagating surface plasmons that are supported by noble metal thin film for voltage sensing is not recent. The effect of voltage on the properties of SPR has been reported as early as 1970 [82, 83, 70]. More recently, the technique has been explored for both sensing the voltage in the electrical double layer capacitance charging window [28] as well as for redox processes at higher potential [84] with pioneering work for formulating the theory of SPR for electrochemical sensing [59].

SPR-based voltage systems: SPR-based voltage sensing systems are similar to

the nanoparticles system in Fig. 2.21, a conventional surface plasmon resonance configuration is combined with electrochemical system. Three-electrode electrochemical systems, which were used in a number of studies [84, 73, 27, 85], are usually more accurate compared to two electrode used by ref [28]. In a two-electrode system, one electrode is attached to the plasmonic thin film (working electrode) while the other is placed in the electrolyte (counter electrode) and used to apply a current and measure the voltage. The disadvantage of this configuration is the contribution of the processes of the counter electrode and the bulk electrolyte to the measured voltage given that fact of targeting the potential of the working electrode only. In order to measure the potential of the working electrode precisely, a third electrode is used (reference electrode), which does not contribute to the applied voltage and serves as a reference point with a constant potential.

Voltage effects on the SPR curve: The response of the SPR system to the applied voltage has been investigated in terms of resonance shift and changes in the shape of the curve. For instance, Lioubimov et al [28] investigated the effect of different aqueous solutions on the system's response . Different amplitude responses (resonance shift) of the SPR have been found for pure water, 5mM NaCl, 5mM KOH and propionic acid. However, the study compared pure water and propionic acid to salt solutions; the first two are considered weak electrolytes with interfacial capacitive properties that are distinct from the salt solutions [86]. Also, the concentration of the sodium chloride used in this study is far from that of the physiological solutions (0.15 M NaCl) - the target of our project. So for these reasons, the obtained results can not be used to draw a conclusion on voltage sensitivity of SPR for biological applications. On the other hand, Roy et al [27] addressed the change in the shape of the resonance curve due to applied voltage providing an analytical expression to accommodate for these changes, but the study included a voltage range that can induce electrochemical reactions. Such changes in the shape of the curve due to the effect on the double layer capacitance were not addressed and are still

not clear.

Nonlinear SPR response: Roy et al [27] obtained experimental results in the capacitive region featured nonlinear SPR response to applied voltage which was not well explained. These findings do not agree with the analysis of Foley et al [73], which uses the SPR response to develop a surface impedance imaging technique assuming (i) a linear capacitive properties and (ii) the voltage de-localization of electrons within the entire the metal's thickness [58]. These two assumptions contradict two established theories: the nonlinear double layer capacitance [75] and the confinement of the voltage effect to the first atomic layer of the metal [23]. This model has been modified to include these two effects by Lopatynskyi et al [84] and Huang et al [85], in which the nonlinearity could be attributed to the properties of the nonlinear interfacial capacitance.

In spite of the efforts described by Huang et al [85] and the other studies, the experimental voltage sensitivity of surface plasmon resonance is still an open question. This could be described in two fundamentals points: (i) the minimum detectable voltage and (ii) the response time of the sensor to the fast voltage excitation. These fundamental experiments in addition to the proper design of the optical system will pave the way towards label-free detection of electrical activity of cells. Therefore, the aim is to extend these theoretical studies in two directions: (i) In-depth understanding of the different factors related to the interface and (ii) optimizing the sensing device towards higher voltage sensitivity.

Chapter 3

Theoretical Analysis of Voltage Sensitivity of Surface Plasmon Resonance

3.1 Introduction

This chapter is concerned with providing an estimate for the SPR voltage sensitivity and therefore electrochemical and optical models have been combined to investigate the system response to voltage perturbations. This analysis is motivated by assessing the potential of SPR for the detection of the electrical activity of excitable cells.

As concluded from chapter 2 that SPR can be used, in principle, to detect the change in the transmembrane potential by direct detection of voltage or the resulting change in refractive index of the cell as a secondary effect. However, changes in refractive index associated with the bioelectrical signal are debatable [67]; the main two hypotheses relate this effect to the refractive index of the cell membrane or the change in the cell volume during the excitation. Moreover, measurements of refractive index change during membrane depolarisation are inconsistent. Calculations

of refractive index associated with membrane depolarisation for squid giant axon is 1×10^{-6} RIUs according to Cohen et al [87], yet it is 5×10^{-3} RIUs for a single Aplysia axon according to Stepnoski et al [88]. Based on the recent study of Hajj et al [89], a change in the order of 10^{-4} RIUs is calculated. Electrical measurements of the transmembrane potential, in contrast, are well characterized, accurate and repeatable [6] demonstrating a well-known change of the transmembrane potential of the excitable cells [6] from a resting state of around -60 mV to the excited state of around +40 mV (Fig. 1.2) when they are chemically [2] or electrically excited [3]. Therefore, the direct potential sensing seems a promising direction towards a reliable detection of this signal. As discussed in Sec. 2.3 that SPR sensing structure could be regarded as an electrode with optical readout; however, its sensitivity to this signal needs to be evaluated by determining the minimum detectable voltage using SPR.

As mentioned in chapter 2, there is a gap in literature regarding the detection limit of SPR systems. In order to evaluate that experimentally, one need to know the specifications of the optical configuration (i.e. the required sensitivity) that needs to be designed for this purpose. To identify these specifications, theoretical analysis of voltage sensitivity is a natural choice. In addition to that, this analysis could be used to:

(a) validate the performance of the voltage sensing system and verify the obtained results by comparison to the theoretical ones as will be discussed in chapter 4.

(b) investigate the effect of the parameters of the interface such as the concentration of the electrolyte and the temperature as will be discussed in this chapter and chapter 6.

(c) provide a thorough understanding of the characteristics of the potential at the interface in addition to the behaviour of the electrical double-layer capacitor, as will be discussed later in this chapter.

First of all, this chapter is introduced by discussing the mechanism of electric energy transfer between the cell membrane and the electrode-electrolyte interface. Therefore, we will look into the models for the cell-electrode interface and how they can be adopted for the purpose of this research. Cell-sensor contact (see Fig. 3.1- (b)) can be modelled by an equivalent electrical circuit (Fig. 3.1- (a)) and this model is the underlying theory for microelectrode arrays (MEAs) which are the commonly used in extracellular recordings [90, 91]. In this model, cell membrane is considered a leaky capacitor (C_m) in series with the interfacial capacitor of the electrode (C_e). The potential across the membrane capacitor reverses its polarity when the cell is excited. This model tells how the transmembrane potential couples to the electrode. Since the equivalent capacitance of the cell membrane and the double layer capacitance of the electrode are in series, they accumulate the same amount of charge upon passing a charging current. So, the voltage across the electrode capacitance (V_e) could be directly found from the voltage across the cell membrane (V_m)- see Eq. 3.1. The ratio between these two capacitances ($\eta_c = C_m/C_e$) is an important concept regarding the energy transfer; the maximum coupling occur when two capacitances match $\eta_c = 1$. This equation will be used to conclude on voltage sensitivity later in chapter six and seven.

$$V_e = V_m \frac{C_m}{C_e} \tag{3.1}$$

In addition to the electrical circuit, optical models have been used to study cell sensor-interface [92, 93] representing the different components with their refractive indices in a multilayer structure. However, for the purpose of this discussion, we need to modify these models to include the effect of the electrical properties of the interface on the optical properties of the electrode - see Fig. 3.2. This is added by modelling the electrolyte using two layers: bulk and interfacial layer (Debye layer - see Sec. 2.3.2). Similarly, a gold thin film is modelled by two layers: the bulk and a very thin layer at the interface (it will be later called Thomas-Fermi length

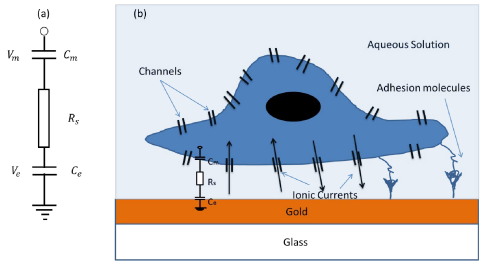


Figure 3.1: Cell-sensor (or electrode) interface and its equivalent electrical circuit

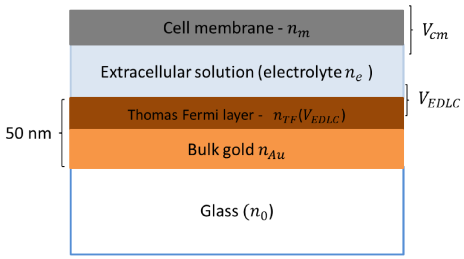


Figure 3.2: An electro-optical model for the cell-SPR sensor interface

layer)Fig. 3.2. These two additional layers (Debye layer and TF layer) represent the contribution of the electrical double layer capacitance (Sec. 2.3.2) to the model [75].

3.2 Modelling of voltage sensitivity of SPR

As discussed on page 57, the work presented in this thesis focuses on the assessment of SPR capacity in the direct detection of the bioelectrical activity rather than the secondary effects on the physical properties of the membrane. Therefore, the model in Fig. 3.2 is simplified in Fig. 3.3 removing the cell membrane layer, for simplicity. This model will be used to estimate the detection limits of surface plasmon resonance and will be used later to evaluate the potential of using the technique for detecting the transmembrane potential making use of the concept of the coupling efficiency (η_c). The theoretical analysis and simulation is performed under two assumptions:

(a) The effect of the applied voltage on the dielectric properties of the electrolyte is negligible since the effective voltage sensing length (Debye layer $\sim$ 1 nm - page 50) is very small compared to the evanescent field depth ($\sim$ 180 nm - page 18).

(b) Gold thin film is modelled with two layers: Thomas-Fermi length and the bulk gold while assuming abrupt interface between the two layers. This is a simplification to a decay of charge density or electric field from the metal surface towards the bulk with a decay length equivalent to Thomas-Fermi length.

The details of the model and the selection of the different parameters will be described below. Fig. 3.3 shows the different layers of the one dimensional model of the voltage sensing configuration.

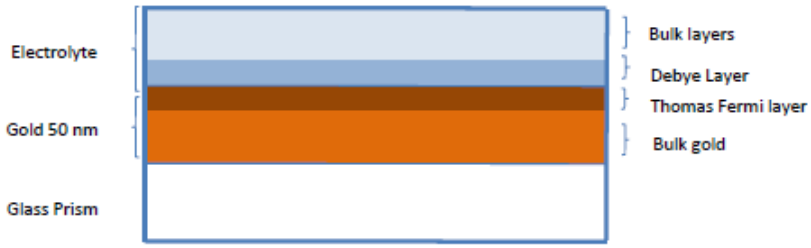


Figure 3.3: A one dimensional model for the voltage sensing structure, It consists of a glass prism, a metal (bulk and Thomas-Fermi length) and Electrolyte (Debye layer and bulk)

3.2.1 Reflection of light from the mulitlayer sensing structure

Voltage sensitivity of SPR systems was studied by producing SPR curves for the sensing structure described in Fig. 3.3. Therefore, the reflectance of p-polarised light was calculated for a range of angles of incidence using the transfer matrix method [94]. This method is described using the structure in Fig. 3.4 which consists of n layers between two semi-infinite media marked with (0) and (n+1) respectively. The transfer matrix relates electric fields of the incident light at the first interface (E_0^f) and the light propagating back to the semi-infinite medium (E_0^b) to the electric field of the light (E_{n+1}^f) leaving the structure to the semi-infinite medium (n+1). This relation is expressed as

$$\begin{pmatrix} E_0^f \\ E_0^b \end{pmatrix} = \begin{pmatrix} S_{11} & S_{12} \\ S_{21} & S_{22} \end{pmatrix} \begin{pmatrix} E_{n+1}^f \\ 0 \end{pmatrix} \tag{3.2}$$

Using the elements of this matrix, reflection of p-polarised light to the semi-infinite medium (substrate in practice) can be found from

$$R = \left(\frac{E_0^b}{E_0^f} \right)^2 = \left(\frac{S_{21}}{S_{11}} \right)^2 \tag{3.3}$$

In order to calculate the transfer matrix, the structure in Fig. 3.4 is characterised by a series of matrices that account for the effect of its layers (L_1 to L_n) and interfaces (I_{01} to $I_{n(n+1)}$). The transfer matrix is given by the product of matrices of interfaces and layers

$$S = I_{01} L_1 I_{12} L_2 I_{23} L_3 .... L_n I_{n(n+1)} \tag{3.4}$$

Let i and i+1 be two adjacent layers in the structure in Fig. 3.4, with complex refractive index n_i and n_{i+1} and thickness d_i and d_{i+1}, respectively. For layer(i), the

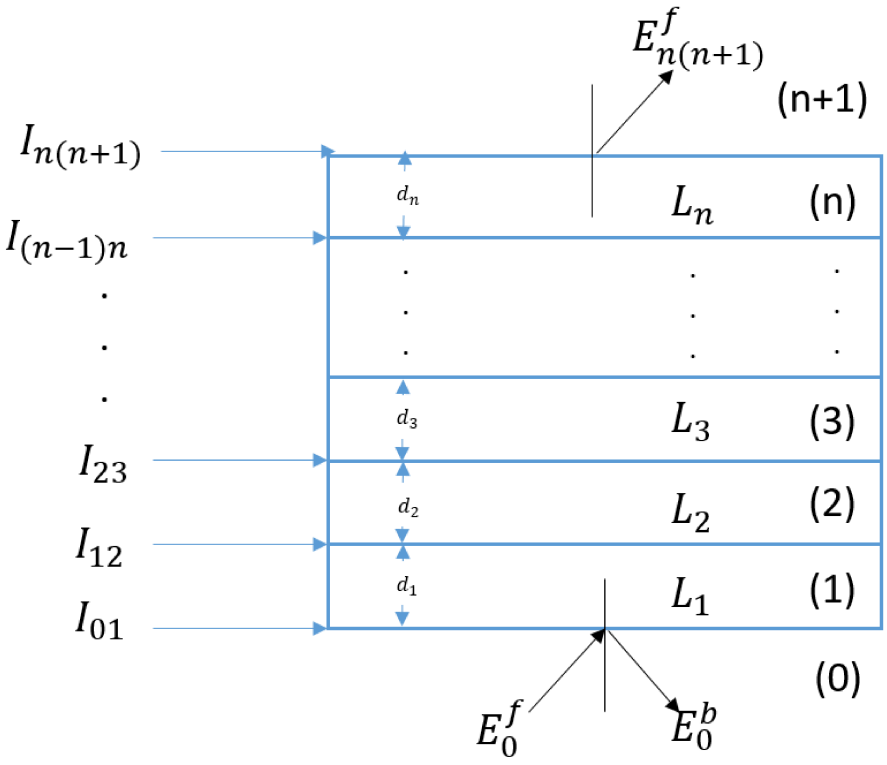


Figure 3.4: A sketch illustrates the use of the transfer matrix to quantify light propagation and reflection from the multilayer structure.

layer matrix is found by

$$L_i = \begin{pmatrix} e^{j\beta} & 0 \\ 0 & e^{-j\beta} \end{pmatrix} \tag{3.5}$$

where β is phase shift of light propagating the layer (i) at angle θ_i which is calculated by

$$\beta = \frac{2\pi}{\lambda} n_i d_i \cos\theta_i \tag{3.6}$$

where d_i is the thickness of the layer (i) and its complex refractive index. For an interface i(i+1), the interface matrix is

$$I_{i(i+1)} = \left(\frac{1}{t_{i(i+1)}}\right) \begin{pmatrix} 1 & r_{i(i+1)} \\ r_{i(i+1)} & 1 \end{pmatrix} \tag{3.7}$$

where $r_{i(i+1)}$ and $t_{i(i+1)}$ are the reflection and the transmission coefficients of p-polarised light crossing the interface (i(i+t)). These coefficients can be found from Fresnel equations[95]:

$$r_{i(i+1)} = \frac{n_{i+1}\cos\theta_i - n_i \cos\theta_{i+1}}{n_{i+1}\cos\theta_i + n_i \cos\theta_{i+1}} \tag{3.8}$$

$$t_{i(i+1)} = \frac{2n_i \cos\theta_i}{n_{i+1}\cos\theta_i + n_i \cos\theta_{i+1}} \tag{3.9}$$

where θ_i and θ_{i+1} are the angles of light in the layer (i) and the layer (i+1) respectively.

The method described above was used in the modelling procedure described in Sec. 3.3 on page 67. In that procedure, SPR curves were produced by calculating the overall reflectance using Eq. 3.3.

3.2.2 The bulk layer of the gold thin film

This layer models the gold thin film that supports the propagating surface plasmons. The optical constant and the thickness of this layer are essential contributions to the multilayer model [24, 29]. The dielectric constant of gold is calculated using mainly one of two models: Drude and Drude-Lorentz; both describe the interaction of light with electrons in the metal [96, 97, 98]. The transition from higher to lower energy levels within the same conduction band (intraband transition) is calculated using Drude model. This model ignores the effect of the bound electrons and therefore it treats the metal as an electronic liquid. The effect of the bound electrons (i.e interband transition) is modelled using Drude-Lorentz approach which accounts for the existence of the nucleus. In this simulation, Drude-Lorentz is used to determine the refractive index of the gold (i.e. the bulk layer)[96]. The Johnson and Christy database of refractive index was used to obtain the value of the refractive index for the wavelength of 633 nm which is $0.18344 + 3.4332i$ [99] [100]. The thickness of this layer was set to 50 nm which produces the SPR curve of the optimal sensitivity [29].

3.2.3 Thomas-Fermi screening layer

This layer has distinct characteristics due to the electric field effect on the free charge density in the metal. The static or low-frequency electric field is screened by the free electrons of the metal surface and thus its effects are confined to this layer. In contrast, electric fields with high frequency (higher than - the plasma frequency) are not screened by electrons due to their mass and density. This layer, in fact, is the effective sensing medium as presented in Eq. 2.11. The concentration of free electrons is found from Eq. 3.10 [101] which is $5.9 \times 10^{28} m^{-3}$. This density is changed by the applied electric field and consequently, the plasma frequency (see Eq. 2.10 and Eq. 2.12). This effect modifies the dielectric constant of this layer. The

dielectric constant of this surface layer is modelled according to Drude's free electron theory [70, 23]. The depth of Thomas-Fermi layer is about 0.5 A° [102] while the radius of gold atom is around 1.74 A° [103]. Therefore this sub-atomic layer (i.e., the penetration depth of the electric field) is considered a fluid of free charge carriers making the Drude model sufficient for modelling its optical properties.

$$N = \frac{N_{Av}\,\rho}{m_A} \tag{3.10}$$

where N is density of free electrons (m^{-3}), N_{Av} is Avogadro Number ($mole^{-1}$), ρ is the mass density (g/m^3) and m_A is the atomic mass ($g/mole$).

3.2.4 The Debye layer

This layer (defined in Sec. 2.3.2) confines the charge carrier density in the electrolyte side describing an exponential decay of the electrostatic energy applied to the surface (see Fig. 2.19). This layer contributes to the model with the properties of the electrical double layer capacitance. This is calculated from Eq. 2.28 using the values of the boundary conditions listed in Table 3.1. The parameters that control the behaviour of this layer and the total capacitance are described below.

(a) Stern potential (ψ_s) (Fig. 2.19) which is dependent mainly on the potential applied to the electrode-electrolyte interface (ψ_0). Stern potential can be found by solving Eq. 2.24 using Taylor expansion to produce a polynomial from Eq. 3.11. So, the equation can be rearranged by putting (ψ_s) in the right-hand side. The order of this polynomial is determined by condition that $\frac{(c_2\psi_s)^n}{n!} > \frac{(c_2\psi_s)^{(n+1)}}{(n+1)!}$

$$\psi_s = \psi_0 - c_1 \sinh\left(c_2\psi_s\right) \tag{3.11}$$

where $c_1 = x_s\sqrt{\frac{8\,k\,T\,n}{\epsilon\epsilon_0}}$ and $c_2 = \frac{ze}{2kT}$

For the charging and the discharging window of the double-layer capacitance, in the range of (-150 mV to +150 mV), a third-order polynomial is sufficient since it satisfies the condition $\frac{(c_2\psi_s)^3}{6} > \frac{(c_2\psi_s)^5}{120}$.

$$\frac{c_1 c_2^3 \psi_s^3}{6} + (1 + c_1 c_2)\psi_s - \psi_0 = 0 \tag{3.12}$$

(b) The type and the concentration of the electrolyte. In this simulation, sodium chloride was used as the electrolyte while a range of concentrations were used to study the behaviour of the capacitance.

(c) The type of the solvent which sets the thickness of the Helmoholtz layer (x_s) since the separation is on the order of the solvent molecule. It also determines the permittivity of this separating dielectric layer. Static or low frequency permittivity of water was chosen to represent the properties of this dielectric separation.

Table 3.1: The parameters of the double-layer capacitance

Parameter	Value	Comments
x_s	0.5 nm	The diameter of water molecule
ϵ	80	The static permitivity of water at 20 $°C$ and a pressure of 1 atm [65]
z	1	Valence of the ion. NaCl is symmetric electrolyte
kT	4.1164×10^{-21}	Thermal energy in Joules

3.2.5 The bulk electrolyte

The bulk electrolyte only contributes to the optical properties of the model since it is electrically neutral [75]. So, the effect of its refractive index can be considered as a baseline for the SPR measurement. In other words, it sets the DC offset for the dynamic nature of the applied voltage signal. The effect of this DC offset on

SPR sensitivity will be discussed in more detail in chapter 5. The refractive index of this layer depends on the concentration of the electrolyte, the wavelength and the temperature - see Eq. 3.13. Starting from the refractive index of distilled water for 1.3319 (at 633 nm), the refractive index of 150 mM NaCl at 20 $°C$ and 633 nm is 1.33339. The thickness of this layer is considered to be semi-infinite.

$$n(\lambda, C, T) = n_0 + \frac{dn}{dC}\Delta C + \frac{dn}{dT}\Delta T + \frac{dn}{d\lambda}\Delta\lambda \tag{3.13}$$

Where n_0 is the initial refractive index at specific wavelength, electrolyte concentration and temperature.

Table 3.2: The effect of temperature (T), wavelength (λ) and concentration (C) of the electrolyte on the refractive index of NaCl aqueous solution

$dn/dT(RIUs/°C))$	$dn/dC(RIUs/M))$	$dn/d\lambda(RIUs/\mu m)$
-10^{-4} [104]	0.0099 [105]	-0.02 [106] [104]

3.3 Modelling procedure and outputs

Before presenting the effect of the voltage on the properties of the SPR, this section presents an evaluation of the modelling procedure by looking into the effect of the voltage on (i) the charge density at the interface, (ii) the translation of this effect to the properties of the free electrons in the metal surface and (iii) the optical properties of the metal surface.

The previous multilayer structure (Fig. 3.3) was used to study the SPR response to changes in the potential at the electrode-electrolyte interface. The potentials were varied in the range of ($\pm$ 200 mV) while all the values described in the model are kept constant for the following procedure.

(a) Stern-Gouy-Chapman model (Eq. 2.28) is used to calculate the double layer capacitance of the interface for each potential and for NaCl concentration (NaCl 150 mM; the physiological concentration).

(b) McIntyre model is used to calculate change in the free electron density in TF length of gold for each potential while Drude model is used to calculate the refractive index of this layer.

(c) SPR curves are constructed, for each potential, by calculating the reflectivity for the multilayer structure presented in Fig. 3.3 using the transfer matrix method and Fresnel equations [107].

(d) To find the location of the minimum reflectivity (the resonance angle), a window of the SPR curve in Fig. 3.5 (± 0.25 deg from the resonance angle) is fitted to a second order polynomial. The root mean square error (RMSE) of the fitted value is 6.9×10^{-05} and $R^2 = 0.9994$. Interpolation was used to increase the number of samples to 2×10^6 data points per degree.

(e) The model is used to find the relation between the change in the refractive index (Δn) and the change in the resonance angle ($\Delta \theta_0$) for mapping the effect of the voltage to its equivalent refractive index.

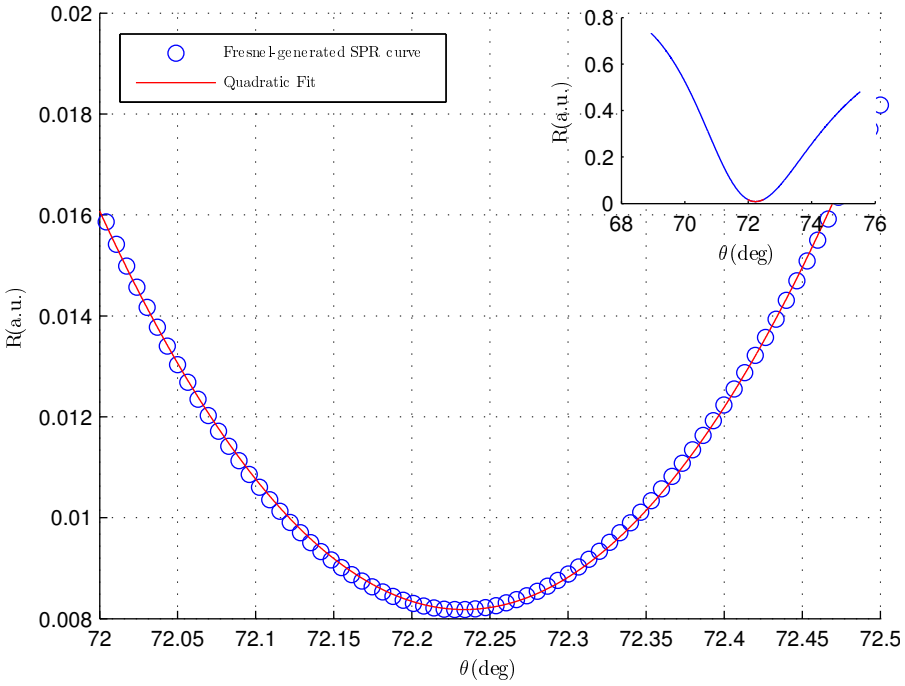


Figure 3.5: Fitting a window of the resonance curve to a quadratic function. The inset shows the complete curve

3.3.1 Charge density at the electrode-electrolyte interface

The effect of the applied voltage on the capacitance and the charge density of the interface is shown in Fig. 3.6 (a) and (b) respectively. The capacitance of the interface shows a strong dependence on the applied voltage. As seen in Sec. 2.3.2, the interface capacitance consists of two series capacitive components (the reason for the name double layer capacitor). The properties of the first component (Helmholtz capacitance) is similar to those of the conventional parallel-plate capacitance (Eq. 2.14) and it is not voltage dependent. The second component (the diffuse layer) results from the decay of the applied electric field to the electrolyte; imposing a weak electrostatic interaction with the charge carriers in the electrolyte. This electrostatic energy competes with the effect of the thermal energy on the charge carriers. By increasing the applied voltage, the effect of the electrostatic interaction increases the ion density in the diffuse layer that amplifies the capacitance of this layer. Generally,

the value of the total capacitance is governed by the diffuse layer capacitance since it is smaller than the Helmholtz capacitance and therefore it underlies the voltage-dependence of the total capacitance. For simplicity, the C *vs* V curve, which is presented in Fig. 3.6-(a), can be pictured as a quadratic curve. This relation explains the trend of Fig. 3.6-(b) that is similar to a 3rd order polynomial function, instead of the conventional linear voltage-charge relation. The obtained theoretical charge density will be used to validate the performance of the voltage sensing system presented in chapter 4.

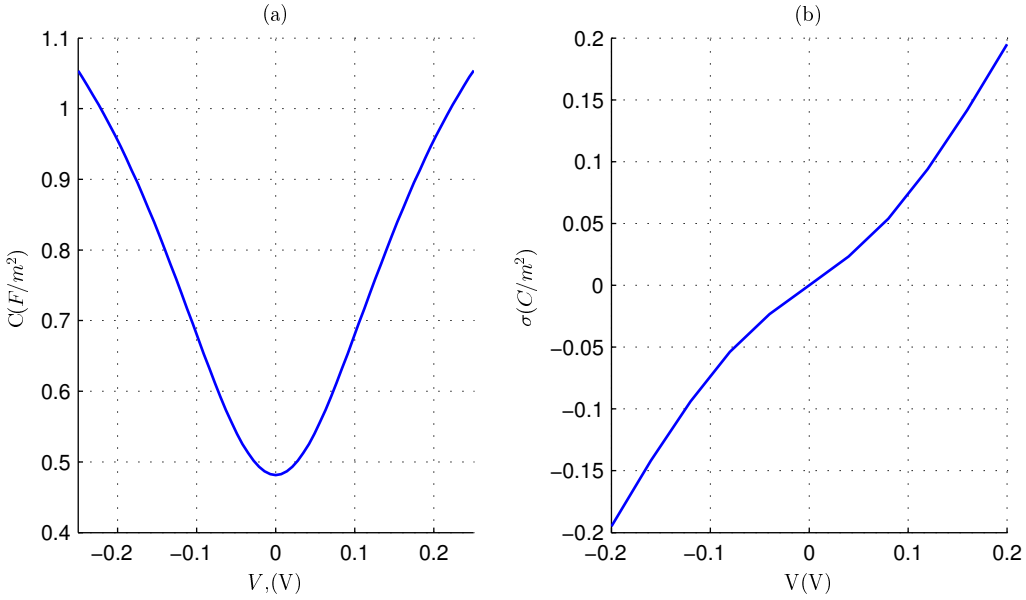


Figure 3.6: Voltage-dependence of (a) interfacial capacitance and the (b) the charge density at the metal side of the electrode-electrolyte interface.

3.3.2 Properties of free electrons in the metal surface

Accumulation of ions near the electrode surface is mirrored by either excess or deficiency of free electron density in the electrode surface (ΔN). The change in the free electron density is presented in Fig. 3.7-(a). This modification of electron density is reflected in the oscillation properties of these free electrons; as expressed in the

plasma frequency Fig. 3.7-(b). It is observed that that ΔN-V curve (in Fig. 3.7-(b)) is a mirror image of σ-V curve (Fig. 3.6-(b)). This is due to the attraction of electrons when negative voltage is applied, similar to repulsion of electrons when positive voltage is applied.

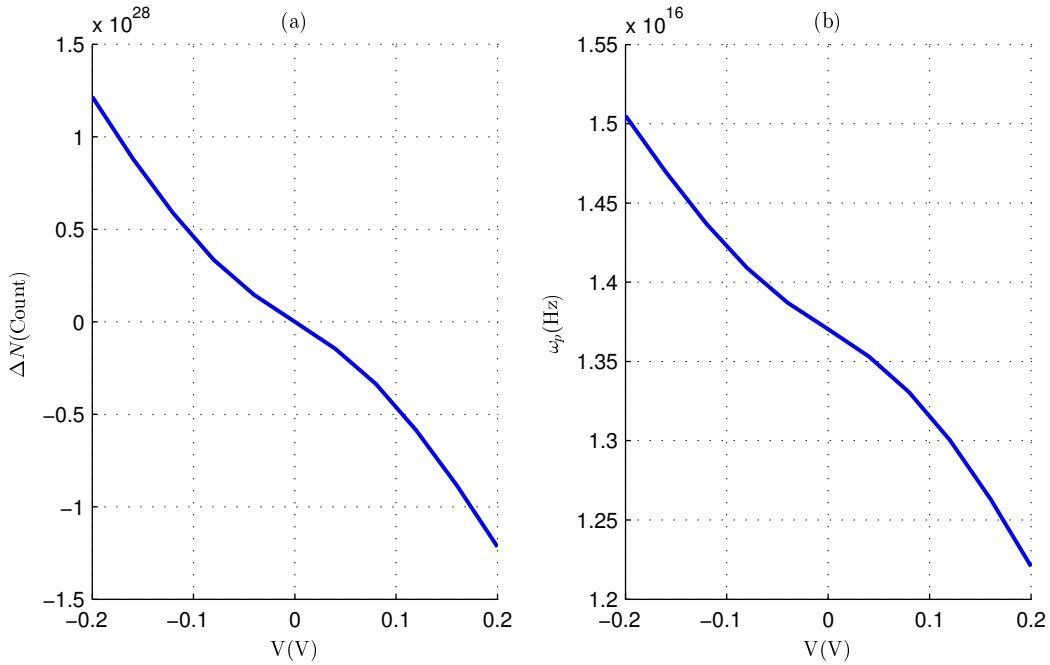


Figure 3.7: Voltage-modified (a) free electron density in the metal surface and (b) plasma frequency of the metal surface

3.3.3 Optical properties of the metal surface

Optical properties of the metal are strongly affected by the change in the plasma frequency. The dispersion of the complex dielectric constant of gold is presented in Fig. 3.8 for a set of plasma frequencies. The conventional permittivity dispersion curve [98] of gold in the range (300 nm - 1000 nm) (Fig. 3.8) was reproduced from Drude's model, which was used in the voltage sensing model. Both the real part of the dielectric constant $|\epsilon_r|$ (Fig. 3.8 -(b)) and the imaginary part ϵ_i (Fig. 3.8-(c)) increases with the plasma frequency. From Fig. 3.8-(b),(c) and Fig. 3.7-(b), the

voltage-modified dielectric constant of the Thomas-Fermi length was obtained as in Fig. 3.9. The absolute value of the real part and the imaginary part of the dielectric constant shows a trend similar to the ω_p-V curve. This observation is predicted by looking into Drude's model (see Eq. 2.13).

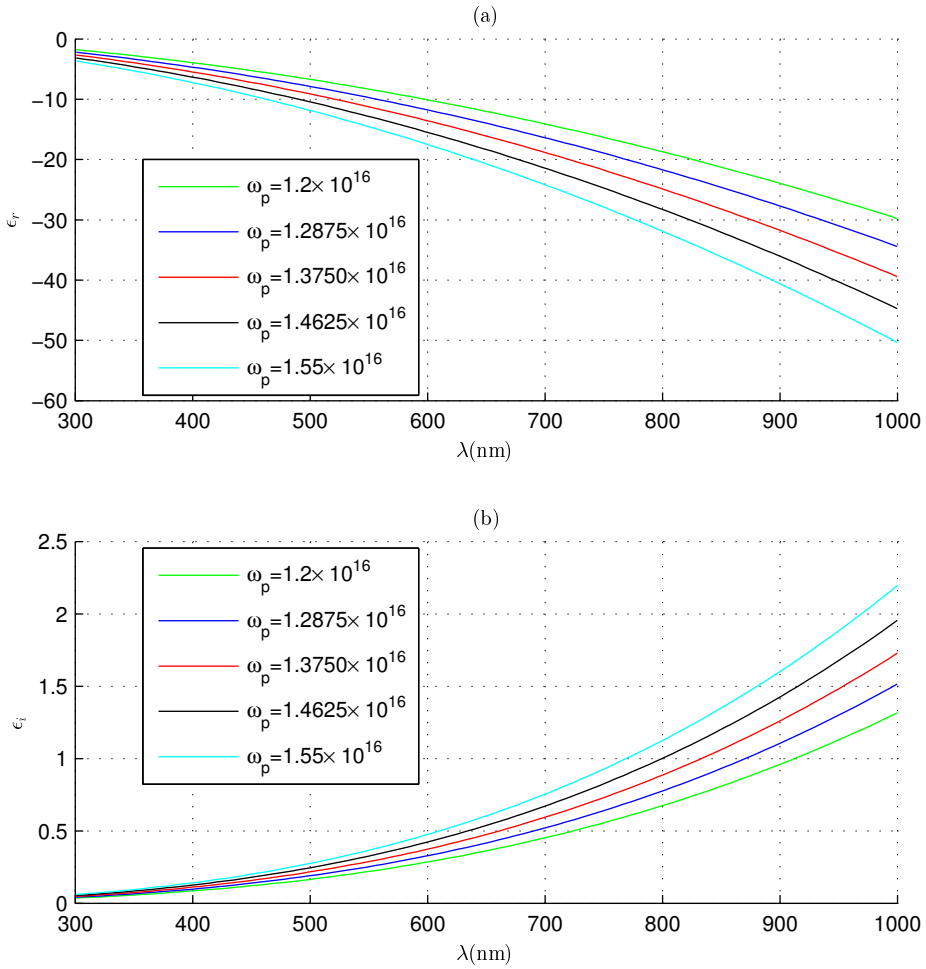


Figure 3.8: Wavelength and plasma frequency dependence of the (a) real and (b) imaginary part of the permittivity of gold.

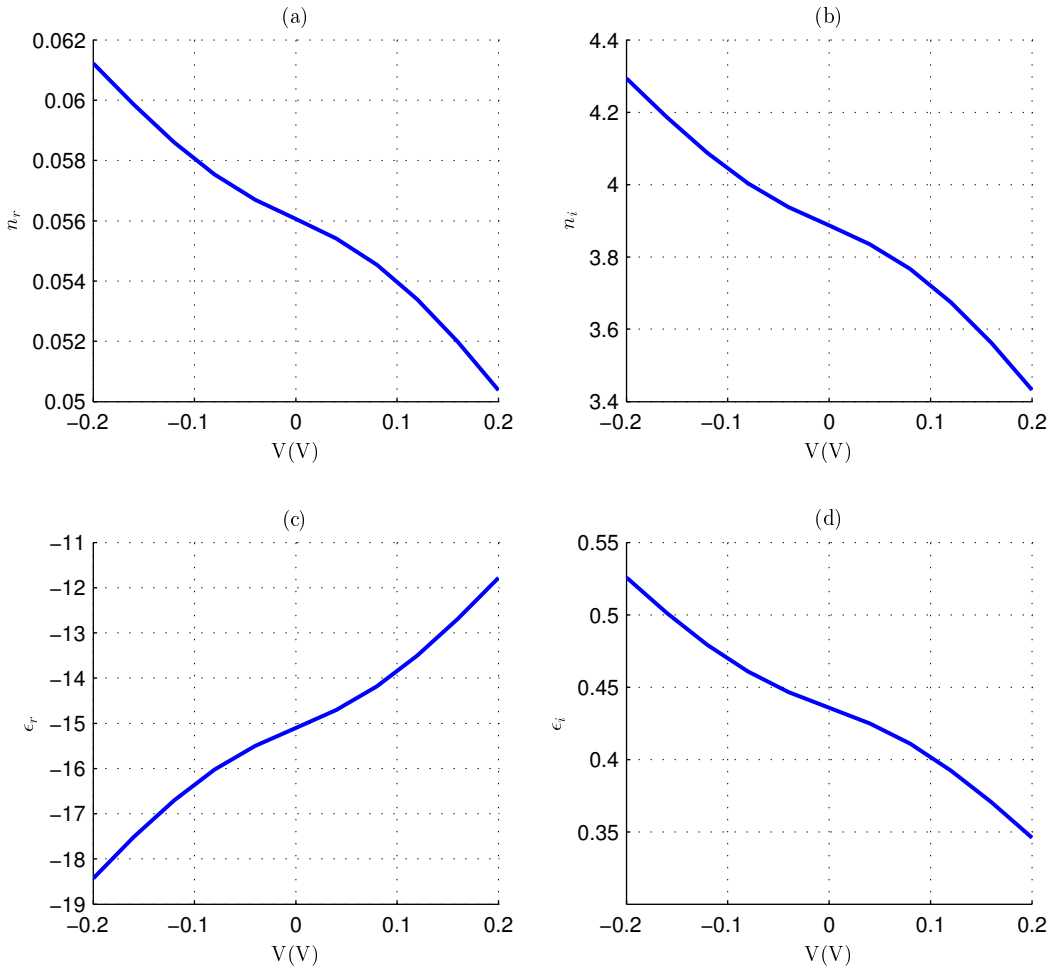


Figure 3.9: Effect of voltage on the real (a and c) and the imaginary (b and d) part of the refractive index (a and b) and the permittivity (c and d)

3.4 Voltage-modified surface plasmon resonance curve

Fig. 3.10 presents the effect of the interfacial voltage on SPR curve. It depicts SPR curves for a series of voltages in the range of $(-0.2 \rightarrow +0.2V)$. Three effects are induced on the curve: (i) a shift in the resonance angle, (ii) changes in the shape of the curve (FWHM) and (iii) changes in the minimum reflectivity of the curve. The voltage dependence of these effects is presented in Fig. 3.11.

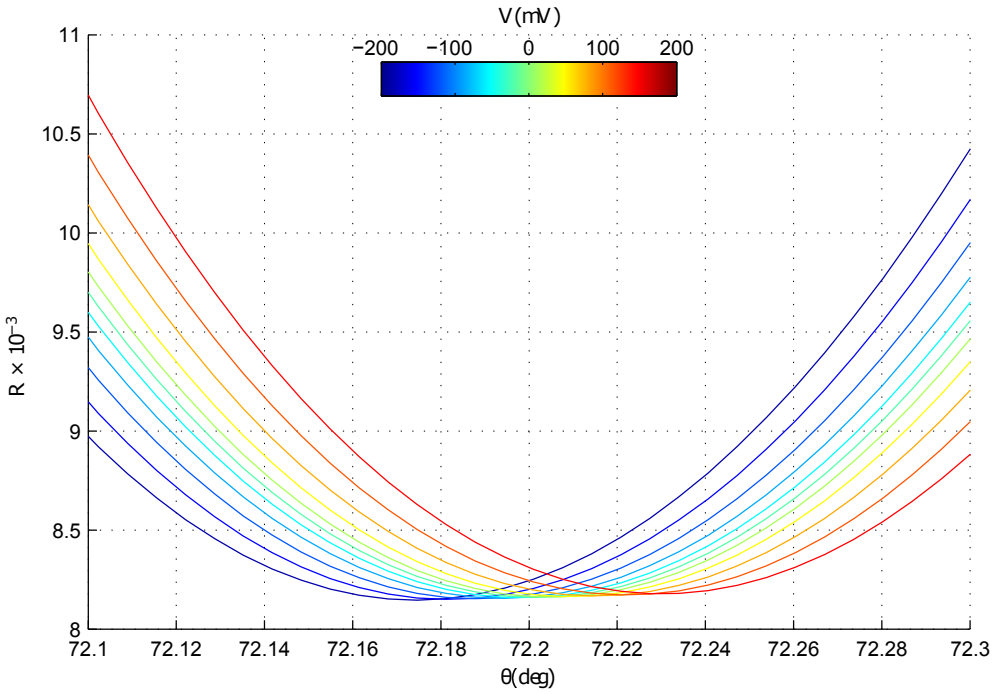


Figure 3.10: The effects of the applied voltage on the SPR curve

From Fig. 3.10 and Fig. 3.11, three behaviours are observed:

(a) The shift in the resonance position is stronger compared to the other FWHM and the minimum reflectivity.

(b) Voltage at the electrode-electrolyte interface mainly modifies the position of the resonance angle of the SPR curve. As in Fig. 3.10, applying a positive

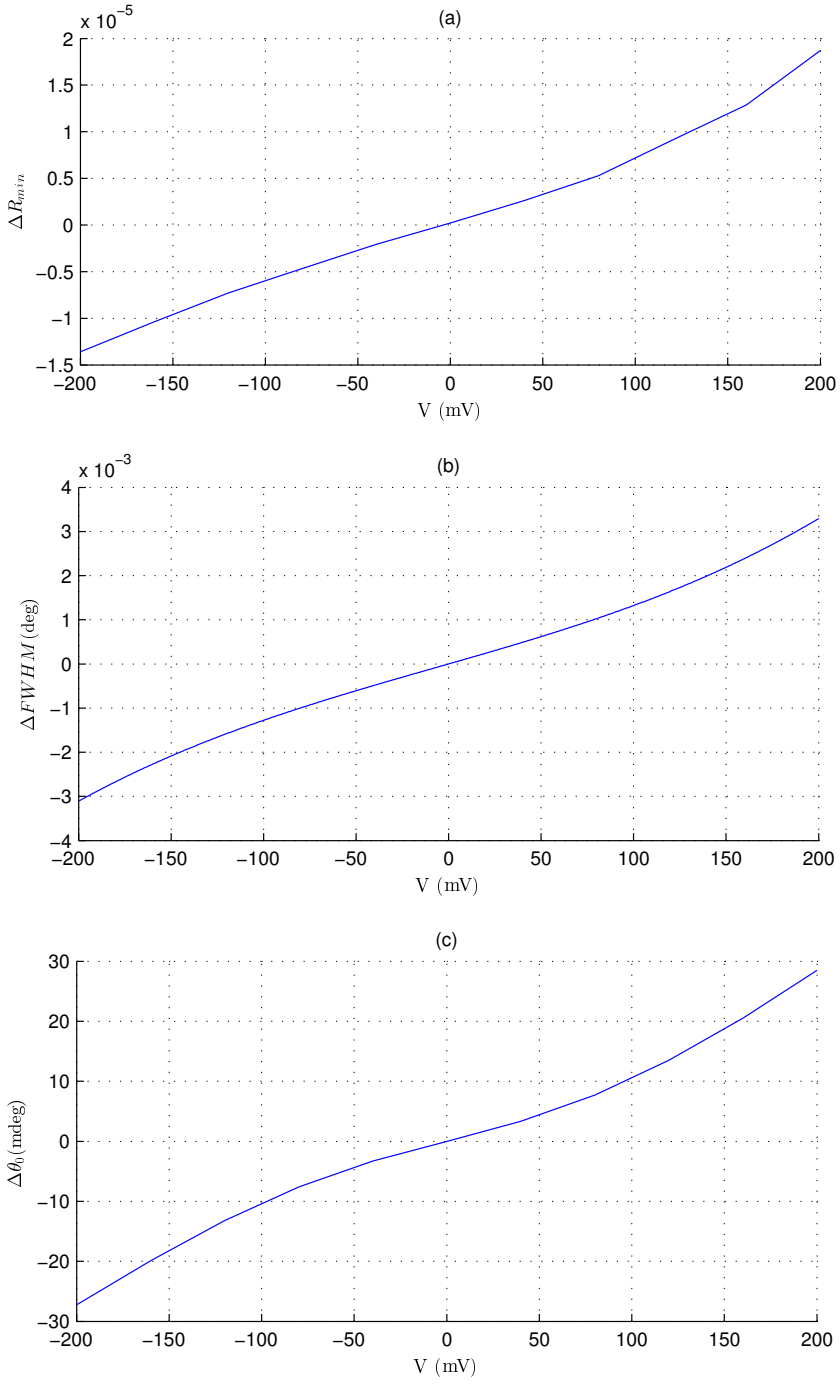


Figure 3.11: The effects of the applied voltage on the properties of the SPR

voltage shifts the resonance angle to the right while applying a negative voltage shifts it to the left.

(c) Fig. 3.11 shows a non-linear relation between voltage and these three parameters.

The observations a and b can be explained by looking into the complex wavevector of the SPs ($k_x = kx_r + ikx_i$) using Eq. 2.1 that is presented on page 14. As seen in Fig. 3.12, the real and the imaginary parts of k_x are calculated using the set of real and imaginary values of permittivity obtained in Fig. 3.9. First, the change in kx_r mainly displaces the resonance position and it is directly related to the resonance angle. As kx_r increases with voltage in the positive direction, it indicates an increase in the resonance angle (resonance position is shifted to the right) which is consistent with the observation (b). Similar agreement is noticed for the case of the negative voltage, in which kx_r decreases with negative voltage matching a shift to the left of the initial resonance position. Second, kx_i determines the propagation length of the SPs (Sec. 2.1.1 on page 13). The rise in kx_i with the positive voltage indicates an increase the damping properties of the metal shortening the decay length of the SP waves, and vice versa for negative voltage. This effect is expected to change the shape of the resonance curve increasing its FWHM. This kx_i - V relation is well-matched with the voltage dependence of the FWHM - see Fig. 3.11-(b). This kx_i - V curve can also be compared to voltage-induced change in the electron density as in Fig. 3.7-(b), in which the positive voltage induces a deficiency in the density of free electrons, which is expected to decrease its decay length.

As seen in Fig. 3.12 that change in kx_r is higher compared to the change in kx_i, which explains the observation (a); the resonance angle shift is stronger compared to the other effects. Although the analysis by using the plasmon dispersion of semi-infinite thickness of the metal (Eq. 2.1) is good to demonstrate how the change in the optical constant affect the characteristics of the SP wave, it is still not accurate. This inaccuracy is due to the structure that consists of a metallic thin film sandwiched by

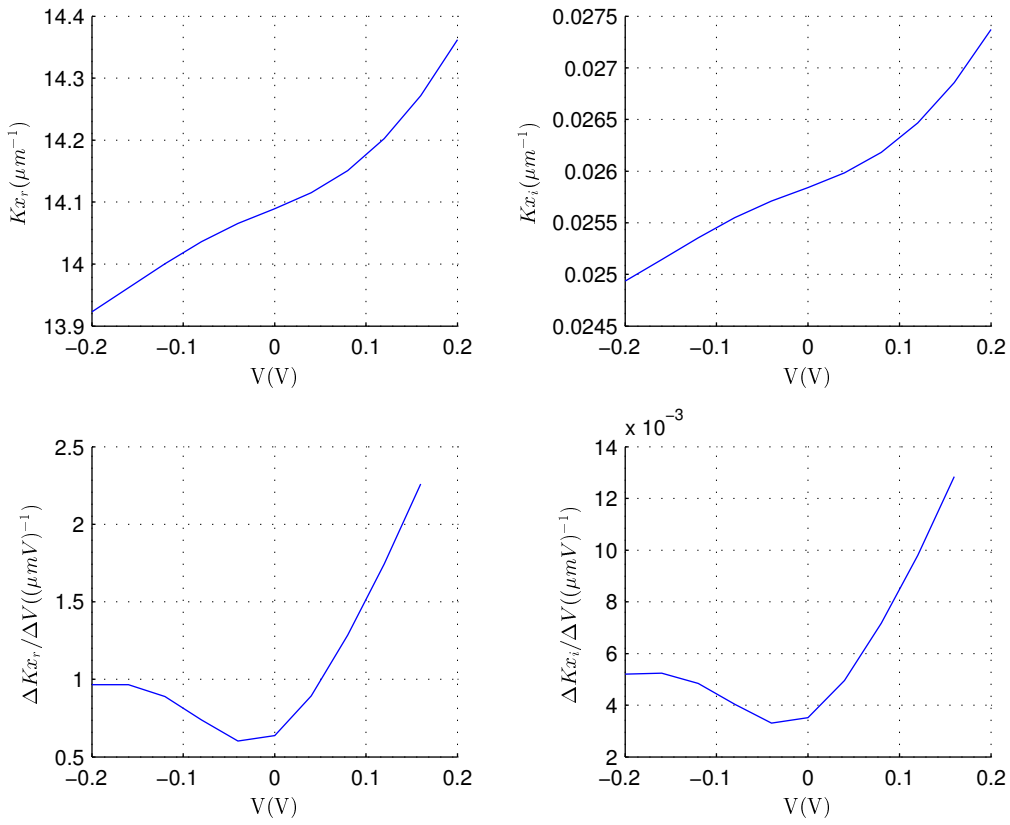


Figure 3.12: (a) Real and (b) imaginary part of the propagation constant of the SP waves as function of the applied voltage, (c) and (d) are the change in the real and the imaginary per volt.

dielectric mediums. Accurate analysis could be performed by deriving the Lorentzian dispersion equation (Eq. 2.3) of the voltage sensing structure, similar to the sensing structures in ref [108, 109, 110]. Deriving such analytical expression for the voltage sensing structure is not straightforward and will be left for the future contribution to the understanding of this phenomena.

The observation (c) is explained from the analysis in Sec. 3.3. In contrast to the conventional capacitors, the interfacial double layer capacitance is voltage dependent due to the competitive thermal and electrostatic energies at the interface. Therefore, the charge accumulation is non-linear with applied voltage and this non-linearity is translated to the properties of the surface plasmon resonance.

As presented in Sec. 2.3.3, the effect of voltage on the shape of the SPR curve is discussed in Roy et al [27]. Yet, there is a lack of a solid comparison between the effect of the voltage (in the double layer charging region) on the shape of the curve and the resonance position. This information is crucial to the design of the optical system for voltage sensing. This gap is bridged by the findings in the observation (a) presenting this analysis for the first time. This analysis also explains the non-linear behaviour of SPR response to voltage which was observed in Roy et al [27, 111] in contrast to the linearity suggested by Foley et al [73]. Roy et al [27] claimed the effect is due to diffusion of the charge carriers in the electrolyte used in the experiment; however, as seen in observation (c), this effect is more fundamental and consistent with the analysis of the properties of the interfacial capacitance in Sec. 3.3.

Voltage-equivalent refractive index

The shift in the resonance position due to the applied voltage is an important parameter. This can be used to estimate voltage sensitivity of surface plasmon resonance. This is done by introducing the voltage-equivalent refractive index units RIUs; a new figure for sensitivity that provides a simple way to understand voltage sensitivity of

SPR with no need to know the optical configuration. This concept is presented in Fig. 3.13. Starting from the resonance angle shift $\Delta\theta_0$ corresponding to the applied voltage (Fig. 3.13-(a)), the equivalent refractive index change (Δn) (Fig. 3.13-(c)) is calculated dividing $\Delta\theta_0$ by the conversion factor ($\Delta\theta_0/\Delta n$) (Fig. 3.13-(b)). This concept is more convenient compared to the system's specific response as in ref [27, 28, 84] or the refractive index contrast figure in ref [111], since all of these approaches are experiment-specific and can not be generalised.

The voltage equivalent refractive index change is presented in Fig. 3.14. From this graph, it is noticed that 1 mV is equivalent to $0.5\mu RIUs$. These results are quite important for the main objective of this chapter and the project. They shed the light on the requirements of the optical system for testing voltage sensitivity of SPR. Therefore, in order to test potentials in mV range, a sensitivity of at least $0.5\mu RIUs$ is required.

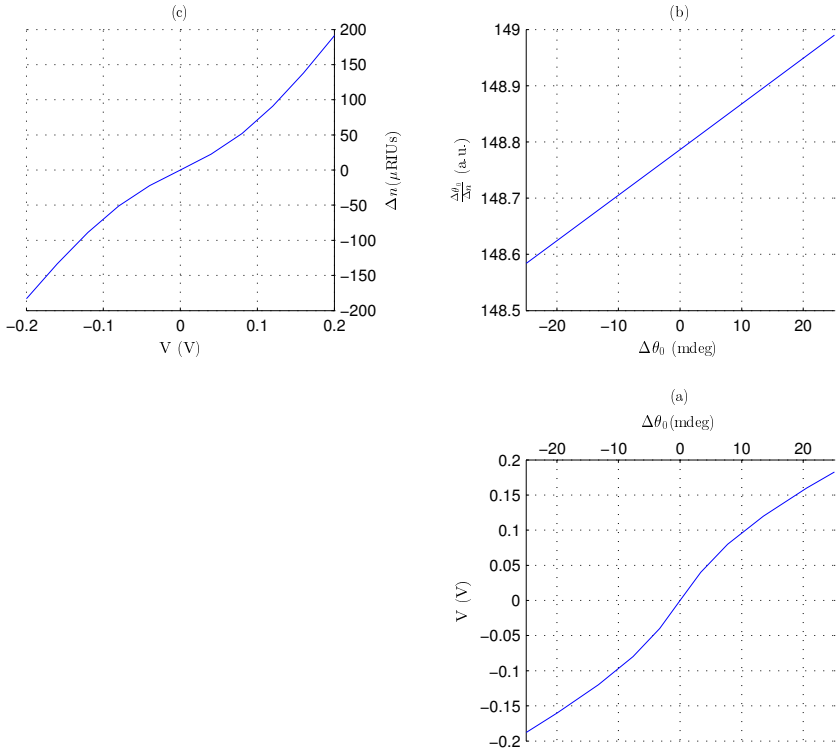


Figure 3.13: The conversion of voltage in graph (a) at the bottom-right to the equivalent refractive index units in (c) at the top-left by using the conversion curve $(\Delta\theta_0/\Delta n)$ in (b)

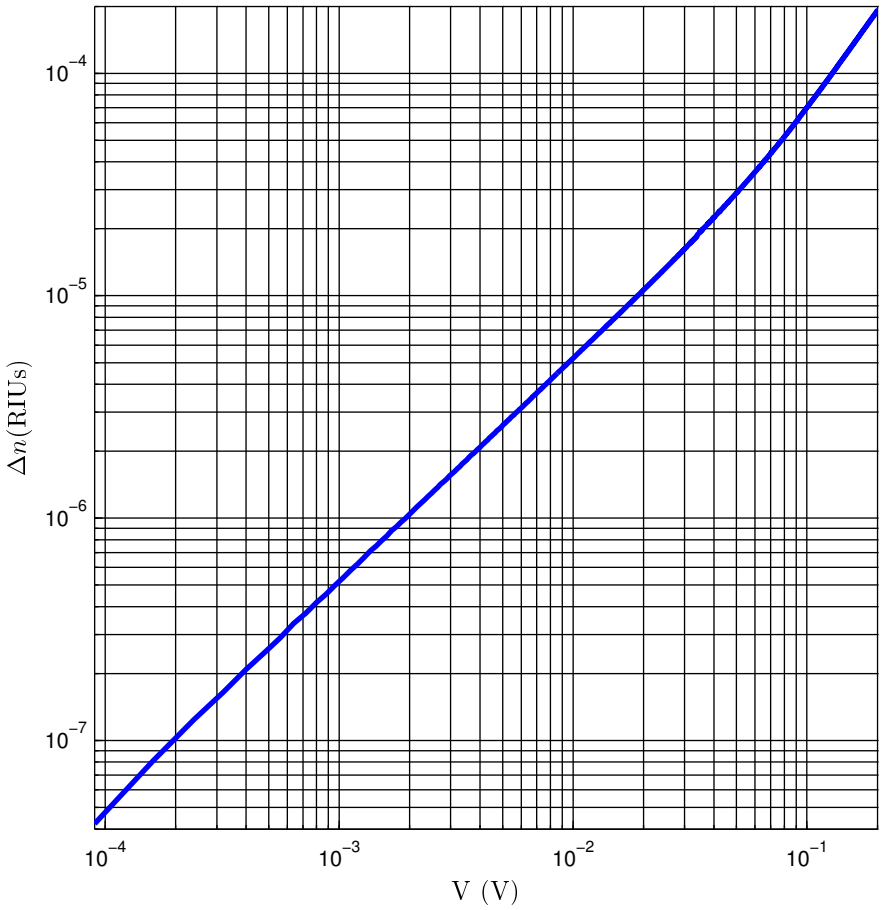


Figure 3.14: The voltage equivalent refractive index change in RIUs

3.5 Effects of electrolyte concentration on voltage sensitivity

To study the role of the concentration in the voltage sensitivity of the SPR, the first step of the procedure in Sec. 3.3 was modified keeping the rest of the procedure the same. The concentration of the sodium chloride was varied for voltages in the range of the ($\pm 200mV$). As described by Eq. 2.28 on page 50, the interfacial capacitance can be found as a function of the applied voltage and electrolyte concentration as shown in Fig. 3.15.

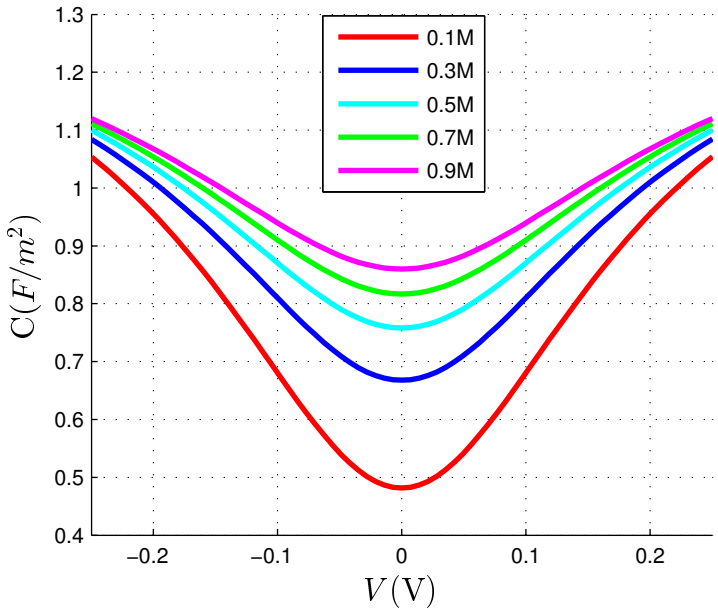


Figure 3.15: Double layer capacitance vs concentration of the electrolyte and the applied potential

The effect of electrolyte on the SPR's voltage sensitivity was investigated because it is expected to affect the interfacial capacitance as observed in Fig. 3.15. For an interfacial potential of 0.1V, the change in the capacitance and also the resonance angle due to the change in the electrolyte concentration is presented in Fig. 3.16(a) and (b). These two graphs show the behaviour of the system when the concentration changes. Also from these two graphs, the relation between the capacitance and the

shift in the resonance position is obtained as in Fig. 3.16(c). There is a linear relation between the resonance shift and the capacitance with a slope of $15 mdeg/F/m^2$, demonstrating a strong dependence on the concentration of the electrolyte.

As concentration of the electrolyte increases, the diffuse layer capacitance becomes closer to the Helmholtz capacitance due to the increase of the ions density in the diffuse layer. Since the two capacitances are in series and diffuse capacitance is smaller than Helmholtz capacitance, the change in the total capacitance is reduced at higher concentrations. The total capacitance variation with voltage or concentration is governed by the value of the diffuse layer capacitance relative to the Helmholtz layer capacitance. For higher voltages, diffuse layer capacitance approaches the Helmholtz layer capacitance and thus the total capacitance becomes less sensitive to molarity change. The same applies for the higher molarities. It is also noted that the total capacitance increases with molarities even if no voltage is applied. This observation is due to increasing the effect of the electrostatic energy versus the competing the thermal energy as seen in Eq. 2.28 on page 50.

The spatial profile of the potential (in the direction perpendicular to the electrode) is also dependent on the concentration of the electrolyte. Eq. 2.28 was used to investigate the effect of the concentration on the potential profile and on the Debye length at the electrode-electrolyte interface. This effect is shown in Fig. 3.17. As concentration increases, the potential decays faster and the Debye length is reduced.

These results present the effect of concentration on voltage only and do not consider the effect on the refractive index of the medium and the consequences on the system's sensitivity and dynamic range, which will be discussed later in chapter five.

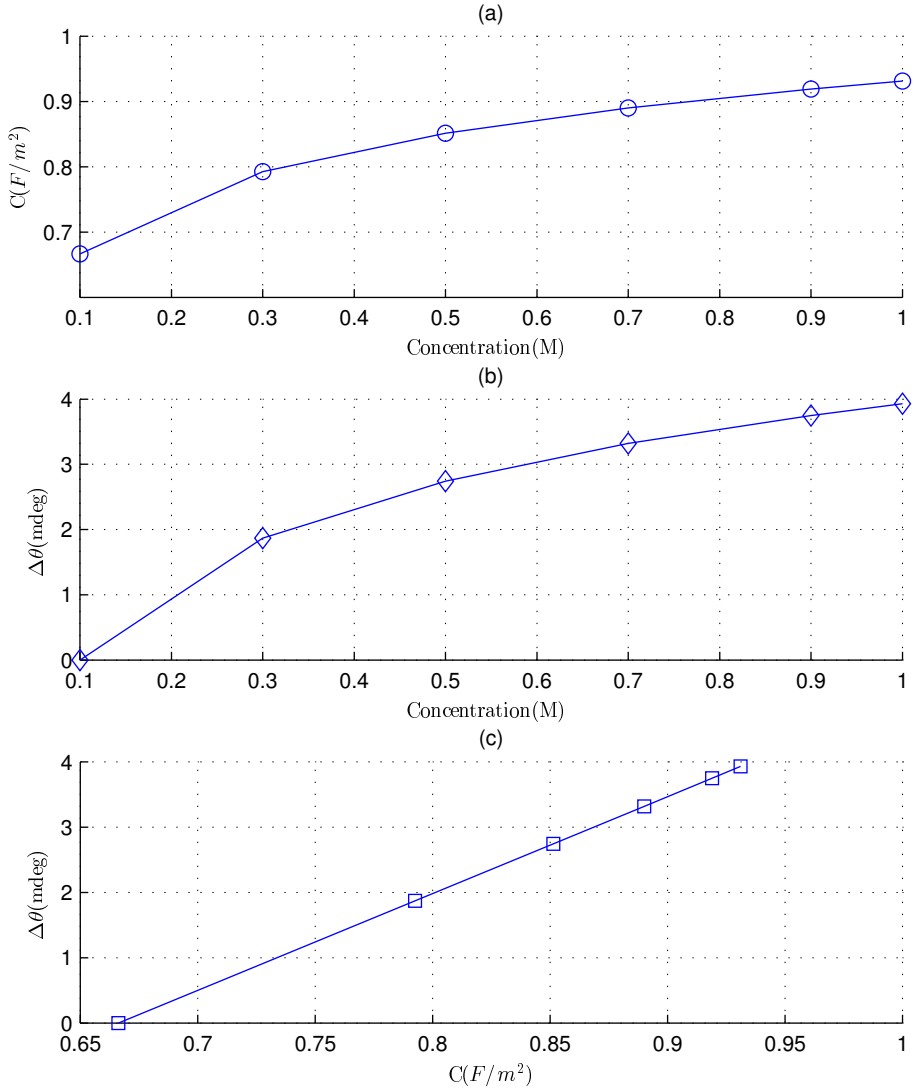


Figure 3.16: The effect of the electrolyte concentration on the voltage sensitivity. (a) concentration dependent interfacial capacitance, (b) and (c) the resonance shift due to change in concentration and the capacitance, respectively. All calculated for for 100mV.

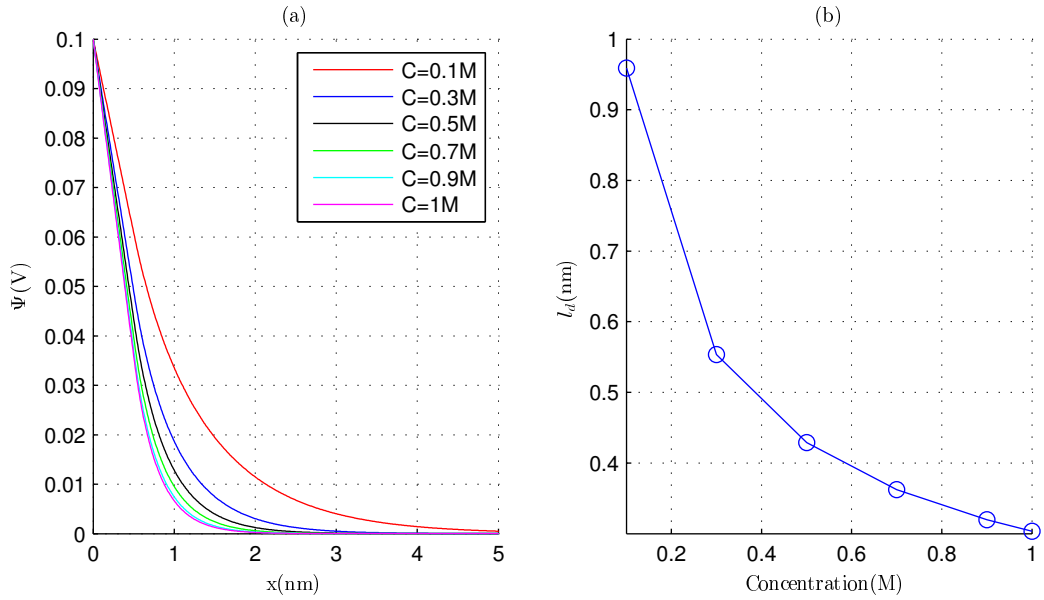


Figure 3.17: The effect of the electrolyte concentration on (a) the profile of the interfacial potential and (b) the Debye length of the metal-electrolyte interface for gold thin film in contact with 0.1 M NaCl

3.6 Effect of temperature on voltage sensing

Temperature effects on the voltage sensitivity of the SPR can been seen from different prospectives. With the picture of the multilayer model of Fig. 3.3 in mind, temperature has effects on the optical properties of the electrolyte, optical properties of the metal film and electrical properties of the interface. First, the temperature's effect on the refractive of index of the sample is known as discussed in Sec. 3.2.5. Second, its contribution to the electrical properties of the interface are seen from (i) the change the properties of the diffuse layer capacitance as expected from Eq. 2.28 and (ii) changes to both Helmholtz and Diffuse capacitances indirectly by affecting the dielectric properties of the solvent (i.e. the separating layer). The temperature dependence of the dielectric properties of water was obtained from Uematsu [112] and presented in Fig. 3.18. It can be expressed as

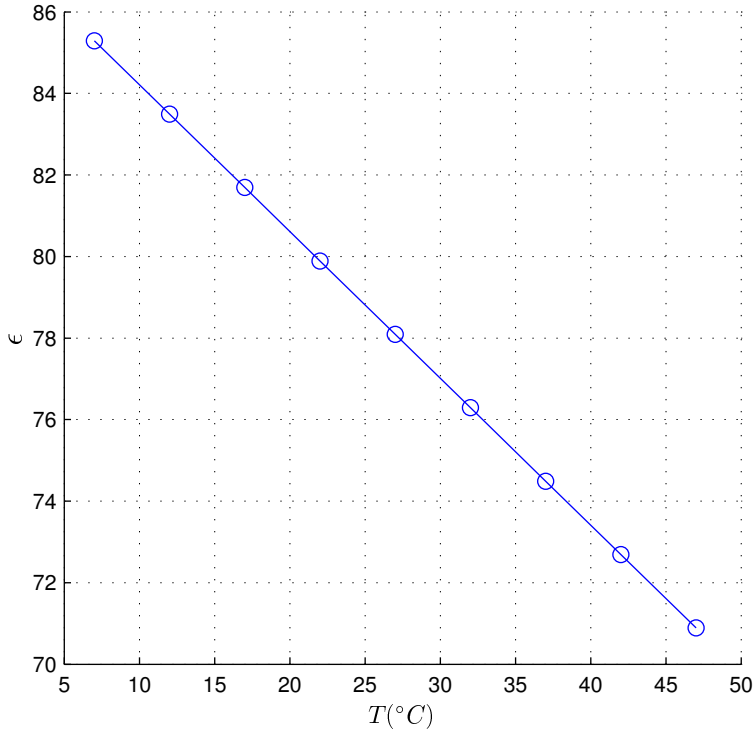


Figure 3.18: Temperature dependence of the static permittivity of water at a pressure of 1 atm [112]

$$\epsilon = \epsilon(T_0) - 0.36T \tag{3.14}$$

where T is temperature in $(^{\circ}C)$ and $\epsilon(T_0) = 87.81$. The modelling procedure described in Sec. 3.3 was used to study the effect of the temperature on the capacitive properties of the interface and the properties of the SPR.

The electrode side also experience the temperature effects changing its optical properties as described by Turhan et al [113]. Changes in the optical properties of the metal results from the temperature effect on the free electron density (N) and the plasma frequency (ω_p). It also affects the damping properties of the free electrons oscillations [113]. To encounter for the effect of the temperature on the optical properties of the metal, the procedure of [113] is adopted to calculate the complex refractive index as a function of change in temperature as described in Eq. 3.15.

$$n_r = n_r(T_0) + \frac{\Delta n_r}{\Delta T}$$
$$n_i = n_i(T_0) + \frac{\Delta n_i}{\Delta T} \tag{3.15}$$

where $n(T_0)$ is the refractive index before temperature charge n_r and n_i are the real and the imaginary part of the refractive index of the SP supporting metal. For gold, $\frac{\Delta n_r}{\Delta T} = 3.408 \times 10^{-4} K^{-1}$ and $\frac{\Delta n_i}{\Delta T} = -1.381 \times 10^{-4} K^{-1}$ [113].

The effect of temperature on SPR measurements and voltage sensitivity is not straightforward. As temperature changes affect the interfacial capacitance, metal dielectric constant and the bulk electrolyte, the effect on these parameters is compared. This comparison is useful to find which parameter is more affected by temperature changes and thus has dominant effect on SPR response. First, the the behaviour of the interfacial capacitance when temperature is changed is presented in Fig. 3.19 and it is noticed that capacitance decreases with temperature. This is not surprising since it increase the thickness of the diffuse layer and reduce the electrostatic effect that result from applying voltage or increasing ion density. For 0.1 V, Fig. 3.19 -(b) demonstrates a linear temperature dependence of the capacitance in the range of $\pm 10^{\circ}$ C.

From Fig. 3.19-(b), a linear fit is used to produce

$$C(\Delta T) = C(T_0) - 0.0063 \Delta T \tag{3.16}$$

Where C is capacitance in F/m^2 and $C(T_0)$ is the capacitance at the initial temperature. Using this information and the $\Delta\theta_0/\Delta C$ from Fig. 3.16-(c), the equivalent shift in the resonance position ($\Delta\theta_0$) is found. This effect is compared to the temperature alterations to the optical properties of the the metal film and the bulk electrolyte in Fig. 3.20. As seen in Fig. 3.20, the SPR response due to the change of the temperature of the electrolyte is stronger than the metal film and the capacitive properties. It is also noted that the electrolyte and the capacitive responses

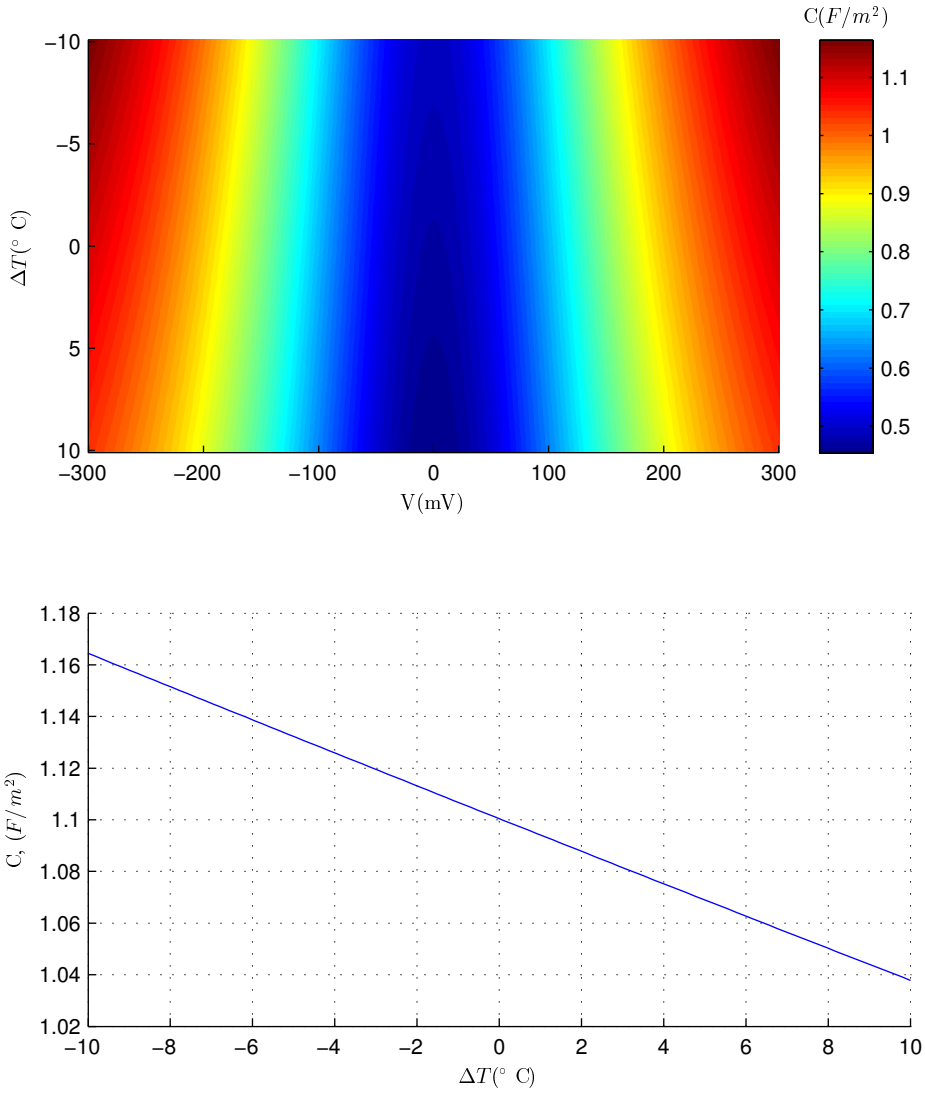


Figure 3.19: (a)The effect of the temperature on the capacitive properties of the double layer capacitor and (b) the trend of the effect on the temperature on the double layer capacitance for a potential of 0.1V

have negative slopes in contrast to the response of the metal film. These findings are important for understanding the effect of temperature on the properties of the electrode-electrolyte interface and the properties of the surface plasmons (SPs). One can estimate the temperature effect on voltage responsivity from the information in

Fig. 3.20. By increasing temperature, the response decreases with a rate of ~ 0.1 mdeg/°C. To put this number in prospective, SPR resonance shift become about (10 mdeg - 0.1 mdeg/°C) when a 100 mV is applied. In other words, responsivity drops by 1% per 1 °C of temperature rise.

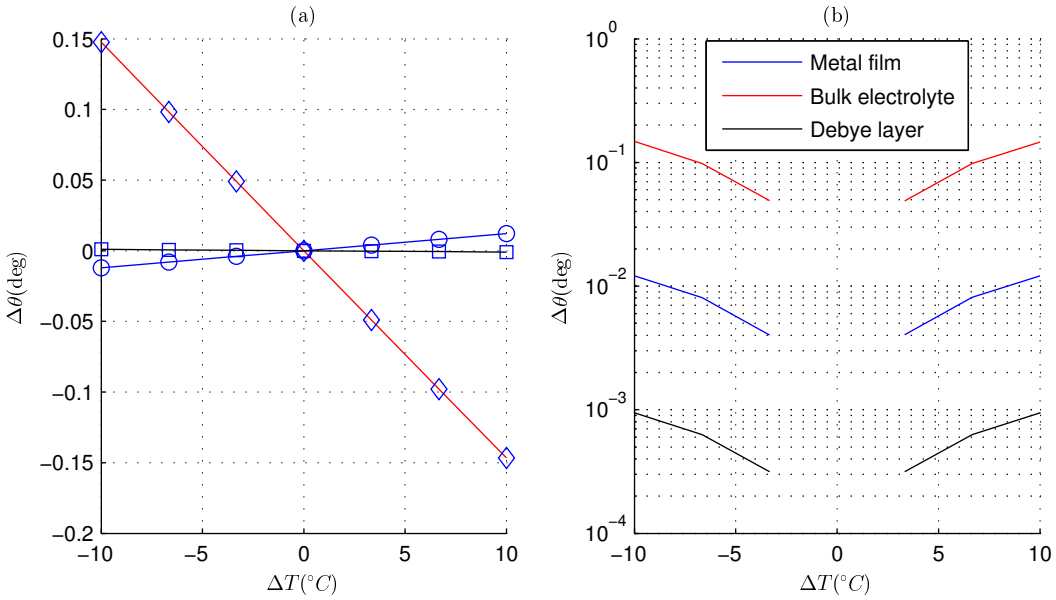


Figure 3.20: The effect of temperature on the response of the SPR due to change in the optical properties of the electrolyte, the metal film and the electrical properties of the interface.

3.7 Conclusions

(a) Voltage sensitivity of surface plasmon resonance was analysed theoretically introducing the voltage equivalent refractive index units; an estimate for voltage sensitivity regardless of the optical system configuration. The findings of this estimate represent the platform for the identifying the specifications of the optical system. In order to detect a voltage in the mV range, a system's sensitivity of at least 0.5 $\mu RIUs$ is required.

(b) Voltage effect on the SPR curve (the shape and the resonance position), was analysed. The effect on the resonance position is stronger than on the shape of the curve (FWHM and the minimum reflectivity); another key information for the design of the SPR detection system. This effect has been explained in the light of the dispersion of the SP waves. Moreover, the non-linear behaviour of the SPR response has been thoroughly studied by looking into the voltage dependence of the interfacial capacitance and the other interface's parameters.

(c) The effect of the concentration of the electrolyte on the voltage sensing has been studied. SPR response scales nonlinearly with increasing the concentration and saturates at $\sim$ 1M. This is attributed to the enhancement of the capacitance of the diffuse layer.

(d) The effect of temperature has been analysing comparing the change in the optical properties of the electrolyte, the optical properties of the metal and the electrical properties of the interfacial capacitance. The change in the optical properties of the electrolyte has the strongest effect, then the optical properties of the metal thin film and finally, the electrical properties of the interfacial capacitance.

(e) The theoretical analysis presented in this chapter provides a tool for studying the effect of the different parameters on the voltage sensitivity, which will be used to validate the performance of the voltage sensing system (chapter 4) and

the experimental investigation of the voltage sensitivity (chapter 6)

(f) The theoretical voltage sensitivity obtained in the chapter shows a promise regarding the detection of the transmembrane potential of the excitable cells. Assuming a 1% energy coupling efficiency ($\eta_c = 0.01$), the 100 mV change in the transmembrane potential is attenuated to 1 mV across the capacitance of the electrode. This analysis maps 1mV to $0.5\ \mu RIUs$ which is achievable by SPR systems [30]. These results will be confirmed experimentally in chapter 6.

Chapter 4

Design and Testing of Voltage-sensitive Surface Plasmon Resonance System

4.1 Introduction

In order to study the voltage sensitivity of surface plasmon resonance, an SPR-based voltage sensing system was designed and tested. It consists of the optical configuration and the electrochemical unit. The optical configuration is used to excite surface plasmons at the metal-electrolyte interface while the electrochemical unit is used to control the potential at this interface. This chapter presents the design of the optical system and the investigation of the sources of instability. The integrated system was tested for detecting the interfacial potential using the electrochemical system and the optical system, simultaneously.

The selection of the optical system: As concluded from the review in Sec. 2.1.2, phase SPR systems are generally more sensitive than amplitude ones, but requires more complex optical system design. Since the differential-intensity SPR system fea-

tures a simple optical system design with a sensitivity similar to phase systems, it has been selected for the voltage sensing. A sensitivity of 10^{-8}RIUs has been reported [26] which is adequate for the purpose of this study as specified in Sec. 3.7.

The selection of the electrochemical system: Voltage of the electrode-electrolyte interface has been controlled using a three-electrode system, which is more accurate compared to the two electrode system for the reasons mentioned in Sec. 2.3.3.

4.2 System Design

The voltage-sensitive differential-intensity SPR system is presented by a simplified diagram in Fig. 4.1. It is made of three main units: (a) the optical system, (b) the differential signal processing unit and (c) the electrochemical system.

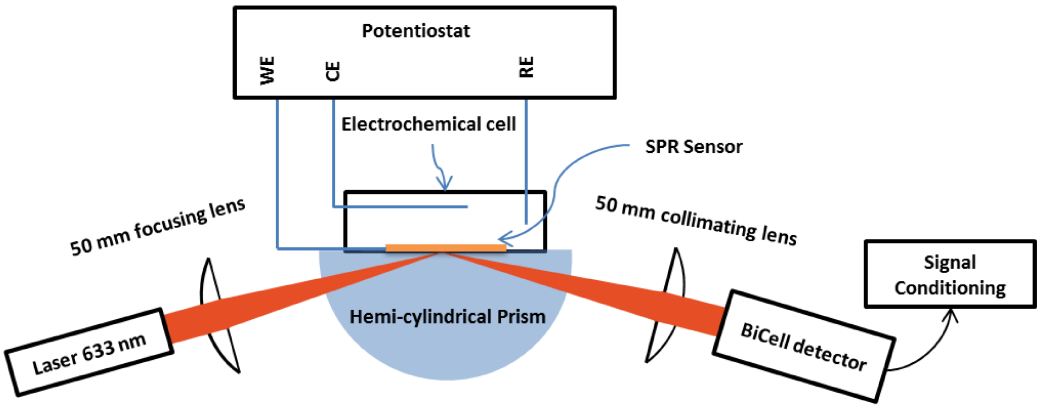


Figure 4.1: A simplified diagram for the voltage sensing system.

4.2.1 Optical system design

A differential-intensity surface plasmon resonance sensing system was constructed (Fig. 4.2), adopting a prism-based Kretchmann-Raether configuration. A 633 nm linearly polarized laser was coupled though a prism ($BK7, n = 1.515$) to the sensor-sample interface. A cylindrical lens was inserted into the beam path to focus the

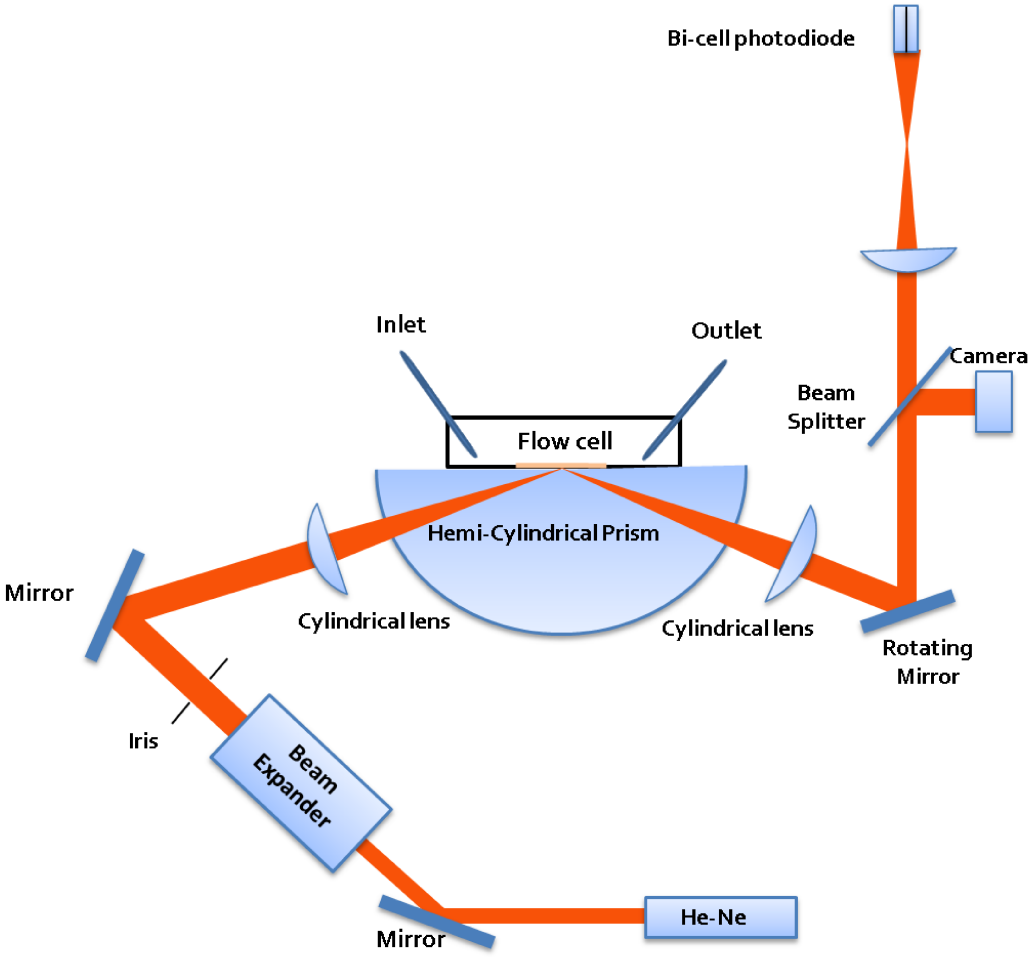


Figure 4.2: Optical system configuration of the plasmonic voltage sensing system.

light beam to a line onto the sensor chip. Refractive index matching oil (Refractive Index 1.515) was used between the prism and the sensor chip to remove undesired reflections from the interfaces. The resonance angle was set to $\approx$ 72 deg to excite surface plasmons at the refractive index of distilled water (1.3319 at 633 nm). Since, the incident angle is greater than the critical angle, total internal reflection occurs at the sensor-sample interface. The reflected light was collimated using a second cylindrical lens and detected using either a CMOS camera (μEye, IDS GmbH) or a custom-designed bi-cell photodiode unit. The maximum angle of convergence of the light beam was $\approx \pm 3$ degrees.

Conditioning of the excitation beam

A He-Ne was used to produce 633nm linearly-polarized light. The beam diameter was 0.68 mm at $1/e$ of the peak intensity of the laser. This beam was expanded by 7.5 times using a pair of positive lenses (10 mm and 75 mm, magnification $M = 75/10$). So, the expanded diameter was 5.1 mm at $1/e$ of the power. The latter was focused on the sensor surface to excite surface plasmons at the sensor-sample interface.

As explained earlier in Sec. 2.1.2, the response of this method depends on the angular width of the excitation beam. So, a graduated iris aperture was used to control the angular width of the focused beam. This flexibility will enable the study of the effect of the angular width. Angular width is related to the diameter of the iris as following:

$$\theta_w = \sin^{-1}\left(\frac{d}{2f}\right) \tag{4.1}$$

where d is the diameter of the beam, f is focal length of the cylindrical lens and θ_w is the angular width.

Conditioning of the reflected beam

The reflected light, from sensor-sample interface, was collimated with a cylindrical lens. This light was detected both by the pixelated camera and the bi-cell photodiode using the beam splitter in (Fig. 4.2).

The collimated beam was detected directly by the camera, but it was demagnified before the bi-cell detector. For this purpose, another lens ($f = 30mm$) was used to focus light at 10 mm from the detector, the total distance between the detector and the lens is 40 mm. This configuration demagnify the beam by 66.7%. The width of the detector is 1.34 mm, so a beam of 4mm in diameter matches the width of the detector. This beam diameter is equivalent to angular width of 2.29 deg.

Differential detection

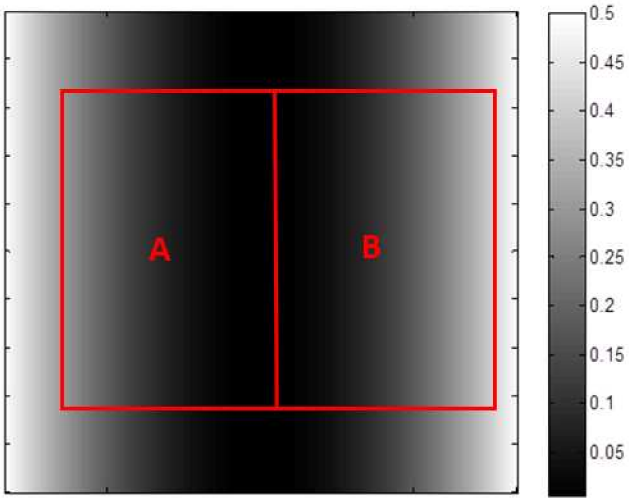


Figure 4.3: The concept of the differential-intensity detection. The bi-cell detector, as presented in red, is superimposed on the image that simulates the light reflected from the metal-electrolyte interface. The dark light in the middle is explained by the excitation of surface plasmons. The dark line shifts to the left and right as the refractive index of the sample decreases or increases respectively. This will results in a change in both A and B leading to change in $(A-B)/(A+B)$.

This optical system is based on the differential detection, in which the reflected beam is balanced on a bi-cell photodiode. So, each unit of the detector records the power of each half of the SPR curve, denoted as A and B. In Fig. 4.3, the concept of the differential detection is illustrated demonstrating how the DI-SPR signal $(A-B)/(A+B)$ is related to the shift in the resonance position. The figure $(A-B)/(A+B)$ is calculated using a custom designed signal processing circuit, described later in this section.

The bi-cell detector was mounted on an x-y stage. This stage enabled the alignment of the bi-cell detector with the reflected beam. Also, the detector was balanced by adjusting the location of the detector until the the signal A-B=0.

4.2.2 Processing of the bi-cell photodiode outputs

The design of a differential-intensity surface plasmon resonance sensor requires processing the outputs of the bi-cell detector in order to calculate the differential signal (A-B/A+B). Fig. 4.4 presents a schematic showing the different components of the processing system. The outputs of the bi-cell detector are photo-currents corresponding to the optical power of each half of the SPR curve. They are sent to a custom-made electronic circuit that is used to convert the photo-current to voltage and calculate the difference and the sum of the two units A and B. A 16 bit National Instrument ADC (NI 6210) is used to convert the two signals to digital signals, which are displayed on LabVIEW user-interface. The $\frac{A-B}{A+B}$ is post-processed using Matlab. A and B are also quantized upon analog-to-digial conversion (using a voltage range of $\pm$5V and 16 bit DAQ) for investigating their effect on the DI-SPR output as discussed in chapter 5.

As mentioned in Sec. 3.7, it is necessary to obtain a high sensitivity surface plasmon resonance system. For this reason, a low noise electronic circuit (presented in Fig. 4.5) is required for conditioning the differential signal. First of all, a precision operational amplifier (ADA4898 from Analog devices: voltage noise 0.9 V/$\sqrt{Hz}$) has been selected for the current to voltage conversion and the post-amplification difference and sum. The photo-current from the two units of the photodiode is sent to two transimpedance amplifiers. Then, the output signals are used as inputs for the differential amplifier that calculates the differential plasmon signal $(A - B)$. They are also sent to the summing amplifier to calculate $(A + B)$.

The gain of the transimpedance amplifier is calculated using the following equation

$$G = \frac{V}{PR} \tag{4.2}$$

Where G is the gain, R is the spectral responsivity and P is the optical power. In

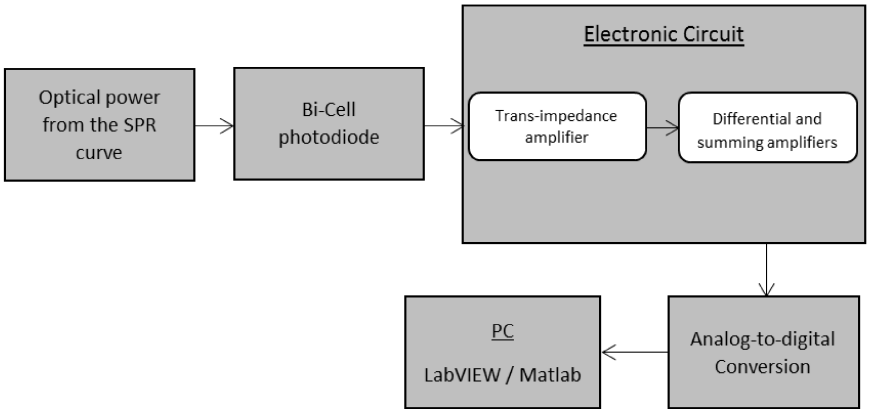


Figure 4.4: A block diagram presents the different components of the processing the bi-cell detector signals.

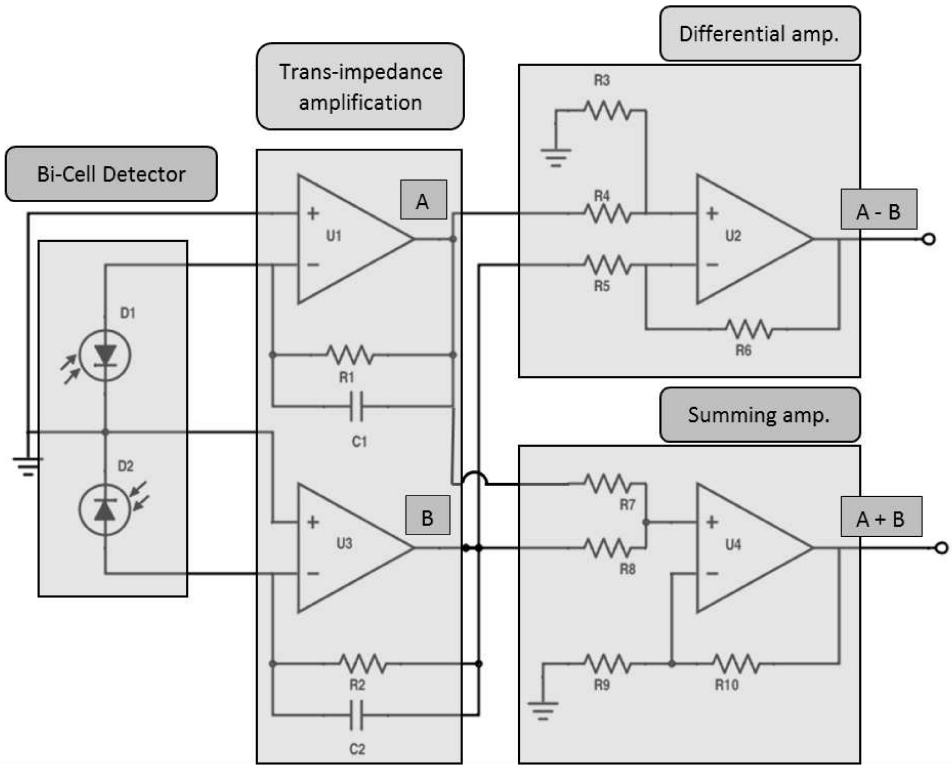


Figure 4.5: A simplified diagram show the electronic circuit that is designed to calculate (A-B) and (A+B).

order to calculate the gain of the transimpedance amplifier, the optical power at the detector was measured. Assuming that the maximum output of the transimpedance amplifier is 70% of the 5 V supply, the gain is calculated using Eq. A.2. The spectral responsivity of the bi-cell photodiode, from the specification sheet, is 0.35 at 633nm. The gain, for optical power of 0.6mW, is achieved by using a 16KΩ resistor at the feedback of the transimpedance amplifier. A 10 nF has been selected setting the systems bandwidth to 1kHz; since the targeted electrical activity has a 1kHz bandwidth. The second step is using a differential amplifier and a summing amplifier to calculate the difference and the sum of the two signals of the previous step with no further amplification.

Thermal noise associated with resistors, flicker and white noise resulted from the amplifiers have been calculated for the bandwidth of the system. The total noise has been calculated for the two transimpedance amplifiers and the differential amplifier taking into account the flicker and the white noise of the amplifiers and the thermal noise of the resistors. Theoretical noise for the difference and the sum are $\approx 1\mu$V.

Sources of noise in the system are classified to electronic, optical, beam pointing and electrochemical. This section is concerned with the electronic noise and the beam pointing error. Optical noise and electrochemical noise are presented in chapter 5 and Sec. 4.2.3 respectively.

Electronic noise

Electronic noise was tested by eliminating the other sources of noise. Traces in Fig. 4.6 were recorded with no optical power at the detector. Therefore, sources of this noise are: the bi-cell detector, the signal conditioning circuit and the data acquisition (quantization noise).

Data acquisition noise (e in mV) is expressed as a fraction (α in the units of LSBrms)

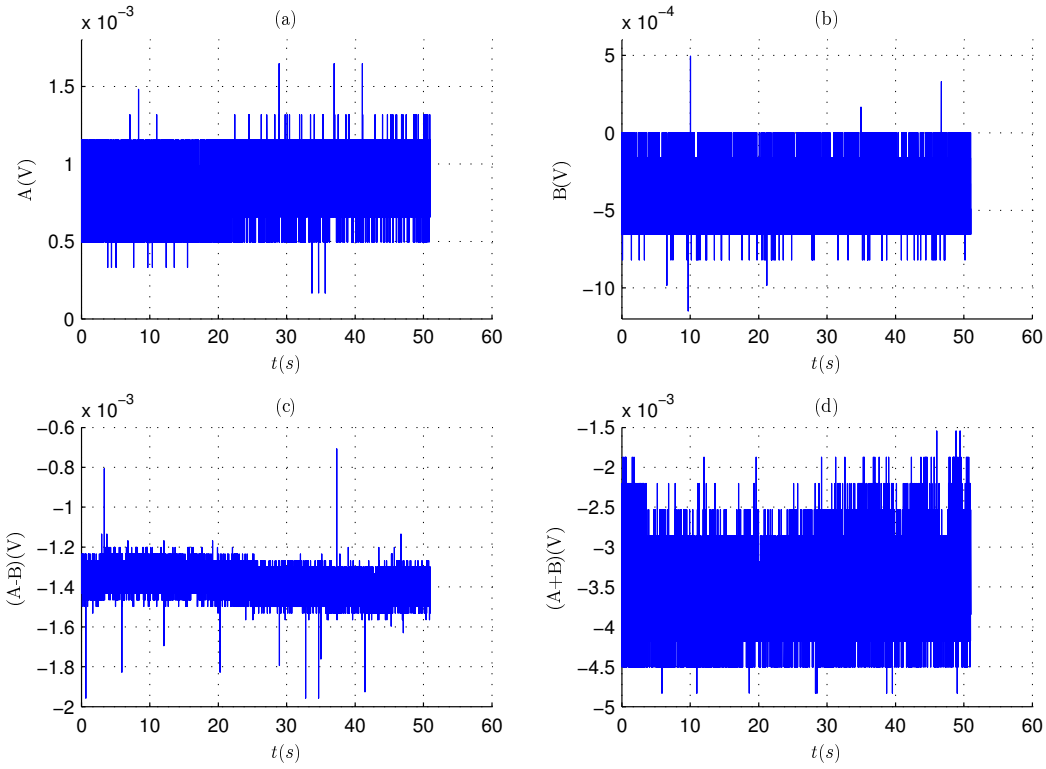


Figure 4.6: The outputs of the bi-cell signal processing A,B, (A-B) and (A+B); A and B the signals from the units of the detector with no optical power at the detector.

of the resolution of the DAQ system (in the units of mV/LSB) as shown in the following equation

$$e = \alpha \frac{V_r}{2^n} \tag{4.3}$$

where n is the number of bits of the DAQ, V_r is the voltage range. According to the manufacturer's specifications of NI 6210, the average α is 0.8 LSBrms. The expected figures of the A, B, A-B and A+B for voltage ranges of ±5 V,±5 V,±1 V and ±10 V respectively are are comparable to the experimental figures in Table 4.1. This noise can be improved further by averaging as shown in Fig. 4.7; it can be reduced by an order of magnitude if the 100 averages are used, however this limits the bandwidth to 10 Hz.

Table 4.1: Electronic noise of the components of the DI-SPR signal that are calculated from experimental traces for a window size of 1 second and compared to the theoretical values. These noise figures are the mean of the noise of the 100 windows.

Parameter	Theoretical σ (mV)	Experimental σ (mV)
A	0.12	0.130 ± 0.0023
B	0.12	0.128 ± 0.0024
$A - B$	0.026	0.043 ± 0.0009
$A + B$	0.23	0.296 ± 0.0399

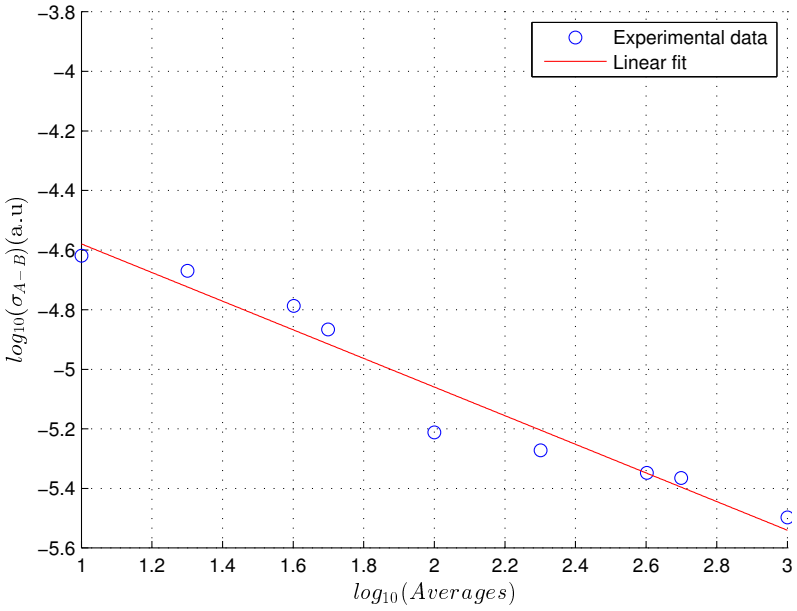


Figure 4.7: Electronic noise is reduced by averaging; improvement is presented for a set of number of averages. Linear regression is performed with a goodness of fit: $R^2 = 0.95$ and the root mean squared error (RMSE)= 0.07923. The slope is -0.48 compared to the expected -0.50.

Beam pointing instability

As the DI-SPR is a position sensing system, it is important to check that the pointing instability of the laser does not hinder the sensitivity of the system. So, the difference, the sum and their ratio are recorded after switching the laser on and waiting to achieve a stable beam pointing. The difference and the sum signals were recorded during the laser warming-up as shown in Fig. 4.8.

These fluctuations are attributed to the pointing instability rather than fluctuation in the laser power, as the latter changes only the sum not the difference. In contrast, the observed oscillation changes both signals. If the difference signal is compared to the sum, we notice that when the difference increases, the sum decreases. These are due to some part of the beam leaves the detector. So, the total power drops while the difference increases due to the increase in the intensity in A and a drop in B.

The decrease or the increase in the difference signal depends on the direction of the movement of the beam. Assuming that beam only oscillates horizontally (Fig. 4.9), the sum decreases in either left of right movement of the beam in contrast to the difference which can decrease or increase depending on the direction of the movement.

A relatively steady baseline is obtained after 40 min of warming-up. However there is still pointing instability dependent on the temperature changes. From this specifications of the laser it is 0.02mRad/^0C after 15 min. For a beam path length of 600 mm, this number maps to an axial translation of 12 μm/^0C. As mentioned previously, the angle-pixel conversion factor is 1 mdeg/μm. The final effect is 12 mdeg/^{0}C. This is equivalent to a refractive index change of 80 μRIUs/^0C. The performance can be improved by a reference channel to cancel these fluctuations, however this requires the use of a quadrant detector instead of the bi-cell [54].

The effect of the beam pointing instability on the system performance depends on

(i) the aperture relative to the width of the bi-cell detector and (ii) the width of the SPR dip compared to the inner edges of the bi-cell. First, the aperture and the detector intersects at a beam width of 4mm (2.29° of the SPR curve) - see page 95. Second, the system is designed making the gap between the two detectors (0.09mm equivalent to 0.3°) smaller than the width of the dip. However, the effect of the beam pointing cannot be avoided in this case as the translation of the dip alters the balance of the bi-cell.

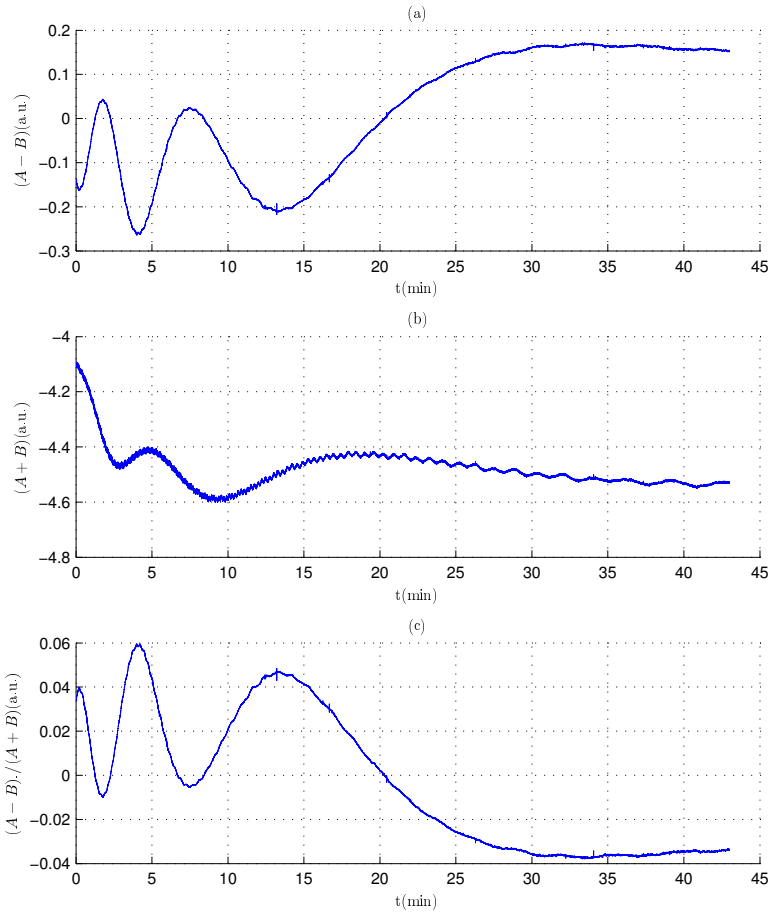


Figure 4.8: The effect of the pointing instability of the laser on the (a) difference (A-B), (b)the sum (A+B) and (c) the ratio.

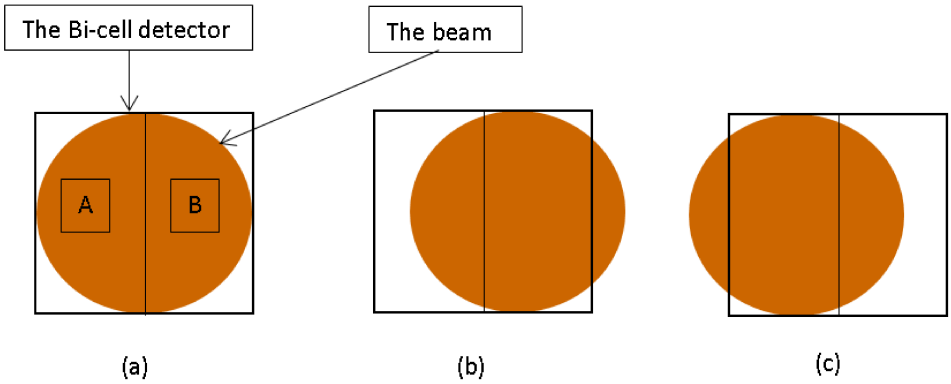


Figure 4.9: A sketch shows the translation of the beam relative to the width of the detector. The sum (A+B) decreases in both case (b) and (c) whereas the difference (A-B) decrease for the case of (b) and increases for the case of (c).

4.2.3 Electrochemical system

The electrochemical system is designed using two main components, an electrochemical cell where the three electrodes are fitted and a potentiostat which is used to clamp the potential at the interface (Fig. 4.1). The voltage of the working electrode (against the reference electrode) is set and controlled by applying current between the counter and the working electrode. A feedback system is designed to achieve the desired voltage.

Electrochemical system can be designed using only two electrodes, as in Fig. 4.10-(a): a working electrode and a counter electrode. The latter also serves as a reference electrode. However, the design, which is presented here, favoured the three-electrode system (Fig. 4.10-(b)) since the reference electrode is placed near the gold surface (i.e. the working electrode) to eliminate the effect of voltage across the solution resistance and the counter electrode. This is important for making more accurate measurements of the interfacial potential.

VerstaStat3, (Princeton applied research, TN, USA) was used in this electrochemical system. A commercial electrochemical cell was obtained from (Reichert Life Science

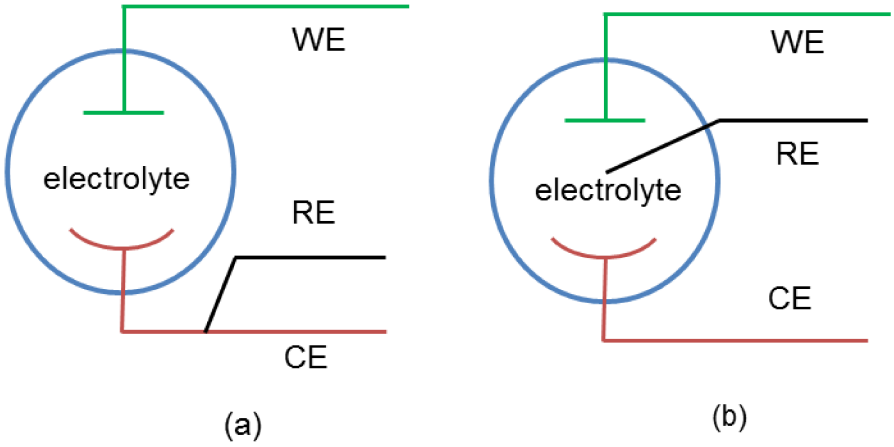


Figure 4.10: Configurations of electrochemical cells. (a) the two-electrode configuration (b)the three-electrode configuration. WE: working electrode, RE: Reference electrode and CE: counter electrode

NY, USA), which is tailored for SPR electrochemistry applications. The system uses three-electrode configuration, in which the gold thin film is used as a working electrode, a platinum wire (obtained from Reichert life science) is used as a counter electrode and silver/silver chloride (AgAgCl) in saturated 3M NaCl was used a reference electrode.

Calibration of the potentiostat

The potentiostat has a dummy internal electrochemical cell which is equivalent to a resistance of 1kΩ. The manufacturer's recommended test is to scan a potential from -1V to 1V and measure the resulting current. This test was repeated frequently to check the performance of the potentiostat. The same procedure was performed using external resistor of 1kΩ, connecting the working electrode to one terminal and the reference and the counter electrode to another terminal. An example of results of these two tests is presented in Fig. 4.11. Linear regression analysis of the experimental data in Fig. 4.11-(a) and (b) was performed with $R^2 = 1, RMSE = 2.45 \times 10^{-7}$ and $R^2 = 1, RMSE = 2.38 \times 10^{-7}$ respectively. The slope of the in

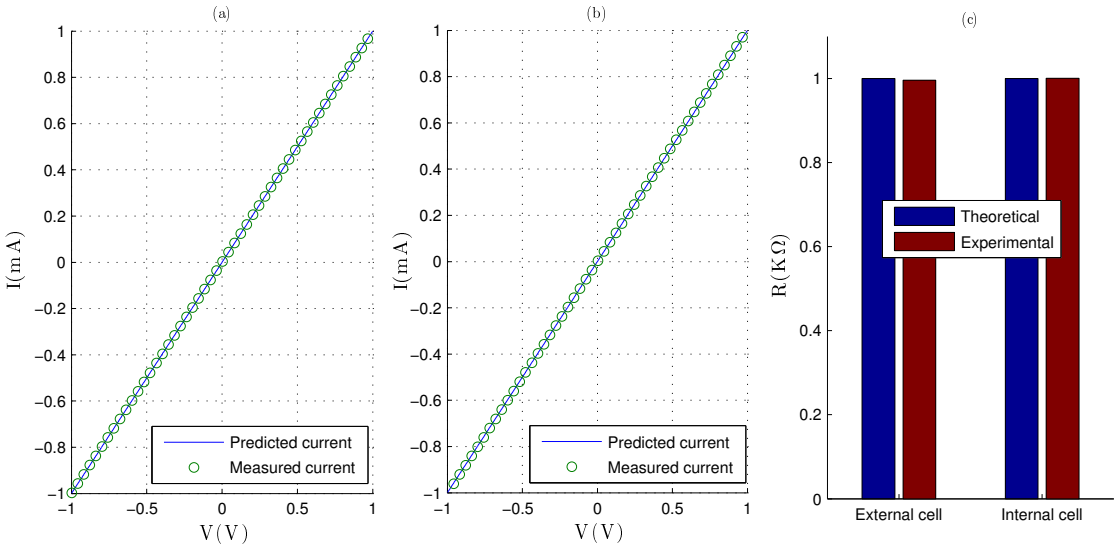


Figure 4.11: Calibration of the potentiostat Versastat3 using (a) internal cell of 1kΩ, (b) external cell of 1kΩ and (c) the comparison of the obtained values with the theoretical ones.

the case of the external and the internal resistance is $9.995 \times 10^{-4} \pm 0.0245\%$ and $1.004 \times 10^{-3} \pm 0.0237\%$. The corresponding resistance of the internal cell and the external cell are $1.0005k\Omega$ and $0.996k\Omega$.

Noise in the electrochemical system

Characterizing noise in the electrochemical system is of particular importance to voltage sensing since this noise is expected to be picked up also by the optical system. The bipolar 100mV waveform (Fig. 4.12) has been recorded before (red traces) and after the use of a Faraday cage. The noise has been calculated for the two cases $14.17 \pm 0.58mV$ and $0.23 \pm 0.01mV$ for the bandwidth of the potentiostat (1 MHz). The noise level has been reduced by a factor (1/60). This figure means that voltage less than 0.23mV cannot be tested using the current electrochemical system. Improvement of the noise performance by using the Faraday cage is noticed in the voltammogram in Fig. 4.14-(b). This will be discussed more in Sec. 4.4.

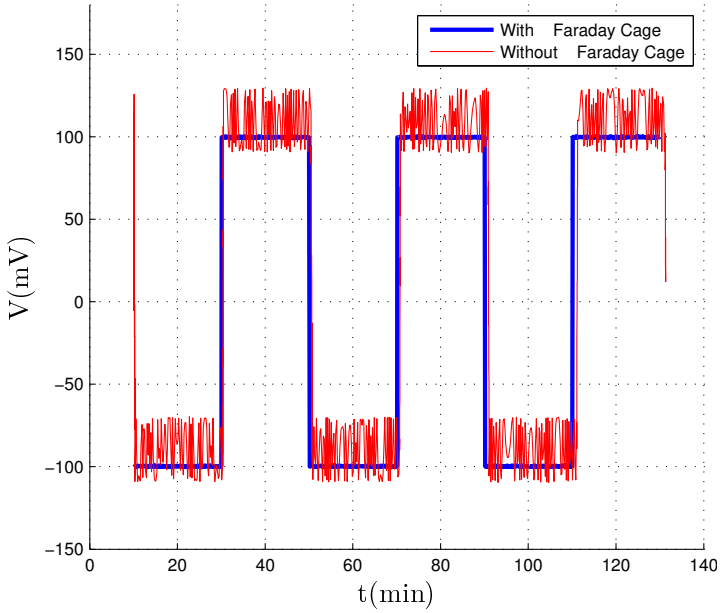


Figure 4.12: Noise in the electrochemical system and the effect of the Faraday cage

4.3 Sample preparation and testing

Two samples were used in the studies of the project; sodium chloride and lithium iodide. These samples are used for refractive index stepping (Chapter 5) and as electrolytes for voltage sensing (Chapter 6). To measure their refractive index, a series of concentrations of both were prepared by dissolving salt in deionised water. A commercial SPR instrument (Reichert SPR7000) was used to measure the refractive index of each of these samples taking the deionised water as a reference baseline. These results, which is an average three measurements, are presented in Fig. 4.13. These experimental results had been used as standards when the response of the DI-SPR was tested. The change in refractive index of sodium chloride with concentration has a slope of 9.4 ± 0.081 mRIU/M which is close to values from literature; 9.9 mRIU/M (See-Table 3.2). For the case of LiI, the response is 18.9 ± 0.06 compared to 21 mRIU/M adapted from Baxter et al [114]. The difference in accuracy of the instruments used in literature and this chapter is one of the possible sources of discrepancy the obtained figures and literature. As these

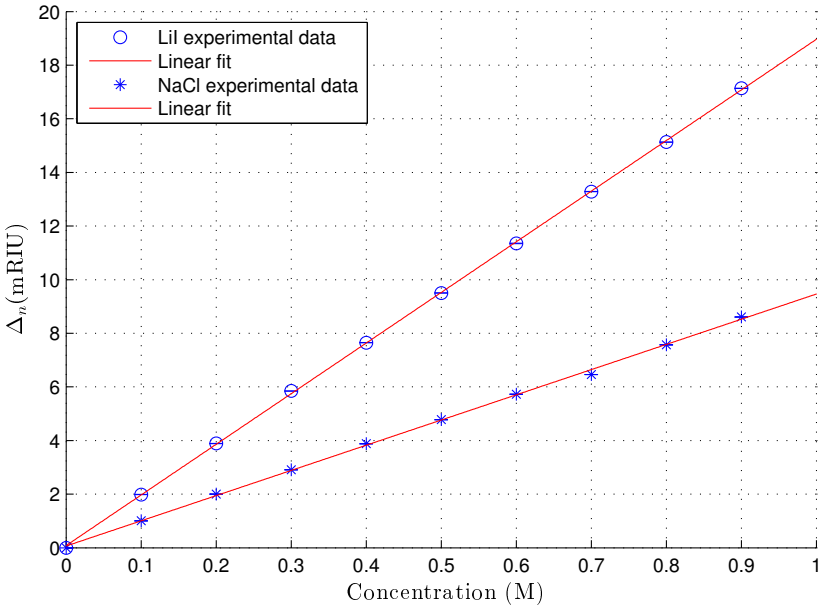


Figure 4.13: Calibration of the refractive index of a series of concentrations of sodium chloride and lithium iodide. The reference of these measurements was the refractive index of the deionised water. Experimental data is fitted to a linear function. The slope is 9.4 mRIU/M for NaCl and 18.9 mRIU/M for LiI with R^2=0.9993 and 0.9999 respectively.

two electrolytes will be used to study the effect of their properties on the system response to the applied voltage, these results help to select the concentrations of the electrolytes to perform measurements within the dynamic range of the system, as will be discussed in chapter 6.

Two types of sensor chips (i.e. gold coated substrates) were used. Sample 1 has been prepared by sputtering approximately 50 nm of gold on a glass slide without the use of the chromium adhesion-promoting layer. Sample 2 is obtained from Reichert Inc. with these specifications: glass substrate refractive index 1.5255, 12.5 mm × 12.5mm, thickness 0.9 mm, and gold thickness 47.5 nm±5nm, undercoated by a layer of chromium of thickness (1±0.5 nm).

4.4 Testing of the voltage sensing system

Cyclic voltammetry has been used to test the integrated optical and electrochemical system. In this experiment, 0.1M NaCl was used as an electrolyte solution. A multi-cycle voltammetry was used to produce a nearly square wave of ± 200 mV (slope of rising and falling edges is 1V/s). The potential starts from the open circuit potential and switched to $(+200mV)$ at a rate of (1V/s) and then switched to $(-200mV)$ and this process is repeated to produce a square wave. The response of the optical system was recorded the same time this experiment is run by the electrochemical system. Before running this experiment, the optical system was tested for exciting surface plasmons and was calibrated by stepping the refractive index of the sample. Then, the differential signal is adjusted to its zero position before the start of the electrochemical tests.

The waveform, presented in Fig. 4.14-(a), was used to test the response of both electrochemical system and the optical system simultaneously. The electrochemical current is plotted against the applied voltage in Fig. 4.14-(b), forming a conventional voltammogram for the window (-200 mV to 200 mV). These results demonstrates a successful removal of the periodic noise observed previously by Huang et al [25].

The response of the electrochemical system has been tested by recording both the charge (Fig. 4.14-(c)) and the current (Fig. 4.14-(e)) while recording the DI-SPR signal (A-B/A+B)(Fig. 4.14-(d)). The response of the SPR system is correlated to the charge, as expected from the modelling in Sec. 3.3. The optical equivalent to the current can be found by taking the derivative of the optical response. Fig. 4.14-(f)) shows the derivative of the DI-SPR signal demonstrating peaks similar to the electrochemical recording of the current. This plasmonic response has also been reported by Shan et al [115].

To put these results into perspective, the current values, shown in Fig. 4.14-(b), are used to estimate the value of the interfacial capacitance, from: $j(t) = Cdv/dt$, where

dv/dt is the voltage scan rate). The capacitance is obtained by dividing the current density by the rate of the voltage scan. As this experiment used a scan rate of unity, the maximum experimental current density at (at t=0,1,2,3..) maps directly to the capacitance per unit area. The obtained results, for ± 200mV (at the peak of the current density) are close to the simulated values in Fig. 3.6 - Sec. 3.3. However, the relation $j(t) = Cdv/dt$ assumes that the capacitance change in response to voltage is instantaneous. Therefore, this estimate does not consider the response time due to the equilibrium of the ions at the Debye layer near the electrode-electrolyte interface. The response time of the system will be discussed in detail in Sec. 6.3.3 on page 170. Moreover, the simulated behaviour is for optimal smooth mono-crystalline gold surface; however, the experimental results are obtained for the commonly used gold thin films, which are not treated to satisfy these criteria.

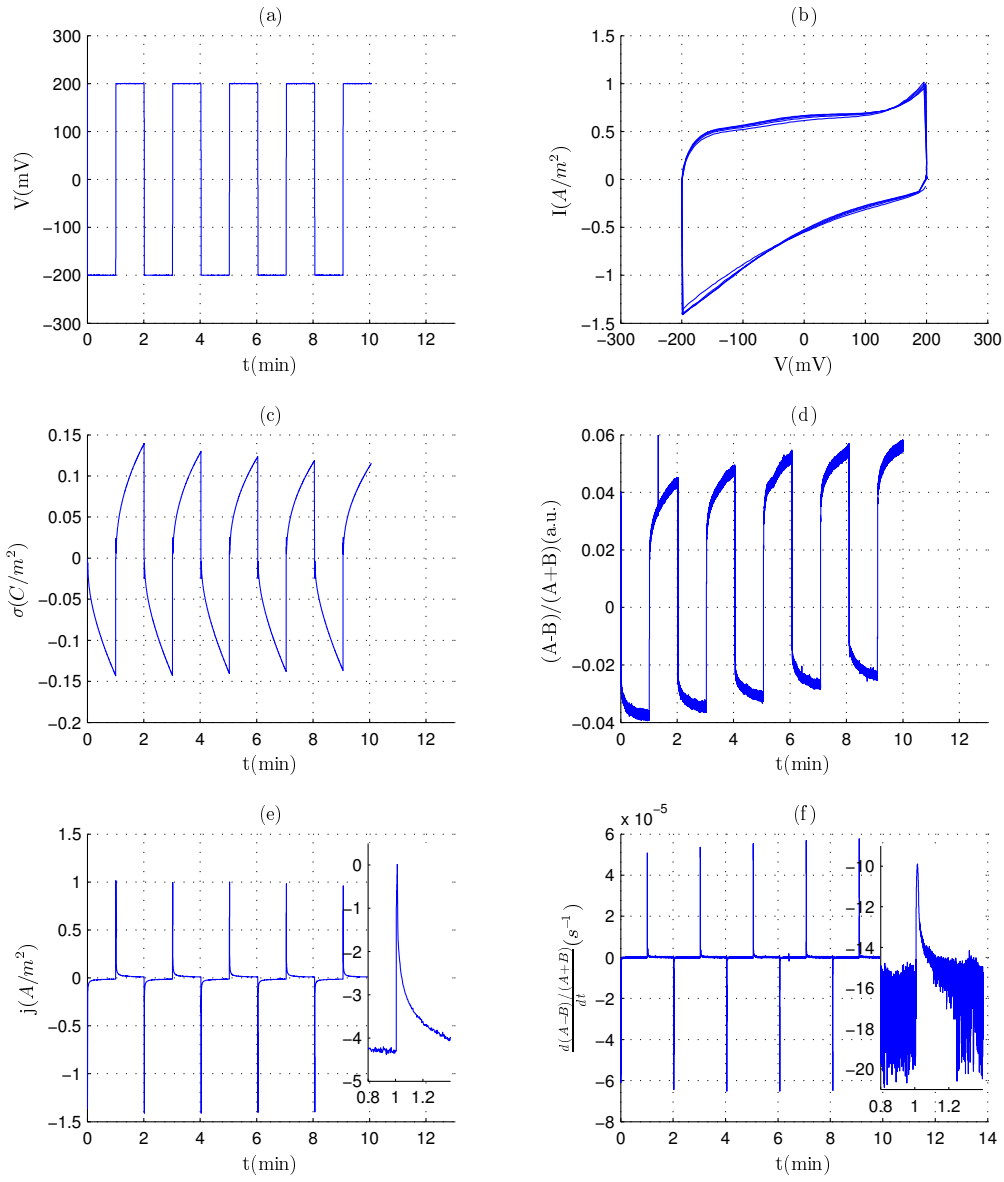


Figure 4.14: Optical vs electrochemical response to the applied voltage waveform: (a) The applied voltage waveform and (b) the resulting voltammogram, respectively. Electrochemical system response is shown as charge(c) and current (e). The response of the optical system is presented by (d) the differential signal (correlated to charge) and (f) its derivative (current equivalent). An example spike in (e) and (f) are presented in the insets on semi-log scale.

4.5 Conclusions

(a) An optical system was designed to excite surface plasmon at metal -electrolyte interface. This system was integrated with an electrochemical system made of a three electrode electrochemical cell and a potentiostat.

(b) Noise in the electrochemical system sets the limits of using the system for investigating voltage sensitivity which cannot exceed 0.1 mV using the current system. The performance level is not challenging for investigating this problem, as we are the signal of interest features a change of 100 mV, see Sec. 3.7.

(c) This chapter provides a description for the system that will be used later on in this thesis to study the different factors that influence voltage sensitivity: factors related to the optical system (chapter 5) as well as other factors related to the electrical properties of the interface (chapter 6).

Chapter 5

Sensitivity of Differential-intensity Surface Plasmon Resonance Applied to Voltage Sensing

5.1 Introduction

The detection limit of a sensing system (i.e., sensitivity) is determined from its response to a perturbation compared to the noise (i.e., the variance of the static or DC signal). Similarly, the voltage sensitivity of the differential-intensity SPR (DI-SPR) can be analysed. Following the discussion in Sec. 2.1.3, DI-SPR responsivity η to dynamic voltage signals can be expressed as a multiplication of the detection responsivity ($\Delta[(A-B)/(A+B)]/\Delta\theta_0$) and the angular responsivity ($\Delta\theta_0/\Delta V$), which is given by

$$\eta = \frac{\Delta(A-B)/(A+B)}{\Delta\theta_0}\frac{\Delta\theta_0}{\Delta V} \tag{5.1}$$

where θ_0 is the resonance angle. The angular responsivity was studied theoretically

in chapter 3 (on page 75) and validated experimentally in chapter 6 (on page 167). However, in-depth understanding of detection responsivity is essential for obtaining high voltage sensitivity. Also, it is important to understand the factors affecting the noise performance of the system.

This chapter describes theoretical and experimental investigations of the responsivity of the DI-SPR, followed by a unique analysis of the noise associated with the output of the system. The findings of this study can be used in different applications of the DI-SPR. The analysis of the DI-SPR noise can be applied to sensing systems where differential detection is performed (e.g., differential-intensity optical fiber sensors) or position sensing using bi-cell/quadrant detectors.

5.2 Theoretical and experimental evaluation of the DI-SPR's responsivity

This section discusses the different models that can be used in analysing the DI-SPR's responsivity. The proposed models are validated experimentally and compared to the state of the art responsivity models. This investigation alongside with noise analysis is essential for estimating the sensitivity of the DI-SPR system.

5.2.1 Theoretical analysis of the responsivity

Proper modelling of DI-SPR's responsivity is critical to calibrating the system's response to voltage. In this section, our suggested second- and third-order expressions are presented compared to Fresnel model and Tao's model (page 22). Since Fresnel model is a realistic representation of the SPR curve, it is used as a reference for comparing other models.

Fresnel Model

The responsivity of the DI-SPR was obtained from Fresnel model by the following steps.

(a) SPR curves were generated using Fresnel equations for the multilayer structure presented in Fig. 3.3.

(b) For each generated curve, the outputs of the bi-cell detector (i.e. A and B) were calculated by the numerical integration of the resonance curve using the angular width as an integration limit. These outputs were used to calculate the differential response $(A-B)/(A+B)$.

(c) The resonance angle (i.e., location of the minimum of the curve θ_0) is calculated, by fitting a narrow range of the resonance curve ($1 \pm$ deg) to quadratic function, interpolating to increase accuracy of finding the location of the minimum.

(d) The previous steps were repeated for different refractive indices of the sample to calculate the responsivity.

(e) The responsivity η is the ratio of the change in the differential response $\Delta[(A-B)/(A+B)]$ and the change in the resonance angle ($\Delta\theta_0$).

(f) The previous steps were repeated while changing different parameters (such as gold film thickness, thickness of chromium layer and refractive index of the sample).

Tao's approximation

Tao et al [26] provided a simple method for calculating the responsivity of the DI-SPR. For this purpose, a quadratic function is used to model the SPR curve including only the second order term $[a_2(\theta-\theta_0)^2]$ from

$$R(\theta) = a_0 + a_1(\theta-\theta_0) + a_2(\theta-\theta_0)^2 + a_3(\theta-\theta_0)^3 + ... \tag{5.2}$$

where R(θ) is reflectivity as a function of the angle of incidence, θ_0 is resonance angle and a_0, a_1, a_2, a_3 are the coefficients of the power series that represents the SPR curve.

To produce the bi-cell signals (A and B), the resultant curve is integrated using the angular width ($\pm\theta_\omega$) as integration limits. A and B are then used to calculate the change in the differential response $\Delta[(A-B)/(A+B)]$ relative to the shift in the resonance angle $\Delta\theta_0$, from which the DI-SPR responsivity is expressed as

$$\eta = \frac{\Delta(A-B)/(A+B)}{\Delta\theta_0} = \frac{3}{\theta_\omega} \tag{5.3}$$

.

The second order and the third order approximations

Although, Tao's model provides a quick estimate of the responsivity of the DI-SPR, it has two disadvantages. First, it implies that an infinite responsivity is obtained as the angular width tends to zero ($\theta_\omega \rightarrow 0$): the equivalent to exciting SPs with a collimated beam. This observation contradicts the findings of Schneider et al [34] that the DI-SPR is more responsive compared to the fixed angle approach (Sec. 2.1.2). Second, it does not include the factors related to the shape of the curve; hence it cannot be used to obtain the responsivity in the case of variation in the properties of the sensing structure. Therefore, this model has been modified, in this thesis, starting from Eq. 5.2 by including the zero order (a_0) and the second order (a_2) terms. The following equation gives the responsivity obtained from the second order polynomial, the derivation is included in appendix A,

$$\eta = \frac{3a_2\theta_\omega}{3a_0 + a_2\theta_\omega^2} \tag{5.4}$$

where

This mathematical expression accounts for the variation of the thickness of the noble

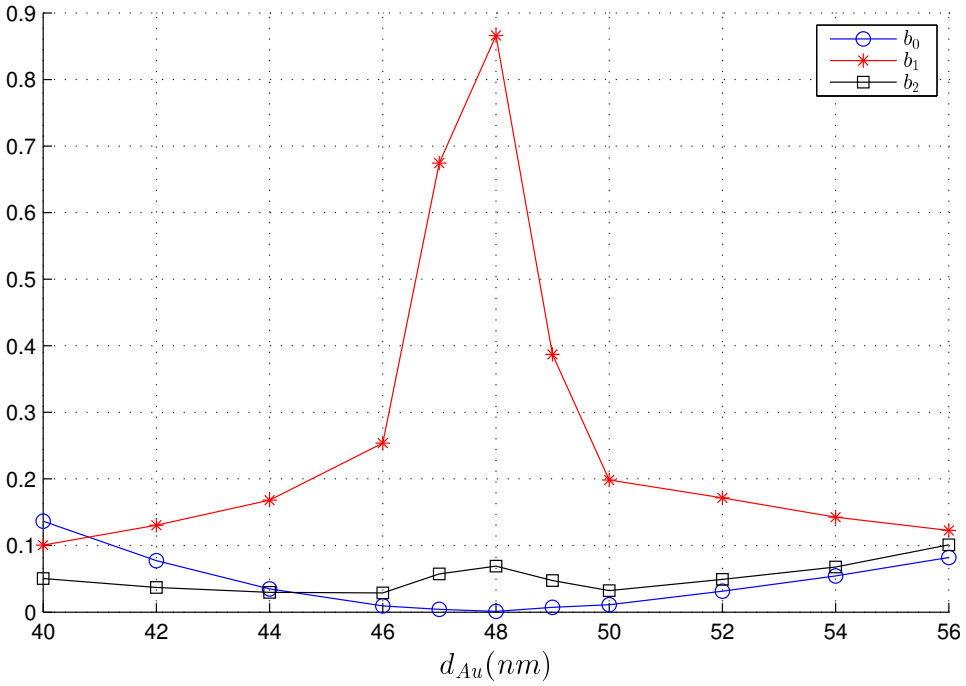


Figure 5.1: The coefficients of the third-order responsivity expression ($b_0, b_1$and b_2). The three coefficients are presented for a set of gold thin film thickness (du_{Au}).

metal (e.g. gold) and the metallic adhesion layer as reflected in the values of a_0 and a_2. It can also be reduced to Eq. 5.3 under the condition ($\lim_{a_0 \to 0} \eta$).

A more accurate representation of the responsivity is achieved by

$$\eta = \frac{3b_1\theta_\omega + 3b_2\theta_\omega^2}{3b_0 + b_1\theta_\omega^2 + b_2\theta_\omega^3} \tag{5.5}$$

which is found by fitting the Fresnel-generated data to this expression. The coefficients of the fitted equation b_0, b_1 and b_2 can be found for different specifications of the sensing structure as in Fig. 5.1. However this equation can not be used to estimate responsivity directly from the resonance curve.

5.2.2 Experimental evaluation of the responsivity

To evaluate the proposed responsivity models, the system described in Sec. 4.2.1 was used to perform the following experiment. In this experiment, we used a sensor chip that was prepared by sputtering approximately 50 nm of gold on a BK-7 glass slide without the use of the chromium adhesion-promoting layer. Refractive index solutions were prepared using different concentrations of sodium chloride (Sigma Bioxtra 99.5%). These solutions were used to measure the system's response to change in the refractive index of the sample. For this purpose, a flow cell (with a 57 μl channel) was mounted on the prism. The response of the system was recorded using the camera while changing the sample in the channel (distilled water $n = 1.3319$ at $633nm$ and 20°C) to another with a different refractive index (1.3334) using a syringe pump. Using these recorded video frames, SPR curves were produced for each frame using a pixel-angle calibration. To calculate the responsivity curve, a virtual differential detection approach (i.e., calculating $A, B, (A-B)/(A+B)$) was implemented by the following two steps.

(a) Tracking the minimum of the SPR curve to calculate the resonance angle corresponding to the two refractive indices and then the resonance shift ($\Delta\theta_0$).

(b) calculating the DI-SPR signal $(A-B)/(A+B)$ for different values of the angular widths of the incident beam that are calculated using a pixel-angle calibration.

This analysis provides the means for calculating the responsivity (η) of the DI-SPR using the system response to changes in the resonance angle or the refractive index.

5.2.3 A comparison between the theoretical and the experimental responsivity

Fig. 5.2 depicts the experimental responsivity as a function of the angular width for the sensing structure described in Sec. 5.2.2. These results are compared to (i) the theoretical responsivity, obtained using the Fresnel model for 50 nm gold when no adhesion layer is undercoated, (ii) Tao's approximation [26] and (iii) the second and the third order approximations (see - Sec. 5.2.1). The following observations can be made from this figure.

(a) At small angular width, the theoretical response (from the Fresnel model, the second and the third order approximations) does not approach infinity as predicted by Tao's approximation (Eq. 5.3), but converges to zero. This trend is also supported by the experimental results.

(b) Both second and third order expressions (Eq. 5.4 and Eq. 5.5) explain the drop of the responsivity at smaller angles. Referring to Eq. 5.4, this drop is due to the inclusion of the second order and the zero order of the polynomial to the responsivity expression. They can be used to estimate the point of maximum responsivity, as given by the term ($\theta_\omega = \sqrt{3a_0/a_2}$).

(c) The second and the third order approximations are validated against the standard Fresnel model. Responsivity of Fresnel model can be reproduced using the third order expression, which, therefore, provides more accurate representation. Compared to the third-order expression, the second-order expression departs at large angular widths, reflecting the effect of the asymmetry of the SPR curve. The coefficients a_0 and a_2 are valuable measures for the properties of the SPR curve; a_0 represents the minimum reflectivity and a_2 reveals information on the gradient.

(d) Tao's approximation is significantly inaccurate for smaller angles ($\theta_\omega < 3a_0/a_2$);

however, it can still be used for larger angular widths with inaccuracy due to the assumption of the symmetry of the curve.

(e) There is a discrepancy between the theoretical and the experimental responsivity that is seen as reduction in the experimental responsivity with a shift in its maximum. These results are explained later by studying how the system behaves with the variations in the properties of the sensing structure. The Fresnel model will be used, with different input parameters, to understand the effect of the factors of the sensing structure. This approach, ultimately, provides better control in the investigation of their effects.

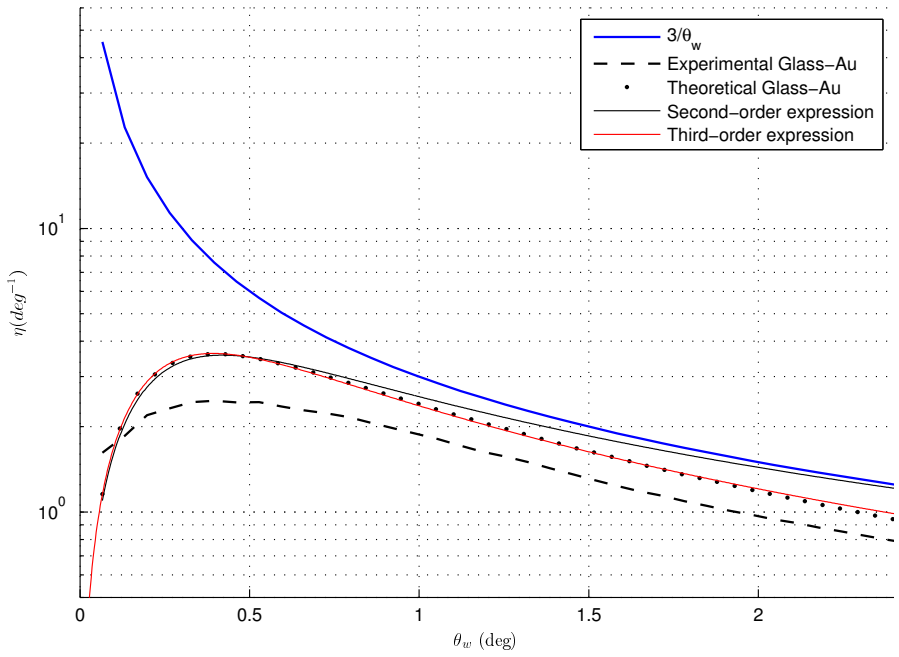


Figure 5.2: Theoretical vs experimental responsivity of DI-SPR. The dotted line presents the theoretical responsivity when glass slides are coated with bare gold. The dash line presents experimental responsivity for the bare gold. Both are compared to Tao's model (blue), the second-order expression (black) and third-order expression (red).

5.2.4 The effect of the sensing structure on the responsivity

This section describes the effect of the sensing structure on the responsivity. It discusses the effect of the thickness of the chromium adhesion layer and the thickness of the gold thin-film using the Fresnel model described in Sec. 5.2.1.

Since the chromium adhesion layer is commonly used, we address its effect on the responsivity. This is performed by calculating the responsivity for a set of thicknesses, from 0nm to 3nm, of this layer. One important effect of the Cr layer is that, for any angular width, there is a reduction in the responsivity as the thickness of the Cr layer increases. This is shown clearly in Fig. 5.3-(a). It is also observed that the angular width of the peak responsivity shifts to the right with increasing Cr thickness. To explain these results, we looked at the effect of the Cr layer on the SPR curve, which is shown in Fig. 5.3-(b), and more specifically, the FWHM and the minimum reflectivity of the curve, in Fig. 5.3-(c) and Fig. 5.3-(d), respectively. As the thickness of Cr increases, both the FWHM and a_0 increases. This is also noticed in the dependence of the coefficients of the polynomial on the thickness of the chromium layer as shown in Fig. 5.5.

The effect of the thickness of the gold thin film was investigated. The responsivity of the differential technique has also demonstrated a noticeable dependence on the thickness of the gold film. Fig. 5.4-(a) shows results obtained by changing the thickness of Au, without an undercoat of chromium. Peak responsivity is obtained, for all angular range, at gold thickness around 48nm, which decreases rapidly on either side of the peak. Fig. 5.4-(a) can be explained by considering the SPR curve in Fig. 5.4-(b) and its parameters: FWHM and a_0 in Fig. 5.4-(c) and Fig. 5.4-(d), respectively. Although the FWHM decreases with increasing Au thickness, the a_0 response shows a turning point at 48nm, which correlates with the responsivity in Fig. 5.4-(a).

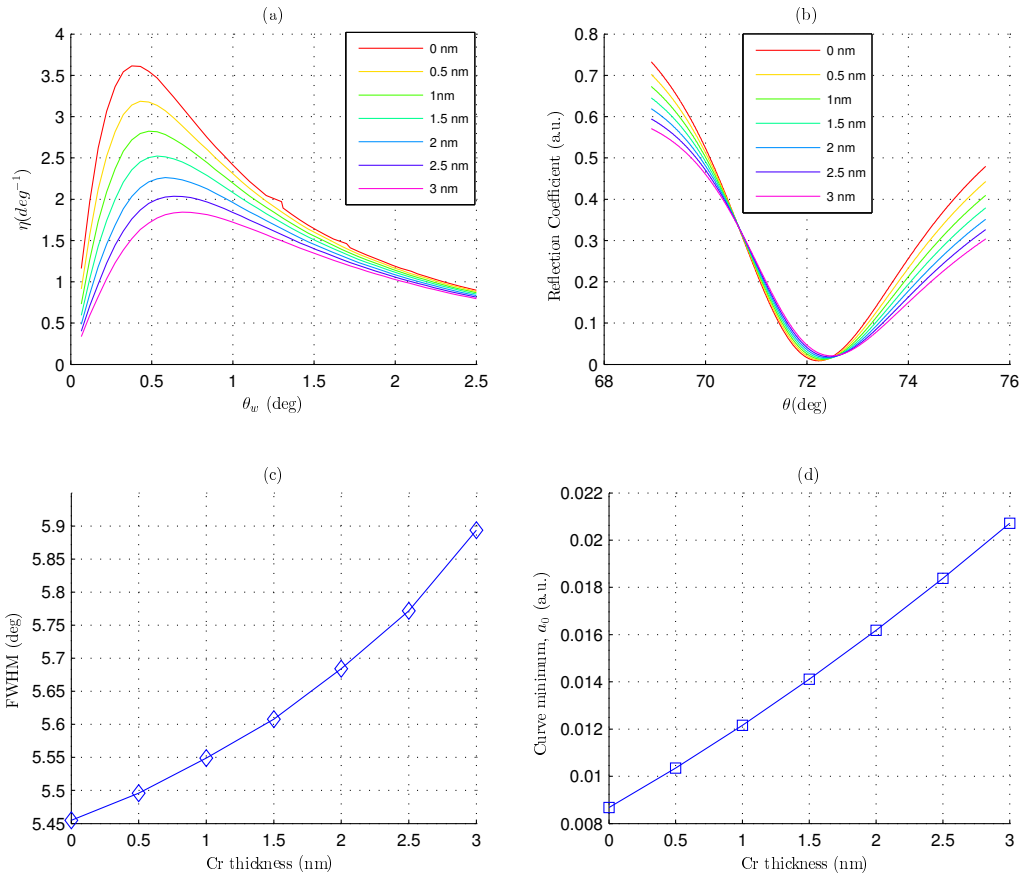


Figure 5.3: The effect of the adhesion layer on the responsivity of the DI-SPR. (a) The angular width dependent responsivity. (b) The effect of the thickness of the adhesion layer on the SPR curve. Curve parameters: (c) FWHM of the curve and (d) reflectivity at the minimum of the curve.

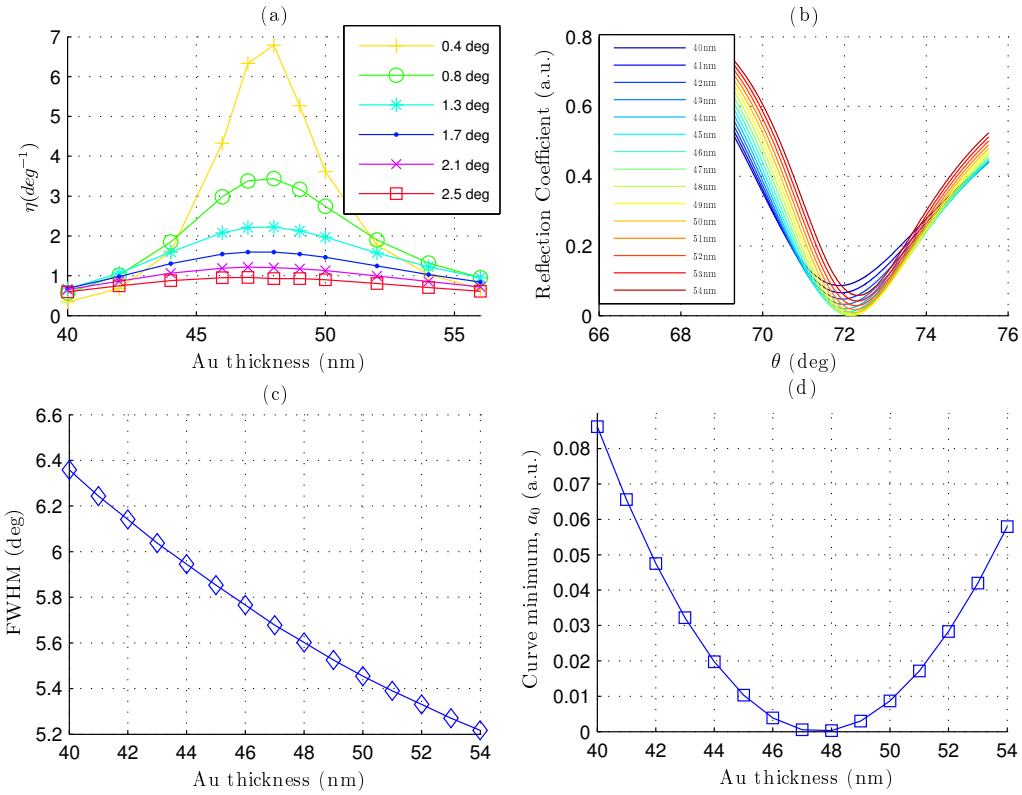


Figure 5.4: The effect of the metal thickness on the responsivity of the DI-SPR. (a) The angular width dependent responsivity. (b) The effect of the metal thickness on the SPR curve. Curve parameters: (c) FWHM of the curve and (d) reflectivity at the minimum of the curve.

A close look into Fig. 5.3 and Fig. 5.4 reveals that the minimum reflectivity a_0 of the SPR curve is strongly related to the responsivity, showing a negative correlation. For instance, a deeper SPR curve, which is noticed around the thickness of 48nm, demonstrates a higher responsivity. Similarly, as the thickness of the adhesion layer increases, the minimum reflectivity becomes higher and so the responsivity decreases. By getting back to theoretical estimation of the responsivity, the above observations are related to the zero order of the polynomial that represents the SPR curve (Eq. 5.4). Fig. 5.5 shows how the coefficients of the SPR curve vary with the thickness of the chromium and the gold thin-film.

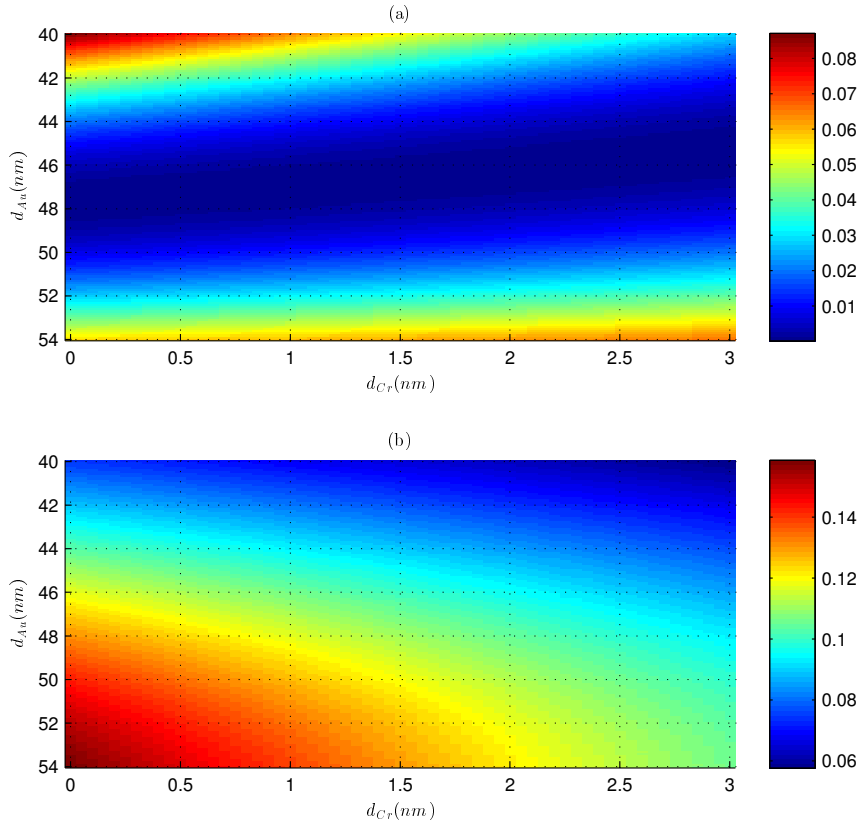


Figure 5.5: The coefficients of the quadratic model of the SPR curve. The zero order (a_0) and the second order (a_2)are presented as for a set of chromium and gold thickness in (a) and (b), respectively.

5.3 Noise performance of the DI-SPR system

This section presents an investigation of the DI-SPR noise. First, analytical expressions are described and then validated experimentally. For this purpose, the pixelated camera was used since it provides flexibility in studying the effect of different parameters. Second, these expressions are applied to study the noise associated with the DI-SPR's output when the bi-cell detector is used. The noise of the different components of the system's output is investigated, particularly the effect of the input power of the bi-cell units and the mismatch of the differential intensity.

5.3.1 Theoretical Analysis of DI-SPR noise

The DI-SPR signal is obtained by dividing the differential intensity of the SPR curve $(A-B)$ by the total intensity $(A+B)$. This section presents analytical expressions for estimating noise associated with the DI-SPR's output, taking into account the coherent and the incoherent noise.

From the statistical principles, noise is considered a random variable. Specific expressions are used to perform the different mathematical operations on these variables [116]. These analytical expressions are well-suited to estimating the noise of the DI-SPR output because the additive noise of the individual components propagates to the final output through the difference (A-B), the sum (A+B) and the division (A-B)/(A+B).

The differential intensity $(A-B)$ and the total intensity $(A+B)$

The total noise resulting from the difference or the sum signal can be obtained from the following expression (obtained from Kendal [116])

$$\sigma^2_{A\pm B} = \sigma^2_A + \sigma^2_B \pm 2\mathrm{cov}(A,B) \tag{5.6}$$

where total noise $\sigma_{A\pm B}$ is expressed in terms of the variance of the two signals (σ_A^2, σ_B^2) and their covariance (cov(A,B)). This expression includes the effect of the correlated components and the uncorrelated components of the noise. It can be reduced to $(\sigma_{A\pm B}^2 = \sigma_A^2 + \sigma_B^2)$ when the uncorrelated noise is dominant (i.e., $\text{cov}(A, B) \to 0$).

The DI-SPR signal $(A - B)/(A + B)$

The noise of the differential response $(A - B)/(A + B)$ can be estimated from the variance of the ratio of two random variables

$$\sigma^2_{\frac{A-B}{A+B}} = \frac{(A+B)^2\sigma^2_{A-B} + (A-B)^2\sigma^2_{A+B}}{(A+B)^4} + \delta \tag{5.7}$$

where $\sigma^2_{\frac{A-B}{A+B}}$ is the noise of the differential response which shows a dependence on the signal and the noise of the differential intensity (A-B) and the total intensity (A+B). The term δ accounts for the Taylor approximation adopted for the derivation of this equation. Full derivation is found in [116]. This expression can be simplified to the expression in Eq. 5.8 under the circumstances $(A-B) \to 0$; the term $((A-B)^2\sigma^2_{A+B})$ $\to 0$. This condition is satisfied at the start of the experiment since the bi-cell detector is balanced. Similarly can be used for the case of measuring a small change in refractive index or voltage; as the mismatch of the bi-cell output is negligible in this case (i.e., $(A - B) \to 0$ for $\Delta\theta_0 \to 0$).

$$\sigma_{\frac{A-B}{A+B}} = \frac{\sigma_{A-B}}{A+B} \tag{5.8}$$

5.3.2 Experimental validation of the analytical expressions of the DI-SPR noise

Experimental procedure

To validate the proposed theoretical expressions (on pages 126 and 127) for estimating the differential-intensity noise, a pixelated camera was used to monitor the intensity fluctuations of the SPR curve over time (i.e., collecting a data set of R(θ, t)). This was performed by recording the reflected light for 30 seconds with a sampling frequency of 10 Hz. Fig. 5.6 shows an example frame, in which the horizontal axis represents the angular information while the vertical axis represents imaging information. The former is labelled in degrees, centred at the resonance position ($\theta_\omega = 0$), and the latter is labelled by the number of pixels. A virtual bi-cell is centred on the resonance angle ($\theta_\omega = 0$), and its width is defined in the dimensions of the angular widths while its height in pixels; it is $\pm$100 pixels in this experiment. A and B are used to denote the two units of the virtual detector.

For each frame, the intensity of the virtual unit (A or B) was estimated by the numerical integration of the intensity of the pixels that forms the area of the cell. The obtained value represents a data point in the time series that is used to calculate the difference $(A - B)$, the sum $(A + B)$ and the ratio $((A - B)/(A + B))$. To test the noise dependence on the angular width, this process was repeated for a set of angular widths starting from 0.066 deg to 2.6 deg using angle-pixel calibration.

For each of these data sets (i.e., 300 samples), the standard deviation (i.e., the noise) and the mean (i.e., the signal) were calculated as a function of the angular width (θ_w) and used to validate the expressions described in Eq. 5.6 and Eq. 5.7 on pages 126 and 127 respectively.

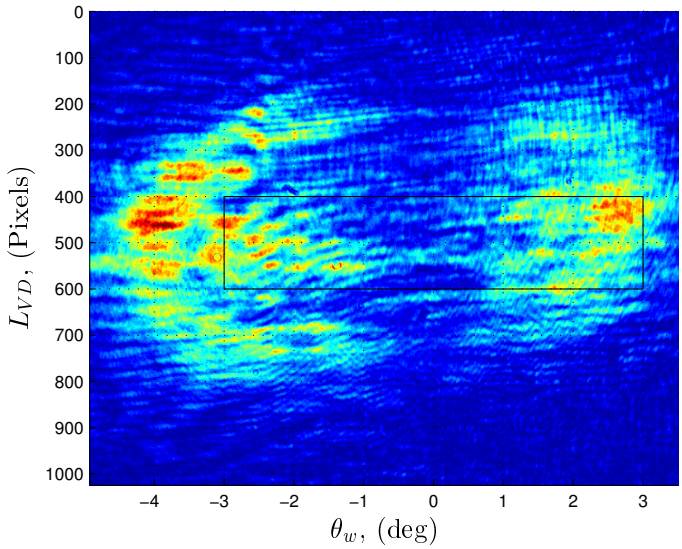


Figure 5.6: The distribution of the intensity of the reflected beam; imaging information on the vertical axis and angular information on the horizontal domain. The vertical axis reflects the inhomogeneity in the sensor material and the sample, while the horizontal axis shows the reflectivity profile of SPR curve. The rectangle shows coordinates of the virtual bi-cell detector that is centred on the resonance angle.

The differential-intensity noise (σ_{A-B}) and the total intensity noise (σ_{A+B})

The experimental validation of Eq. 5.6 and Eq. 5.7 using the pixelated camera is presented. First, the propagation of noise to the difference ($A - B$) and the sum ($A+B$) is depicted in Fig. 5.7. Noise of both increases as the angular width increases. This dependence is explained in detail in Sec. 5.3.3. As seen in Fig. 5.7, noise that is predicted by the analytical expression of Eq. 5.6 demonstrated a good agreement with the noise calculated experimentally, whereas the summing in quadrature ($\sigma_A^2 + \sigma_B^2$) does not estimate this noise accurately.

A close look at Fig. 5.7 suggests a contribution of both coherent and incoherent noise components to the total noise of the difference and the sum. The presence of the coherent noise is validated by looking at the correlation between A and B. For this purpose, Pearson correlation coefficient (ρ) of the two signals (Fig. 5.8-(a)) is calculated, for slots of 10 seconds, as shown in Fig. 5.8-(b). A positive correlation between A and B is observed when there is coherent fluctuations between the two signals. These coherent oscillations are removed when the signal A-B is processed as observed in Fig. 5.9-(b). On the other hand, the correlation coefficient drops when the incoherent noise dominates. For instance, a drop of the correlation coefficient is noticed in the last 5 seconds of Fig. 5.8-(a). This drop indicates uncorrelated oscillations between A and B, which is manifested in a drift of the baseline of A-B.

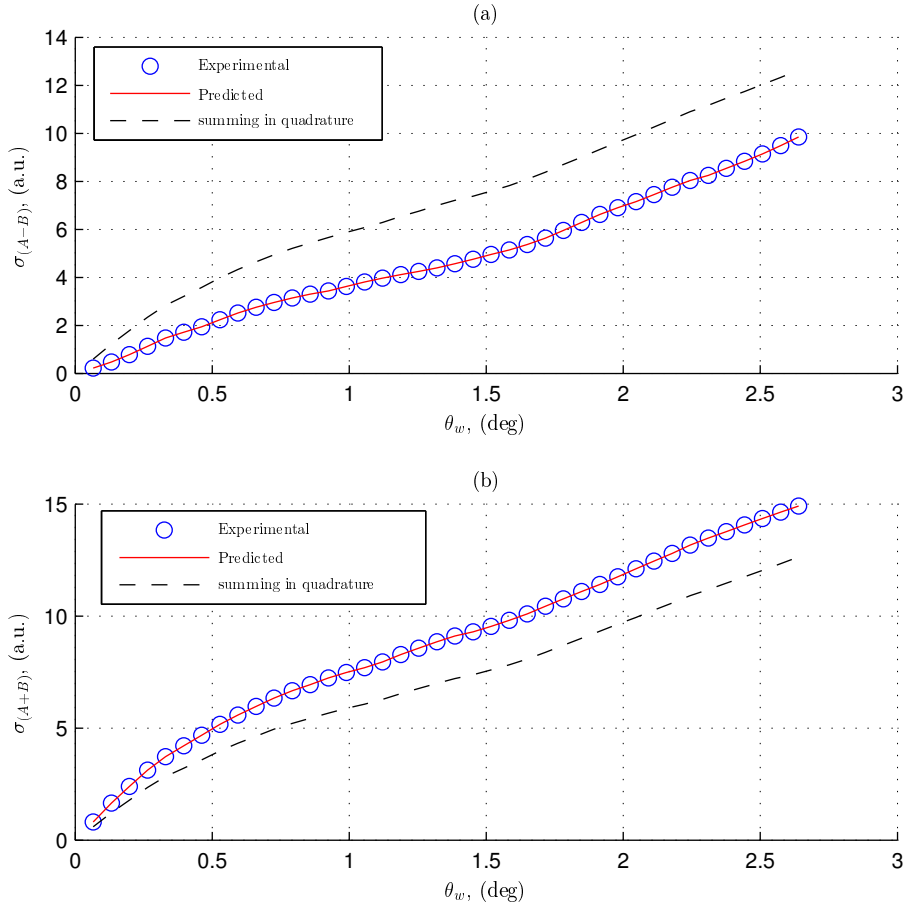


Figure 5.7: Noise of the differential intensity and the total intensity of the virtual bi-cell detector in (a) and (b). The circle represents the experimental data; the solid red line gives the prediction of the difference or the sum of the two random variables (see pages 126 and 127). The dash line represents the case of only incoherent oscillations

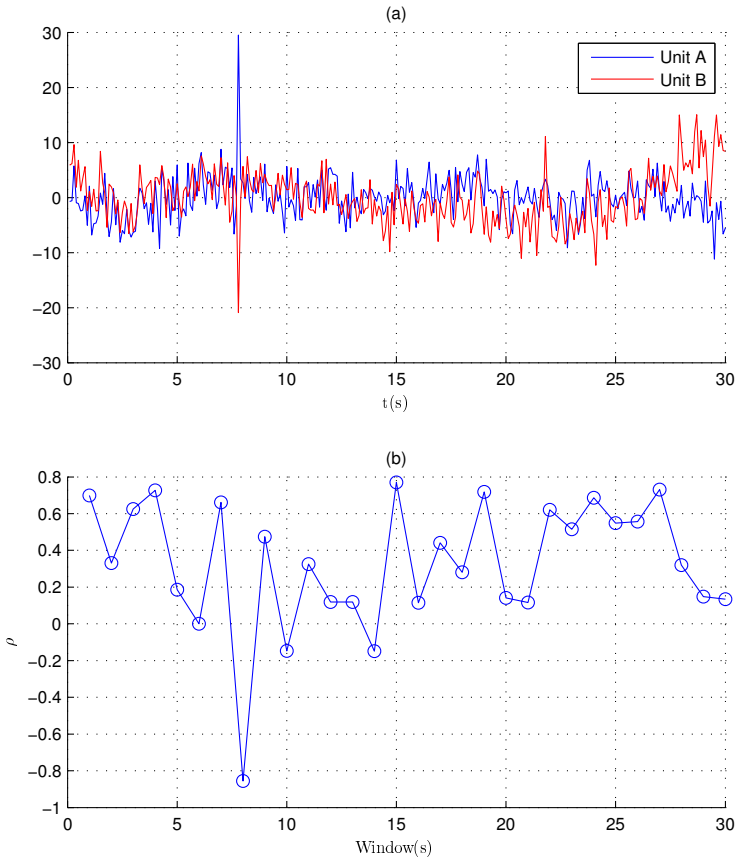


Figure 5.8: Correlation between the signal of the two units of the virtual bi-cell detector

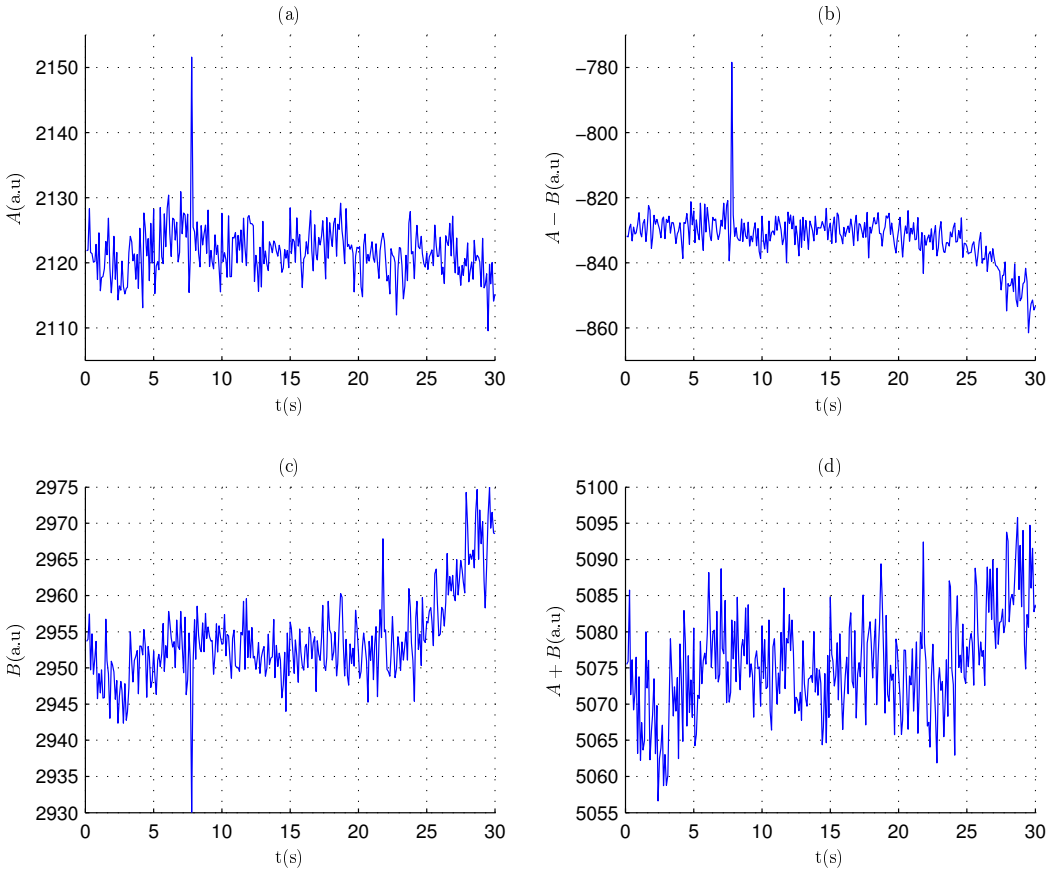


Figure 5.9: Fluctuations in the signal of each half of the resonance curve A, B and the components of the differential signal (A-B) and (A+B). These data are generated from an angular width of 1 deg, as an example, using the virtual bi-cell detector.

The Noise of the DI-SPR's output ($\sigma_{\frac{A-B}{A+B}}$)

Fig. 5.10 presents a comparison between noise of the DI-SPR that is estimated by Eq. 5.7 and the noise calculated experimentally as described in Sec. 5.3.2. From Fig. 5.10, the proposed expression demonstrates a good agreement with the experiment, and therefore can be used to predict the total noise of the DI-SPR. It can be used alongside responsivity to estimate the sensitivity of the system and its dependence on different parameters as discussed in Sec. 5.4. The noise dependence on the angular width and the approximated expression of Eq. 5.8 are discussed in more detail in Sec. 5.3.3.

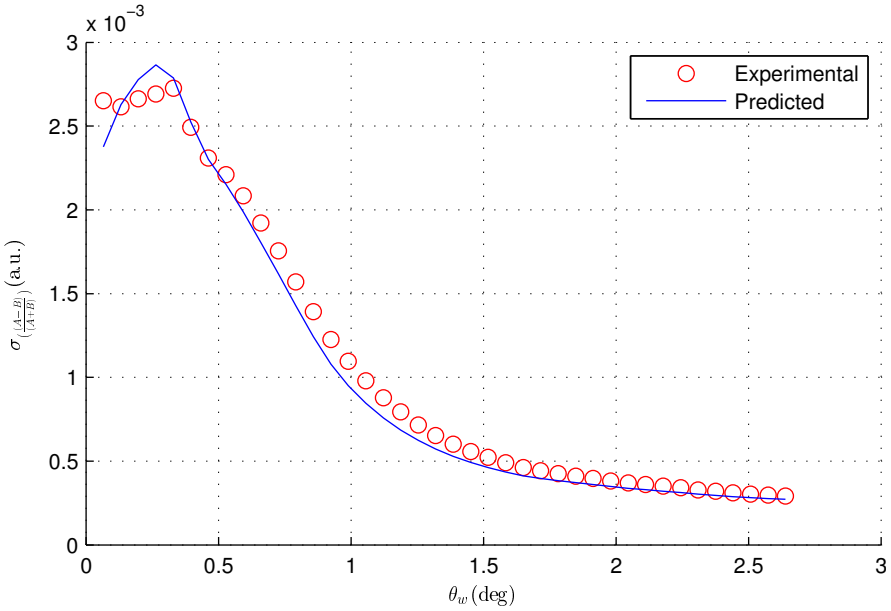


Figure 5.10: Experimental noise of DI-SPR compared to the expression of the ratio of random variables. The experimental noise is calculated using the virtual bi-cell detector

5.3.3 Evaluation of the noise of the DI-SPR using bi-cell detector

As this project is focused on the use of the bi-cell detector, the sources of noise of its components and their contribution to the noise of the system output are investigated. The study applies the previous analytical expressions to calculate the propagation of noise to the difference, the sum and their ratio, taking both coherent and incoherent noise into consideration. Before the discussion of the noise associated with different stages of signal processing, the calculations of the noise and the signal of the SPR curve as a function of the angular width are presented.

The signal and the noise of the SPR curve

To understand how the signal and the noise vary with the angular width, the distribution of the total power on the SPR needs to be found. This is necessary to calculate the different types of noise (e.g., shot noise, relative intensity noise) as a function of the angular width. With the knowledge of the power of the reflected light, which constructs the SPR curve (P_T), the power per pixel (P_i) can be found from Eq. 5.9; the term in the brackets is the area under curve per pixel normalized by the total area under the curve. The pixels are mapped to the equivalent angular widths using a pixel-angle calibration. The power for different angular widths is calculated by the numerical integration of the produced power curve using the angular width as integration limits.

$$P_i = P_T\left(\frac{r_i}{\Sigma_{i=1}^{n} r_i}\right) \tag{5.9}$$

where r_i is the local reflection coefficient (i.e., at the pixel i) and n is the number of pixels.

The produced power curve provides the means of predicting the signals and noise of

the bi-cell units A and B. Two sources of noise are related to the detected power: the shot noise and the relative intensity noise. The calculation of the relative intensity noise and the shot noise is described below.

Relative intensity noise is a frequency dependent noise characterized normally as a percentage β of the average power. This figure (β) is found from the laser's specification sheet and can also be determined experimentally. Eq. 5.10 gives the relative intensity noise of the laser as a function of the power and the bandwidth.

$$V_n^{RIN}(\theta_w) = C\beta P(\theta_w)\sqrt{\Delta f} \tag{5.10}$$

where C is a conversion factor, in V/W, that equals the product of the gain (G) and the spectral responsivity (R), $V_n^{RIN}(\theta_w)$ is the voltage equivalent RIN noise as a function of the angular width, $P(\theta_w)$is the power of the reflected light as a function of the angular width and Δf is the bandwidth of the system.

Shot noise is a white noise that arises from the uncorrelated arrival of photons. Its equivalent voltage noise can be found from the mean photo-current (i.e., power P $\times$ spectral responsivity R) and current-to-voltage conversation gain (G).

$$V_n^{sh}(\theta_w) = G\sqrt{2qP(\theta_w)R\Delta f} \tag{5.11}$$

where q is the elementary charge and $V_n^{sh}(\theta_w)$ is the voltage-equivalent shot noise.

Shot noise and the relative intensity noise are calculated as a function of the angular width with the knowledge of the angular distribution of the power P(θ_w), the bandwidth Δ f =1 KHz, the transimpedance gain G=16KΩ, the spectral responsivity R=0.35 A/W and the RIN coefficient β = 0.001 %/ $\sqrt{Hz}$.

Signal/Noise of the components of the differential response A and B

The noise of the components of the bi-cell detector A, B, A-B and A+B was measured. The beam had been balanced on the bi-cell detector before these signals were recorded at a sampling frequency of 1 KHz for a duration of a one minute. This process was repeated for different angular widths of the excitation beam. Also, the power of the reflected beam, at the detector, was measured for the different angular settings. Angular width was selected by varying the diameter of the illumination beam as described in Sec. 4.2.1 on page 95.

Fig. 5.11 shows how the signal of each half of the curve (Fig. 5.11-(a)) and (Fig. 5.11-(b)) scales with the angular width. This is explained by looking at how power increases with the angular width (Fig. 5.11 -(c)). This graph presents the theoretical (obtained from the power as a function of the angular width explained earlier in Sec. 5.3.3 on page 135) and the experimental evaluation of the power-angular width behaviour.

Fig. 5.12 demonstrates the noise of the signals of the bi-cell detector as a function of the angular width, as well as the power, of the excitation beam. This experimental noise is compared to the primary sources of noise, including the shot noise, the relative intensity noise and the electronic noise (i.e., the quantization noise). As concluded from chapter 3, the signal processing circuit is limited by the digitization noise and it can be improved by averaging.

The shot noise and the relative intensity noise are calculated from the experimental values of the power as described in Sec. 5.3.3. As seen from Fig. 5.12, the two noise components are dependent on the power: the relative intensity noise and the shot noise. The curve of the relative intensity noise is steeper than the shot noise, since it is proportional to the power while the shot noise is proportional to the square root of the power. In general, the system is limited by the electronic (quantization noise) for small power levels ($\approx< 30\mu W$) while the effect of the relative intensity

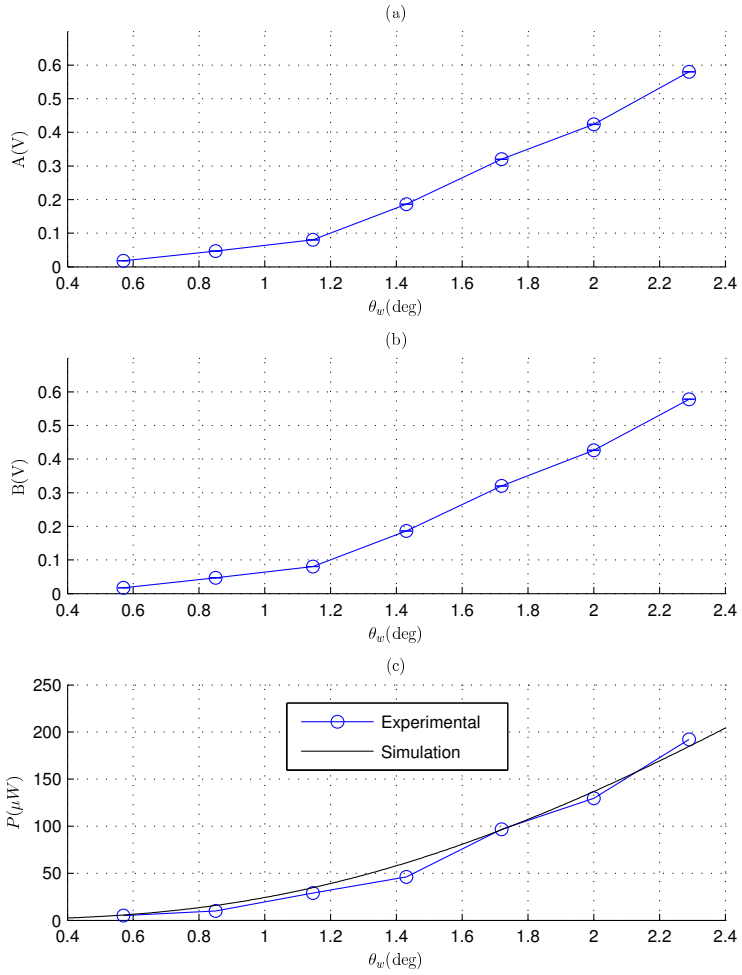


Figure 5.11: (a) and (b) are the signals of the bi-cell detector compared to (c) the angular width dependence of the power.

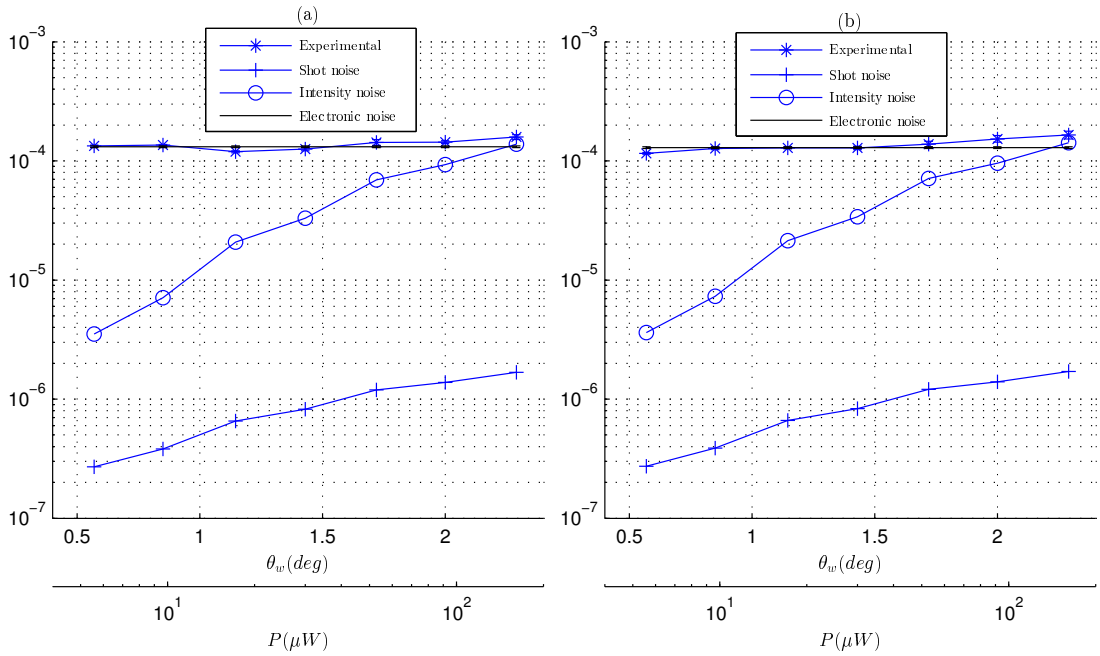


Figure 5.12: Noise associated with the signals (A and B) of the bi-cell detector in volts (represented by the $*-$) compared to the electronic noise (represented by the solid line), the relative intensity noise (represented by the $o-$) and the shot noise (represented by the $+-$).

noise becomes dominant for higher power levels.

Signal/Noise of $(A - B)$

The calculation of the components of the DI-SPR response (A-B) and (A+B) was performed electronically. Therefore, there will be a contribution of electronic noise in addition to the propagation of noise from the primary signals A and B. In Fig. 5.13, the experimental noise of the differential intensity (σ_{A-B}) (represented by $*-$) is compared to the experimental electronic noise of the differential output (represented by solid line). The system is limited by electronic noise for low power levels ($\approx 10\mu W$), but the effect of the optical noise increases afterwards.

The reduction of the noise to signal ratio (NSR) is evaluated by comparing the

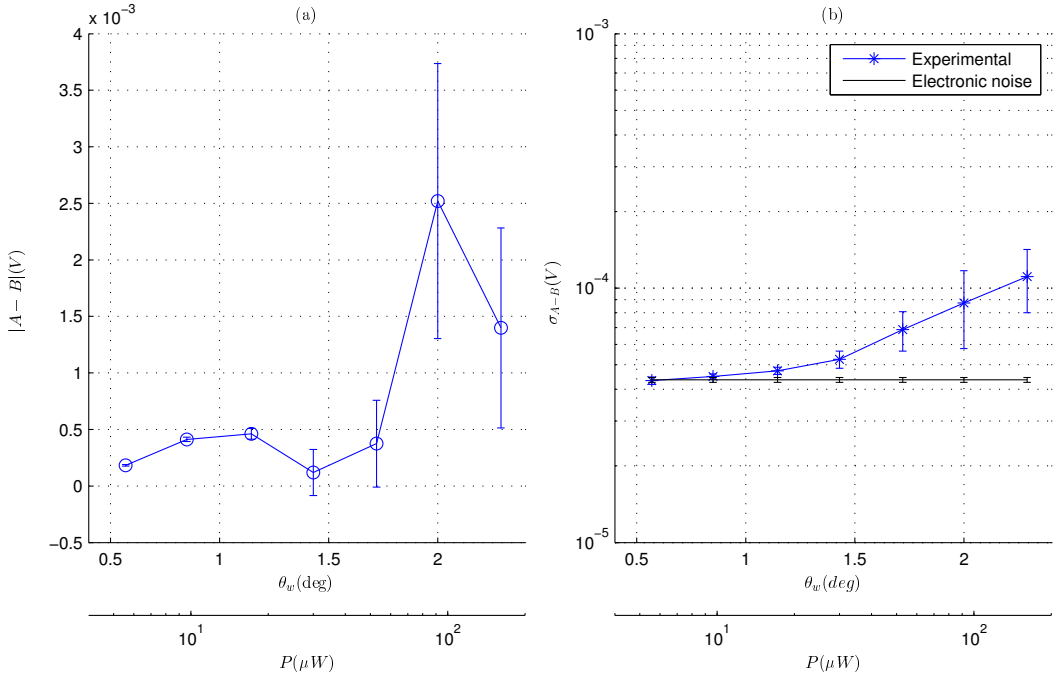


Figure 5.13: (a) The balanced intensity by mechanical nulling to make $A - B \approx= 0$, which is (b) a comparison between differential intensity noise and the electronic noise of the differential circuit

NSR of the differential intensity $A - B$ to the NSR of the intensity A and B. To estimate the reduction of the coherent noise, the electronic noise was subtracted from the total noise, before calculating the NSR. In order to calculate the NSR of the A-B signal, the noise σ_{A-B} is divided by A instead (A-B). The reason behind this selection is that A-B is approximately zero as observed in Fig. 5.13. Otherwise, the NSR of A-B would appear infinity or worse than the NSR of A or B.

As seen in Fig. 5.14, the noise is reduced by using the differential intensity approach for smaller angular widths; however, no significant reduction is observed at larger angular widths. This is investigated by looking at the correlation between the two units of the signal A and B. Positive correlation indicates presence of coherent oscillations due to the laser for example while negative correlation indicates the presence of beam pointing oscillation or SPR angle fluctuations. A week correlation shows the random uncorrelated noise. As seen in Fig. 5.14-(b), the correlation coefficient changes to the negative for last three data points. This negative correlation between A and B is an indicator of incoherent oscillations. As beam diameter gets close to the width of the detector at the higher angular width, the effect of beam position oscillations due to pointing instability or microphonics starts to dominate.

To sum up, this differential intensity approach is successful in removing the coherent intensity fluctuations; however, noise due to the presence of the incoherent fluctuations has not been removed. This noise is removed by using a reference channel and a quadratic detector [117]. This long-term drift is not considered a source of a significant instability considering the detection fast voltage signals.

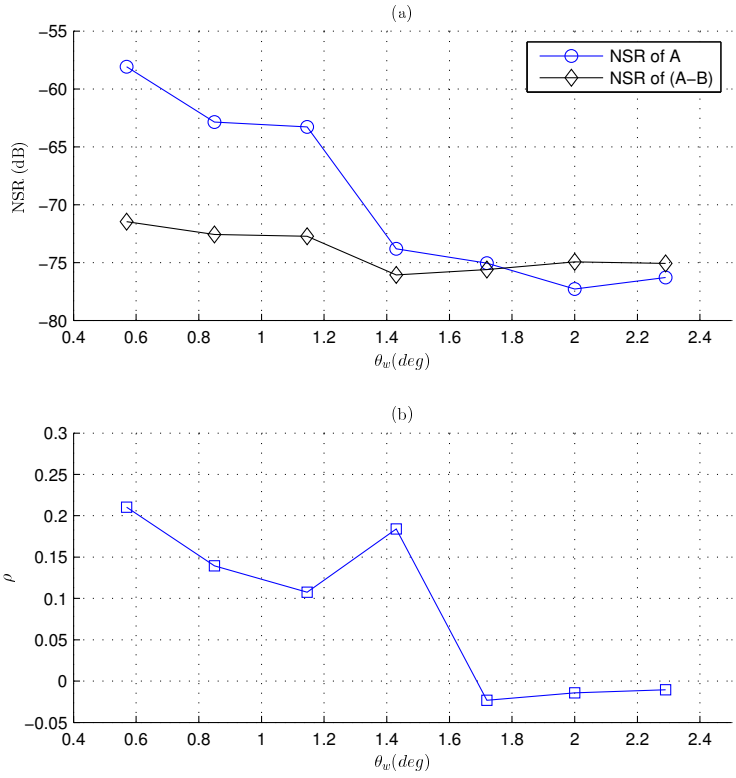


Figure 5.14: (a) The reduction of the noise-to-signal ratio NSR by the differential intensity approach by reducing the coherent noise, (b) the degree of coherence between A and B as represented by Pearson correlation coefficient.

Signal/Noise of $(A + B)$

The total intensity signal $(A + B)$ increases with the angular width as depicted in Fig. 5.15, while the noise does not show a noticeable dependence on the angular width since the noise of the total intensity is limited by the quantization noise. As described by Eq. 5.8 - $\frac{\sigma_{A-B}}{A+B}$, the noise of the total intensity can be ignored in the case of small refractive index changes once the output of the bi-cell detector is balanced. This assumption is suited to voltage applications since the applied voltage is expected to be equivalent to small refractive index change (in the range of 10^{-5} RIUs) as discussed in Sec. 3.7. On the other hand, the total intensity plays a critical role in the overall noise of the differential response as explained in detail later in this section.

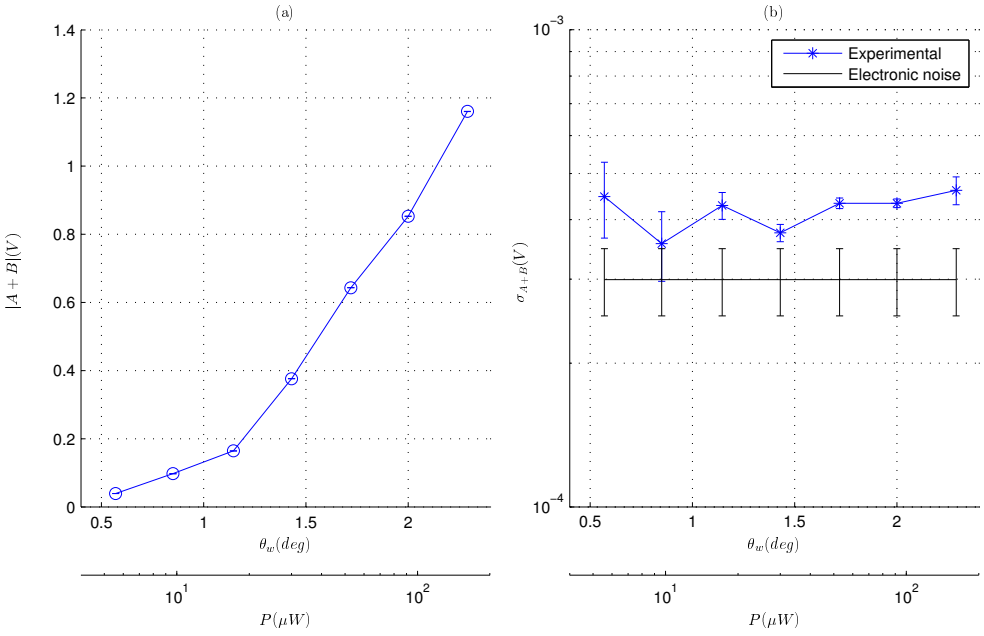


Figure 5.15: (a) The total intensity (A+B) as a function of the angular width and the power of the excitation beam, (b) the experimental noise of $(A+B)$ compared to the electronic noise of the summing circuit.

Noise of $(A-B)/(A+B)$

The overall noise of the differential response ($(A-B)/(A+B)$) is presented in Fig. 5.16. As noticed from this figure, the experimental noise (represented by $o-$) increases when the angular width of the excitation beam decreases. This is also compared with the approximated expression of Eq. 5.8 - $\frac{\sigma_{A-B}}{A+B}$, on page 127, (black line) demonstrating a good agreement.

The approximated expression presents the overall noise in terms of the differential intensity noise (i.e. noise related to the information signal) normalized by the total intensity. Since $A+B >> \sigma_{A+B}$, the angular width dependence of the overall noise is explained by its proportionality to the reciprocal of the total intensity. The latter is dependent on the input power at the detector and the shape of the SPR curve as predicted by

$$A+B = p\eta_o(a_0\theta_w + \frac{a_2\theta_w^3}{3} + ..) \tag{5.12}$$

where η_0 is the efficiency of the system, P is the input power and a_i are the coefficients of a polynomial function of the SPR curve.

This expression explains how noise is reduced by increasing the input power or making the SPR curve steeper (i.e., increasing a_2). A similar effect can be obtained by increasing the minimum reflectivity (a_0); however, this negatively impacts the responsivity as explained in Sec. 5.2.1.

The noise of the differential response is also considered for the scenario of a shot noise limited system, as seen in Fig. 5.16. The current system is limited by the quantization noise for angular width $\theta_w \leq 1$ deg; however, shot noise-limited performance would be possible by using a high resolution DAQ system (e.g., with a 24-bit DAQ quantization error of 0.12 μV would be achieved). In this case, noise would be reduced by almost two orders of magnitudes.

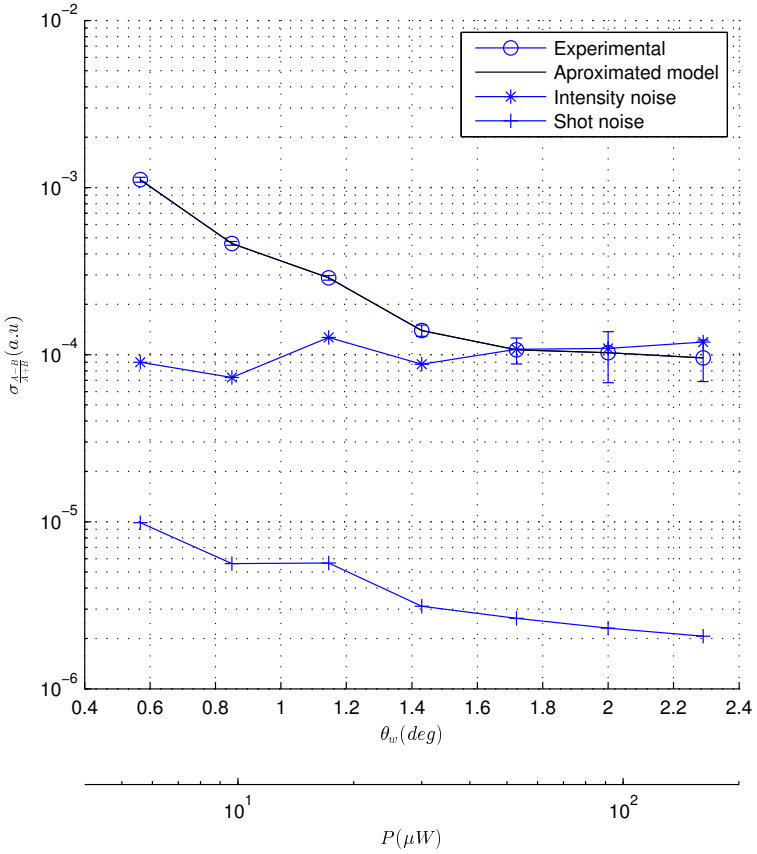


Figure 5.16: The experimental overall noise of the differential response ($o-$) is compared to the the approximation of $\frac{\sigma_{A-B}}{A+B}$ given by Eq. 5.8 on page 127 (the black solid line). The scenarios of the relative intensity ($*-$) or shot noise ($+-$) limited system are also presented

5.4 Sensitivity

The sensitivity of a sensing system is set by its responsivity to a measurand as well as its noise performance. Responsivity of the DI-SPR was predicted with accurate models and validated experimentally. From these expressions, responsivity can be calculated directly from the SPR curve with no need for refractive index stepping. Additionally, noise of the differential response is predicted from the differential intensity noise (σ_{A-B}) and the reciprocal of the total intensity ($A + B$).

Concluding from the investigation of the previous two factors, the system sensitivity is found by dividing the noise of the DI-SPR by the responsivity. As the DI-SPR noise is affected significantly by the total intensity ($A + B$), it is thus strongly dependent on the detected power. Similarly, the differential intensity noise is power-dependent as it is affected by the shot noise. The detected power is better expressed in terms of the laser power (P) and the power efficiency of the system (η_o). Extending this analysis, sensitivity (s) can be expressed in terms of input power (P), the power efficiency of the optical system (η_o), SPR curve parameters (a_0, a_2 and θ_w) and the differential intensity noise as

$$s = \frac{\sigma_{A-B}(3a_0 + a_2\theta_w^2)}{P\eta_o(3a_0a_2\theta_w^2 + a_2^2\theta_w^4)} \tag{5.13}$$

.

Fig. 5.17 presents the experimental sensitivity of the system as a function of the angular width. This experimental data is compared to the sensitivity that is predicted by Eq. 5.13, for an input power of 10 mW, experimental system efficiency of 6%, experimental SPR curve parameters $a_0 = 0.03, a_2 = 0.16$ and the experimental σ_{A-B}. The experimental sensitivity follows the trend of the expected sensitivity with discrepancy due to ignoring higher order coefficients in Eq. 5.12. It is also noted that better sensitivity is obtained at higher values of the angular width ($\theta_w \geq 1.6$). Current sensitivity of the system is 0.5 $\mu RIUs$. This sensitivity is achieved using

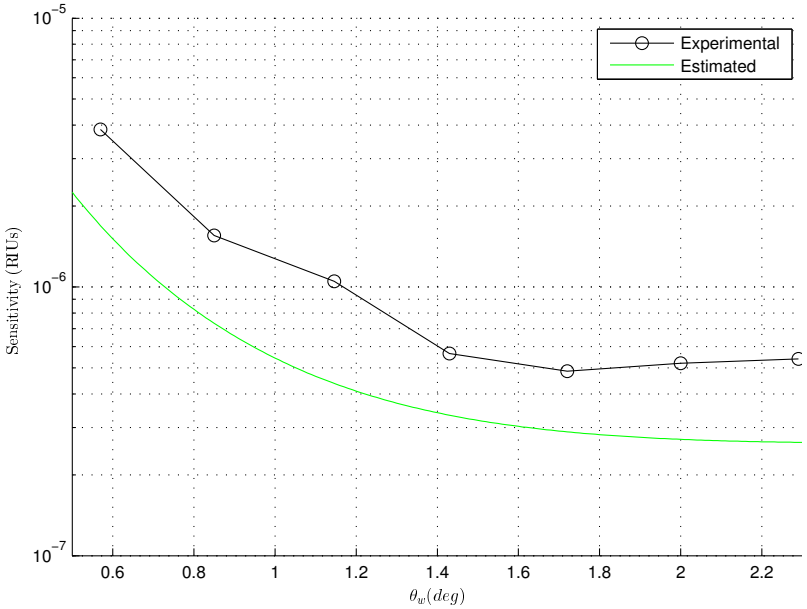


Figure 5.17: The experimental sensitivity of the system as a function of the angular width of the excitation beam compared to the analytical sensitivity (solid line).

samples with chromium adhesion layer that reduces the sensitivity of the system as discussed in Sec. 5.2.4.

The sensitivity decreases for smaller values of the angular width as the noise increases with the reciprocal of the total power. Due to this increase, the peak responsivity at small angular width (see Fig. 5.2) is not used to maximize sensitivity. Sensitivity is rather obtained at larger angular widths. However, by averaging the differential intensity $(A-B)$, a significant reduction in noise at small angular widths is noticed, as shown in Fig. 5.18-(b). This approach presents a mechanism for enhancing the sensitivity by harvesting the peak responsivity. In Fig. 5.18-(c), the sensitivity of the angular widths $(0.8 < \theta_w < 1.7°)$ is improved by more than twice if the number of averages are ≥ 100. As discussed earlier in Sec. 5.3.3 on page 141, incoherent noise from the pointing instability dominates for higher angular width as the beam diameter increases relative to the detector width.

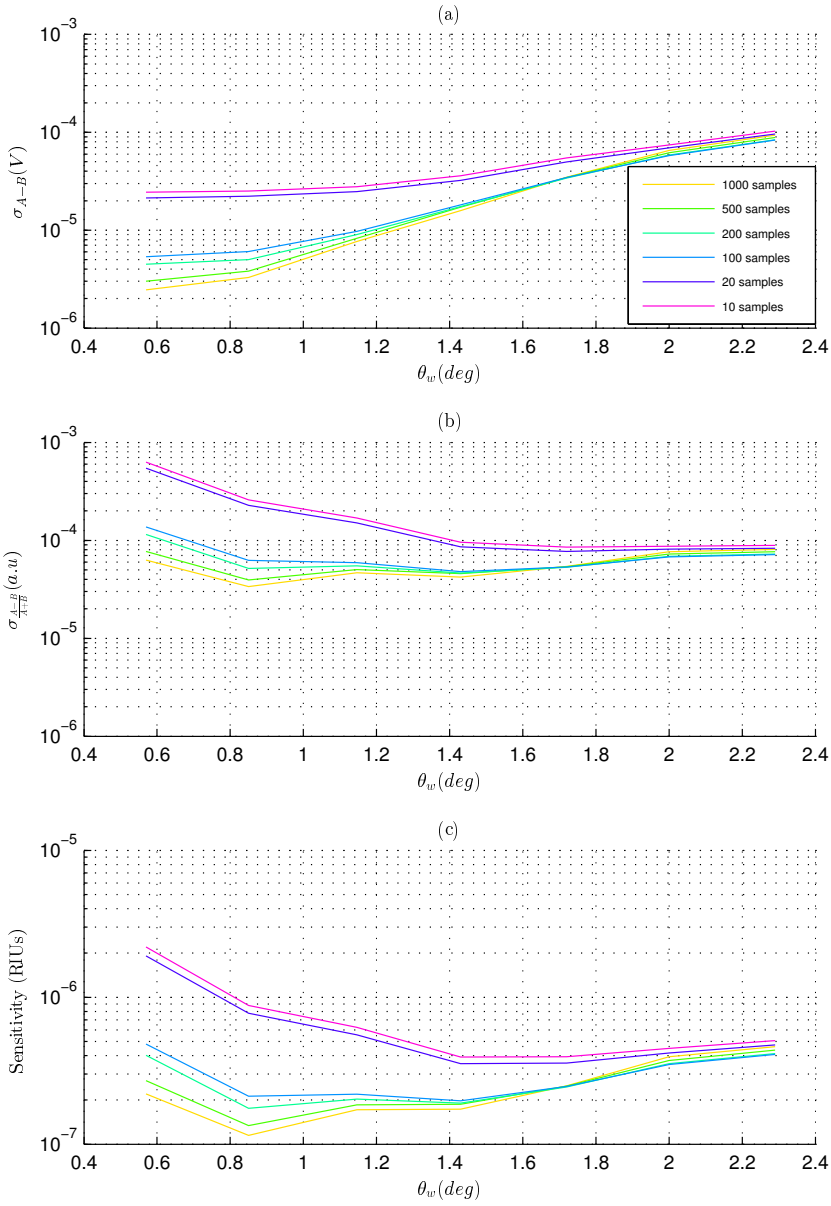


Figure 5.18: Improvement of the sensitivity by averaging the differential intensity signal $(A-B)$. The noise of $(A-B)$and the noise of DI-SPR signal $(A-B)/(A+B)$ are presented in (a) and (b), respectively.

5.5 The effect of the balance of the bi-cell detector on the sensitivity of the DI-SPR

This section aims to provide understanding on how responsivity and noise vary due to refractive index change. This discussion also suggests ways to prevent the sensitivity from dropping as the SPR curve shifts.

5.5.1 Refractive index stepping

The system, described in section Sec. 4.2.1, was used to test the effect of the change in the refractive index of the sample on the responsiivity and the noise of the DI-SPR. First, SPs were excited at the gold-water interface and the reflected beam was balanced on the bi-cell detector (i.e $A - B \rightarrow 0$). Second, the refractive index of the sample was changed by flowing different concentrations of sodium chloride solutions in steps of 0.1M till 0.9M and then returning back to the distilled water at the end. The flow handling system described in Sec. 4.2.1 was used to push these solutions in the flow under a flow rate of 250 ul/min. The bi-cell signals A-B and A+B were recorded simultaneously. These concentrations steps are equivalent to 1 mRIUs as obtained from the literature (see Sec. 3.2.5) and validated by the experiment in Sec. 4.2 on page 93. From the experiment, the signal, the noise and the responsivity have been calculated for each refractive index change. The signal and the noise were found by calculating the mean and the standard deviation of $(A - B)$, $(A + B)$ and $(A - B)/(A + B)$ using the steady part of these signals. The responsivity is found by calculating $(\Delta[(A - B)(A + B)]/\Delta\theta_0)$ for each refractive index change.

5.5.2 DI-SPR signal and noise when the detector is unbalanced

The signal and the noise of $(A-B)$, $(A+B)$ and $(A-B)/(A+B)$ are measured experimentally while stepping the refractive index of the sample, as described in Sec. 5.5.1. The response of these signals to different refractive index steps is presented in Fig. 5.19. It is noted that the differential intensity $(A-B)$ has a lower response compared to the DI-SPR signal $(A-B)/(A+B)$, but it offers a wider dynamic range (see Fig. 5.19-(a) and Fig. 5.19-(c)). Its dynamic range is limited by the finite width of the detector compared to the SPR dip. On the other hand, $(A-B)/(A+B)$ is limited by the effect of the asymmetry of the curve as noticed in the increased $(A+B)$ for higher refractive index change - see Fig. 5.19-(b).

The results in Fig. 5.19 have been analysed by calculating the signal (i.e., the mean) and the noise (i.e., the standard deviation) of the steady part of $(A-B)$, $(A+B)$ and $(A-B)/(A+B)$.

The following is observed from Fig. 5.20.

(a) $(A-B)$, $(A+B)$ and $(A-B)/(A+B)$ increase with refractive index of the sample. The linear range of $(A-B)/(A+B)$ is limited to ≈ 4 mRIUs.

(b) As observed in Fig. 5.20-(e), the response drops as a the refractive increases due to the increase of the asymmetry of the SPR curve. The asymmetry of the curve increases $\Delta(A+B)$ and thus reduces the overall response $(A-B)/(A+B)$. The drop of the responsivity limits the dynamic range of the system.

(c) In Fig. 5.20- (b) and (d), noise of $(A-B)$ increases significantly with the refractive index, whereas noise in $(A+B)$ does not demonstrate a significant increase. This is explained by the limiting source of noise in each. In the case of $(A-B)$, relative intensity noise is dominant, which increases with the asymmetry between A and B. As refractive index increases, SPR curve shifts

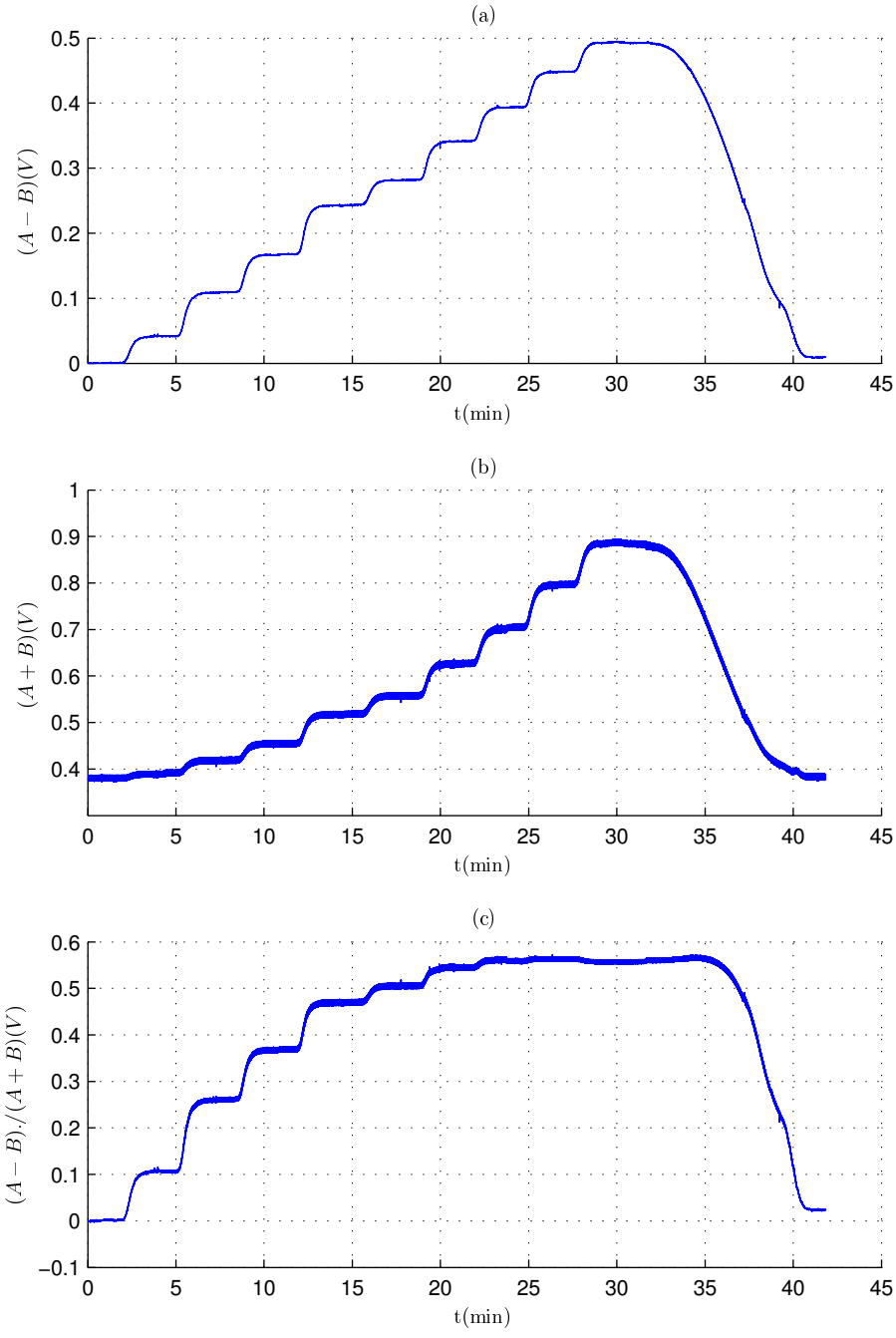


Figure 5.19: The response of the DI-SPR to change in refractive index. The difference, sum and the ratio are shown in (a), (b) and (c), respectively

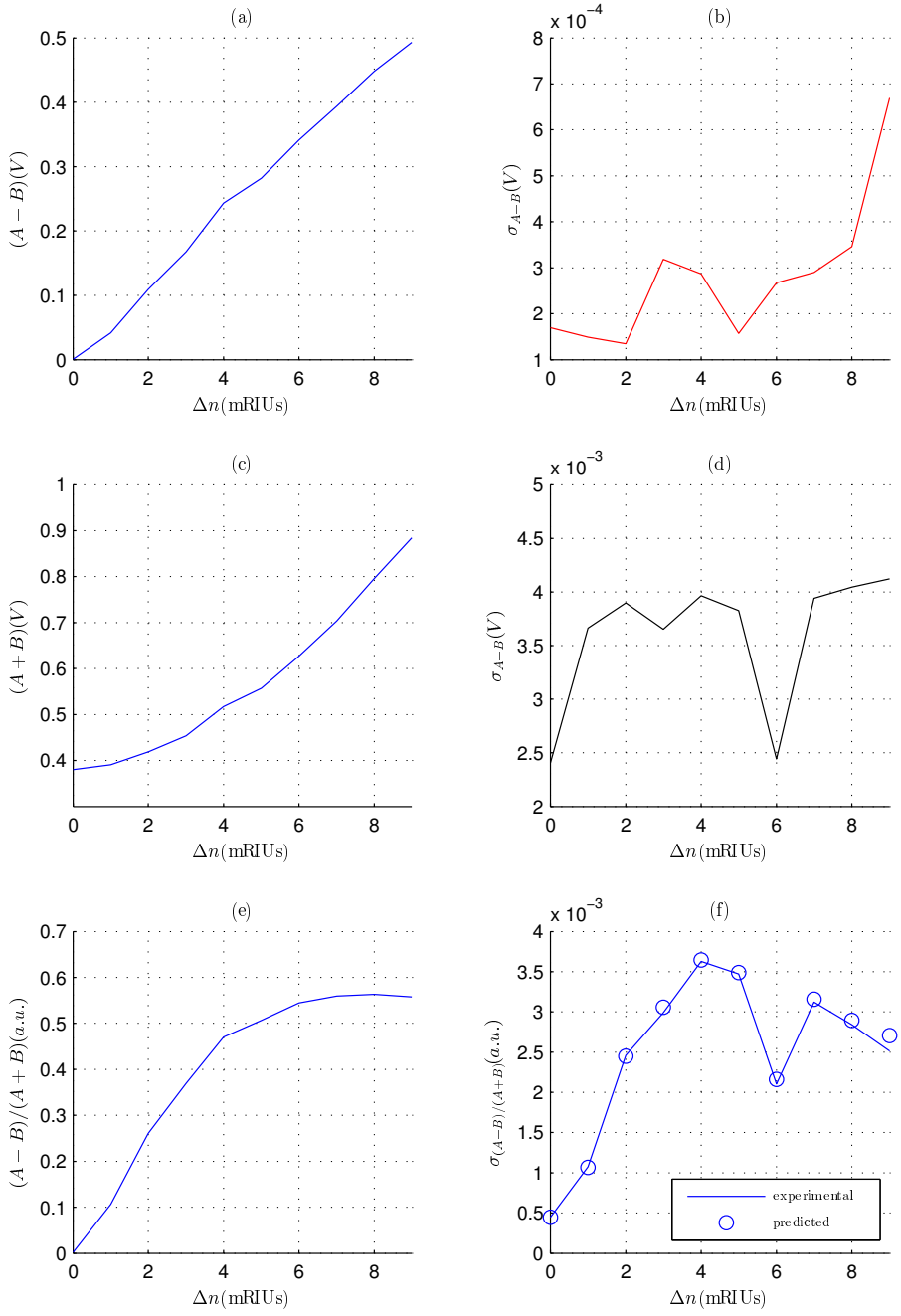


Figure 5.20: The signal and the noise of $(A-B)$, $(A+B)$ and $(A-B)/(A+B)$ for different steps of the refractive index change in (a, c, e) and (b, d, f), respectively. The change in refractive index unbalance the detector as the SPR curve shifts.

to the right and the asymmetry between A and B increases, which explains why the noise in $(A-B)$ rises. In the case of $(A+B)$, electronic noise is more dominant, and thus no significant dependence is noticed.

(d) Noise of $(A-B)/(A+B)$ demonstrates a dependence on the refractive index of the sample. This is due to the contribution of the signal and the noise of $(A-B)$ and $(A+B)$ to the total noise. This hypothesis is validated by calculating the total noise from Eq. 5.7 using signal and the noise of $(A-B)$, $(A+B)$ in Fig. 5.20.(a-d). A good agreement between the measured and the predicted noise is observed, thus supporting this hypothesis.

Using the experimental data in Fig. 5.20, the responsivity of the DI-SPR was calculated as a function of refractive index change and presented in Fig. 5.21. Maximum responsivity is not observed at the start due to the limitations of the mechanical scanning; it is rather reduced to $\approx 70\%$. To understand the impact of the responsivity change on the dynamic range, the effect is discussed in detail later in this section.

The responsivity in Fig. 5.20 is obtained for an angular width of 1.4 deg. From Sec. 5.2.2 - Fig. 5.2, the maximum responsivity of this angular width is 1.6 (deg^{-1}); however, the experimental value is 1 (deg^{-1}). This discrepancy is attributed to the variation in the properties of the sensing structure as explained in Sec. 5.2.4 on page 122.

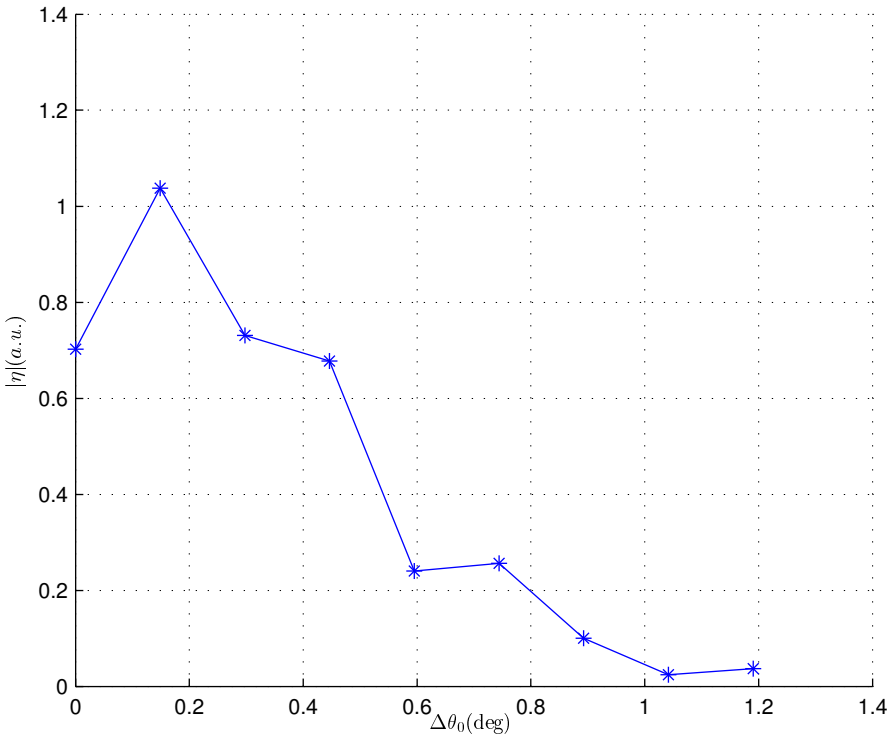


Figure 5.21: The experimental responsivity of the DI-SPR falls when the detector is unbalanced as the resonance position shifts due increasing the refractive index of the sample.

5.5.3 Responsivity and the dynamic range

SPR curves were produced using the Fresnel model (i.e., asymmetric curves) and also a second order approximation of the SPR curve, with the zero order a_0 included (i.e., symmetric curves). The zero order of the function has not been ignored, as Fig. 5.3-(d) and 5.4-(d) suggest a strong link between a_0 and the system response as discussed earlier in Sec. 5.2.1 and Sec. 5.2.2.

As seen from Fig. 5.22, both Fresnel and the second-order function show a drop of the responsivity when there is a change in the refractive index of the sample (expressed in corresponding resonance shift - $\Delta\theta_0$). However, the Fresnel model demonstrated the information regarding the asymmetry of the curve about the resonance angle. As seen in Fig. 5.22-(b), the maximum responsivity is shifted to the left and it is not located at the origin (i.e. the initial resonance angle) in contrast to the quadratic case -Fig. 5.22-(a). In the case of using a bi-cell detector, this shift is rectified by mechanical translation of the detector so that the condition $((A-B)/(A+B))$ equal to zero is satisfied. However, if a linear array detector [118] or a CCD [62] is used, the offset can be calculated and transformed to the corresponding number of pixels. This adjustment is critical to obtain a high voltage sensitivity by making sure that the modulation signal is at the static point of the highest responsivity.

This analysis also presents valuable information about the trade-off between the responsivity and the dynamic range. For any angular width, the dynamic range can be defined with reference to the drop of the responsivity from its maximum value. Therefore, as in Fig. 5.23, two definitions of the dynamic range can used; the change in the resonance position where the responsivity drops to 95% or 50% of the peak value. A similar trade-off is also observed by changing the value of the angular width. This is only observed for the case of angular width greater than 0.4 deg. In this range, the dynamic range increases as the angular width increases, but the responsivity is reduced; see Fig. 5.23-(a) and Fig. 5.23-(b). However, for angular

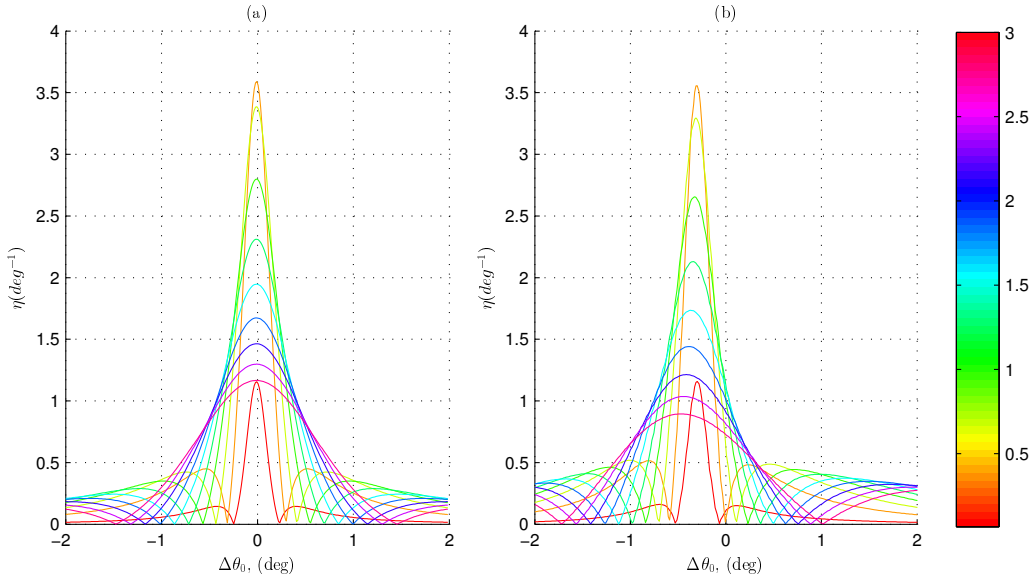


Figure 5.22: The drop in the responsivity as the SPR curve is shifted from its initial position, presenting a comparison between (a) the quadratic approximation of the resonance curve and (b) numerical simulation using a one dimensional, multi-layer model of the sensing device. The colormap refers to different angular widths.

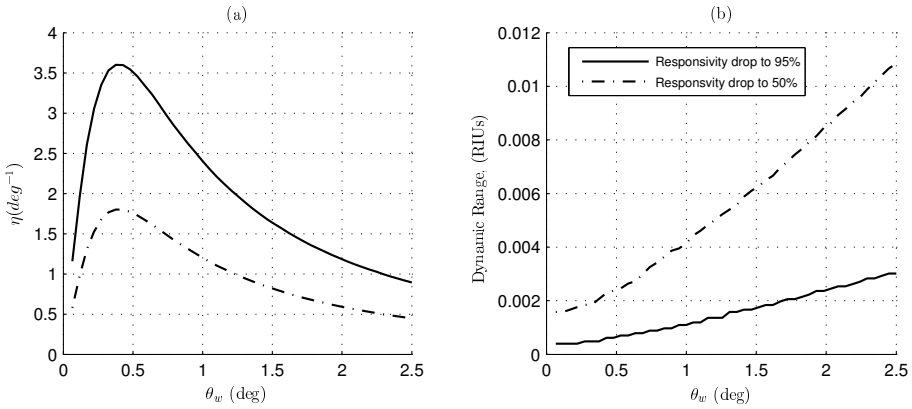


Figure 5.23: Theoretical demonstration of a tradeoff between (a) the responsivity and (b) the dynamic range as controlled by the selection of the angular widths of the excitation beam. The dynamic range can be defined in relation to the drop off in the responsivity: Responsivity drops to 95% of the peak (solid line) or 50% of the peak (dotted line).

widths smaller than 0.40 deg neither responsivity nor dynamic range is improved. This flexibility, which is offered by the angular width, is valuable for experimental design. To measure a low concentration sample, under the assumption of a flat noise-angular width curve, the design of the experiment favours the sensitivity over the dynamic range, and therefore a small value of the angular width is selected and vice versa.

The drop in responsivity, as SPR curve shifts (5.22 and Fig. 5.21), is due to the use of a fixed reference point for the differential detection (i.e., the initial resonance angle) while the resonance position shifts in response to the change in refractive index. So, increasing the dynamic range by moving the reference using a pixelated detector is suggested elsewhere [118]. This process is also useful for reducing the effect of the asymmetry on the DI-SPR noise. The advantage is essential in experiments in which wide dynamic range is needed, however, this is not the case when small voltage signals are considered.

5.6 Conclusions

(a) Critical analysis of the sensitivity of the DI-SPR is extremely important for detecting small voltage signals. Therefore, responsivity and noise sources in the system have been considered in detail.

(b) Starting with either experimental or theoretical SPR curve, the responsivity of the system can be obtained as a function of the angular width of the excitation beam. This analysis provides an efficient way to estimate the responsivity with no need for refractive index stepping. It is also valuable for calculating the voltage-equivalent refractive index figure (see Sec. 3.7) in chapter 6.

(c) Noise of the differential response is estimated using the statistical analysis of the ratio of two random variables. The formula is simplified for the case of measuring small angular shift. As this research is motivated by detecting small voltage signals, the simplified expression is well suited for predicting the noise of the system. This simplified expression predicts the noise with the knowledge of the differential intensity noise and the total intensity at the detector. These statistical approaches can be applied in general to sensing system that uses this normalised differential intensity.

(d) This chapter demonstrated how the differential intensity approach removes the intensity oscillations in the detected beam; this is very useful as this type of noise limits the performance of the intensity SPR systems as discussed in [47] and [119].

(e) By understanding the factors affecting the responsivity and the noise, the sensitivity of the system can be estimated as a function of the power at the detector, the curve parameters, and the differential intensity noise.

(f) An angular width of the excitation beam in the range of 1-1.4 deg is recommended when using the DI-SPR system described in this thesis. This range is

chosen to avoid the incoherent oscillations caused by beam pointing error.

(g) Current system's sensitivity is 0.5 μRIUs. In the context of voltage measurements, this is sufficient for measuring $\approx$ 1 mV (see - Sec. 3.7), as will be validated in Chapter 6. This sensitivity can be further improved as explained in chapter 7.

(h) Sensitivity is affected by the properties of the sensing structure as reflected in the coefficients of the SPR curve. Also, it drops as the refractive index of the sample increases. As the interest is directed at measuring small signals, this drop can be ignored. However, the maximum initial sensitivity should be assured by nulling the differential intensity signal $(A - B)$.

Chapter 6

Experimental Voltage Sensitivity of Surface Plasmon Resonance Systems

6.1 Introduction

This chapter presents the experimental investigation of SPR's response to perturbation of interfacial voltage. In these experiments, the electrochemical system was used to control the potential of the interface while the response is monitored using the DI-SPR system described in chapter 5. Sodium chloride was used as an electrolyte at the physiological concentration (0.15M NaCl) to model the ionic properties of the extracellular solution, unless otherwise specified.

First, the system's response to series of interfacial potentials is presented in Sec. 6.3.1 followed by experiments that are designed to confirm the underlying mechanism of the SPR response. Second, the experimental voltage-equivalent refractive index units, a generic figure for SPR response to voltage, is presented in Sec. 6.3.2 and compared to the theoretical results. This figure is important for experimental design

in applications where SPR systems are used to detect an externally applied voltage [73], in addition to the detection of the bioelectrical signals.

Third, two electrolytes (sodium chloride and lithium iodide) are compared regarding the system's response to the applied voltage (Sec. 6.3.4). The mass difference between the lithium and the chloride is high (a ratio of 18) in comparison to sodium and chloride (a ratio of 1.5). This experiment addressed whether the charge or the mass of the ion species controls the response of the SPR system.

Fourth, the detection limits of the system is discussed in Sec. 6.3.5 using two types of virtual bioelectrical signals: the neuronal action potential and the cardiac action potential. These experiments investigate the system's response to fast bioelectrical signals which are modelled by computer-generated virtual bioelectrical signals; they are generated from the fast potential mode of the potentiostat.

Finally, a preliminary experiment on the resolution of imaging localized potential is presented. The obtained information is used to compare voltage resolution to SPR resolution. These preliminary results describe the factors that influence the detection of the electrical signals on the lateral scale.

6.2 Materials and Methods

Two types of electrolytes were used in the experiments of this chapter, sodium chloride and lithium iodide. Sodium chloride and lithium iodide were obtained from Sigma Aldrich and different concentrations were prepared using deionized water as a solvent. For all experiments described in this chapter, the following procedure was followed.

The electrochemical cell and the tubings were cleaned following the manufacturers cleaning protocol. The electrochemical cell was mounted on the prism with the sensor's chip in-between. A deionized water (dH2O) was flowed, initially, in the

channel and the formation of the SPR curve was monitored on the pixelated camera. The produced SPR curve was checked by capturing the reflected light for a range of incident angles using the pixelated camera.

The channel was filled with the electrolyte of interest while the change in refractive index, from the refractive index of dH2O, was monitored for calibration purposes.

As discussed in chapter 5, the performance of the DI-SPR depends on the selection of the angular width of the excitation beam. An angular width of 1 deg was selected for the experiments in this chapter as a trade-off between the sensitivity and stability of the system. By using this angular setting, the coherent noise in the system is cancelled. For angular width greater than 1.4, the beam pointing instability starts to dominate. As described in chapter 5- Fig. 5.18 on page 148, the signal-to-noise ratio is improved by averaging at this setting.

Another important parameter is the location of the detector relative to the reflected beam. To ensure that the system was set at the operating point of the maximum sensitivity (see Sec. 5.5 - on page 149), the bi-cell detector was mechanically adjusted until the differential intensity becomes zero. This step is repeated whenever the type or the concentration of the electrolyte is changed. This is essential since when the electrolyte or its concentration are changed, the refractive index of the samples changes reducing the responsivity of the system, as discussed in Sec. 5.5.

For experiments where two types of electrolytes were compared or a series of concentrations were used, the same sensor chip had been used throughout the experiment to eliminate the effect of sample's variations on the responsivity as presented in Sec. 5.2.4.

The potentiostat was warmed up for half an hour before the experiment and then connected to the three-electrode cell that was used in the experiment. The Voltage waveform of interest was applied and the response was measured using both the

electrochemical and the SPR systems.

6.3 Results and Discussions

6.3.1 Voltage-dependant voltage responsivity

This section is concerned with the experimental study of the system's response to series of voltages. The voltage waveform, shown in Fig. 6.1-(a), was applied at the electrode-electrolyte interface using the electrochemical system described in Sec. 4.2.3 on page 105. The response of the DI-SPR to this waveform is presented in Fig. 6.1-(b).

The response of the system to the applied voltage in the range of (-200 mV and +200 mV) is presented in Fig. 6.2. Since the system features a time-varying response, the response presented in Fig. 6.2 is calculated after 9 seconds from the start of each voltage step. The system demonstrated a noticeable nonlinear response to the applied voltage regardless of its polarity. This behaviour indicates that the applied electrical energy is transduced through the nonlinear capacitance of the interface. As described earlier in Sec. 3.3.1 - page 69, a simplified approach considers the interfacial capacitance to be proportional to the square of the applied voltage; $C = f(V^2)$. As SPR response is proportional to the charge accumulation (see- Sec. 4.4- page 110) ($\Delta\frac{A-B}{A+B} \propto CV$), the SPR response shows a cubic-function trend ($\Delta\frac{A-B}{A+B} \propto f(V^3)$).

For each of the applied voltages, the system does not respond instantaneously as one would expect as it is governed by charging the double-layer capacitor which features a remarkably high capacitance in the order of $1F/m^2$. Moreover, the system is expected to feature a nonlinear response since the capacitor is voltage dependent. The response time is discussed in Sec. 6.3.3 (page 170).

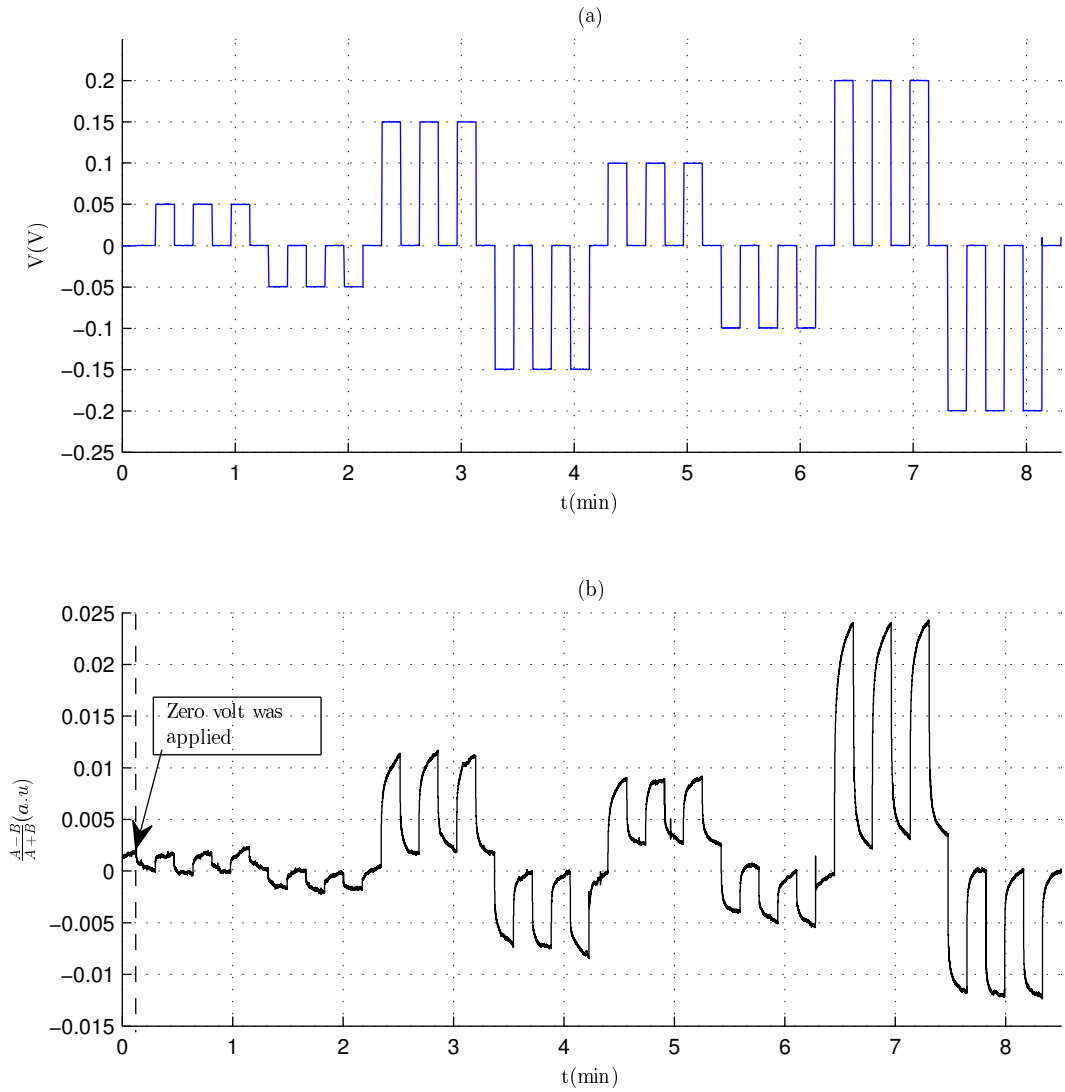


Figure 6.1: (a) The input voltage waveform. Voltage is applied versus an Ag/AgCl reference electrode at a rate of 10V/s (b) The response of the DI-SPR system to the input waveform for 0.15M NaCl.

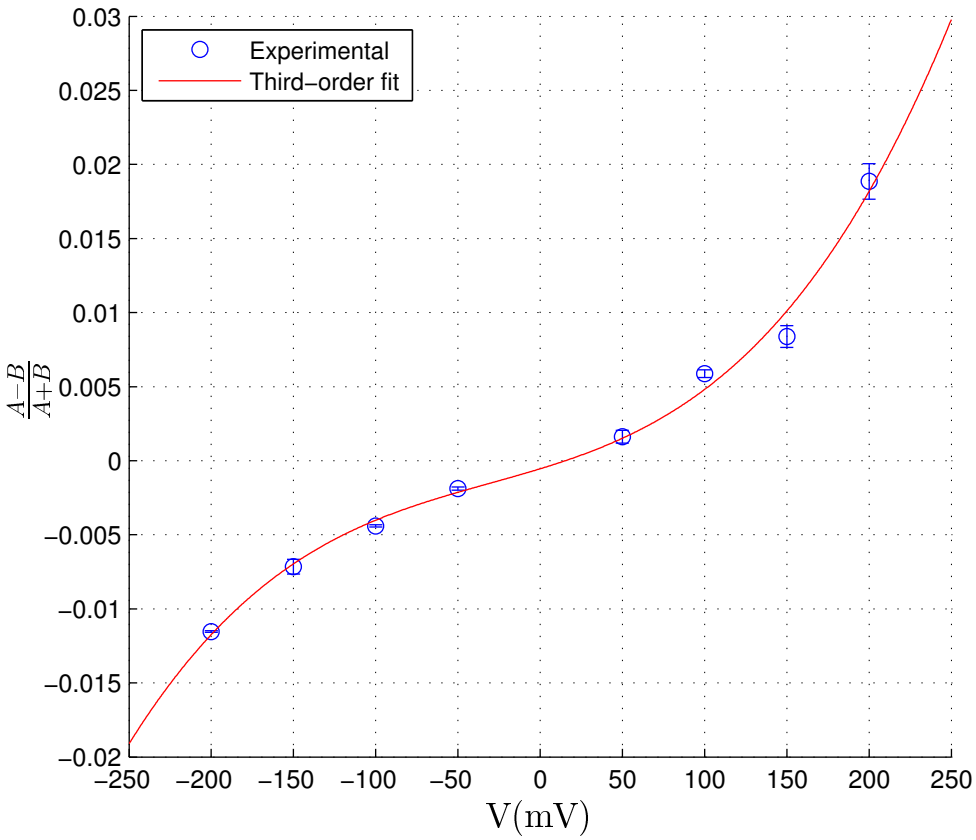


Figure 6.2: The response of the DI-SPR system for a series of applied voltages in the range of (-200 $\rightarrow$ +200) mV; average of three cycles.

6.3.2 Voltage-equivalent refractive index units

In chapter 3, the concept of the voltage equivalent RIUs is introduced. In this section it is calculated experimentally and compared to the results of the theoretical approach. The calculation of this figure from the experimental response to the applied voltage is discussed below.

Starting from the DI-SPR response to applied voltages, which is presented in Fig. 6.2, the equivalent resonance shift ($\Delta\theta_0$) can be obtained by using the calibration expression of the DI-SPR responsivity (Eq. 5.4 - page 117). The obtained resonance shift can be mapped to the equivalent refractive index change.

The DI-SPR's responsivity, as described in chapter 5, can be obtained directly from the experimental SPR curve by fitting to a second order polynomial function. From the experimental SPR curve in Fig. 6.3-(a), the polynomial coefficients are $a_2 = 0.18$ and $a_0 = 0.16$. Using these coefficients, responsivity is calculated as a function of the angular widths using Eq. 5.4 as presented in Fig. 6.3-(b).

For the operating point of this experiment ($\theta_w = 1deg$), the DI-SPR responsivity is given by $\Delta\frac{A-B}{A+B} = 0.7\Delta\theta_0$. This is used to produce the resonance shift that corresponds to the applied voltage as presented in Fig. 6.4. As discussed in Sec. 3.4 on 78, $\frac{\Delta\theta_0}{\Delta n} = 148.8deg/RIUs$. Using this conversion factor, Fig. 6.4 is mapped to the voltage-equivalent refractive index change. Fig. 6.5 presents the experimental voltage-equivalent refractive index changes compared to the theoretical estimates from Sec. 3.4.

There is a discrepancy between the experimental and the theoretical results. The theoretical results assume an ideal case of using flat monocrystalline gold surfaces; as discussed in Pajkossy [120], the non-ideal surface structure results in deviation from the expected capacitive behaviour. As the project is directed at the characterization of the voltage sensitivity of surfaces that are commonly used in SPR measurements, the practical response is thus obtained for rough and polycrystalline

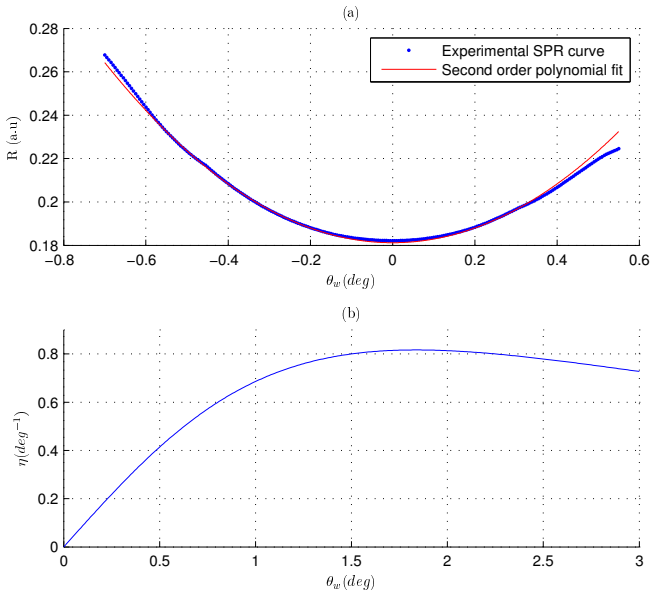


Figure 6.3: (a) Experimental SPR curve fitted to a second order polynomial and (b) experimental responsivity of the DI-SPR.

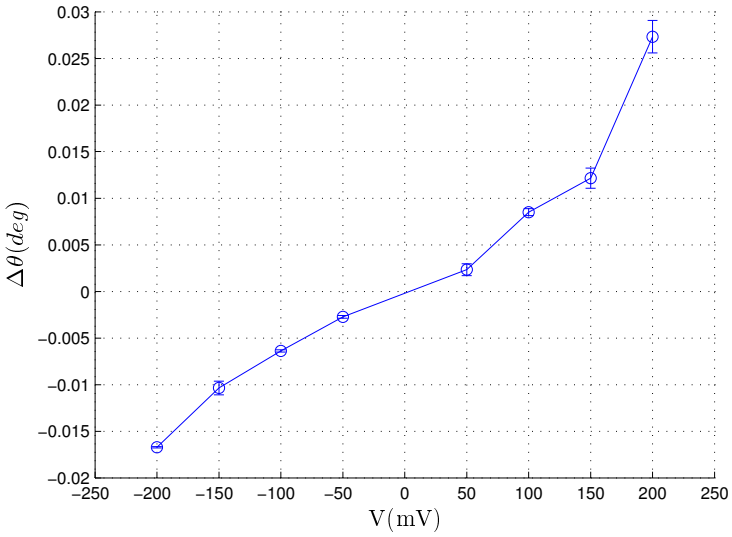


Figure 6.4: Experimental resonance shifts ($\Delta\theta_0$) for a series of applied voltages.

surfaces [121, 28, 84]. Modelling the voltage sensitivity of the polycrystalline surface is not straightforward, it is also not possible with the 1D model adopted in this work. To model the effect of the roughness, the spatial profile of the capacitive

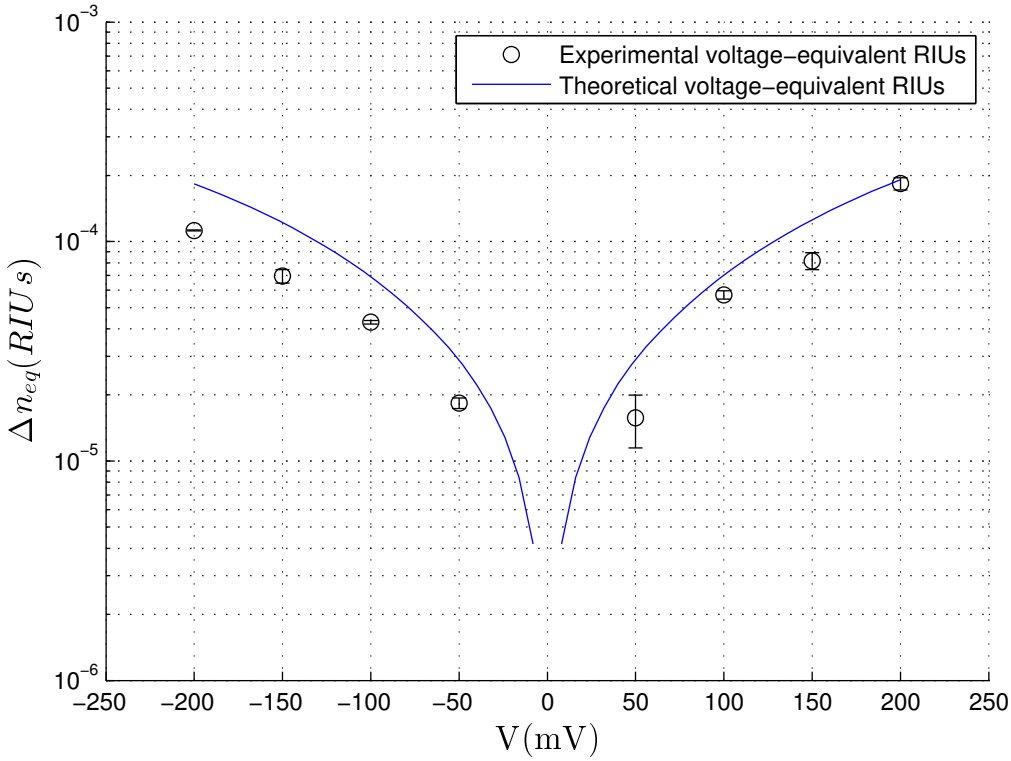


Figure 6.5: Experimental voltage-equivalent refractive index units compared to the theoretical figure.

properties of the interface has to be modelled [122] with a lateral resolution that is sufficient enough for the periodicity of the roughness. The contribution of the surface roughness and structure to the capacitive properties of the surface is beyond the scope of this work and will be discussed in detail in Sec. 7.2. Other possible factors for the observed discrepancy is the response time of the capacitance to the applied voltage. As the capacitance is voltage-dependent, its change following the applied voltage might be delayed since the equilibrium of charge distribution needs to be reached.

The DI-SPR noise is calculated, for a time scale of 1 second, which is 5 $\times 10^{-5}$. Since the DI-SPR response is 5 $\times 10^{-3}$ for 100 mV, the detection limit is therefore expected to be 1mV. This maps to 3.7 $\times 10^{-7}$ RIUs for these experimental conditions. This number is cross-checked with sensitivity of the DI-SPR at $\theta_w = 1deg$, as shown in Fig. 6.6. The sensitivity of the DI-SPR system is obtained from the experimental SPR curve using Eq. 5.13 on page 146.

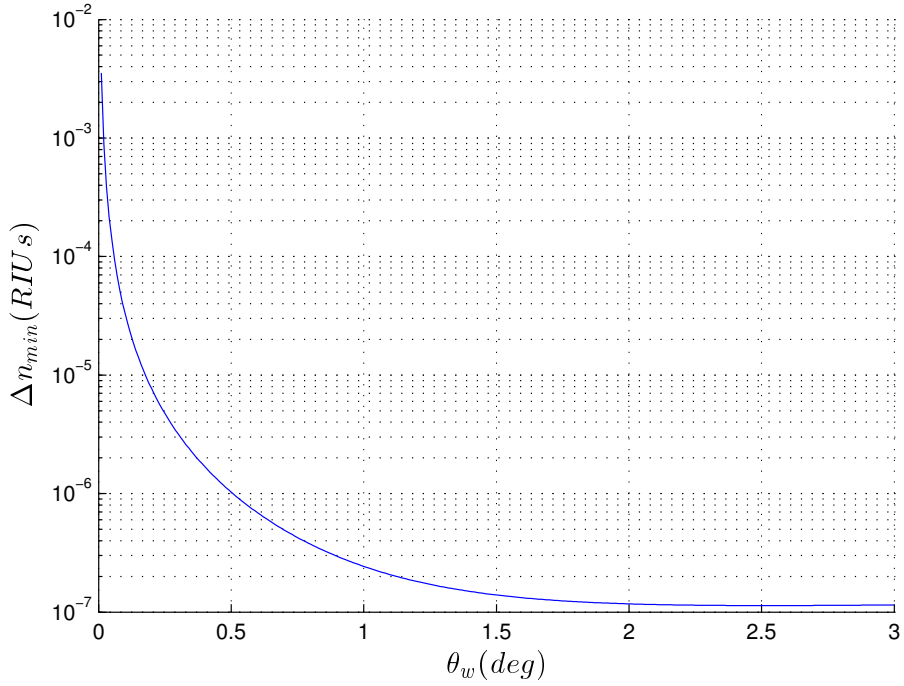


Figure 6.6: Experiment-specific refractive index sensitivity of the DI-SPR as a function of the angular width of the excitation beam calculated using Eq. 5.13 for an input power of 10 mW, efficiency of 6% and SPR curve coefficients $a_0 = 0.18$ and $a_2 = 0.16$.

.

6.3.3 Response time of the gold-electrolyte interface to applied voltage

When voltage is applied to the electrode-electrolyte interface, surface charge density is altered charging the interfacial double-layer capacitor. The accumulation of charges in the Debye layer is not instantaneous compared to the applied voltage. In order to quantify the dynamics of this process, the SPR response to a potential change from 0 to +100 mV at a scan rate of 10V/s is investigated. The applied potential reaches 100mV after 0.01s featuring a ramp function for $t \leq 0.01$ and a direct potential for $t > 0.01s$. Fig. 6.7 shows the response of the SPR sensor for $t > 0.01s$. The effect of the ramp function could be ignored on the basis that its

time scale is small compared to the time scale of the overall response.

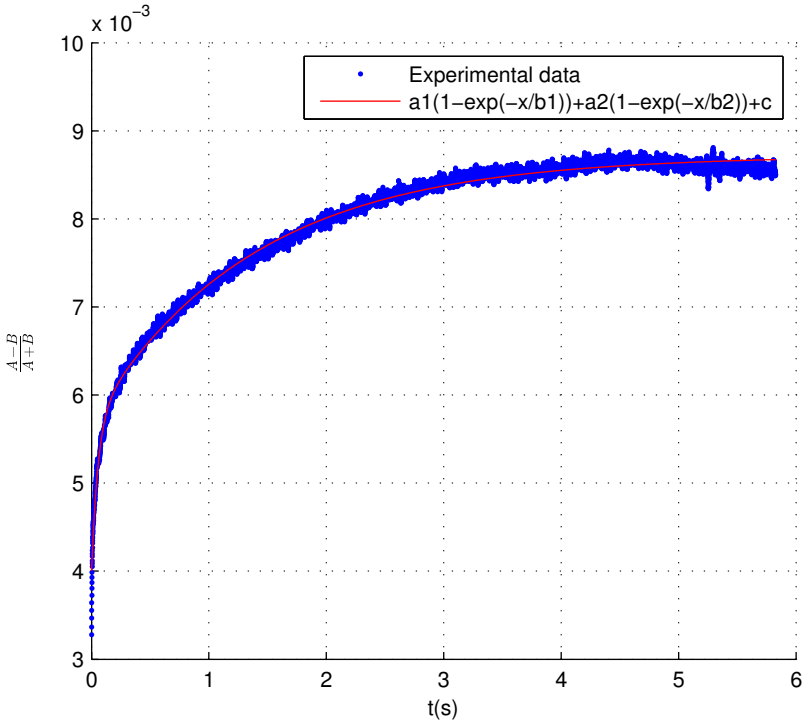


Figure 6.7: Dynamic response of the SPR system to the applied voltage fitted to a second-order exponential function.

It is noticed from Fig. 6.7 that the response time of the sensor does not fit to a first order exponential function where time constant is $\tau = RC$. It rather fits to the second order exponential function $y(t)$ below (goodness of fit: $R^2 = 0.993$ and root-mean-square error $(RMSE) = 6.8 \times 10^{-5}$)

$$y(t) = a_1(1 - e^{-t/\tau_1}) + a_2(1 - e^{-t/\tau_2}) + c \tag{6.1}$$

where $\tau_1 = 37ms$, $\tau_2 = 1.35s$ are time constants and $a_1 = 2.4{\times}10^{-3}$ and $a_2 = 3{\times}10^{-3}$ are steady state amplitudes and c=0.0033.

The graph in Fig. 6.7 can be visualised as two processes with different dynamics: a fast response with a time constant of 37 ms and a slow response with a time

constant of 1.36s. The time constants and the occurrences of these processes can be visualised better by taking the derivative of Eq. 6.1:

$$y'(t) = \frac{a_1}{\tau_1} e^{-t/\tau_1} + \frac{a_2}{\tau_2} e^{-t/\tau_2} \tag{6.2}$$

with the same definitions of the coefficients of Eq. 6.1. Plotting the natural logarithm of $y'(t)$ versus time compared to the natural logarithm of the first and the second term shows the overall response compared to the fast and slow responses. The dynamics observed in Fig. 6.8 is consistent with the reported response of charging nonlinear capacitors [123]. As the diffuse layer capacitor is voltage dependent, the behaviour of the system follows nonlinear dynamics with a time constant that also depends on the applied voltage. The nonlinear capacitance is reported to extend the charging time resulting in the slow response [124]. However, in this discussion, the response is simplified by fitting to the second order function presented by Eq. 6.1. Therefore, the time-varying response is characterised by two time constants τ_1 and τ_2 being used for the ranges $t \leq 0.2$ and $t > 0.2$ respectively.

The first term of the fitted function in Eq. 6.1 can be used to predict the response of the SPR system to pulses with short durations (≤ 0.2 or $5\tau_1$). The response of the system, as a percentage of the steady state $a_1 = 2.4 \times 10^{-3}$, is presented in Fig. 6.9. As can be found from this graph, the response drops to 10% if the duration was 0.1τ. This analysis can be used to predict the time dependent response of the system to the action potential of neurons since the pulse last only for 2- 5 ms.

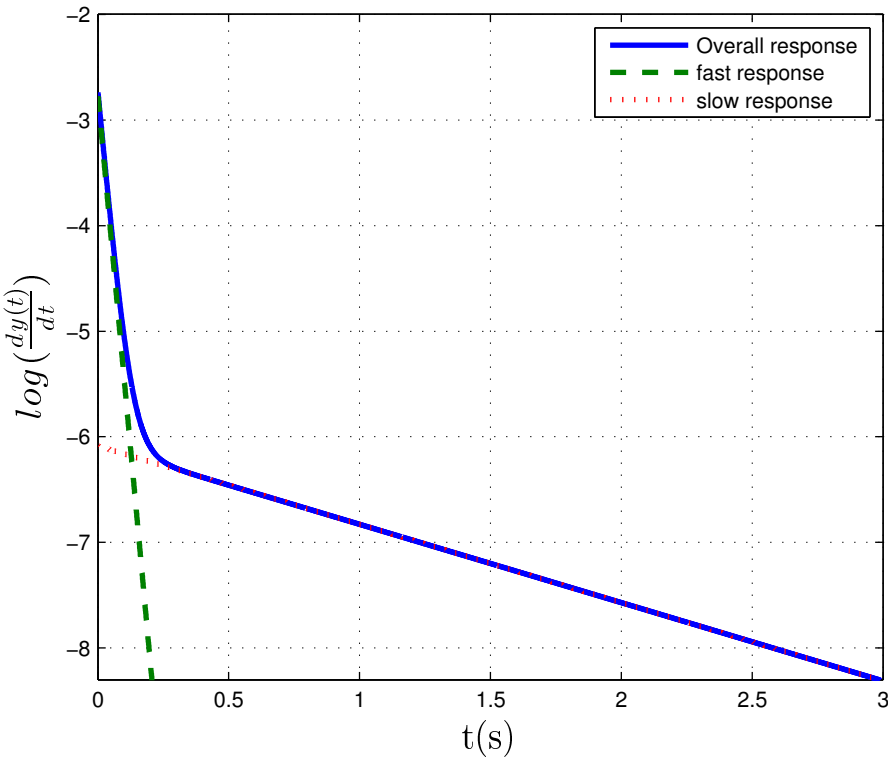


Figure 6.8: A comparison between time constants and onset times of the fast and the slow responses of the system to the applied voltage which is presented on a semi-log scale. Note: log refers to the natural logarithm.)

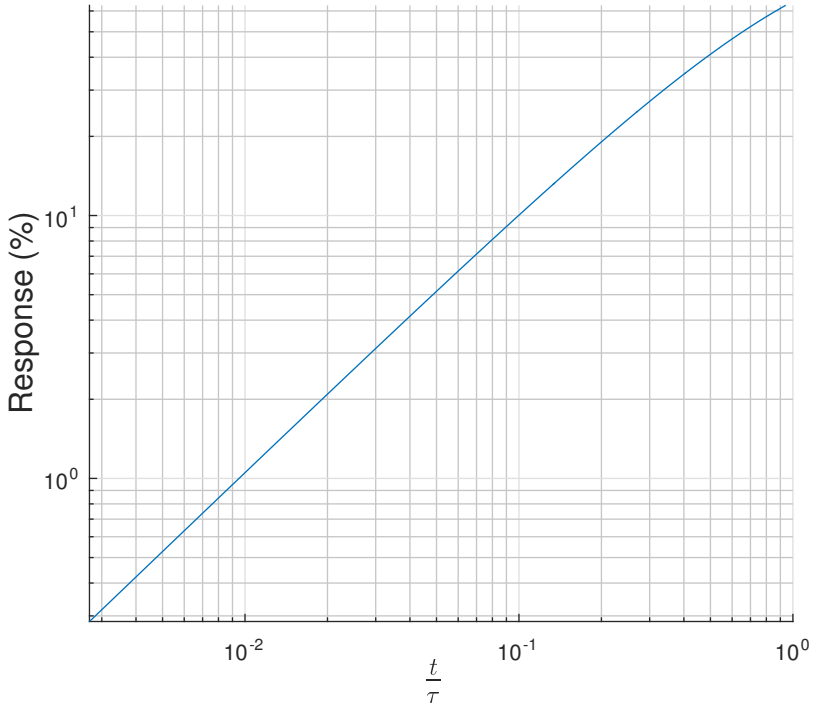


Figure 6.9: Expected response of the system for pulses with duration less than $5\tau = 0.2s$ presented as a function of the (t/τ).

6.3.4 Charge mass at the interface

This experiment aimed to study if the obtained SPR response is dominated by the accumulation of charges at the interface. The response of 0.1M sodium chloride solution is compared to the response of the same concentration of lithium iodide solution. These concentrations are selected to fall within the dynamic range of the system; so the system could be easily adjusted when switching between the two electrolytes.

Both electrolytes are symmetric; anions and cations are monovalent. The mass of the lithium is 18 times smaller than the mass of the iodide in contrast to mass difference between sodium and chloride (Table 6.1). Given this mass contrast, LiI is expected to feature a higher response in the positive cycle compared to NaCl if the mass of the ion dominates the SPR response in comparison to the charge density effect. For this reason, LiI electrolyte is suitable to perform a control experiment to validate the dominance and the localization of the charge effect.

Table 6.1: A comparison between the atomic mass numbers of the ions of the sodium chloride and the lithium iodide.

Element	Atomic mass (amu)
Li	7.0
I	127.0
Na	23.0
Cl	35.5

The response of the system to the two electrolytes is presented in Fig. 6.10. From this graph, it is noticed that the mass contrast between anions of the two electrolytes is not reflected in the response to the applied voltage. This indicates that charge density at the interface dominates mass contrast.

These results are interpreted by looking at the scale of the Debye layer (Sec. 3.2.4)

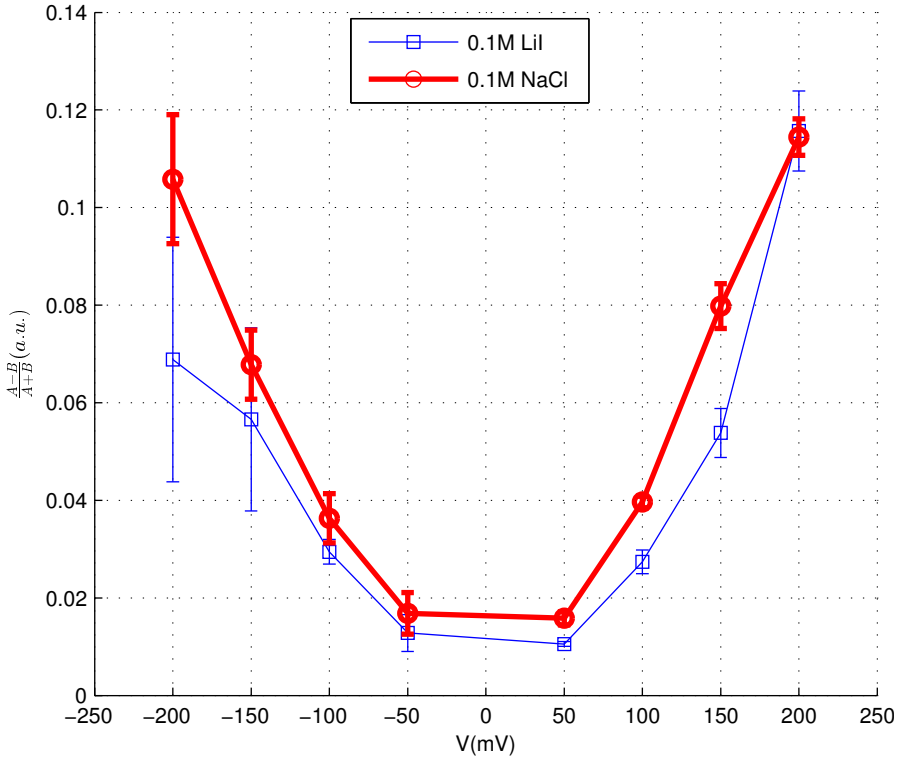


Figure 6.10: A comparison between the response of the SPR system to two types of electrolytes: 0.1M LiI and 0.1M NaCl.

compared to the evanescent penetration depth (Sec. 2.1.1), in Fig. 6.11. The Debye length (the voltage-sensitive layer) is approximately 100 times smaller compared to the evanescent depth (the plasmonic sensitive layer).

The absence of the mass effect indicates that the replacement of ions with their counterions, upon change of voltage polarity, occurs at a very confined scale within the evanescent field. Therefore, the charging current does not alter the neutrality of the bulk layers of the electrolyte or the average refractive index of the evanescent layer. Whereas, from the charge density point of view, there is a significant change in the electrostatic properties of the Debye layer due to the change of the polarity of the electrode. In practice, this observation does not impact the detection of the bioelectrical signals, as there are ionic currents that perturb charge density at both cell membrane and the electrode-electrolyte interface.

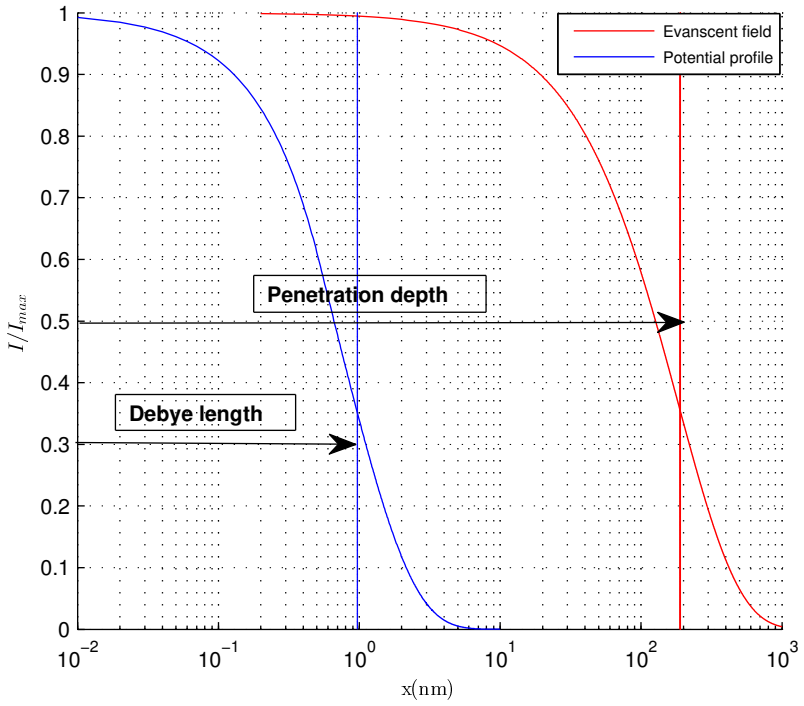


Figure 6.11: A comparison between the length of the Debye layer and the evanescent field depth.

6.3.5 SPR Sensitivity to fast voltage signals

One of the key questions of this thesis is whether SPR can respond to fast bioelectrical signals. This section presents the experimental results of the response of the SPR to fast potential modulations. For this purpose, two virtual bioelectrical signals are computer-generated and applied to the electrode-electrolyte interface. Fig. 6.12-(a) shows a sequence of virtual action potential pulses (duration of 5ms and change from -60mV to +60mV); the corresponding charging and discharging current is shown in Fig. 6.12-(b)) and the real time SPR response is shown in Fig. 6.12-(c)). Fig. 6.12-(d),(e) and (f)) shows the three signals on a magnified scale.

The response of the DI-SPR to 100 mV signal at 1 kHz is reduced by an order of magnitude compared to the response to slow voltage signals discussed in Sec. 6.3.1; 100 mV maps to 0.6 $\times 10^{-3}$ instead of 5 $\times 10^{-3}$- see Fig. 6.2 and Fig. 6.12-(b)) for comparison. The detection limit is expected to be shifted to 10 mV instead of 1mV described earlier. Similar drop of responsivity at higher frequency was reported by Huang et al [25]. In that study, the response of gold ultra-thin films to voltage perturbation was investigated and a detection limit of 100 mV at 20 Hz was reported. Therefore, the study [25] used lock-in detection to increase the sensitivity of the system at higher frequency. The performance reported in this thesis is superior in terms of signal-to-noise ratio; a detection limit of 10 mV at 1 kHz is achieved. A better performance would be achieved by using lock-in detection at voltage modulation.

The observed drop of the system response to pulses with duration of 5ms is attributed to the extended response time of the system that is discussed previouly in Sec. 6.3.3. Moreover, the frequency dispersion of the double-layer capacitance at the electrode-electrolyte interface is also reported [125, 126]. The capacitance of the interface decreases with frequency, unless atomically flat thin films or electrodes are used [125]. This behaviour is also observed in SPR-based voltage sensing

[28, 25]. The system behaviour, similar to the theoretical capacitance of Stern-Gouy-Chapman, is restored by thermal annealing gold thin films as recommended by Kerner et al [127, 125].

The detection of the bioelectrical signals is limited by the energy transfer between the capacitance of the cell membrane and the capacitance of the electrode-electrolyte interface; the maximum occurs when the two matches (see-Eq. 3.1). In practice, the interface has $\approx 0.5\ F/m^2$ (For 0.1M NaCl, for mV range - see Fig. 3.15) whereas the cell membrane has a typical capacitance of $0.01\ F/m^2$ [6]. Therefore, only 2% of 100 mV signal is expected to be the voltage across the electrode-electrolyte interface. Therefore, in order to detect these signal, at least 2mV sensitivity is needed.

In order to examine the response to different voltage amplitudes, a pulse train with a peak-to-peak voltage spikes, in the range of 100mV to 10mV, is applied to electrode electrolyte interface (see-Fig. 6.13-(a))). The cardiac action potential (duration of 200 ms) is selected since there is a possibility for averaging 100 data points to improve the detection limit to a 1mV as will be discussed below. Fig. 6.13-(b) show the response to the applied waveform. The response of the SPR to 10 mV is shown on a magnified scale in Fig. 6.13-(c) (d)).

One of the possible scenarios for improvement is averaging 100 data points to increase the signal to noise ratio by 10; so the detection limit is returned to 1 mV which is enough for the measuring the signal of interest. This approach could be used to detect the action potential of cardiac cells in real-time since the duration is 200ms; however, it can not be used for the action potential of neurons sine the duration is 2-5 ms. Averaging in this case could be done by recording 100 spikes and average them to enhance the signal to noise ratio by 10, but with sacrifice of real time measurements. Another possible solution is to design an SPR system with at least 3×10^{-8} RIUs, which maps to 1 mV, to enable real-time detection. More signal enhancement mechanisms are described in the future work in chapter 7

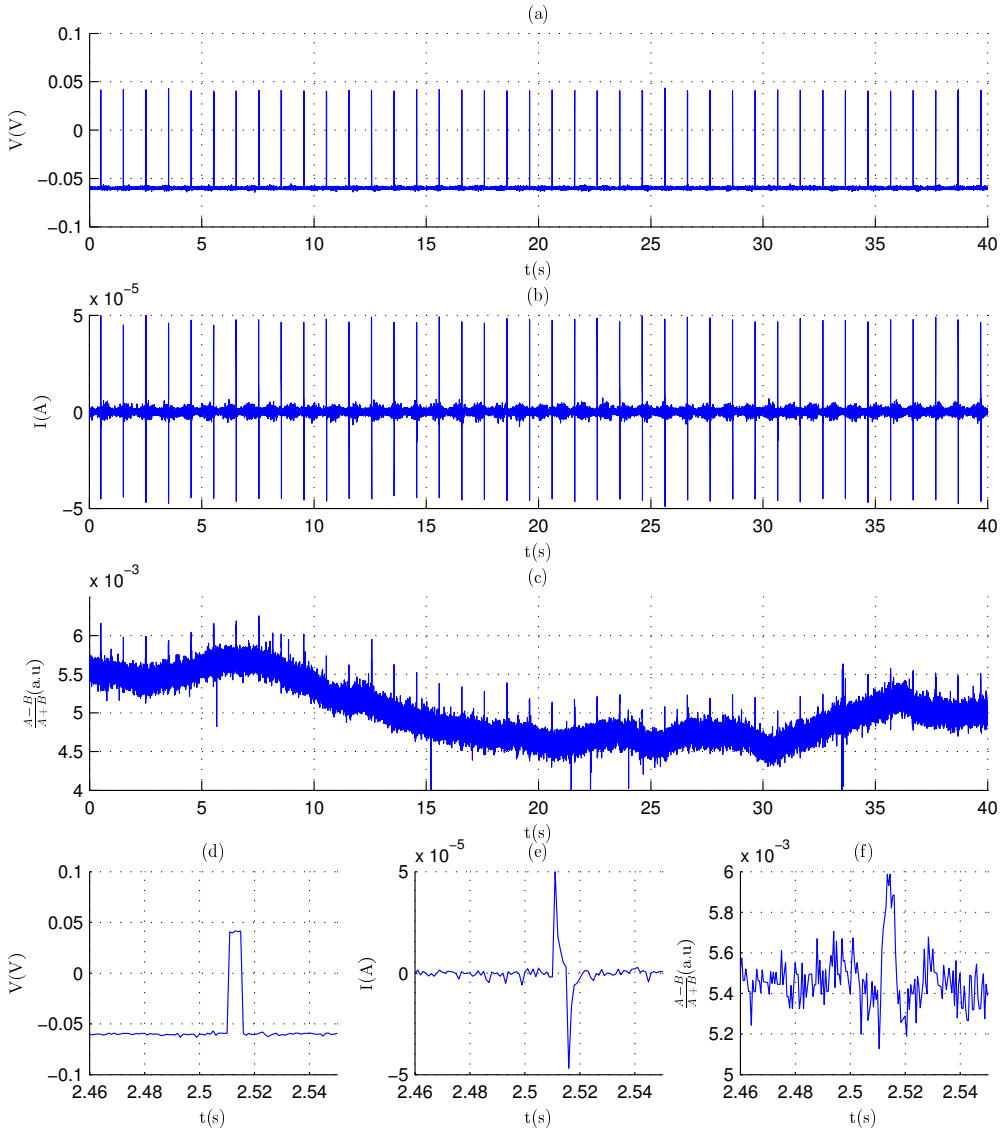


Figure 6.12: The DI-SPR response to the computer-simulated action potential. In (a) the applied 100mV voltage signals and corresponding charging and discharging currents are shown in (b). The simultaneous SPR response is presented in (c). (d-f) shows the a window of the three signals on a magnified scale

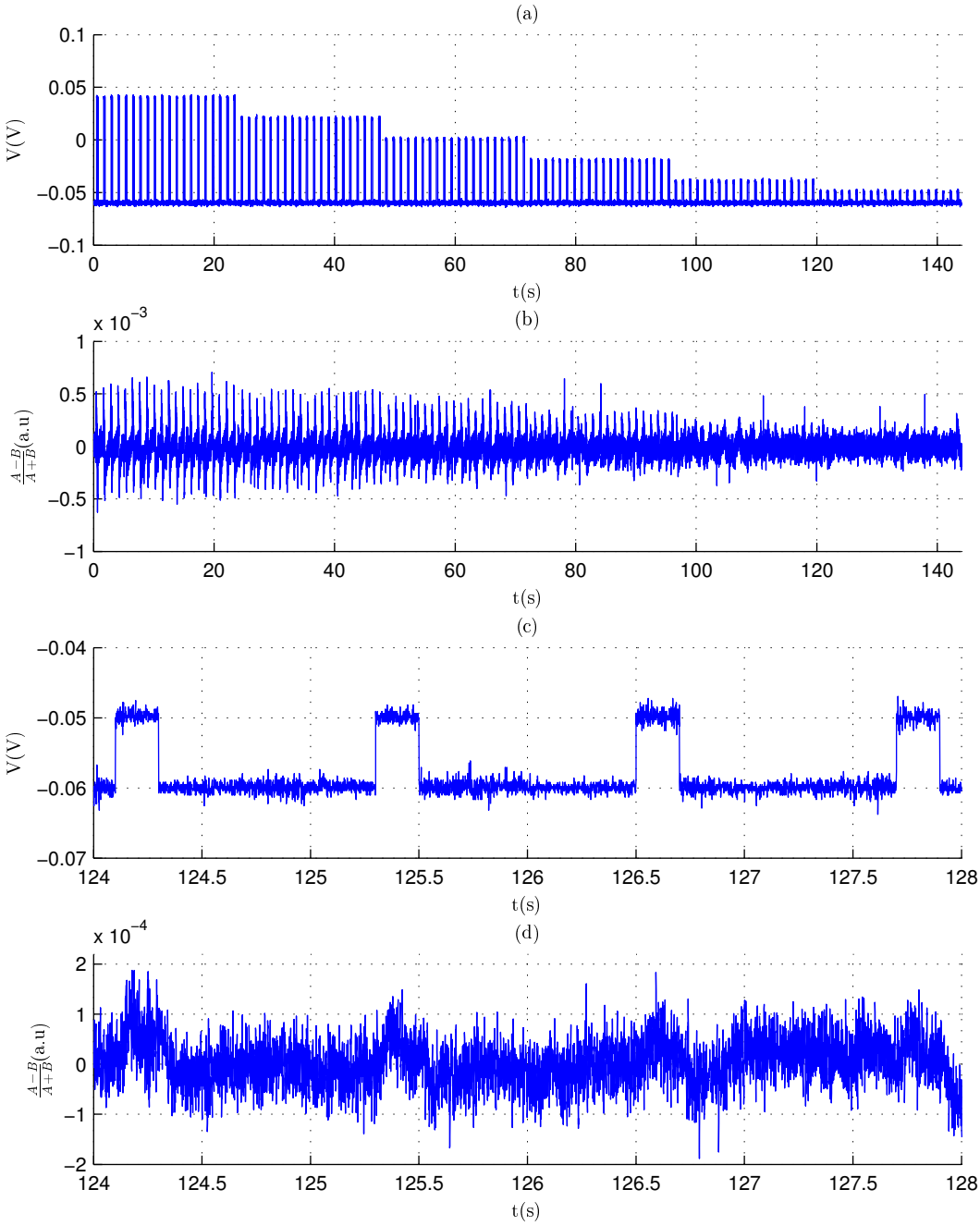


Figure 6.13: (a) The DI-SPR response to (b) computer-generated "cardiac action potential" with amplitudes reduced insteps to 20mV. (d) shows the response of the DI-SPR to (c) 10 mV signal

6.3.6 Imaging locally-applied voltage

This chapter has so far considered the experimental sensitivity of SPR to fast electrical signals in addition to the localization of the effect in the vertical direction making a roadmap for using the technique for the detection of bioelectrical signals. However, since the proposed sensing structure is based on using a non-patterned gold thin-film, it is necessary to explore whether this conductive film is capable of resolving a locally applied voltage (i.e. the lateral resolution of the sensor).

Using the SPR setup in Sec. 4.2(page 93), SPs are excited by focusing a beam of light to a line onto the sample's surface. The use of the pixelated camera offers the advantage of providing imaging information along the focused line. Thus, the obtained maps present the angular information on the horizontal axis and the spatial profile of the SP excitation, along the focused line, in the vertical axis (Fig. 5.6 - page 129). In other words, SPR curves can be produced for each row of pixels. By placing a needle electrode in close proximity to the surface and aligning it to be perpendicular to the focused line, the hypothesis of detecting localised potential can be tested. The focused line can be translated, relative to the tip of the electrode, to validate that the obtained signal is from the electrode.

To study the localization of the voltage, a preliminary experiment was performed using needle electrode to apply a local potential perturbation. As illustrated in Fig. 6.14, a tungsten needle electrode, (Model 7B, Micromanipulator, NV, USA) with a curvature radius of 500 nm, was placed close to the gold surface using a precision piezoelectric stage (TPZ001 Thorlabs). The displacement from surface was measured using a strain gauge (TSG001 Thorlabs). At a separation distance of 10 μm, a $\pm$ 250mV waveform was applied between the needle electrode and the gold surface while a sequence of frames was captured by the pixelated camera at sampling rate of 10 frames per second.

For each frame, SPR curves were produced from an average of five rows (25 μm). The

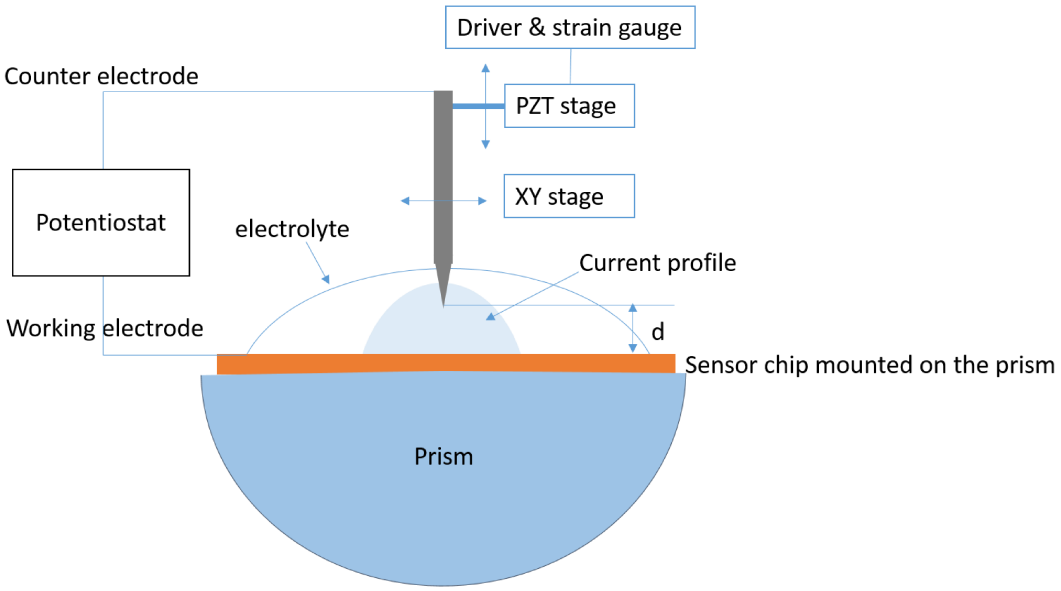


Figure 6.14: Experimental setup for imaging localised potential. Needle electrode was placed close to the gold surface (sensor chip mounted on the prism) and aligned to be perpendicular to the focused line of light using the xy stage.

spatio-temporal dynamic of the resonance position of these SPR curves corresponds to the spatio-temporal dynamics of the applied voltage. The spatial profile of the applied voltage is produced by calculating the change in the resonance position corresponding to the applied voltage for each of these regions of interest (ROI). The average of three measurement is calculated for the set of ROIs. Fig. 6.15 shows the spatial distribution of the voltage. A peak is observed at 0.79 mm in Fig. 6.15-(a), which moves with the translation of the line relative to the electrode (Fig. 6.15-(b)). Fig. 6.15-(c) show the voltage profile on a magnified scale.

The information that is produced by this experiment can be used to infer the limits of voltage resolution from the following analysis. At a separation distance of 10 μm, the voltage signal is projected to $\sim$ 80 μm as calculated from the profile in Fig. 6.15-(c)). Assuming that the route of the current from the electrode tip to surface has a conical shape. The divergence angle of this cone is $\sim$ 152 deg; found from the distance between the two electrodes and the spatial profile of the voltage signal

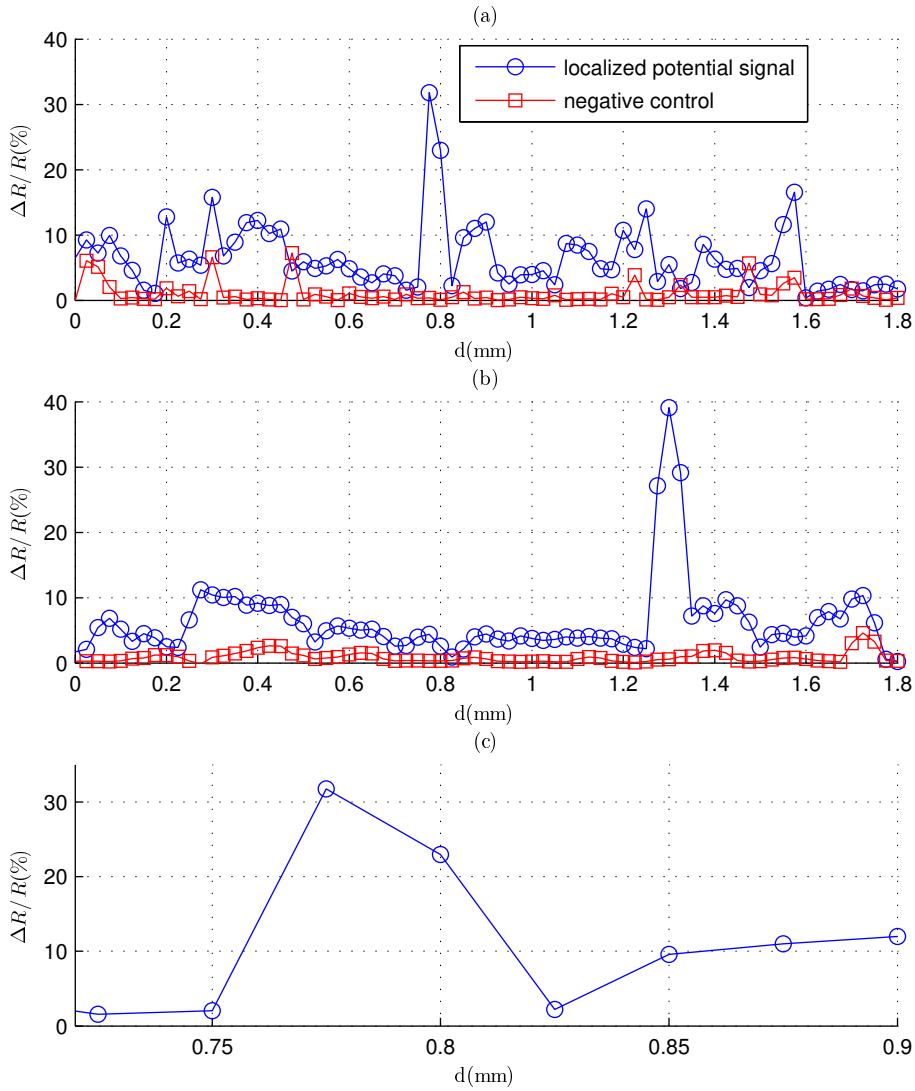


Figure 6.15: spatial profile of locally applied potential using a needle electrode. The peak of the response translates with location of the tip as shown in two different positions in (a) and (b). The square-marked curve shows the profile where there is no potential change at the interface.

$\tan(0.5\theta) = (40/10)$. For a typical cell-surface cleft gap ($\sim$ 50 nm)[61], the voltage signal produced by a point source in the cell is projected to 0.2 μm on the surface. SPR resolution depends on the propagation length of the excited SPs unless specific arrangements are made to improve it as discussed in Sec. 2.1.4. For a wavelength of 633nm in water, it is 3 μm. A comparison between these two figures concludes that the system is limited by the resolution of the SPs prorogation length.

The discussion is relative to the concept of the seal gap (resistance) between the cell and the electrode; this resistance is used to characterize the quality of coupling between the cell and the micro-electrode, in the case of the extracellular recording of the electrical signal (see Sec. 1.1.2) [128]. This parameter has its importance from the finite size of the electrode relative to the cell and thus it controls the energy transfer between the two. However, the SPR thin film has a infinite area compared to the cell area. This implies that no significant leakage occurs at the interface between the cell and the SPR thin-film. Moreover, the findings of this voltage localization experiment demonstrated that signal from the cell project to an area that is equal to the cell area.

The experimental setup would be improved by removing the speckles that result from the use of the coherent light source. These patterns affect the quality of the image of the locally applied voltage. The effect of speckles on SPR measurements is discussed by Liu et al [129]. They can be reduced or eliminated by using a rotating diffusion disk or replacing the laser with an incoherent light source (e.g. LED). The disadvantage of using light emitting diodes is the difficulty to be collimated, which can be overcome by using a pinhole before the collimator with a sacrifice of input power [129]. This experiment would benefit from the use of a high NA objective based SPR imaging system. Using such a setup, a 2D map of the applied voltage can be compared to the resolution of the SP microscope.

Chapter 7

Conclusions and Future Work

7.1 Conclusions

This thesis presents theoretical and experimental evaluation of voltage sensitivity of surface plasmon resonance. This work is motivated by the quest for label-free optical detection of the electrical activity of excitable cells. Electrical activity of excitable cells is a key biological signal that underlies a number of physiological processes, such as the heart function. Measuring this signal at the level of the single cell interests many biomedical applications.

The state-of-the-art techniques are based on labelling the cell membrane with voltage-sensitive markers. The development of these voltage-sensitive dyes has resulted from the demand for parallel recording of the activity from a cell population with a sub-cellular resolution. These requirements are not achieved by the commonly used microelectrode arrays or the single cell intracellular recordings. Although voltage sensitive dyes have successfully overcome these limitations, they still suffer from the limited number of emitted photons due to the conventional labelling problems; overcoming this limitation is a challenge for reliable long-term recording.

Surface plasmon resonance (SPR) has been investigated as a label-free alternative to voltage-sensitive dyes. Since surface plasmons are very sensitive to the metal and dielectric properties of the interface, they have been attempted to detect the electrical activity from rat's brain cortex [64] and from rat's sciatic nerve [63]. However, the challenge of recording at the level of the single cell is preceded by answering vital questions. First, the voltage detection limit of SPR needs to be characterized to design a suitable experimental setup. Second, the technique needs to be tested in terms of response to fast bio-signals.

This research is directed at addressing these questions to pave the way for designing the experimental setup with adequate sensitivity for the bio-signal. Voltage sensitivity is expressed in terms voltage-equivalent refractive index units; a generic term for the sensitivity regardless of the type of optical system. By using this information, voltage sensitivity of any SPR system can be directly found from its refractive index sensitivity.

Electronic readout of the bioelectrical signals is limited by (i) the fundamental sources of noise such as thermal noise and shot noise and (ii) the coupling efficiency of the electrical energy between the cell membrane and the electrode-electrolyte interface. As the proposed optical readout is not a direct measurement of the voltage signal, in contrast to the electronic readout, there are two additional limitations. First, it is limited by the response of the sensing system to the voltage (in terms of the resonance shift per volt). This limit is set by the sensing structure. The second factor is the contribution of the optical system to the noise, which limits the sensitivity of SPR systems.

This thesis, first, addressed the factor of the sensing structure to estimate the resonance shift for the applied voltage using theoretical approaches. An integrated model has been designed simulating the electrode-electrolyte interface with a multilayer structure. The electrode, here, is the plasmonic metal thin film and the electrolyte is 0.15 mM sodium chloride solution. The boundary conditions are manipulated by

the applied voltage and the response is calculated from the theories of the interfacial double-layer capacitance, the Drude model and the Fresnel model.

The interfacial capacitance is formed by two layers in the electrolyte, which are separated by a molecular dielectric layer from the Thomas-Fermi screening length in the metal. The applied voltage results in charging this capacitor. The accumulated charge in the electrolyte is mirrored by excess or deficiency of electrons in the metal's surface. The latter effect modifies the optical properties of this layer, which is calculated from Drude's model. Using this model, SPR curves were generated for a set of voltages and the associated shifts in the resonance position were calculated. The resonance shifts were mapped to the equivalent refractive index changes to estimate the voltage-equivalent refractive index units. The thin-film sensing structure demonstrated a nonlinear response to the voltage, which is attributed to the nonlinear interfacial capacitance.

Second, this thesis presented the experimental validation of these theoretical results. For this purpose, an SPR-based voltage-sensing system has been designed combining a three-electrode electrochemical system with a custom-designed differential intensity SPR system. The system response to the applied voltage featured a nonlinear behaviour supporting the theoretical findings. To validate that the obtained response is due to the effect of charging the interfacial capacitance, the system's response to the applied voltage was evaluated for two types of electrolytes: LiI and NaCl. The atomic mass of the iodide ion is 18 times higher than the atomic mass of the lithium ion, in contrast to sodium and chloride ions that have close atomic masses. The comparison of these two electrolytes is suitable to study the dominance of the charge effect. Both electrolytes show a similar response to the applied voltage confirming that the obtained response is due to the accumulation of charges in the Debye layer near the electrode-electrolyte interface.

The mass-charge effect is illustrated by considering the effective sensing depth of the SPR (i.e. the evanescent field's depth) in comparison to the Debye length

(the effective voltage sensing layer). This comparison is a good indicator for the localization of the voltage sensing effect at a confined layer at the interface. As the Debye layer is $\approx$ 100 times smaller than the evanescent field's depth, the absence of the mass effect indicates that the replacement of ions with counterions due to switching polarity of the input signal occurs at a confined layer at the interface (i.e.Debye layer). Therefore, the average refractive index of the evanescent field does not experience significant changes.

Voltage sensitivity of surface plasmon resonance has been evaluated using theoretical and experimental approaches introducing the voltage equivalent refractive index units (RIUs). The experimental voltage equivalent refractive index change for 10 mV is 4 μRIUs compared to theoretical 5 μRIUs. The current system's sensitivity is in the range of 0.37 μRIUs; this maps to $\approx$ 1mV. However, this detection limit is shifted to 10 mV when a 5 ms voltage pulse is applied to the system. This limitation is due to the extended charging time of the double-layer capacitor at the metal-electrolyte interface.

The 100 mV change in the membrane potential is expected to be mapped to 2mV at the electrode-electrolyte interface; the ratio between the capacitance of the cell membrane and the capacitance of the interface is 0.02. This means, to detect the electrical activity of the excitable cells, a 1 mV sensitivity is required. In this thesis, we have discussed that the sensitivity can be improved to 1 mV by averaging 100 measurements points. With the current sensitivity of the system after averaging, it would be possible to detect the electrical activity of the cardiac cells in real time; the duration of 200ms is sampled with 400 data points at 2kHz sampling frequency. However, for neurons, averaging 100 samples is difficult at this sampling frequency because the duration of the signal is only 2-5ms. To detect the neuronal action potential in real time, at least 3 $\times 10^{-8}$ RIUs is required. This sensitivity is achievable by phase-based SPR systems [30]. Similar sensitivity is possible using the DI-SPR as will be discussed later in Sec. 7.2.

A preliminary experiment on the spatial voltage resolution of the SPR system was performed by applying a localized potential between a needle electrode and the metal's thin film. The voltage resolution, for gold-electrolyte interface (0.15M NaCl), is estimated to be 0.2 μm. In general resolution of SPR systems is limited by the propagation length of the excited SPs, unless special arrangements are considered. Comparing the propagation length of the SP, 3μm for a wavelength of 633nm in water, to the estimated voltage resolution, the voltage resolution is limited by the propagation length of the excited SPs. This finding indicates that the SPR system can be used to spatially resolve the electrical activity at the level of the single cell.

In this thesis, the differential-intensity SPR system has been used to study the voltage sensitivity of surface plasmon resonance. The factors that affect the sensitivity of the system have been investigated. A better model for estimating the responsivity of the system has been suggested; it can be used to estimate the sensitivity from the theoretical or the experimental SPR curves. As the response of the DI-SPR system is calculated by normalizing the differential intensity of the SPR curve to the total intensity, the propagation of the noise of the individual components to the final signal has been analysed. The analysis used the rules of the mathematical operations on random variables to estimate the DI-SPR noise. The approach demonstrated how the differential detection cancels the coherent noise of the system. It also demonstrated that the overall noise is proportional to the differential intensity noise (σ_{A-B}) normalized by the total intensity ($A + B$). This finding presents how the overall noise is reduced by increasing the power at the bi-cell detector.

The results presented in this thesis shed the light on how the DI-SPR instrument can be calibrated for different experimental settings. For instance, by changing the angular width of the excitation beam, one can perform a tradeoff between sensitivity and dynamic range with respect to experimental requirements. Moreover, experimental settings such as input power can be accurately selected to match the

detection limit of a particular application.

7.2 Future Work

The future directions of this thesis are researching ways to enhance the voltage sensitivity of SPR by improving the voltage responsivity of the sensing structure, in addition to improving the sensitivity of the DI-SPR. In addition, the current system can be used to test the hypothesis of recording the electrical activity of excitable cells.

(a) **Recording the electrical activity of the excitable cells**.

The system's ability to detect the electrical activity of excitable cells can be confirmed at the single-cell level. Cultured cardiac myocytes can be used as a proof of concept for the application of plasmonic voltage sensor in the detection of electrical activity of excitable cells. Cells can be cultured on gold surfaces using different surface functionalisations [61]. These cells produce mechanical work (beating) associated with the electrical activity; this additional signal is expected to produce interference to the SP signals. One of the possible solutions for this problem is paralysing these cells by using excitation-contraction decoupling drugs such as blebbistatin or 2, 3-butanedione monoxime (BDM), which inhibit one of the essential motor proteins, myosin [130]. These two drugs have been routinely used to enable optical recording from cardiac cells [131]. Sodium channel blockers (eg. Tetrodotoxin(TTX)) and calcium channel blockers can also be used to suppress the electrical activity of the cell to design a negative control experiment.

For the measurement of the electrical activity at the single-cell level, it is crucial to consider the power of the light per area of the single-cell. This is important as the sensitivity of the DI-SPR scales with the detected power.

(b) **Plasmonic nanoparticles-based enhancement of the sensitivity of the thin-film SPR**

In this research direction, it is better to study the contribution of the surface roughness to voltage sensitivity of SPR before considering the gold nanoparticles' (AuNPs') enhancement, first by comparing the response of sensors chips that are produced by thermal evaporation and sputtering before and after thermal annealing. The effect of the surface roughness on the double layer capacitance was analysed by the Kornykev's group [132] [133]. The study outlined that the effect of the roughness on the capacitive properties of the surface depends on the length characterising the roughness relative to the Debye length (a few nanometres). This theory is consistent with the findings of [134] that nanoscale roughness decreases the double layer capacitance of the electrode, whereas it increases with the microscale. Based on the theory, the surface properties of three types of SPR can be compared: SPR sensors prepared by thermal evaporation, SPR sensors prepared by sputtering and SPR sensors with immobilization of the AuNPs on the thin film.

Previous research reports that (AuNPs) are used to enhance the sensitivity of SPR [56]. Although, the produced SPR curve has lower resonance quality, higher response to refractive index is observed. This enhancement has been applied to the detection of small biomolecules such as DNA with no amplification. This approach is also promising from the voltage sensing point of view for two reasons. The immobilization of gold nano-particles is expected to enhance the capacitive properties of the surface based on the findings of the previous research; capacitance is enhanced by microscale roughness. In addition, the aspect ratio of the sensing nano structure plays an important role in its voltage sensitivity, as reported by [78]. So, immobilizing nano-particles on the thin-film is expected to enhance the sensitivity from this point of view.

(c) **Enhancement of the sensitivity of the DI-SPR system**

This thesis presents an analytical expression (Eq. 5.13) for estimating the sensitivity of the DI-SPR systems. This expression presents the sensitivity as a function of the optical power at the detector, the responsivity of the system to changes in refractive index and the noise of the differential signal. It provides the flexibility for investigating different strategies for improving the sensitivity. For instance, better sensitivity can be achieved by increasing the power at the detector. This can be performed by using a light source of higher power or reducing the components of the optical system to increase its efficiency. This is illustrated by considering the two scenarios discussed below, for a sensing structure that is based on a BK7 glass coated with 50 nm of gold (SPR curve coefficients $a_0 = 0.08$, $a_2 = 0.14$) and a differential intensity noise $\sigma_{A-B} = 5 \times 10^{-5}$.

The power of the light source

With the current system's efficiency (ratio of power at the detector to the input power) of 6%, the sensitivity of the system is increased with the power of the light source, as presented in Fig. 7.1. By increasing the power by an order of magnitude, the sensitivity is improved by an order of magnitude; however, increasing the power should be handled cautiously by considering the tolerance of the living cells. The photodamage of living cells is reported to be ~ 1.6 MW/cm^2 at a wavelength of 680 nm [135].

The efficiency of the optical system

The current efficiency of the system is 6%; found from the ratio of the power at the detector and the input power from the light source. In general, efficiency can be related to the number of components of the system(n) with an average efficiency for each component (η_{avg}); from Eq. 7.1, the average efficiency (per component) of the current system is 76% as there are 10 optical elements and the experimental efficiency is 6%. Now this efficiency can be improved to 57%

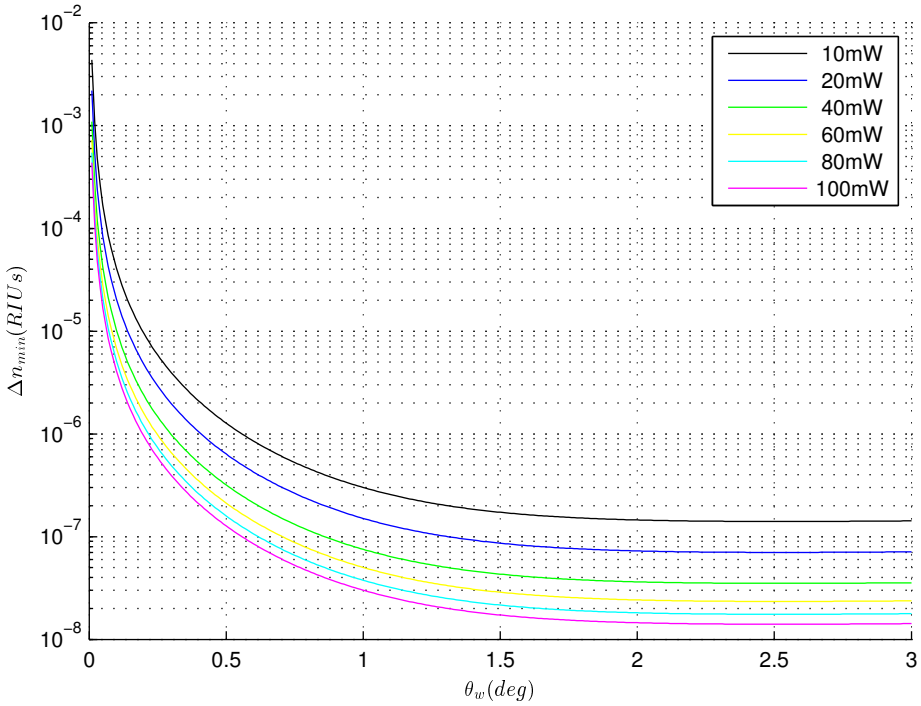


Figure 7.1: Improvement of the sensitivity of the DI-SPR system by increasing the input power of the system

by reducing the number of components to two components; in practice this is possible by focusing the light from the light source on the prism using a cylindrical lens while matching the reflected beam directly on the detector. In this scenario, sensitivity can be improved by an order of magnitude, as presented in Fig. 7.2.

$$\eta = \eta_1\eta_2\eta_3..\eta_n = \eta_{avg}^n \tag{7.1}$$

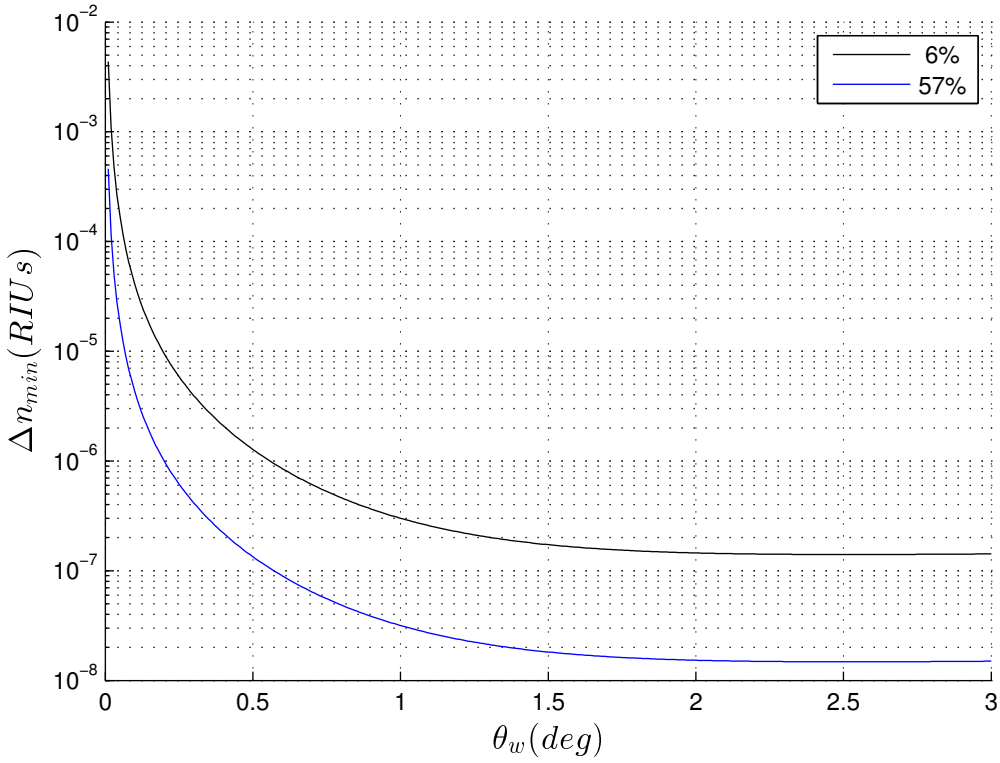


Figure 7.2: Improvement of the sensitivity of the DI-SPR system by reducing the number of the components to increase the detected optical power

In summary, future directions for enhancing the voltage sensitivity of SPR have been suggested. These investigations could increase the sensitivity by optimizing the optical system design in addition to exploring the effect of the metal surface properties on sensitivity. The output of these efforts is expected to have impacts on

providing reliable and sensitive detection of bioelectrical signals and sensitive SPR measurements in general.

Appendix A

Derivation of the second-order expression for the DI-SPR responsivity

Fig. A.1 show SPR curves with a resonance shift $\Delta\theta$, the integration limits are used to produce A-B and A+B for two resonance positions as calculated below. This analysis assumes a symmetrical SPR curve around the resonance angle.

The difference and the sum of each half of the SPR curve, before the resonance position shift, are presented in (A.1) and (A.2).

$$(A-B)_1 = \int_{-\theta_w}^{0} a_0 + a_2\theta^2 \, d\theta - \int_{0}^{-\theta_w} a_0 + a_2\theta^2 \, d\theta \tag{A.1}$$

$$(A+B)_1 = \int_{-\theta_w}^{\theta_w} a_0 + a_2\theta^2 \, d\theta \tag{A.2}$$

The DI-SPR output $(\frac{A-B}{A+B})_1 = 0$ at the start since $(A-B)_1 = 0$. Therefore, $\Delta\frac{A-B}{A+B} = \frac{(A-B)_2}{(A+B)_2}$

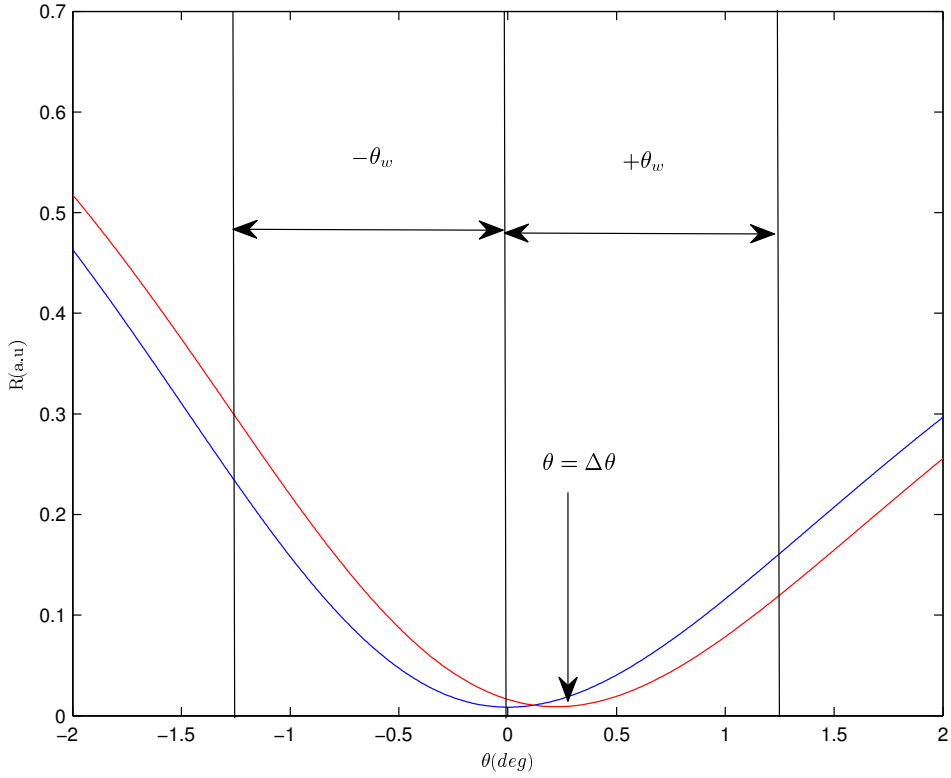


Figure A.1: A graph shows how A and B are obtained when SPR angle shift.

$$(A-B)_2 = \int_{-\theta_w}^{0} a_0 + a_2(\theta - \Delta\theta)^2 \, d\theta_w - \int_{0}^{-\theta_w} a_0 + a_2(\theta - \Delta\theta)^2 \, d\theta \approx 2a_2\theta_w^2\Delta\theta \quad \text{(A.3)}$$

$$(A+B)_2 = \int_{-\theta_w}^{\theta_w} a_0 + a_2(\theta - \Delta\theta)^2 \, d\theta = 2a_0\theta_w + \frac{2a_2\theta_w^3}{3} \quad \text{(A.4)}$$

$$\Delta\frac{A-B}{A+B} = \frac{3a_2\theta_w}{3a_0 + a_2\theta_w^2}\Delta\theta \quad \text{(A.5)}$$

The responsivity (η) of DI-SPR is

$$\eta = \frac{3a_2\theta_w}{3a_0 + a_2\theta_w^2}\Delta\theta \quad \text{(A.6)}$$

Bibliography

[1] E.N. Marieb and K. Hoehn. *Human anatomy & physiology*. Pearson Education, 2007.

[2] S. G. Cull-Candy and D. C. Ogden. Ion channels activated by L-Glutamate and GABA in cultured cerebellar neurons of the rat. *Proceedings of the Royal Society of London B: Biological Sciences*, 224(1236):367–373, May 1985. ISSN 0962-8452, 1471-2954. doi: 10.1098/rspb.1985.0038. URL `http://rspb.royalsocietypublishing.org/content/224/1236/367`.

[3] S. G Cull-Candy, C.G Marshall, and D. Ogden. Voltage-activated membrane currents in rat cerebellar granule neurones. *The Journal of Physiology*, 414(1):179–199, July 1989. ISSN 1469-7793. doi: 10.1113/jphysiol.1989.sp017683. URL `http://onlinelibrary.wiley.com/doi/10.1113/jphysiol.1989.sp017683/abstract`.

[4] F. Hofmann and H. Bading. Long term recordings with microelectrode arrays: Studies of transcription-dependent neuronal plasticity and axonal regeneration. *Journal of Physiology-Paris*, 99(23):125 – 132, 2006. doi: http://dx.doi.org/10.1016/j.jphysparis.2005.12.005.

[5] B.l Hille et al. *Ion channels of excitable membranes*, volume 507. Sinauer Sunderland, MA, 2001.

[6] J. G. Nicholls, A. R. Martin, B. G. Wallace, and P. A. Fuchs. *From neuron to brain*, volume 271. Sinauer Associates Sunderland, MA, 2001.

[7] A.M. Katz. *Physiology of the Heart*. Lippincott Williams & Wilkins, 2010.

[8] M.W. Barnett and P.M. Larkman. The action potential. *Practical neurology*, 7(3):192–197, 2007.

[9] S. H. Wright. Generation of resting membrane potential. *Advances in Physiology Education*, 28(4):139–142, 2004.

[10] J. Pinnell, S. Turner, and S. Howell. Cardiac muscle physiology. *Continuing Education in Anaesthesia, Critical Care & Pain*, 7(3):85–88, 2007.

[11] D. Debanne, B.H. Gähwiler, and S.M. Thompson. Long-term synaptic plasticity between pairs of individual CA3 pyramidal cells in rat hippocampal slice cultures. *The Journal of Physiology*, 507(1):237–247, 1998.

[12] O. Caspi, I. Itzhaki, I. Kehat, A. Gepstein, G. Arbel, I. Huber, J. Satin, and L. Gepstein. In vitro electrophysiological drug testing using human embryonic stem cell derived cardiomyocytes. *Stem cells and development*, 18(1):161–172, 2009.

[13] A. Stett, U. Egert, E. Guenther, F. Hofmann, T. Meyer, W. Nisch, and H. Haemmerle. Biological application of microelectrode arrays in drug discovery and basic research. *Analytical and bioanalytical chemistry*, 377(3):486–495, 2003.

[14] A. Blazeski, R. Zhu, D.W. Hunter, S.H. Weinberg, E.T. Zambidis, and L. Tung. Cardiomyocytes derived from human induced pluripotent stem cells as models for normal and diseased cardiac electrophysiology and contractility. *Progress in biophysics and molecular biology*, 110(2):166–177, 2012.

[15] R. Brette and A. Destexhe. *Handbook of neural activity measurement*. Cambridge University Press, 2012.

[16] D. Ogden and P. Stanfield. Patch clamp techniques for single channel and whole-cell recording. In *Microelectrode techniques: the Plymouth workshop handbook*, volume 2. Company of Biologists Cambridge, 1994.

[17] M.E.J. Obien, K. Deligkaris, T Bullmann, D.J. Bakkum, and U. Frey. Revealing neuronal function through microelectrode array recordings. *Frontiers in neuroscience*, 8, 2014.

[18] M.E Spira and A. Hai. Multi-electrode array technologies for neuroscience and cardiology. *Nature nanotechnology*, 8(2):83–94, 2013.

[19] S. Chemla and F. Chavane. Voltage-sensitive dye imaging: Technique review and models. *Journal of Physiology-Paris*, 104(1):40–50, 2010.

[20] L.M. Loew. Design and use of organic voltage sensitive dyes. In *Membrane potential imaging in the nervous system*, pages 13–23. Springer, 2011.

[21] T. H. Grandy, S. A. Greenfield, and I. M. Devonshire. An evaluation of in vivo voltage-sensitive dyes: pharmacological side effects and signal-to-noise ratios after effective removal of brain-pulsation artifacts. *Journal of Neurophysiology*, 108(11):2931–2945, 2012. ISSN 0022-3077. doi: 10.1152/jn.00512.2011. URL `http://jn.physiology.org/content/108/11/2931`.

[22] Y. Wang, W.and Yang, S. Wang, V.J. Nagaraj, Q. Liu, J. Wu, and N. Tao. Label-free measuring and mapping of binding kinetics of membrane proteins in single living cells. *Nature chemistry*, 4(10):846–853, 2012.

[23] J.D.E. McIntyre. Electrochemical modulation spectroscopy. *Surface Science*, 37(0):658 – 682, 1973. ISSN 0039-6028. doi: http://dx.doi.org/10.1016/0039-6028(73)90357-9. URL `http://www.sciencedirect.com/science/article/pii/0039602873903579`.

[24] H. Raether. *Surface Plasmons on Smooth and Rough Surfaces and on Gratings*. Springer, 1986.

[25] Y. Huang, M.C. Pitter, and M.G. Somekh. Time-dependent scattering of ultrathin gold film under potential perturbation. *ACS applied materials & interfaces*, 4(8):3829–3836, 2012.

[26] N.J Tao, S. Boussaad, R.A. Huang, W.L.and Arechabaleta, and J. DAgnese. High resolution surface plasmon resonance spectroscopy. *Review of Scientific instruments*, 70(12):4656–4660, 1999.

[27] J. E. Garland, K. A. Assiongbon, C. M. Pettit, and D. Roy. Surface plasmon resonance transients at an electrochemical interface: time resolved measurements using a bicell photodiode. *Analytica Chimica Acta*, 475(12):47–58, January 2003. ISSN 0003-2670. doi: 10.1016/S0003-2670(02)01224-2. URL `http://www.sciencedirect.com/science/article/pii/S0003267002012242`.

[28] V. Lioubimov, A. Kolomenskii, A. Mershin, D.V. Nanopoulos, and H.A. Schuessler. Effect of varying electric potential on surface-plasmon resonance sensing. *Appl. Opt.*, 43(17):3426–3432, Jun 2004. doi: 10.1364/AO.43.003426. URL `http://ao.osa.org/abstract.cfm?URI=ao-43-17-3426`.

[29] R.M. Schasfoort and A.J. Tudos. *Handbook of surface plasmon resonance*. Royal Society of Chemistry, 2008.

[30] J. Homola, S. S. Yee, and G. Gauglitz. Surface plasmon resonance sensors: review. *Sensors and Actuators B: Chemical*, 54(1):3–15, 1999.

[31] J. R. Sambles, G.W. Bradbery, and F. Yang. Optical excitation of surface plasmons: an introduction. *Contemporary Physics*, 32(3):173–183, 1991.

[32] C. Thirstrup and W. Zong. Data analysis for surface plasmon resonance sensors using dynamic baseline algorithm. *Sensors and Actuators B: Chemical*, 106(2):796–802, 2005.

[33] C. M. Pettit, K. A. Assiongbon, J. E. Garland, and D. Roy. Time resolved detection of electrochemical effects by surface plasmon resonance measurements: a simple technique using a large area single cell photodiode. *Sensors and Actuators B: Chemical*, 96(12):105–113, November 2003. ISSN 0925-4005. doi: 10.1016/S0925-4005(03)00509-4. URL `http://www.sciencedirect.com/science/article/pii/S0925400503005094`.

[34] M. Schneider, A. Andersen, P. Koelsch, and H. Motschmann. Following fast adsorption processes with surface plasmon spectroscopy: reflectivity versus mismatch tracking. *Sensors and Actuators B: Chemical*, 104(2):276–281, 2005.

[35] X. Fan, I.M. White, S.I. Shopova, H. Zhu, J.D. Suter, and Y. Sun. Sensitive optical biosensors for unlabeled targets: A review. *analytica chimica acta*, 620 (1):8–26, 2008.

[36] Y. Mao, Y. Bao, W. Wang, Z. Li, F. Li, L. Niu, et al. Development and application of time-resolved surface plasmon resonance spectrometer. *American Journal of Analytical Chemistry*, 2(05):589, 2011.

[37] M.G. Somekh. Surface plasmon and surface wave microscopy. In *Optical imaging and Microscopy*, pages 275–307. Springer, 2003.

[38] Y.H Huang, H.P Ho, S.Y Wu, and S.K. Kong. Detecting phase shifts in surface plasmon resonance: a review. *Advances in Optical Technologies*, 2012, 2011.

[39] A.V. Kabashin and P.I. Nikitin. Surface plasmon resonance interferometer for bio-and chemical-sensors. *Optics Communications*, 150(1):5–8, 1998.

[40] A.V. Kabashin and P. I. Nikitin. Interferometer based on a surface-plasmon resonance for sensor applications. *Quantum Electronics*, 27(7):653–654, 1997.

[41] P.I. Nikitin, A.N. Grigorenko, A.A. Beloglazov, M.V. Valeiko, A.I. Savchuk, O.A. Savchuk, G. Steiner, C. Kuhne, A. Huebner, and R. Salzer. Surface

plasmon resonance interferometry for micro-array biosensing. *Sensors and Actuators A: Physical*, 85(1):189–193, 2000.

[42] S.Y. Wu, H.P. Ho, W.C. Law, C. Lin, and S.K. Kong. Highly sensitive differential phase-sensitive surface plasmon resonance biosensor based on the mach–zehnder configuration. *Optics Letters*, 29(20):2378–2380, 2004.

[43] M.G. Somekh, S. Liu, T.S. Velinov, and C.W. See. High-resolution scanning surface-plasmon microscopy. *Applied optics*, 39(34):6279–6287, 2000.

[44] B. Zhang, S. Pechprasarn, J. Zhang, and M.G. Somekh. Confocal surface plasmon microscopy with pupil function engineering. *Optics express*, 20(7): 7388–7397, 2012.

[45] H.P. Ho, W.C. Law, S.Y. Wu, X.H. Liu, S.P. Wong, C. Lin, and S.K. Kong. Phase-sensitive surface plasmon resonance biosensor using the photoelastic modulation technique. *Sensors and Actuators B: Chemical*, 114(1):80–84, 2006.

[46] J. Wang, R.J. Smith, R.A. Light, J.L. Richens, J. Zhang, P. OShea, C. See, and M.G. Somekh. Highly sensitive multipoint real-time kinetic detection of surface plasmon bioanalytes with custom CMOS cameras. *Biosensors and Bioelectronics*, 58:157–164, 2014.

[47] M. Piliarik and J. Homola. Surface plasmon resonance (SPR) sensors: approaching their limits? *Optics express*, 17(19):16505–16517, 2009.

[48] D. Cai, Y. Lu, K. Lin, P. Wang, and H. Ming. Improving the sensitivity of SPR sensors based on gratings by double-dips method (DDM). *Optics express*, 16(19):14597–14602, 2008.

[49] S. Ekgasit, C. Thammacharoen, F. Yu, and W. Knoll. Influence of the metal film thickness on the sensitivity of surface plasmon resonance biosensors. *Applied spectroscopy*, 59(5):661–667, 2005.

[50] S. Pechprasarn and M.G. Somekh. Surface plasmon microscopy: resolution, sensitivity and crosstalk. *Journal of microscopy*, 246(3):287–297, 2012.

[51] B. Huang, F. Yu, and R.N. Zare. Surface plasmon resonance imaging using a high numerical aperture microscope objective. *Analytical chemistry*, 79(7): 2979–2983, 2007.

[52] J. Homola. Surface plasmon resonance sensors for detection of chemical and biological species. *Chemical reviews*, 108(2):462–493, 2008.

[53] J.S. Lane, J.L. Richens, K.A. Vere, and P. OShea. Rational targeting of subclasses of intermolecular interactions: elimination of nonspecific binding for analyte sensing. *Langmuir*, 30(31):9457–9465, 2014.

[54] H.Q. Zhang, S. Boussaad, and N.J. Tao. High-performance differential surface plasmon resonance sensor using quadrant cell photodetector. *Review of Scientific instruments*, 74(1):150–153, 2003.

[55] D.R. Shankaran, K.V. Gobi, and N. Miura. Recent advancements in surface plasmon resonance immunosensors for detection of small molecules of biomedical, food and environmental interest. *Sensors and Actuators B: Chemical*, 121 (1):158–177, 2007.

[56] R. DAgata, R. Corradini, C. Ferretti, L. Zanoli, M. Gatti, R. Marchelli, and G. Spoto. Ultrasensitive detection of non-amplified genomic DNA by nanoparticle-enhanced surface plasmon resonance imaging. *Biosensors and Bioelectronics*, 25(9):2095–2100, 2010.

[57] O. Zagorodko, A.Y. Spadavecchia, J.and Serrano, I. Larroulet, A. Pesquera, A. Zurutuza, R. Boukherroub, and S. Szunerits. Highly sensitive detection of DNA hybridization on commercialized graphene-coated surface plasmon resonance interfaces. *Analytical chemistry*, 86(22):11211–11216, 2014.

[58] A.B. Dahlin, B. Dielacher, P. Rajendran, K. Sugihara, T. Sannomiya, M. Zenobi-Wong, and J. Vörös. Electrochemical plasmonic sensors. *Analytical and bioanalytical chemistry*, 402(5):1773–1784, 2012.

[59] S Wang, X. Huang, X. Shan, K.J. Foley, and N. Tao. Electrochemical surface plasmon resonance: basic formalism and experimental validation. *Analytical chemistry*, 82(3):935–941, 2010.

[60] B. Rothenhäusler and W. Knoll. Surface plasmon microscopy. *Nature*, pages 615 – 617, 1988.

[61] K. Toma, H. Kano, and A. Offenhausser. Label-free measurement of cell–electrode cleft gap distance with high spatial resolution surface plasmon microscopy. *ACS nano*, 8(12):12612–12619, 2014.

[62] O.R. Bolduc, L.S. Live, and Jean-François Masson. High-resolution surface plasmon resonance sensors based on a dove prism. *Talanta*, 77(5):1680–1687, 2009.

[63] S. Ae Kim, K. Min Byun, J. Lee, J. Hoon Kim, D. Albert Kim, H. Baac, M.L Shuler, and S. June Kim. Optical measurement of neural activity using surface plasmon resonance. *Optics letters*, 33(9):914–916, 2008.

[64] S. Kim, S.J. Kim, H. Moon, and S.B. Jun. In vivo optical neural recording using fiber-based surface plasmon resonance. *Optics letters*, 37(4):614–616, 2012.

[65] J. Zhang and A.V. Atay, T.and Nurmikko. Optical Detection of Brain Cell Activity Using Plasmonic Gold Nanoparticles. *Nano Lett.*, 9(2):519–524, February 2009. ISSN 1530-6984. doi: 10.1021/nl801891q. URL `http://dx.doi.org/10.1021/nl801891q`.

[66] L.B. Cohen, R.D. Keynes, and B. Hille. Light scattering and birefringence changes during nerve activity. *Nature*, 218:438–441, 1968.

[67] S.H. Choi, S.J. Kim, C.H. Im, S. A. Kim, and D. Kim. Quantitative model for the change of optical resonance in neural activity detection systems based on surface plasmon resonance. *Optics & Laser Technology*, 43(5):938–948, July 2011. ISSN 0030-3992. doi: 10.1016/j.optlastec.2010.12.010. URL http://www.sciencedirect.com/science/article/pii/S0030399210002926.

[68] J. Feinleib. Electroreflectance in metals. *Phys. Rev. Lett.*, 16:1200–1202, Jun 1966. doi: 10.1103/PhysRevLett.16.1200. URL http://link.aps.org/doi/10.1103/PhysRevLett.16.1200.

[69] W.N. Hansen and A. Prostak. Electromodulation of the optical properties of gold. *Phys. Rev.*, 174:500–503, Oct 1968. doi: 10.1103/PhysRev.174.500. URL http://link.aps.org/doi/10.1103/PhysRev.174.500.

[70] D. M. Kolb. Spectroscopie et rflectancereflectance spectroscopy in the study of electrode surfaces. *J. Phys. Colloques*, 38:C5–167–C5–177, 1977. doi: 10.1051/jphyscol:1977522. URL http://dx.doi.org/10.1051/jphyscol:1977522.

[71] R.J. Gale. *Spectroelectrochemistry: theory and practice*. Springer Science & Business Media, 2012.

[72] S. Wang, X. Huang, X. Shan, K.J. Foley, and N. Tao. Electrochemical surface plasmon resonance: Basic formalism and experimental validation. *Analytical Chemistry*, 82(3):935–941, 2010. doi: 10.1021/ac902178f. URL http://pubs.acs.org/doi/abs/10.1021/ac902178f. PMID: 20047281.

[73] K.J Foley, X Shan, and N. J. Tao. Surface impedance imaging technique. *Analytical Chemistry*, 80(13):5146–5151, 2008. doi: 10.1021/ac800361p. URL http://pubs.acs.org/doi/abs/10.1021/ac800361p.

[74] R. Burt, G. Birkett, and X.S. Zhao. A review of molecular modelling of electric double layer capacitors. *Physical Chemistry Chemical Physics*, 16(14):6519–6538, 2014.

[75] A. J. Bard and L. R. Faulkner. *Electrochemical Methods: Fundamentals and Applications*. Wiley New York, 2001.

[76] M. R Wright. *An introduction to aqueous electrolyte solutions*. John Wiley & Sons, 2007.

[77] B.E. Conway. *Electrochemical supercapacitors: scientific fundamentals and technological applications*. Springer Science & Business Media, 2013.

[78] Y. Huang, M.C. Pitter, and M.G. Somekh. Morphology-dependent voltage sensitivity of a gold nanostructure. *Langmuir*, 27(22):13950–13961, 2011.

[79] R. MacKenzie, C. Fraschina, B. Dielacher, T. Sannomiya, A.B. Dahlin, and J. Vörös. Simultaneous electrical and plasmonic monitoring of potential induced ion adsorption on metal nanowire arrays. *Nanoscale*, 5(11):4966–4975, 2013.

[80] H. Nishi, S. Hiroya, and T. Tatsuma. Potential-scanning localized surface plasmon resonance sensor. *ACS nano*, 9(6):6214–6221, 2015.

[81] A.J. Haes and R.P. Van Duyne. A unified view of propagating and localized surface plasmon resonance biosensors. *Analytical and Bioanalytical Chemistry*, 379(7-8):920–930, 2004.

[82] F. Abels, T. Lopez-Rios, and A. Tadjeddine. Investigation of the metal-electrolyte interface using surface plasma waves with ellipsometric detection. *Solid State Communications*, 16(7):843 – 847, 1975. ISSN 0038-1098. doi: http://dx.doi.org/10.1016/0038-1098(75)90876-5. URL `http://www.sciencedirect.com/science/article/pii/0038109875908765`.

[83] R. Ktz, D.M. Kolb, and J.K. Sass. Electron density effects in surface plasmon excitation on silver and gold electrodes. *Surface Science*, 69(1):359 – 364, 1977. ISSN 0039-6028. doi: http://dx.doi.org/10.1016/0039-6028(77)

90181-9. URL http://www.sciencedirect.com/science/article/pii/0039602877901819.

[84] A. M. Lopatynskyi, O. G. Lopatynska, M. D. Guiver, L. V. Poperenko, and V. I. Chegel. Factor of interfacial potential for the surface plasmon-polariton resonance sensor response. *Semicond. Phys. Quantum Electron. Optoelectron*, 11(4):329–336, 2008.

[85] Y. Huang, M.C. Pitter, M.G. Somekh, W. Zhang, W. Xie, H. Zhang, H. Wang, and S. Fang. Plasmonic response of gold film to potential perturbation. *Science China Physics, Mechanics and Astronomy*, 56(8):1495–1503, 2013.

[86] P. Brüesch and T. Christen. The electric double layer at a metal electrode in pure water. *Journal of applied physics*, 95(5):2846–2856, 2004.

[87] L.B. Cohen, B. Hille, R. Keynes, D. Landowne, and E. Rojas. Analysis of the potential-dependent changes in optical retardation in the squid giant axon. *The Journal of physiology*, 218(1):205, 1971.

[88] R.A. Stepnoski, A. LaPorta, F. Raccuia-Behling, G. E. Blonder, R. .E Slusher, and D. Kleinfeld. Noninvasive detection of changes in membrane potential in cultured neurons by light scattering. *Proc Natl Acad Sci U S A*, 88(21):9382–9386, November 1991. ISSN 0027-8424. URL http://www.ncbi.nlm.nih.gov/pmc/articles/PMC52721/.

[89] B. Hajj, S. De Reguardati, L. Hugonin, B. Le Pioufle, T. Osaki, H. Suzuki, S. Takeuchi, H. Mojzisova, D. Chauvat, and J. Zyss. Electro-optical imaging microscopy of dye-doped artificial lipidic membranes. *Biophysical journal*, 97 (11):2913–2921, 2009.

[90] N. Joye, A. Schmid, and Y. Leblebici. Electrical modeling of the cellelectrode interface for recording neural activity from high-density microelectrode arrays. *Neurocomputing*, 73(13):250 – 259, 2009. ISSN 0925-2312. doi: http://dx.doi.

org/10.1016/j.neucom.2009.09.006. URL http://www.sciencedirect.com/science/article/pii/S0925231209003300.

[91] V. Thakore, P. Molnar, and J.J. Hickman. An optimization based study of equivalent circuit models for representing recordings at the neuron-electrode interface. *IEEE Trans Biomed Eng*, 59(8):2338–2347, August 2012. ISSN 0018-9294. doi: 10.1109/TBME.2012.2203820. URL http://www.ncbi.nlm.nih.gov/pmc/articles/PMC3909926/.

[92] S. Kim, W. Chegal, J. Doh, H. Mo Cho, and Dae Won Moon. Study of cell-matrix adhesion dynamics using surface plasmon resonance imaging ellipsometry. *Biophysical Journal*, 100(7):1819 – 1828, 2011. ISSN 0006-3495. doi: http://dx.doi.org/10.1016/j.bpj.2011.01.033. URL http://www.sciencedirect.com/science/article/pii/S0006349511001160.

[93] K.-F. Giebel, C. Bechinger, S. Herminghaus, M. Riedel, P. Leiderer, U. Weiland, and M. Bastmeyer. Imaging of cell/substrate contacts of living cells with surface plasmon resonance microscopy. *Biophysical Journal*, 76(1):509 – 516, 1999. ISSN 0006-3495. doi: http://dx.doi.org/10.1016/S0006-3495(99)77219-X. URL http://www.sciencedirect.com/science/article/pii/S000634959977219X.

[94] R.M.A. Azzam and N.M. Bashara. *Ellipsometry and polarized light*. Elsevier science, 1987.

[95] E. Hecht. *Optics*. Addison-Wesley, 2002. ISBN 9780805385663. URL https://books.google.co.uk/books?id=7aG6QgAACAAJ.

[96] C. Kittel. *Introducrtion to solid state physics*. John Wiley and Sons, Inc, 2005.

[97] P. B. Johnson and R. W. Christy. Optical constants of the noble metals. *Phys. Rev. B*, 6:4370–4379, Dec 1972. doi: 10.1103/PhysRevB.6.4370. URL http://link.aps.org/doi/10.1103/PhysRevB.6.4370.

[98] P. Jahanshahi, M. Ghomeishi, and F.R.M. Adikan. Study on Dielectric Function Models for Surface Plasmon Resonance Structure, Study on Dielectric Function Models for Surface Plasmon Resonance Structure. *The Scientific World Journal, The Scientific World Journal*, 2014, 2014:e503749, January 2014. ISSN 2356-6140, 2356-6140. doi: 10.1155/2014/503749,10.1155/2014/503749. URL http://www.hindawi.com/journals/tswj/2014/503749/abs/,http://www.hindawi.com/journals/tswj/2014/503749/abs/.

[99] P. B. Johnson and R. W. Christy. Optical constants of the noble metals. *Phys. Rev. B*, 6:4370–4379, Dec 1972. doi: 10.1103/PhysRevB.6.4370. URL http://link.aps.org/doi/10.1103/PhysRevB.6.4370.

[100] M. Polyanskiy. Optical constants of au (gold), 2008-2016. URL http://refractiveindex.info/?shelf=main&book=Au&page=Johnson.

[101] H. M. Rosenberg. *The solid state*. Oxford University Press Oxford, 1988.

[102] J. W. Schultze and G. Staikov. *Electrochemistry in Molecular and Microscopic Dimensions: Proceedings of the 53rd Annual Meeting of the International Society of Electrochemistry: Jointly Organized with the GDCh-Fachgruppe Angewandte Electrochemie, Düsseldorf, Germany, 15-20 September 2002*, volume 48. Elsevier, 2003.

[103] J. C. Slater. Atomic radii in crystals. *The Journal of Chemical Physics*, 41 (10), 1964.

[104] A. N. Bashkatov and E.A. Genina. Water refractive index in dependence on temperature and wavelength: a simple approximation. *Proc. SPIE*, 5068:393–395, 2003. doi: 10.1117/12.518857. URL http://dx.doi.org/10.1117/12.518857.

[105] P. Schiebener, J Straub, J.M.H. Levelt Sengers, and J.S. Gallagher. Refractive

index of water and steam as function of wavelength, temperature and density. *Journal of physical and chemical reference data*, 19(3):677–717, 1990.

[106] M. H. George and R. Q. Marvin. Optical constants of water in the 200-nm to 200-μm wavelength region. *Appl. Opt.*, 12(3):555–563, Mar 1973. doi: 10.1364/AO.12.000555. URL `http://ao.osa.org/abstract.cfm?URI=ao-12-3-555`.

[107] M. Born and E. Wolf. *Principles of optics: electromagnetic theory of propagation, interference and diffraction of light*. Cambridge university press, 1999.

[108] E. B. Helene, S.F. A. Bert, P.H. K. Rob, and G. Jan. Determination of thickness and dielectric constant of thin transparent dielectric layers using surface plasmon resonance. *Optics Communications*, 82(56):425 – 432, 1991. doi: http://dx.doi.org/10.1016/0030-4018(91)90353-F.

[109] J.M. Chen, W.and Chen. Use of surface plasma waves for determination of the thickness and optical constants of thin metallic films. *JOSA*, 71(2):189–191, 1981.

[110] E. Hutter, S. Cha, J.F. Liu, J. Park, J. Yi, J.H. Fendler, and D. Roy. Role of substrate metal in gold nanoparticle enhanced surface plasmon resonance imaging. *The Journal of Physical Chemistry B*, 105(1):8–12, 2001.

[111] M.C. Huang, Y.and Pitter, M.G. Somekh, W.Y. Zhang, W.and Xie, H. Zhang, H. Wang, and S. Fang. Plasmonic response of gold film to potential perturbation. *Science China Physics, Mechanics and Astronomy*, 56(8):1495–1503, 2013. ISSN 1674-7348. doi: 10.1007/s11433-013-5173-7. URL `http://dx.doi.org/10.1007/s11433-013-5173-7`.

[112] M. Uematsu and E.U. Frank. Static dielectric constant of water and steam. *Journal of Physical and Chemical Reference Data*, 9(4):1291–1306, 1980.

[113] S. K. Ozdemir and G. Turhan-Sayan. Temperature effects on surface plasmon resonance: design considerations for an optical temperature sensor. *Journal of Lightwave Technology*, 21(3):805, 2003.

[114] G. P. Baxter, A. C. Boylston, E. Mueller, N. H. Black, and P. B Goode. The refractive power of the halogen salts of lithium, sodium and potassium in aqueous solution. *Journal of the American Chemical Society*, 33(6):901–922, 1911.

[115] X. Shan, S. Wang, W. Wang, and N. Tao. Plasmonic-based imaging of local square wave voltammetry. *Analytical chemistry*, 83(19):7394–7399, 2011.

[116] M.G. Kendall. *Advanced Theory Of Statistics Vol-I*. Charles Griffin: London, 1987.

[117] H. Q. Zhang, S. Boussaad, and N. J. Tao. High-performance differential surface plasmon resonance sensor using quadrant cell photodetector. *Review of Scientific Instruments*, 74(1), 2003.

[118] J. Rhee, D. Wang, N.J. Tao, and Y. Joo. CMOS image sensor array for surface plasmon resonance spectroscopy. In *Electronic Imaging 2004*, pages 34–41. International Society for Optics and Photonics, 2004.

[119] A.V. Kabashin, S. Patskovsky, and A.N. Grigorenko. Phase and amplitude sensitivities in surface plasmon resonance bio and chemical sensing. *Optics Express*, 17(23):21191–21204, 2009.

[120] T. Pajkossy. Impedance spectroscopy at interfaces of metals and aqueous solutionssurface roughness, CPE and related issues. *Solid State Ionics*, 176 (25):1997–2003, 2005.

[121] C. Celedón, M. Flores, P. Häberle, and J.E. Valdés. Surface roughness of thin gold films and its effects on the proton energy loss straggling. *Brazilian journal of physics*, 36(3B):956–959, 2006.

[122] S Trasatti and E. Lust. The potential of zero charge. In RalphE. White, J.OM. Bockris, and B.E. Conway, editors, *Modern Aspects of Electrochemistry*, volume 33 of *Modern Aspects of Electrochemistry*, pages 1–215. Springer US, 1999. ISBN 978-0-306-45968-9. doi: 10.1007/0-306-46917-0_1. URL `http://dx.doi.org/10.1007/0-306-46917-0_1`.

[123] J.R. Macdonald and M.K. Brachman. The charging and discharging of nonlinear capacitors. *Proceedings of the IRE*, 43(1):71–78, Jan 1955. ISSN 0096-8390. doi: 10.1109/JRPROC.1955.277920.

[124] K.T. Chu and M.Z. Bazant. Nonlinear electrochemical relaxation around conductors. *Phys. Rev. E*, 74:011501, Jul 2006. doi: 10.1103/PhysRevE.74.011501. URL `http://link.aps.org/doi/10.1103/PhysRevE.74.011501`.

[125] Z. Kerner and Tás Pajkossy. On the origin of capacitance dispersion of rough electrodes. *Electrochimica Acta*, 46(2):207–211, 2000.

[126] T.C. Halsey. Frequency dependence of the double-layer impedance at a rough surface. *Physical Review A*, 35(8):3512, 1987.

[127] Z. Kerner and T.ás Pajkossy. Impedance of rough capacitive electrodes: the role of surface disorder. *Journal of Electroanalytical Chemistry*, 448(1):139–142, 1998.

[128] J. R. Buitenweg, W.L.C. Rutten, and E. Marani. Geometry-based finite-element modeling of the electrical contact between a cultured neuron and a microelectrode. *Biomedical Engineering, IEEE Transactions on*, 50(4):501–509, 2003.

[129] L. Liu, J. Guo, Y. He, P.i Zhang, Y. Zhang, and J. Guo. Study on the despeckle methods in angular surface plasmon resonance imaging sensors. *Plasmonics*, 10(3):729–737, 2015. ISSN 1557-1963.

[130] E.M. Ostap. 2, 3-butanedione monoxime (BDM) as a myosin inhibitor. *Journal of Muscle Research & Cell Motility*, 23(4):305–308, 2002.

[131] D. Lang, M. Sulkin, Q. Lou, and I.R. Efimov. Optical mapping of action potentials and calcium transients in the mouse heart. *Journal of visualized experiments: JoVE*, (55), 2011.

[132] L.I. Daikhin, A.A. Kornyshev, and M. Urbakh. Double-layer capacitance on a rough metal surface. *Physical Review E*, 53(6):6192, 1996.

[133] L.I. Daikhin, A.A. Kornyshev, and M. Urbakh. Double layer capacitance on a rough metal surface: surface roughness measured by debye ruler. *Electrochimica acta*, 42(19):2853–2860, 1997.

[134] E.F. Douglass Jr, P.F. Driscoll, D. Liu, N.A. Burnham, C.R. Lambert, and W.G. McGimpsey. Effect of electrode roughness on the capacitive behavior of self-assembled monolayers. *Analytical chemistry*, 80(20):7670–7677, 2008.

[135] J.X. Cheng and X. S. Xie. *Coherent Raman scattering microscopy*. CRC press, 2016.